Die approbierte Originalversion dieser Dissertation ist in der Hauptbibliothek der Technischen Universität Wien aufgestellt und zugänglich.
http://www.ub.tuwien.ac.at

The approved original version of this thesis is available at the main library of the Vienna University of Technology.
http://www.ub.tuwien.ac.at/eng

Privatdoz. Sven Barth

Prof. Guido Kickelbick

TECHNISCHE UNIVERSITÄT WIEN
Vienna University of Technology

DISSERTATION

Homo- And Heterometallic Group 13 Alkoxides For Material Synthesis: Effects Of Precursor Design On Nanomaterial Composition

ausgeführt zur Erlangung des akademischen Grades eines
Doktors der technischen Wissenschaften

unter der Leitung von
Privatdoz. Dipl.-Chem. Dr.rer.nat. Sven Barth

E165
Institut für Materialchemie

eingereicht an der Technischen Universität Wien
Fakultät für Technische Chemie

von

Dipl.-Ing. Felix Biegger, BSc.
0726127
Fröbelgasse 62/10, 1160 Wien

Wien, April 2016

Dipl.-Ing. Felix Biegger

"… a scientist must be absolutely like a child.
If he sees a thing, he must say that he sees it,
whether it was what he thought he was going to see or not.
See first, think later, then test. But always see first.
Otherwise you will only see what you are expecting."

- From "*So long, and thanks for all the fish*" by Douglas Adams (1952-2001) -

STATUTORY DECLARATION

I herewith declare that I have authored this thesis independently, that I have not used other than the declared sources / resources, and that I have explicitly marked all material which has been quoted either literally or by content from the used sources.

EIDESSTATTLICHE ERKLÄRUNG

Ich erkläre hiermit an Eides statt, dass ich die vorliegende Dissertation selbstständig und ohne fremde Hilfe verfasst, andere als die angegebenen Quellen und Hilfsmittel nicht benutzt und die den benutzten Quellen wörtlich und inhaltlich entnommenen Stellen als solche erkenntlich gemacht habe.

PARTS OF THIS WORK HAVE BEEN PUBLISHED

- *"Synthesis and Characterisation of Thioether functionalised Gallium and Indium Alkoxides"* S. Barth, F. Biegger, M. Puchberger, *Dalton Transaction,* **2015**, 44, 16439-16445.
- *"Monomeric Aminoalcoholates of Aluminium(III), Gallium(III) and Indium(III)"* F. Biegger, S. Barth, *Monatshefte für Chemie,* **2016**, 147, 341-348

PARTS OF THIS WORK HAVE BEEN SUBMITTED FOR PUBLICATION

- *"Thioether-functionalised Gallium and Indium Alkoxides in Materials Synthesis"* F. Biegger, C. Rameshan, A. K. Opitz, C. Noll, T. Haunold, H. Lang and S. Barth, *New Journal of Chemistry*, **2016**, submitted

ACKNOWLEDGEMENT

There are several people without whom this thesis would never have seen the light of day.

First and foremost, I would like to thank my PhD supervisor Privatdoz. Dr. Sven Barth for guiding me through this thesis, for his patience, encouragement, countless SEM and EDX measurements and for his always open door.

Prof. Ulrich Schubert has my thanks for giving me the opportunity to work within his research group and for continuous support. I thank Prof. Guido Kickelbick for being my secondary examiner.

I also want to thank…

… Christoph Rameshan, Thomas Haunold and Kresimir Anic for XPS measurements.

… Alexander Opitz for impedance spectroscopy.

… Julian Noll and Prof. Heinrich Lang for TGA/DSC-MS measurements.

… Patrik for being a wonderful lab- and PhD buddy, for giving advice, making rude jokes, satisfying my coffee addiction, sharing my passion for guitars and electronics and for being a great friend.

… Michael S. for not blowing up the tube furnace with his high pressure cells after all and Lukas for keeping his attitude.

… Matthias C. for his introduction to single-crystal XRD measurements and for showing me the addicting world of electronics.

… Berthold, who never declined to help with twin refinement and crystal structure related problems.

… all present and former colleagues Alexey, Bettina, Catarina, Christian (for his never ending enthusiasm and work moral), Christine, Dennis, Dominik, Elisabeth, Greta, Harald, Jia, Jingxia, Johannes, Leonie, Martin (I still demand an axe!), Martina, Melitta, Michael P. (for LT- and 2D NMR), Miriam, Oliver, Paul (thanks for layout and grammar support), Sarah, Stefan C., Stephan R-P. and Yulia for various support, discussions and the good working atmosphere.

… Vera for her work during the summer and for always keeping up the good mood.

… Anita for organisational stuff, Horst for repairing countless pieces of glassware, Rupert for maintenance of various equipment and Werner for despite “not having any money” buying expensive equipment and keeping XRD machines in good shape.

… all members of WG Kirchner and Weinberger as well as the department of physical chemistry for the fun evenings and borrowed chemicals.

… Patrik, Paul, Alexey and Mathias for proof-reading parts of this thesis.

… all my friends for life outside the university. Special thanks to the “Jasser-Runde” (Christina, Julia, Theo, Paul, Pauli and Christoph) for many fun nights at the Käuzchen.

… Philipp D. for numerous concert visits and occupying me outside of university.

… my parents for enabling my studies, their words of encouragement and continuous support throughout the years. Special thanks to my mum for various IT support.

… my brother Philipp for taking longer with his PhD.

… my sister Madeleine for supply of 1st grade cookies. The institute will be forever indebted.

… the ‘Theater an der Wien’ for the canteen and the ridiculously big portions.

Thank you!

ABSTRACT

A series of homoleptic aminoalcoholates of aluminium, gallium and indium was synthesised and characterised. The monomeric nature of all alkoxides was indicated by NMR spectroscopy in solution and was confirmed for the solid state via single-crystal XRD. These monomeric derivatives are the first structurally characterised homoleptic alkoxides of these metals, which was achieved by a combination of coordinative saturation via the amine donor functionality and steric shielding.

Additionally, novel thioether functionalised gallium and indium alkoxides are presented. NMR spectroscopic investigations propose a monomeric state for these alkoxides with a weak interaction of the thioether moiety with the metal centre. In case of asymmetrically functionalised alcoholates featuring amine or ether donors alongside the thioether functionality, coordination of the latter is suppressed and only the stronger amine or ether donor interacts with the metal centre. These findings have been confirmed for the solid state via single-crystal XRD for a limited number of derivatives.

Applying these thioether functionalised alkoxides in molecule-to-material conversion processes showed their potency to act as single-source precursors for the formation of oxysulphide materials, which are typically prepared via multi-step or multi-source procedures. Employing LPCVD, gallium alkoxides were converted to amorphous $Ga_2O_{3-x}S_x$ thin films with strong dependence of the sulphide content of temperature and precursor species. Sulphide contents reached a maximum of x = 1.17 at low temperatures (400 °C) as obtained via EDX analysis. XPS measurements showed that thin films grown at low temperatures incorporated thioether fragments from incomplete decomposition. Pure sulphide containing oxide coatings could be obtained at temperatures >500 °C with sulphide contents up to 12 at%. Impedance spectroscopy of selected thin films deposited on interdigitated electrodes showed drastically increased electrical conductivity accompanied by lower activation energy upon oxysulphide formation when compared to a Ga_2O_3 reference.

Investigations of the mechanism of sulphide incorporation via TGA-MS revealed a strong supportive role of the amino functionality in asymmetric aminoalcoholates leading to *in situ* formation of H_2S as a potent sulphidisation agent. Using hot-injection methods all alkoxides could be converted into oxysulphide sub-micron particles exhibiting high sulphide contents. Indium based materials showed particularly high sulphide contents with pure In_2S_3 phases found in XRD analysis, most likely because of lowered In-O bond strength and hence facilitated conversion to the sulphide. AACVD processes using indium based alkoxides showed the formation of sulphide rich $In_2O_{3-x}S_x$ thin films and 1D nanostructures.

Lastly, a series of transition metal gallates $[M^{II}Ga_2(O^tBu)_8]$ was prepared and characterised via single-crystal XRD showing the expected spirocyclic arrangement. Using them in sol-gel and LPCVD processes led to the formation of the respective $M^{II}Ga_2O_4$ spinels for M=Co, Ni. In contrast, for M=Fe, non-stoichiometric deposits and phase separation was observed, most likely caused by susceptibility of the precursor towards oxidation. Copper gallates exhibited thermal instability and increased reactivity leading to copper deficient thin film deposits and phase separation upon sol-gel processing.

KURZFASSUNG

Die vorliegende Arbeit beschreibt die Synthese und Charakterisierung von neuen homoleptischen Aluminium, Gallium und Indium Aminoalkoholaten, deren monomere Nuklearität anhand von Einkristall-XRD und NMR-Spektroskopie gezeigt werden konnte. Die präsentierten Verbindungen sind die ersten literaturbekannten Beispiele für homoleptische, monomere Alkoxide dieser Metalle, was durch effektive Kombination von koordinativer Sättigung und sterischer Abschirmung erzielt wurde.

Des Weiteren wird eine Serie von Thioether-funktionalisierten Gallium und Indium Alkoxiden untersucht. Die Ergebnisse der NMR-Spektroskopie deuten auf die Bildung monomerer Spezies in Lösung hin und zeigen eine schwache Wechselwirkung zwischen Thioether und Metallzentrum. Im Falle von asymmetrisch funktionalisierten Alkoxiden, die sowohl Thioether- als auch Amino- bzw. Ethergruppen beinhalten, wird die Koordination des Thioethers durch die stärkeren Donoren unterdrückt. Diese Resultate konnten mittels Einkristall-XRD für einige Verbindungen für den Festkörper bestätigt werden.

Die neuen Thioether-funktionalisierten Alkoxide konnten als molekulare Vorstufen zur *in situ* Herstellung von Oxysulfiden verwendet werden, die üblicherweise über mehrstufige Prozesse oder aus mehreren Vorstufen erzeugt werden. Dabei wurden über LPCVD amorphe Gallium Oxysulfid-Schichten $Ga_2O_{3-x}S_x$ hergestellt, deren Sulfidgehalt über Prozesstemperatur und Auswahl der Vorstufe gesteuert werden konnte. Anschließende EDX Analysen der Filme ergaben dabei maximale Sulfidgehalte von x = 1.17 bei 400 °C, jedoch wurde über XPS gezeigt, dass durch unvollständige Zersetzung bei niedrigen Temperaturen zusätzlich Thioether-Fragmente in die Schicht eingebaut wurden. Reine Oxysulfid-Beschichtungen mit Schwefelgehalten von bis zu 12 at% konnten bei Temperaturen >500 °C erzeugt werden. Die elektrische Leitfähigkeit von ausgesuchten $Ga_2O_{3-x}S_x$ Dünnfilmproben konnte über Impedanzspektroskopie bestimmt werden, wobei im Vergleich zu reinem Ga_2O_3 eine starke Erhöhung der Leitfähigkeit und Erniedrigung der Aktivierungsenergie festgestellt wurde.

Analysen des Zersetzungsverhaltens über TGA-MS deuteten auf eine starke unterstützende Rolle der Aminofunktionalität in asymmetrischen Aminoalkoholaten hin, da eine signifikant erhöhte Menge H_2S nachgewiesen werden konnte, welche die *in situ* Bildung der Oxysulfide ermöglicht. Über Heißinjektions-Methoden konnten zudem alle Thioether-funktionalisierten Vorstufen in Oxysulfid-Partikel umgewandelt werden, wobei für Indium basierte Systeme besonders hohe Sulfidgehalte und phasenreines In_2S_3 nachgewiesen werden konnte, was vermutlich auf die geringere In-O Bindungsenergie und dadurch vereinfachte Sulfidbildung zurückzuführen ist. Darüber hinaus konnten aus Indium Alkoxiden mittels AACVD Prozess $In_2O_{3-x}S_x$ Dünnfilme und 1D Nanostrukturen mit hohen Sulfidgehalten hergestellt werden.

Abschließend wurde eine Reihe an Übergangsmetall-Gallaten $[M^{II}Ga_2(O^tBu)_8]$ hergestellt und über Einkristall-XRD analysiert, wodurch die erwartete spirozyklische Struktur bestimmt werden konnte. Sol-Gel- und LPCVD-Prozesse ermöglichten die Umwandlung zu Spinellverbindungen der Zusammensetzung MGa_2O_4 für M=Co, Ni. Im Gegensatz dazu konnte für M=Fe bisher kein phasenreines $FeGa_2O_4$ erzeugt werden, was auf die hohe Sauerstoffsensibilität der Vorstufe und des amorphen Oxids zurückzuführen ist. Kupfer-Gallate wiesen zudem thermische Empfindlichkeit und erhöhte Hydrolyseempfindlichkeit auf, was zu Kupferverarmung in Dünnfilmen und Phasenseparation im Sol-Gel-Prozess führte.

LIST OF COMPOUNDS

Abbreviation	Formula	Systematic name
Al1	$Al(OCH(CH_2NMe_2)_2)_3$	Aluminium tris(1,3-bis(dimethylamino)propan-2-olate)
Al2	$Al(OCH(CH_2NEt_2)_2)_3$	Aluminium tris(1,3-bis(diethylamino)propan-2-olate)
Ga1	$Ga(OCH(CH_2NMe_2)_2)_3$	Gallium tris(1,3-bis(dimethylamino)propan-2-olate)
Ga2	$Ga(OCH(CH_2NEt_2)_2)_3$	Gallium tris(1,3-bis(diethylamino)propan-2-olate)
Ga3	$Ga(OCH(CH_2S^nBu)_2)_3$	Gallium tris(1,3-bis(^{n}butylthio)propan-2-olate)
Ga4	$Ga(OCH(CH_2S^tBu)_2)_3$	Gallium tris(1,3-bis(^{t}butylthio)propan-2-olate)
Ga5	$Ga(OCH(CH_2S^nBu)(CH_2NEt_2))_3$	Gallium tris(1-^{n}butylthio-3-diethylamino-2-propanolate)
Ga6	$Ga(OCH(CH_2S^tBu)(CH_2NEt_2))_3$	Gallium tris(1-^{t}butylthio-3-diethylamino-2-propanolate)
Ga7	$Ga(OCEt(CH_2S^nBu)_2)_3$	Gallium tris(1-^{n}butylthio-2-^{n}butylthiomethyl-2-butanolate)
Ga8	$Ga(OCEt(CH_2S^tBu)_2)_3$	Gallium tris(1-^{t}butylthio-2-^{t}butylthiomethyl-2-butanolate)
Ga9	$Ga(OCEt(CH_2S^nBu)(CH_2NEt_2))_3$	Gallium tris(1-^{n}butylthio-2-(diethylamino)methyl-2-butanolate)
Ga10	$Ga(OCEt(CH_2S^tBu)(CH_2NEt_2))_3$	Gallium tris(1-^{t}butylthio-2-(diethylamino)methyl-2-butanolate)
Ga11	$Ga(OCH(CH_2S^nBu)(CH_2OEt))_3$	Gallium tris(1-^{n}butylthio-3-ethoxy-2-propanolate)
Ga12	$Ga(OCH(CH_2S^tBu)(CH_2OEt))_3$	Gallium tris(1-^{t}butylthio-3-ethoxy-2-propanolate)
In1	$In(OCH(CH_2NMe_2)_2)_3$	Indium tris(1,3-bis(dimethylamino)propan-2-olate)
In2	$In(OCH(CH_2NEt_2)_2)_3$	Indium tris(1,3-bis(diethylamino)propan-2-olate)
In3	$In(OCH(CH_2S^nBu)_2)_3$	Indium tris(1,3-bis(^{n}butylthio)propan-2-olate)
In4	$In(OCH(CH_2S^tBu)_2)_3$	Indium tris(1,3-bis(^{t}butylthio)propan-2-olate)
In5	$In(OCH(CH_2S^nBu)(CH_2NEt_2))_3$	Indium tris(1-^{n}butylthio-3-diethylamino-2-propanolate)
In6	$In(OCH(CH_2S^tBu)(CH_2NEt_2))_3$	Indium tris(1-^{t}butylthio-3-diethylamino-2-propanolate)
In7	$In(OCEt(CH_2S^nBu)_2)_3$	Indium tris(1-^{n}butylthio-2-^{n}butylthiomethyl-2-butanolate)
In8	$In(OCEt(CH_2S^tBu)_2)_3$	Indium tris(1-^{t}butylthio-2-^{t}butylthiomethyl-2-butanolate)
In9	$In(OCEt(CH_2S^nBu)(CH_2NEt_2))_3$	Indium tris(1-^{n}butylthio-2-(diethylamino)methyl-2-butanolate)
In10	$In(OCEt(CH_2S^tBu)(CH_2NEt_2))_3$	Indium tris(1-^{t}butylthio-2-(diethylamino)methyl-2-butanolate)
In11	$In(OCH(CH_2S^nBu)(CH_2OEt))_3$	Indium tris(1-^{n}butylthio-3-ethoxy-2-propanolate)
In12	$In(OCH(CH_2S^tBu)(CH_2OEt))_3$	Indium tris(1-^{t}butylthio-3-ethoxy-2-propanolate)

FeGa	$FeGa_2(O^tBu)_8$	Tetrakis(μ_2-^{t}butylato)-tetrakis(^{t}butylato)-digallium-iron(II)
CoGa	$CoGa_2(O^tBu)_8$	Tetrakis(μ_2-^{t}butylato)-tetrakis(^{t}butylato)-digallium-cobalt(II)
NiGa	$NiGa_2(O^tBu)_8$	Tetrakis(μ_2-^{t}butylato)-tetrakis(^{t}butylato)-digallium-nickel(II)
CuGa	$CuGa_2(O^tBu)_8$	Tetrakis(μ_2-^{t}butylato)-tetrakis(^{t}butylato)-digallium-copper(II)

TABLE OF CONTENTS

Acknowledgement V

Abstract VIII

Kurzfassung IX

List of compounds X

Chapter 1 Introduction 1

1.1 Metal alkoxides 2

1.1.1 Definition, structural aspects and functionalisation 2

1.1.2 Synthesis of metal alkoxides 6

1.1.3 Heterometallic alkoxides 8

1.1.4 Applications of metal alkoxides 10

1.2 Molecule-to-material processes 10

1.2.1 Chemical vapour deposition 10

1.2.2 Aerosol-assisted CVD 14

1.2.3 Sol-gel processing 15

1.2.4 Hot-injection methods 16

1.3 Thermolysis mechanisms and incorporation of heteroatoms 16

1.4 Materials targeted in molecule-to-material conversion 18

1.4.1 Gallium oxides 18

1.4.2 Gallium sulphides 19

1.4.3 Gallium oxysulphides 20

1.4.4 Indium oxides 21

1.4.5 Indium sulphides 22

1.4.6 Indium oxysulphides 23

1.4.7 Heterobimetallic oxides 24

1.5 Motivation and research goals 25

Chapter 2 Results and Discussion 27

2.1 Aminoalcoholates of Al(III), Ga(III), In(III) 28

2.2 Coordination behaviour of thioether functionalised gallium and indium alkoxides 34

2.3 Molecule-to-material conversion of thioether functionalised alkoxides 45

2.3.1 Thin film deposition via LPCVD 45

2.3.2 Electrical properties of $Ga_2O_{3-x}S_x$ thin films 51
2.3.3 Synthesis of powders via hot-injection pyrolysis 54
2.3.4 Investigation of the decomposition mechanism 57
2.3.5 Synthesis of thin films and 1D structures via AACVD 59
2.4 Heterometallic alkoxides 67
2.4.1 Synthesis and characterisation 67
2.4.2 Molecule-to-material conversion of heterometallic alkoxides 71
2.5 Summary and Conclusion 75
Chapter 3 Experimental 79
3.1 General methods and materials 80
3.2 Instrumentation 80
3.3 General procedures 83
3.3.1 Low-pressure chemical vapour deposition 83
3.3.2 Hot-injection pyrolysis 84
3.3.3 Aerosol-assisted chemical vapour deposition 84
3.3.4 Sol-Gel processing of heterometallic tert.-butanolates 85
3.4 Syntheses 85
Chapter 4 Appendix 97
4.1 Glossary 98
4.2 List of figures, schemes and tables 100
4.3 List of references 103
4.4 Crystallographic data 121
4.5 Curriculum Vitae 135

CHAPTER 1

INTRODUCTION

"Marconi is a good fellow. Let him continue.

He is using seventeen of my patents."

- Nikola Tesla (1856–1943) -

Material research and development is an ever growing field of science and technology because of increasing demand for novel materials – whether for everyday use or highly sophisticated applications. Especially uniting several properties, e.g. conductivity, hardness, brittleness, luminescence and so forth, in one material to meet the needs of the designated application is still a very demanding task and as such a continuous challenge for researchers of various scientific disciplines. Therefore, fundamental knowledge about molecular interactions and resulting structures on both the atomic and macroscopic scale is of great importance for understanding how certain properties can be achieved and influenced.

During the last several decades, discovery, utilisation and vast improvement of semiconductors had one of, if not the biggest impact on modern society.[1] Today, semiconductors are an essential part of everyday live and can be found in nearly every device ranging from discrete electronic elements, such as diodes or transistors, to solar panels, flexible displays and computer processors. In addition, the demand for miniaturisation, e.g. for increasing processing power or storage devices, as well as the concomitant development of nanotechnologies necessitate the development of novel precursor systems.[2, 3]

Especially in light of the structure-properties relationship of functional materials, bottom-up approaches have gained increased attention. These molecule-to-material processes build up materials from molecular building blocks allowing for better control and selective tuning of the material's properties.[4, 5] Over the years, several molecular precursor classes for semiconductors have been developed, each showing their distinct set of advantages and drawbacks. Although metal alkoxides have been used in synthetic chemistry as early as the 1890's, this class of compounds has been readily applied for materials synthesis purposes as a result of their structural diversity and ease of chemical modification.[6]

1.1 METAL ALKOXIDES

1.1.1 Definition, structural aspects and functionalisation

Per definition, metal alkoxides or alcoholates are substances with the general formula $[M(OR)_x]_n$, where *R* is a saturated alkyl group, *M* a metal or metalloid with valency *x* and *n* the degree of molecular association.[7, 8] In contrast, the structurally related class of aryloxides features an aromatic group leading to different physicochemical properties, e.g. due to higher acidity of the phenol group compared to aliphatic alcohols.

Alkoxides show a set of unique features, most of which arise from the rather high electropositivity of the central atom. First off, judging only from the difference in electronegativity between metal centre and alkoxo oxygen one would expect ionic character of the bond, especially for

highly electropositive elements such as alkali metals. However, metal alkoxides feature mostly covalent bond character, which leads to solubility in various organic solvents as well as fairly high volatility.[8] This phenomenon is explained by a number of factors including (i) partial π-bonding character via donation of electron density from occupied p-orbitals of the alkoxo oxygen into empty orbitals of the metal centre with suitable π-geometry as shown in figure 1-1,[9, 10] (ii) inductive effects of the alkyl chain reducing the electron pulling effect of the oxygen atom,[11, 12] and (iii) the formation of alkoxo bridges leading to oligomeric compounds (figure 1-1 (d)).[13-15]

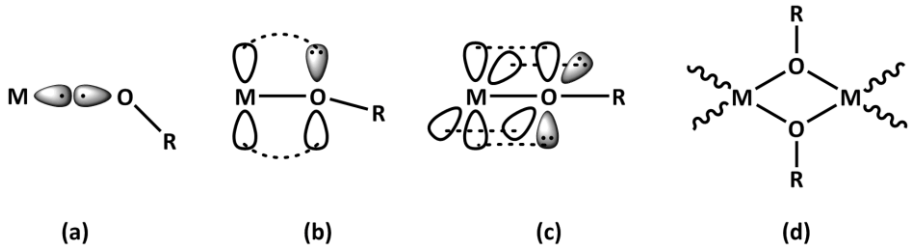

Figure 1-1: Schematic illustration of (a) σ- and (b,c) π-bonding and (d) μ_2-alkoxo bridges in metal alkoxides. Redrawn from reference [9].

The formation of alkoxo bridges is the second striking feature of metal alkoxides. It is based on the fact that metals generally exhibit a coordination number exceeding their valency.[16, 17] For instance, it is well known that the most stable valency of titanium is +IV; its preferred coordination number, however, is six, leading to coordinative expansion and the formation of hypervalent coordination compounds. The degree of oligomerisation is highly dependent on a number of factors. The most important influences are (i) the steric demand of the alkyl rest, especially branching at C_α,[12, 18-21] (ii) the ionic radius and Lewis acidity of the metal centre[22-25] and (iii) the choice of solvent.[13] Generally, the degree of oligomerisation increases with size and Lewis acidity of the metal centre and decreases with increasing steric demand of the alkoxo ligands.[8] As such, methoxides often form polymeric derivatives while *tertiary*-butoxides (^{t}butoxides) tend to form smaller oligomers, e.g. a dimer in case of gallium.[26, 27] Choosing donating solvents, such as ethers or amines, generally leads to a decrease of nuclearity because of coordination of solvent molecules, which in turn block coordination sites and thus can inhibit alkoxo bridging.[28, 29]

The degree of oligomerisation obviously has drastic impacts on the physicochemical properties of metal alkoxides. Especially solubility, volatility and reactivity are often key features to be applicable in material synthesis. These properties generally decrease with increasing nuclearity of the metal alkoxide.[30] However, in most cases it is desirable to combine good solubility or volatility with moderate reactivity.[31] The latter is particularly important in concern of handling and storage of precursors. Therefore, sophisticated precursor design is of great importance to achieve tailored properties for specific application.

There are mainly two approaches for tuning the properties and degree of oligomerisation of metal alkoxides. The first route is to use sterically demanding ligands to effectively shield the metal centre and thus inhibit formation of bridging alkoxide moieties. This approach has been thoroughly investigated during early works of alkoxide chemistry and has been reviewed several times in recent years.[22, 32, 33] For example, early studies by the groups of Bradley and Mehrotra clearly showed a decrease in aggregation of aluminium, titanium and zirconium amyloxides with increasing steric demand.[12] They could also illustrate that steric factors overweight inductive effects of the alkyl chain as neopentoxides showed equal nuclearity to secondary amyloxides rather than primary ones. It should be noted though that using sterically demanding ligands can, while lowering the nuclearity, still lead to non-volatile compounds due to increased molecular weights of the bulky ligands.[34]

The second possibility is to influence aggregation and thus the alkoxide's properties via coordinative saturation of the metal centre. This approach uses additional donating groups to achieve the preferred coordination sphere and thus blocking of coordination sites rendering them unavailable for alkoxo bridging. However, it has to be kept in mind that usually strong donors are necessary as their coordination has to compete with the formation of alkoxo bridges, which in turn can be thermodynamically favourable especially in case of oxophilic metals and sterically less demanding alkoxo groups.[8, 28]

One approach towards coordinative saturation with donating groups is to add donating molecules, such as ethers, alcohols or amines. In fact, many homoleptic alkoxides crystallise as neutral alcohol adducts from the respective alcohols, such as $[Zr(O^iPr)_4 \cdot HO^iPr]$ (^iPr=isopropyl, $(CH_3)_2CH$-).[35] The coordinating alcohol can however be removed rather easily by either applying high vacuum or recrystallisation from aprotic solvents such as *normal*-hexane (^{n}hexane), which demonstrates the comparably weak dative bonding of the donor. Other examples of donor-stabilised monomeric alkoxides were presented by Hoffman and co-workers, who showed easy conversion of dimeric indium ^{t}butoxide $[In(O^tBu)_3]_2$ to a monomeric state $[In(O^tBu)_3 \cdot Me_2Npy]$ (Me=methyl, CH_3-) simply by adding a Lewis basic pyridine (py) derivative.[21, 36]

Another method to achieve coordinative saturation is to use chelating ligands, in other words donating groups, which are covalently bound to the alkoxo ligand itself. This includes the well-known class of ß-diketonates and ß-ketoesters, but also alcohols with covalently bound donor moieties in α- or ß-position. Additionally, there have been several reports of bi- or multidentate alcohols being applied in alkoxide chemistry; however, these are almost exclusively applied in heteroleptic derivatives or for metals with high valency.[37-40] In addition, for alkoxides employing polyols such as triethanolamine ($N(C_2H_4OH)_3$) extensive hydrogen bridging can be observed, which is of course unfavourable for achieving a lowered nuclearity, but can act favourably in sol-gel processing (*vide infra*).[41]

ß-diketonates usually show very strong M-O bonds and chelating effects leading to high volatility, good solubility in organic solvents and moderate hydrolysis rates. Thus, they are often applied in synthesis of oxide materials in gas-phase and solution-based processes.[42, 43] For instance, Devi and co-workers demonstrated the applicability of a series of gallium malonates in metal-organic chemical

vapour deposition (MOCVD) of Ga_2O_3.[44] The precursors could be handled safely in air and showed high deposition rates. However, thin film samples exhibited increased amounts of carbon contamination. Similarly, MOCVD experiments of titanium ß-ketoamides produced TiO_2 coatings, but they also exhibited carbon contaminations at high temperatures despite the postulated preferable decomposition pathways of ß-ketoamides.[45] Carbon contamination is a commonly found drawback of ß-diketonates in pyrolytic chemical vapour deposition (CVD) processes, when not using additional oxidising gases or post growth annealing.[34] However, they are still widely used in atomic layer deposition (ALD) or sol-gel processing, where this drawback can be circumvented.[30, 31, 43, 46-48]

Ethers and amines are by far the most commonly applied functional groups in alkanols with a secondary coordination site, similar to their use as external donors (e.g. THF, py; THF=tetrahydrofuran).[49-60] In fact, literature reports so far have almost exclusively described ethers and amines for donor stabilisation. This is mainly due to the fact that ethers and amines are known to coordinate as σ-donors that can introduce intramolecular back-biting by formation of strong dative bonds with most metals. The latter can in turn be explained with the hard and soft acids and bases (HSAB) principles, according to which hard Lewis bases prefer coordination to hard acids, while soft bases preferably bond to soft acids.[61, 62] As ethers and amines both can be categorised as hard Lewis bases and metal atoms in high oxidation states are considered hard Lewis acids, they complement each other well.[63] Literature reports on other donor types are therefore very limited, however some reports on phosphine functionalisation can be found.[64, 65] These reports show that also softer Lewis bases are able to stabilise low nuclearity in metal alkoxides even if the observed dative bond to the hard metal centre is weaker.

Recently, a large number of donor functionalised heteroleptic alkoxides, in particular of group 13 metals, have been prepared and reviewed by the group of C. J. Carmalt.[9, 66-69] They were able to conclusively show the stabilisation of low nuclearity, i.e. monomeric or dimeric molecules, via the use of ether or amine functionalisation. They also demonstrated that the low nuclearity is retained even upon volatilisation via coordination of the donor leading to good applicability in gas phase processes for the synthesis of oxide materials.[70]

Donor groups are most often applied in the ß-position because of the thermodynamically favoured formation of a five-membered metallacycle as opposed to a four-cycled one in case α-functionalisation.[70] However, as shown in figure 1-2, even simple bidentate donor functionalised alkoxo ligands, e.g. methoxyethanol (HOC_2H_4OMe) or dimethylaminoethanol ($HOC_2H_4NMe_2$), exhibit a plethora of possible coordination modes, ranging from non-chelating terminal coordination to μ_3-bridging chelating coordination.[41]

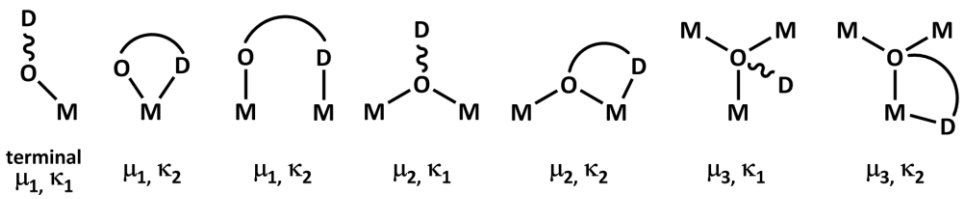

Figure 1-2: Possible coordination modes for a bidentate donor functionalised alkoxo ligand. Redrawn from reference [46].

Besides bidentate alkoxo ligands, also multidentate species have been used. Depending on ligand design and especially the rigidity and length of the organic backbone, it was found that often not all available donors actually coordinate to metal centres.[53, 71] This can be the result of either strain on the organic backbone of the ligand upon multiple coordination or because of steric overcrowding depending on the organic groups at the donor. This basically leads to one or more pending donor arms, which can be seen as further steric shielding.

This increased amount of structural possibilities complicates predicting structures for a certain metal-ligand combination. In addition, it was found that donor functionalisation alone is often not enough to ensure a monomeric nuclearity of metal alkoxides. This is attributed to the fact that donor sites either remain in a non-coordinating arrangement, or that the alkoxo group can still form a bridge between metal centres despite coordinative saturation via the donating moiety.[41, 57, 66] Therefore, it became common practise to use a combination of donor functionalisation and steric bulk, e.g. branching at C_α using secondary or tertiary alcoholates.[72-74]

In conclusion, functionalisation and modification of metal alkoxides remains a demanding task and is strongly dependent on the desired properties (volatility, reactivity, decomposition, solubility, etc.) and thus on the application. Therefore, it is often necessary to employ tailor-made ligand species to finely balance steric demand, donor capabilities and molecular weight.

1.1.2 Synthesis of metal alkoxides

Over the years, a plethora of different synthesis routes was developed accessing alkoxides of almost every main, transition and even f-group metals.[8] All synthesis methods show certain advantages and drawbacks and the most suitable has to be chosen, which is mostly dependent on the metal centre involved. For instance, alkoxides of very electropositive metals, such as alkali metals, can be directly synthesised from the metal and alcohol under formation of H_2 gas with near quantitative yields without major drawbacks.[75, 76] For less reactive metals, however, synthesis approaches starting from metal halides are a common choice.

When starting from metal halides, the most common route is transmetallation, also referred to as salt elimination or metathesis. As shown in scheme 1-1, a metal halide is reacted with a reactive alkali metal alkoxide, which leads to the formation of the desired metal alkoxide and the alkali metal

salt. Metathesis reactions generally proceed in high yields due to the thermodynamically favoured formation of the alkali salt.[77, 78] In addition, using non-polar solvents, such as toluene or hexane, will lead to the precipitation of the alkali salt, which results in shifting of the equilibrium towards the product side.[79] Furthermore, work-up is simplified as the precipitate can be easily removed by filtration. However, dependent on the alkali metal and size of the alcoholate ligands, retention of the alkali metal and halide are possible, which results in anionic at-complexes or bridged species.[80, 81] Besides metathesis reactions, it is also possible to directly react metal halides with the respective alcohol. However, the reaction does not always proceed to completion potentially yielding mixed alkoxo-halides[82, 83] or simple alcohol adducts of the halides.[84-86] In addition, the release of corrosive gases can damage the equipment or lead to unwanted side reactions.

$$MX_z + z/n\,[M'OR]_n \longrightarrow 1/m\,[M(OR)_z]_m + z\,M'X$$

X = Cl, Br, I
M' = Li, Na, K

Scheme 1–1: Transmetallation reaction.

Alcohol exchange reactions, shown in scheme 1-2, are another viable option for the synthesis of homo- and heteroleptic metal alkoxides.[23, 87, 88] However, while the reaction itself is straightforward, it is a classic equilibrium reaction and thus suffers from some drawbacks.[89] The alcoholysis reaction rate strongly depends on the steric demand of the alcohols involved and the resulting shielding of the metal centre.[90, 91] Therefore, heteroleptic alcoholates are often produced in particular for bulky tertiary alcohols. Full conversion to homoleptic alkoxides usually requires prolonged reaction times and removal of the liberated alcohol to shift the equilibrium towards the targeted product.[23, 92]

$$1/n\,[M(OR)_x]_n + x\,R'OH \rightleftharpoons 1/m\,[M(OR')_x]_m + x\,ROH$$

Scheme 1–2: Alcohol exchange reactions.

Another very common synthesis route employs metal amides as starting materials, as shown in scheme 1-3. This approach takes advantage of the highly oxophilic character of most metals in combination with the good leaving group character and volatility of most amines.[93-95] For these reasons, alcoholysis of metal amides is usually a comparably fast reaction with good yields and high purity of the products.[96] In general any secondary amide is applicable, but especially hexamethyldisilazides (HMDS) have gained increased attention. HMDS derivatives often exhibit low nuclearity, which results in high volatility and thus easy purification via sublimation. In addition, it ensures Lewis acidic metal centres, which undergo fast alcoholysis.[97, 98] Another advantage of the amide route is the high selectivity of the alcoholysis reaction. For instance, heteroleptic halide amide precursors will selectively exchange only the amide group for an alcoholate enabling easy access to heteroleptic metal alkoxides by subsequent substitution of the halide via transmetallation.[67, 99]

$$1/n\ [M(NR_2)_x]_n + x\ R'OH \longrightarrow 1/m\ [M(OR')_x]_m + x\ HNR_2$$

Scheme 1–3: Alcoholysis of metal amides.

Besides the already mentioned synthesis routes, there are several other methods to form metal alkoxides with potential starting compounds including hydrides, alkyls, oxides or hydroxides. These methods have not been used in the presented work as they have limited suitability for the development of new derivatives under laboratory conditions and therefore will not be discussed in more detail here. Electrochemical synthesis, for instance, is more important for large scale production, but has limited use for fundamental research. For detailed information about these synthesis routes refer to review articles by Mehrotra and Bradley.[8, 13, 28, 75] Lastly, it should be mentioned that metal alkoxides are highly sensitive to atmospheric moisture due to the Lewis acidity of the metal centre. Thus, careful preparation of glassware, desiccating all solvents and reagents as well as working under inert atmosphere is always necessary.

1.1.3 Heterometallic alkoxides

Heterometallic alkoxides, i.e. alkoxides featuring at least two different metals, are another class of important precursors that have gained increased attention over the last few decades and have been reviewed several times.[37, 41, 100, 101] This is mainly due to their applicability in synthesis of mixed-metal oxide materials and the ease of chemical modification of the precursor molecules with respect to reactivity, volatility and metal ratio.

As mentioned before, retention of metal halides in metathesis reactions is a frequently observed phenomenon, which is generally avoided in the synthesis of homometallic alkoxides. However, it represents a possibility for simple access to heterometallic alkoxides, especially for small alkali metal ions, such as lithium, which is readily retained in several known alkoxides. For example, anodic synthesis of $Ni(O^iPr)_2$ in LiCl electrolyte solution gave $[Ni(O^iPr)_2ClLi(HO^iPr)]_2$, which can be seen as a Lewis acid-base adduct of $[Ni(O^iPr)_2Cl]^-$ and $[Li(HO^iPr)]^+$ units.[102] Similarly, heterometallic, heteroleptic halide alkoxides (mainly chlorine) can often be synthesised directly from a metal alkoxide and a metal halide; in particular for low coordinate species with sterically demanding ligands, where chlorine can adopt a bridging position.[100, 103, 104]

A second straightforward approach to heterometallic alkoxides is simple mixing of two homometallic alkoxides to form acid-base adducts, as shown in scheme 1-4. Unfortunately, the metal ratio of the heterometallic alkoxide often differs drastically from the employed alkoxide mix and is hard to predict.[101, 105] For instance, mixing $[Pb(O^iPr)_2]_3$ and $[Zr(O^iPr)_4]$ in a 1:1 molar ratio does not lead to the expected 1:1 heterometallic alkoxides. Instead, a mixture of $[Pb_4Zr_2(O^iPr)_{16}]$ and $[Pb_2Zr_4(O^iPr)_{20}]$ is formed.[106, 107] In addition, some metal alkoxides do not show any reactivity towards

formation of a heterometallic complex at all. As such, $[Sn(O^tBu)_2]_2$ readily reacts with $[Sr(O^tBu)_2]_n$ giving the expected complex $[SrSn_2(O^tBu)_6]$, but does not undergo reaction with $[Ca(O^tBu)_2]_n$. These issues can be sometimes circumvented via *in situ* generation of the alcoholates.[108, 109] This approach is still common practise mostly for homoleptic heterometallic alkoxides incorporating alkali metals, which usually form the desired adducts based on the neutralisation of acidic and basic alkoxides.[110-112]

$$y/n\ [M(OR)_x]_n + y'/n'\ [M'(OR')_{x'}]_{n'} \longrightarrow [M_yM'_{y'}(OR)_x(OR')_{x'}]_m$$

Scheme 1–4: Lewis acid-base adduct formation for the synthesis of heterometallic alkoxides.

Alkali metal derivatives are often used as synthons for subsequent transmetallation reactions to access other heterometallic species.[113] Treating an alkali heterometallic alkoxide with metal halides generally results in the formation of the alkali metal halide and the respective heterometallic alkoxide as shown in scheme 1-5.

$$1/n\ [M_yM'_{y'}(OR)_z]_n + y'/y''\ M''X_{y''} \longrightarrow 1/m\ [M_yM''_{y'/y''}(OR)_z]_m + y'\ M'X$$

M' = Alkali metal
X = Halide

Scheme 1–5: Transmetallation reaction for the synthesis of heterometallic alkoxides.

Heterometallic alkoxides show similar structural features compared to homometallic derivatives and thus their reactivity is also comparable. For instance, they can be readily functionalised via ligand exchange reactions and also donor functionalised alcohols can be used to tailor the properties towards a certain application.[58] However, the diversity of coordination modes for even simple donor functionalised alcohols can lead to dissociation of the heterometallic species making control over metal ratios a difficult task. For example, it was reported that even the addition of diethylether or THF can be enough to cause dissociation of $[BaCu(O^tBu)_2(thd)_2]$ (thd=tetramethlyheptanedione) into homometallates.[114] Similarly, mixing $[Y(thd)_3]$ and $[Cu(O(CH_2)_2NMe_2)_2]$ will result in a mixture of hetero- and homometallic alkoxides due to ligand exchange reactions.[115] As a consequence it is common practice to employ simple alcoholates to control the metal ratios in these heterometallic alkoxides.

1.1.4 Applications of metal alkoxides

Metal alkoxides have been widely used in several applications due to their wide variety of tuneable features. Consequently, they have been mainly employed as precursors in the synthesis of oxide materials and as catalysts in organic chemistry.[116, 117] Generally speaking, methods for the synthesis of oxide materials can be separated into gas phase processes, such as CVD and ALD, and solution based methods, e.g. sol-gel processing. These techniques, their requirements for precursors and detailed applications will be discussed in chapter 1.2.

Applications of alkoxides as catalysts in organic chemistry are mostly centred around polymerisation reactions of cyclic esters, carbonates or olefins as well as oxidation and reduction reactions, such as the Meerwein-Ponndorf-Verley reaction.[117-119] All of these reactions take advantage of the Lewis acidity of metal alkoxides, often in combination with oxophilic character of the central atom. This enables fast coordination of additional species leading to steric confinement of the coordinated species as well as their electronic activation as a result of electron transfer upon coordination.

Alkoxide mediated ring-opening polymerisation of cyclic esters and carbonates as a way to obtain biodegradable polymers (especially polylactides) has mostly been limited to the more acidic metals such as Al^{III}, Mg^{II}, Ti^{IV} and Zr^{IV} – also for economic reasons.[120] However, over the last years, also heavier group 13 metal alkoxides have shown promising results with high activities towards several lactones.[121] Besides polycondensation reactions, metal alkoxide catalysts have been recently applied in insertion polymerisation of olefins as potential alternatives for classic Ziegler-Natta catalysts.[122, 123]

1.2 MOLECULE-TO-MATERIAL PROCESSES

1.2.1 Chemical vapour deposition

Chemical vapour deposition (CVD) is per definition a gas phase process, which results in the deposition of a solid material via a chemical reaction on an activated (usually heated) surface.[124, 125] Generally, the process constitutes of homogenous gas phase reactions and heterogeneous reactions occurring on or near the surface of a thermally activated substrate.

CVD was initially developed as early as the 1890 for the deposition of tungsten on filaments in light bulbs, but grew into one of the most important deposition techniques over the last decades, in particular in the electronics industry and for deposition of hard and protective coatings.[126, 127] Nowadays, a wide array of different materials can be produced via CVD processes including, but not limited to, conductors (Al, Pt, Rh, etc.),[60, 128, 129] semiconductors (Si, Ge, II-VI, III-V, etc.)[130-134] and

ceramics (oxides, borides, silicides, nitrides, etc.).[135-137] Besides a variety of materials, CVD also offers the opportunity to deposit various morphologies, such as particles, thin film coatings or one-dimensional (1D) nanostructures as well as the possibility for homo- and heteroepitaxial growth.[138-140] The morphology of the deposit strongly depends on the deposition parameters, such as temperature and growth rate, but also on the substrate. For instance, epitaxial growth requires close matching of lattice parameters of growing layer and underlying substrate.[141]

Over the years, several specific CVD techniques have been developed, which either differ from classic thermally activated CVD in the way of activation or specify certain aspects of the process (e.g. precursor delivery system, operational pressure, etc.). Low-pressure CVD (LPCVD) for example represents classic thermally activated CVD under reduced pressure, where thermal activation is usually achieved via resistive or high-frequency heating.[127] LPCVD was mainly developed to either use precursors with low volatility or to increase precursor flow in mass transport/diffusion limited processes (*vide infra*). Plasma enhanced CVD (PECVD) employs plasma for thermal activation and has the major advantage of lowered deposition temperatures while still retaining good deposition rates. However, PECVD equipment is far more complex and thus more expensive.[142] MOCVD on the other hand is classified by the use of metal-organic precursors, which often have the advantage of lowered decomposition temperatures.[143-145] Aerosol-assisted CVD (AACVD) relies on precursor supply via an aerosol rather than the usual volatilisation of a pure precursor. AACVD will be discussed in detail in chapter 1.2.2.

Despite differences of existing CVD variants, key steps in all deposition methods – depicted schematically in figure 1-3 – remain the same and include:[125, 146]

i. Generation of the gaseous precursor species and transport into the reaction chamber.
ii. Diffusion through the boundary layer (the diffusion controlled layer just above the substrate) to the activated substrate's surface.
iii. Adsorption of the precursor species on the substrate.
iv. Heterogeneous reaction on the substrate surface leading to deposits.
v. Diffusion of the deposits on the surface leading to nucleation and growth of the solid deposit.
vi. Desorption of reaction by-products, diffusion through the boundary layer and removal from the reactor chamber.

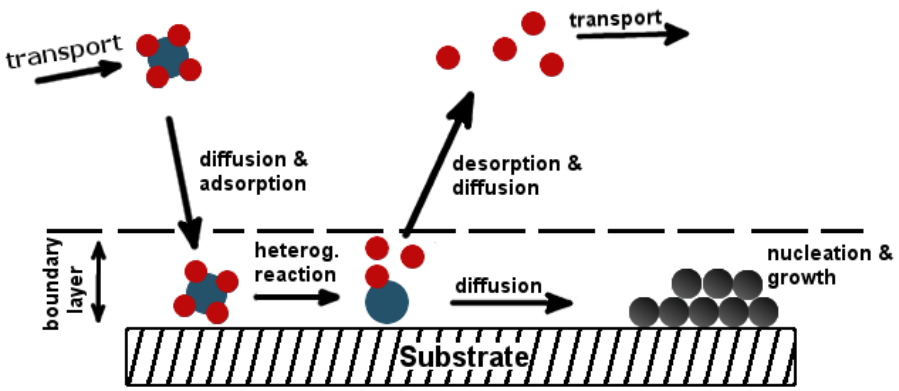

Figure 1-3: Schematic representation of key steps in CVD processes. Redrawn in style of reference [146].

Especially depending on temperature, homogenous reactions can occur in the gas phase leading to a premature decomposition/reaction of the precursor molecules and formation of nuclei or solids in the gas phase. These can lead to particulate matter being deposited onto the substrate and generally needs to be avoided if dense thin films or coatings are pursued.[127] One possibility to circumvent particle formation is to use cold-wall reactor setups, where the substrate is directly heated, but not the reactor itself. In hot-wall reactors on the other hands the substrates are indirectly heated by heating the whole reactor.[124] In contrast, chemical vapour synthesis (CVS) relies on homogeneous gas phase decomposition and nucleation for particle synthesis.[147, 148]

The most important process parameters in CVD processes are substrate temperature, pressure and flow rate. Figure 1-4 shows the influence of temperature on the deposition rate. At low substrate temperatures, deposition rates strongly increase with temperature. This indicates a kinetically limited process as chemical reactions and surface mobility are slow compared to the precursor transport through the boundary layer. In contrast, temperature dependence of the deposition rate is strongly decreased at higher substrate temperatures. In this temperature regime, mass transport/diffusion of precursor molecules is the rate limiting step, while surface reactions and surface diffusion are comparably fast. At even higher temperatures, the process is thermodynamically controlled. For endothermic reactions the growth rate is slowly increasing with temperature; for exothermic reactions however, growth rate will decrease as the driving force (ΔG) will weaken. It should be noted that LPCVD is generally considered to be kinetically limited as a result of increased mass transport at reduced pressures.[124, 149]

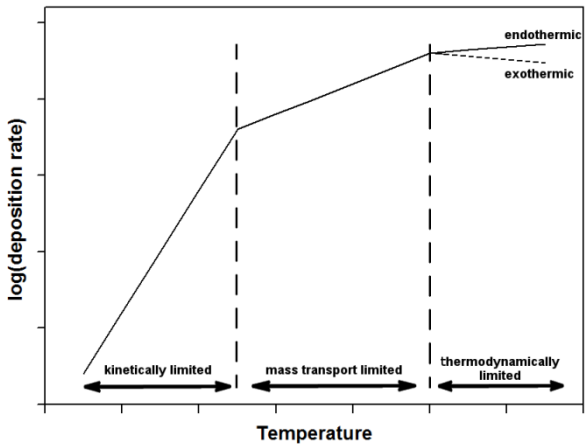

Figure 1–4: Temperature dependence of deposition rate and growth regimes. Redrawn in style of reference [127].

CVD exhibits several distinctive advantages over other deposition techniques, namely:

i. Deposition of pure materials under solvent-free conditions with good reproducibility.
ii. Low deposition temperatures and reasonably simple device setup, i.e. low costs.
iii. Wide variety of applicable precursors leading to deposition of a large number of different compounds.
iv. As opposed to physical vapour deposition (PVD), CVD is a non-line-of-sight deposition leading to uniform coatings on complex shaped substrates.
v. Control over morphology, orientation and crystal structure of the deposit via specific precursor design and deposition parameters.
vi. Deposition rates can be readily adjusted via control of vapour flux.
vii. Good adhesion of thin films on the substrate.

Drawbacks of CVD techniques are often related to the used precursor species and include:

i. Chemical safety hazards, such as toxic or pyrophoric nature of precursors or by-products.
ii. Difficulties with deposition of multi-component systems from different sources.
iii. CVD is a highly complex process especially compared to physical deposition methods. Therefore, it often requires more testing and adjusting process parameters to achieve optimal conditions.

Problems for deposition of multi-component systems are the result of different vapour pressures (i.e. precursor flux), and varying decomposition kinetics of different precursors in multi-source precursor systems leading to variations in stoichiometry of the deposits. Most of these issues, however, can be overcome by specifically tailored precursors and reactor design. In particular single-source precursors have shown great potential and are favoured in deposition of multi-component systems since they incorporate all necessary elements in the correct stoichiometric ratios leading to reproducible and stoichiometric products.[150, 151]

Sophisticated precursor design obviously remains a difficult task and has to balance advantages and drawbacks. However, there are certain criteria that an ideal CVD precursor should meet:[49]

i. High vapour pressure to ensure stable and continuous precursor flow rates; thus preferably liquid state.[152]
ii. High stability at room temperature (long shelf lifetimes).
iii. Moderate decomposition/deposition temperatures, but with enough buffer to volatilisation temperatures to prevent premature decomposition in the gas phase.
iv. Suitable decomposition rates with good control over stoichiometry and morphology giving pure deposits. By-products should be volatile and easily removed via the exhaust.
v. Easy and safe handling, non-toxicity of precursor and by-products.
vi. Cheap and easy production on a large scale in high purity.

Especially with regards to safety issues, industry has been shifting towards organometallic precursors.[153] However, other applicable precursor species include halides,[134, 154] alkyls,[155, 156] hydrides[80, 157] and carbonyls,[158, 159] just to name a few. Depending on the applied precursor species and on the material class of the deposit, various types of reactions can be used to achieve deposition including thermal decomposition,[36, 160-163] oxidation,[164] reduction[165, 166] or nitridation.[167, 168] However, for the latter three examples addition of a second reacting gas is necessary, which makes the setup more complex as gas flows have to be carefully regulated to prevent unwanted homogenous gas phase reactions.

1.2.2 Aerosol-assisted CVD

As mentioned above, CVD processes generally require volatile precursors to ensure stable precursor delivery. AACVD is a type of CVD processing, which circumvents the need for precursor volatility. Instead, the precursor is delivered to the reactor as an aerosol rather than volatilised/sublimed from its pure form.[169, 170] Hence, the prime requirement for precursors in AACVD is solubility and as such, a far greater number of precursor species can be used. Additionally, AACVD is performed under atmospheric pressure, which generally leads to a comparably simple setup. Nevertheless, AACVD can be combined with plasma-assistant CVD and other techniques making it a very versatile method. Other advantages are high-throughput and easier control of stoichiometry in multi-component systems by simple mixing of precursor species.[125, 171]

While the fundamental process steps remain the same for all CVD methods, AACVD exhibits a few additional ones, which are related to the precursor feed system:

i. Formation of the aerosol. Most common methods for aerosol generation are ultrasonic, electrostatic and pneumatic jet atomisation, which will yield droplets of different sizes and size distributions.[171]

ii. Transportation of the aerosol droplets to the heated substrate, where the solvent evaporates, leaving the gaseous precursor. Evaporation of the solvent is highly dependent on droplet size and therefore, small and uniform droplets are desired to ensure uniform precursor concentrations.

The remaining process steps leading to deposition are similar to those described in chapter 1.2.1. It should be noted though that the complete evaporation of the solvent has to take place to ensure a CVD type deposition. If solvent evaporation is not complete prior to adsorption on the substrate a spray-pyrolysis mechanism will take place leading to particle deposits. In contrast to AACVD, where the aerosol is used for precursor transportation to the substrate at atmospheric pressure, liquid-injection CVD is operated at reduced pressure leading to instant evaporation of the solvent upon entry of the reaction chamber resulting in the atomised precursor species.[172]

Despite the increased number of process parameters over conventional CVD and hence slightly more complex setup, AACVD provides good control over morphology and phase of the deposit.[173, 174] Besides temperature, growth duration and precursor concentration, choice of solvent can have drastic impacts on the final product, mainly due to differences in heat capacity and evaporation rate.[169, 175]

1.2.3 Sol-gel processing

Sol-gel processing is a wet-chemical approach for the production of ceramic materials from molecular precursors. It offers access to a wide variety of morphologies reaching from particles to thin films and aerogels with simple setups under mild conditions.[176, 177] The process applies a series of controlled hydrolysis reactions of alkoxo groups forming intermediate alkoxo-hydroxides, which undergo subsequent water- or alcohol condensation reactions leading to M-O-M bonds. At a certain degree of condensation, the molecular weight reaches a point where the molecule becomes insoluble, thus forming a colloidal suspension of particles, called the sol. If condensation is allowed to proceed further and the percolation point is reached, a gel is formed.[178]

The sol-gel process was initially developed for silicon based materials and was later adapted to metal alkoxides. However, there are a few distinct differences that have to be addressed when using metal alkoxides. Silicon alkoxides show highly covalent bond character and low Lewis-acidity and as such do often not react with water at neutral pH. Thus, the process is usually performed with acid or base catalysts depending on the desired product morphology. For metal alkoxides, hydrolysis is much faster due to high bond polarity and Lewis-acidity of the metal centre leading to precipitates rather than gels.[30] Therefore, metal alkoxides are typically chemically modified with strong chelating ligands to achieve slower and more controlled hydrolysis rates or additional surface modifiers are added to alter the hydrolysis behaviour.[179-182]

1.2.4 Hot-injection methods

Hot-injection processes are widely used methods for the production of nanoparticles. The process is based on fast injection of a precursor solution into a hot liquid, which will instantly create a supersaturated solution and formation of nuclei.[177] Due to the simultaneous formation of a big amount of crystallisation nuclei, uniform crystal growth can be observed, which generally helps to achieve narrowing of the size distribution of the resulting nanoparticles. Hot-injection methods are generally performed with the addition of surfactants or even employ the surfactant as the solvent. The surfactants are able to stabilise the formed nanoparticles to give a stable colloid and help with further narrowing the size distribution mainly by preventing agglomeration.[183]

Hot-injection pyrolysis employs high boiling point solvents, such as squalane, squalene, octadecene, dodecylamine or tricotylphosphine oxide, to allow direct thermolysis of injected precursors and subsequent formation of nuclei and nanoparticles. Besides a simple experimental setup, hot-injection methods have the advantage of good size control of the nanoparticles via temperature, precursor and surfactant concentration and heating duration.[184] In addition, it allows for *in situ* preparation of heterostructures, post-growth modification and even heteroepitaxial growth on submersed substrates.[185, 186]

1.3 Thermolysis mechanisms and incorporation of heteroatoms

Understanding the decomposition mechanism of molecular precursors upon thermolysis is crucial for the design of functional precursor for a designated material. The decomposition pathway and effectiveness of thermolysis is also of great interest to achieve pure materials with a defined stoichiometric composition. While pyrolysis mechanisms in CVD reactions have been investigated for various precursor species by a number of techniques, the pyrolysis mechanism of metal alkoxides is still not completely elucidated.[155, 165, 187-191] Nevertheless, it has been established that ß-hydride elimination, ß-hydride transfer and intramolecular ether formation are the most likely mechanisms for simple non-functionalised alcoholates, such as ethoxides or ^{t}butoxides.[131, 192]

Doping is generally considered as the intentional introduction of minimal amounts of impurities into a semiconductor crystal lattice on substitutional lattice sites.[193] Despite the use of minimal concentrations (e.g. 10^{18}-10^{19} cm^{-3} for heavily doped GaAs), the material's properties can be drastically altered and thus a high purity starting material is essential.[194-196] Depending on the valency of the dopant with respect to the host material, discrete donor or acceptor levels are introduced between valence and conduction band leading to a reduced excitation energy and a concomitant increase in charge carrier concentration (electrons or holes). For compound semiconductors, such as III-V or III-VI

compounds, it is generally possible to use cation or anion doping.[197-199] As a consequence, doping of semiconductors has emerged as an essential technique to control various electronic and physico-chemical properties of a material. For instance, doping can be used to effectively alter/tune electrical and ion conductivity[200, 201] or the band gap.[202-204]

Solid solutions on the other hand are mixtures of two or more solid compounds where the solutes are statistically distributed within the crystal lattice of the solvent.[205] Because the solutes are generally present in concentrations far greater than in doping, formation of a solid solution is typically only possible, if the constituents have the same crystal system and the substituting atoms are of similar size so that the crystal system of the host is retained.[206] Formation of solid solutions also has a major impact on the material's properties (density, reactivity, magnetism, optical properties..) resulting from distortion of the crystal lattice and disruption of the crystals homogeneity.[206-208] For instance, III-V semiconductors are well known to readily form solid solutions, e.g. $Al_xGa_{1-x}As$, which allows alteration of band gap, conductivity and photophysical properties.[209-211] Other recent examples include the formation of metastable $Ge_{1-x}Sn_x$ nanowires to achieve a transition from an indirect to a direct band gap.[212, 213]

Generally, there are two pathways to incorporate heteroatoms into a material. Firstly, there are post-growth procedures, which are most often performed via annealing in a reactive atmosphere or ion implantation.[214, 215] For instance, commonly applied nitrogen doping of oxides generally requires annealing in strong nitration agents, such as NH_3, while sulphur incorporation is often achieved by either oxidation of sulphides or sulphidisation of oxides in H_2S.[216, 217] However, post-growth processes often suffer from inhomogeneous distribution of dopants due to diffusion limitations and will typically lead to increased concentrations at the surface, which could result in varying properties in the material.[197, 218, 219] It should be noted that effects resulting from doping or formation of solid solutions are strongly dependent on heteroatom concentration and distribution and thus on the crystal structure of the host material. For instance, close packed or layered structures or even channels in the crystal can cause differences in doping levels and distribution.

The second approach is *in situ* incorporation of heteroatoms during the growth/synthesis of the material. One can further distinguish multi- and single-source approaches, with multi-source approaches being far more commonly used. These typically proceed via simple mixing of precursor species in the desired ratios and subsequent processing, such as sintering, gas phase reactions or sol-gel processes.[203, 220-223] Single-source approaches on the other hand include for instance arsenic or phosphorus n-type doping of germanium via CVD of $E(GeH_3)_3$ with E= P, As or the formation of a solid solution of carbon and silicon in germanium from decomposition of $Ge(SiMe_3)_4$.[224-226] Reports on incorporation of hetero-atoms from single-source precursors into oxide materials are thus far almost exclusively limited to fluorine introduction from fluorinated precursors in CVD processes. Fluorination of precursor species was initially introduced as a way to increase volatility, but was found to be incorporating fluorine into the growing materials.[41, 227] It has to be highlighted though that *in situ* processes, in particular using molecular precursors, require clean decomposition to ensure controllable material properties, as other unintentional contaminations can also lead to altered properties.

1.4 Materials targeted in molecule-to-material conversion

1.4.1 Gallium oxides

There are three known gallium oxides, namely Ga(I), Ga(II) and Ga(III) oxide; however, Ga_2O_3 is the only stable oxide.[228-230] Ga_2O_3 exhibits five different polymorphs (α, β, γ, δ and ε) with the β-phase being the only stable one under normal conditions.[231-235] β-Ga_2O_3 crystallises in the monoclinic space group *C2/m*, with gallium occupying equal amounts of tetrahedral and octahedral sites. Oxygen atoms are located in a distorted body centred cubic arrangement. The structure of β-Ga_2O_3 is depicted in figure 1-5.[236]

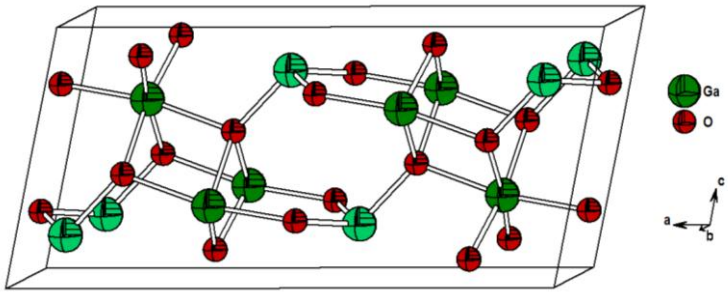

Figure 1-5: Crystal structure of β-Ga_2O_3. Tetrahedral sites are depicted in pale green. Data taken from reference [236].

β-Ga_2O_3 is a wide band gap semiconductor with a direct band gap of approx. 4.8-4.9 eV exhibiting n-type conductivity at temperatures above 600 °C.[237-239] Because of the very large band gap, Ga_2O_3 materials are transparent in the UV-A to UV-C and visible region of the spectrum, which is often exploited in applications in optoelectronic devices.[240-245] The second important application is as sensing material for various gases at high temperatures. For instance, Ga_2O_3 is known to change its electrical conductance depending on O_2 concentration at temperatures above 900 °C making it a viable high-temperature resistor-type oxygen sensor.[239, 246] At temperatures below 900 °C however, it reacts well to reducing gases, such as CO or ethanol, in surface-control-type sensors.[247-249] Other fields of application include catalysis, e.g. for photocatalytic water splitting or reduction of NO_x.[250-252]

Bulk samples of Ga_2O_3 are easily prepared by thermolysis of $Ga(NO_3)_3$ or other simple inorganic salts or by direct oxidation of the metal.[228] Due to the demand for thin films rather than bulk material in most technologically relevant applications coupled with the need for high-purity materials, synthesis via gas phase methods are generally preferred. As mentioned before, these techniques do not only enable deposition of stoichiometric materials, but often allow good control over phase and morphology

of the deposit. This is particularly important for many III-VI semiconductors, as the existence of multiple phases can lead to increased defect concentrations, which will also affect the materials properties.[253, 254] Many applications thus rely on gas phase processes and Ga_2O_3 has been synthesised via CVD,[134, 156, 162, 238, 255-258] PVD,[239, 259] pulsed laser deposition (PLD),[240, 260] ALD[261-263] or spray pyrolysis,[264] but also via sol-gel processes.[265, 266] Suitable precursors include metallic gallium,[267] halides,[134] hydrides,[80, 268] alkyls,[156, 262, 269] ß-diketonates and especially in recent years metal alkoxides.[9, 15, 27, 162, 263, 270-272]

1.4.2 Gallium sulphides

Similar to gallium oxides, gallium sulphides have been reported in all three possible oxidation states of gallium.[228, 273, 274] However, only GaS and Ga_2S_3 are of technological importance. GaS, which is a II-VI semiconductor with a direct band gap of 3.05 eV and indirect one of 2.59 eV showing n-type conductance, is most stable in its ß-phase crystallising in the hexagonal space group $P6_3/mmc$.[275-278] Paired with its layered structure these properties have led to applications of GaS in thin film devices such as photodetectors[279] or field-effect transistors.[280]

In addition to the hexagonal ß-GaS, there is also cubic GaS, which has thus far been only accessible via a MOCVD approach showing excellent phase control via precursor design. [281, 282] MacInnes and co-workers employed the sulphido cubane precursor $[(^tBu)GaS]_4$, which basically retained its cubic core structure upon thermolysis and forced its structure onto the crystalline deposit. The importance of precursor design becomes evident as using the chemically related precursor $[(^tBu)_2Ga(S^tBu)]_2$ lead to the more stable hexagonal ß-GaS, while dithiocarbamate $[(^tBu)_2Ga(S_2CNMe_2)]$ produced a metastable, distorted wurtzite-type structure.[161, 281]

Ga_2S_3 also exhibits multiple crystal structures. However, the monoclinic α'-phase is the only one with exact Ga:S=2:3 stoichiometry, while α- and ß-phases both exhibit small deviations from the ideal composition, typically around $Ga_{1.98}S_3$ to $Ga_{2.02}S_3$.[283, 284] As shown in figure 1-6, the α-phase crystallises in a superlattice of the wurtzite structure in hexagonal space group $P6_1$, while the ß-modification exhibits the wurtzite structure ($P6_3mc$).

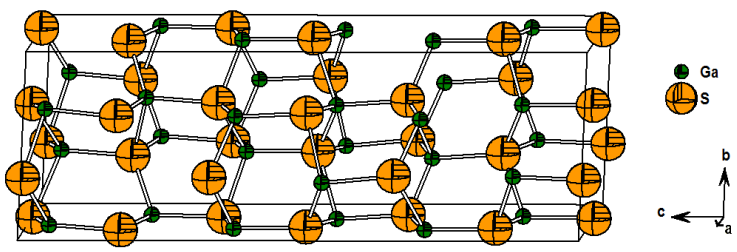

Figure 1-6: Crystal structure of α-Ga_2S_3. Data taken from reference [284].

Ga_2S_3 is a compound III-VI semiconductor with a direct band gap of approx. 3.4 eV[285-287] and was reported to show photoluminescence in the green region of the visible spectrum (2.4 eV), which was attributed to gallium vacancies in the α-Ga_2S_3 lattice leading to acceptor levels above the valence band.[287-289] Hence, Ga_2S_3 has found applications in optoelectronics,[290-292] very often as a constituent of chalcogenide glasses.[293-296] Other applications include Ga_2S_3 for surface passivation layers in III-V semiconductor devices.[286, 297]

As with most binary inorganic materials, gallium sulphides can be directly synthesised from the elements at elevated temperatures, while obtained oxidation state and phase are very sensitive to the used ratio of elements as well as synthesis temperature.[277, 283, 284, 287, 298] Technologically more important thin films are mainly produced via reactive gas phase processes such as CVD or ALD.[144, 299-301] Single-source precursors for gallium sulphides include thiolates,[144, 281] thiocarboxylates,[285] xanthates,[302, 303] dithiocarbamates,[161] and sulphido cubanes.[281, 282]

1.4.3 Gallium oxysulphides

As mentioned before, anion doping or formation of a solid solution is an efficient way for controlled alteration of semiconductor properties, such as band gap, conductivity or photoluminescence. Regardless, literature reports on gallium oxysulphides, $Ga_2O_{3-x}S_x$, are very rare. In fact, most reports deal with complex heterometallic gallium oxysulphide glasses, which – despite exhibiting interesting optical properties – essentially remain solid solutions of various oxides and sulphides.[304-306] Post growth modifications, e.g. sulphidisation of oxides with H_2S, usually suffer from the fact that sulphidisation generally is limited to the surface yielding core-shell type structures forming heterojunction devices rather than uniform oxysulphides.[286, 307]

The only alleged example on gallium oxysulphides was reported by Kim *et al.*, who used solid state reactions of Ga_2O_3 and sulphur at 1000 °C to produce $Ga_2O_{3-x}S_x$ powders with x = 0-0.05.[308, 309] Despite conclusively showing the beneficiary effects on photo- and cathodoluminescence, they lacked evidence of actual oxysulphide formation. XRD analysis of the obtained phases only showed oxide phases without significant shifting of the reflexes as would be expected for small sulphur amounts used in the study. Moreover, the authors did not report any cleaning steps after synthesis, such as simple washing, to remove potential residual elemental sulphur. As such, without further proof via X-ray photoelectron spectroscopy (XPS) or X-ray absorption spectroscopy techniques (XANES and EXAFS), the incorporation of sulphur and the formation of oxysulphides cannot be conclusively proven.

1.4.4 Indium oxides

Similar to gallium oxides, In(I) and In(III) oxides have been reported in literature, but only In_2O_3 is thermodynamically stable and of technological importance.[310] In_2O_3 is a light yellow solid preferentially crystallising in the cubic space group $Ia\bar{3}$, which is depicted in figure 1-7.[311, 312] The body-centred cubic crystal structure features indium in octahedral sites and oxygen in tetrahedral positions. Additionally, there is a rhombohedral phase with corundum-type structure, which is usually formed at 1000 °C and 65 kbar, but was recently reported to be accessible via MOCVD from $InMe_3$ and H_2O or via prolonged ball-milling of the cubic phase.[313-316]

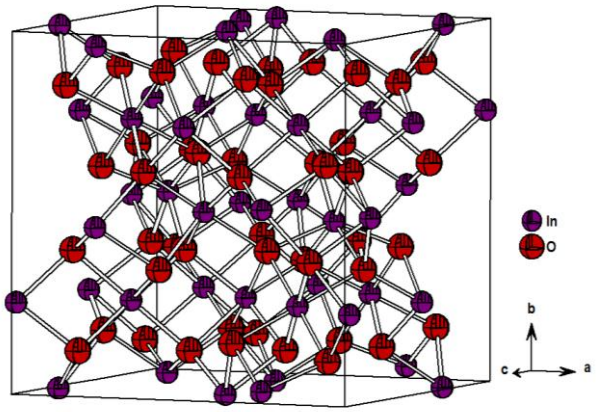

Figure 1–7: Unit cell of cubic In_2O_3. Data taken from reference [312].

Both phases of In_2O_3 were reported as n-type wide band gap semiconductors, which were long thought to have a direct band gap of 3.5-3.7 eV and an indirect one of 2.7 eV.[138, 315, 317] However, combination of theoretical and experimental investigations on single-crystalline materials recently showed that the materials only have a direct band gap of 2.9 eV and 3.0 eV, respectively.[318] It was further demonstrated that the quasi-indirect transition is caused by dipole-forbidden electronic transitions from the valence band maximum to the conduction band minimum.[319, 320] The second striking feature of In_2O_3 is that even pure, undoped material exhibits relatively high electrical conductivity while keeping its high transparency in the visual regime. One of the popular theories ascribes this high conductivity to oxygen vacancies due to the natural sub-stoichiometry with an oxygen deficiency of up to 1 % even when grown under equilibrium conditions.[321, 322] However, conductivity and high number of charge carriers were also found in non-degenerate films, which was found to be caused by electron accumulation at (111) and (001) surfaces associated with unoccupied donor surface states.[318, 323] Because of the rare combination of transparency and conductivity In_2O_3 has become one of the most important transparent conducting oxides (TCOs), in particular in its tin doped version indium tin oxide (ITO).[324] In_2O_3 is thus widely used as a top electrode in various displays, solar cells, LED and OLED devices and electrochromic windows, but it was also reported as active layer in field-effect transistors or as gas sensing material.[325-330]

Bulk In_2O_3 can be easily prepared by thermal treatment of $In(NO_3)_3$ or $In(ac)_3$ at elevated temperatures. More importantly, In_2O_3 thin films have been produced via several methods, including MOCVD,[21, 36, 331] AACVD,[50, 170] PVD,[332, 333] ALD,[334-336] PLD,[337] spray-pyrolysis[338] and sol-gel processes.[339-341] As with the previous materials, there is an increasing trend to use single-source precursors, but In_2O_3 has been produced using halides,[342] alkyls,[52, 334] alkoxides,[9, 21, 36, 138, 326] and ß-diketonates.[272, 343]

1.4.5 Indium sulphides

Indium sulphides exist in two stable oxidation states, namely in InS and In_2S_3, while In_2S was falsely reported but later found to be unstable.[310, 344] InS features the orthorhombic space group *Pnnm* and is considered a medium band gap semiconductor with 2.44 eV with n-type conductivity.[285, 345, 346] This has led to applications in the field of optoelectronic and photovoltaic materials, but InS has also been used as passivation layer on InP devices, analogous to GaS on GaAs.[347-349]

In(III) sulphide, In_2S_3, shows an extensive polymorphism with five different crystal structures known to date. [350-355] The thermodynamically most stable ß-phase crystallises in the tetragonal space group $I4_1/amd$, which is shown in figure 1-8. In_2S_3 exhibits a band gap around 2.1 eV and n-type conductivity. However, p-type conductivity can be achieved by incorporating excess sulphur or doping with InP.[356, 357] Similar to InS, In_2S_3 is a potential candidate for application in photovoltaics and optoelectronics. [358-362]

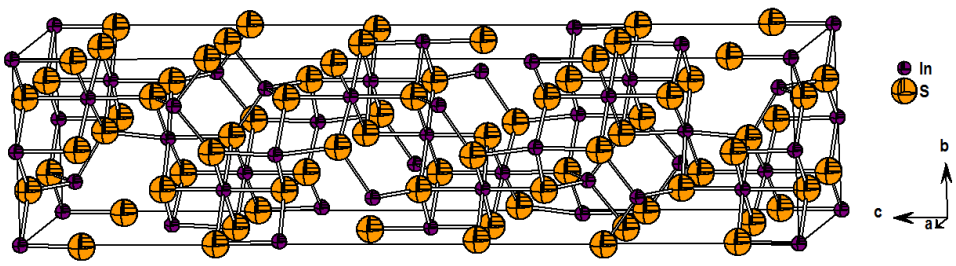

Figure 1-8: Crystal structure of tetragonal ß-In_2S_3. Data taken from reference [350].

Bulk samples of indium sulphides are easily prepared either by direct synthesis from the elements, precipitation of indium salts with NaHS or via passing H_2S gas through a solution of $InCl_3$.[357, 363-366] As a consequence of the multitude of existing phases and oxidation states, phase control is both difficult and essential. For instance, Nomura and co-workers demonstrated the sensitivity towards In:S ratio in single-source precursors leading to InS or In_2S_3 upon thermolysis.[367] MacInnes on the other hand were able to selectively deposit tetragonal InS thin films by retaining In_2S_2 cyclic features from the precursor $[(^tBu)_2InS^tBu]_2$.[347, 368]

Other routes to indium sulphides, especially thin films, include PVD,[369-371] CVD,[144, 372, 373] solution pyrolysis,[374] spray pyrolysis,[360, 375, 376] ALD,[359, 377, 378] and chemical bath deposition,[379, 380] just to name a few possibilities. Suitable multi-source precursors include halides,[378, 380, 381] alkyls,[361] or ß-diketonates[359, 377] in combination with a sulphidisation agent such as H_2S, thiols or thioacetamide. Common single-source precursors are dithiocarbamates,[372] heteroleptic alkyl thiolates,[338, 347, 368, 373] thiocarboxylates,[382] dithiocarboxylates,[383] or xanthates.[384] It should be noted that indium thiolates are usually not volatile enough for CVD applications as they often form polymeric structures, but they are efficient precursors for solution pyrolysis.[253, 347]

1.4.6 Indium oxysulphides

Similar to gallium oxysulphides, reports on indium oxysulphides are rather rare, although indium oxysulphides seem favourable for the replacement of CdS buffer layers in Cu(Ga,In)Se based solar cells.[385-387] Reports exclusively deal with post-growth treatment for partial conversion of oxides or sulphide materials or multi-source approaches.[388, 389]

As such, wet chemical approaches, e.g. chemical bath deposition, suffer from difficult control over phase, morphology and film composition. In addition, another drawback is facilitated oxidation leading to additional formation of sulphates as well as formation of hydroxysulphides, $In(S,OH)_x$ rather than oxysulphides, $In_2O_{3-x}S_x$.[385, 390-392] Similar problems were encountered in a series of publications by Haleem and Ichimura, who reported on electrochemical film deposition from $In_2(SO_4)_3$ and $Na_2S_2O_3$ for the formation of $In_2S_xO_y(OH)_z$ films. In addition to sulphates and hydroxides, they found that the thin films contained metallic indium nanoparticles, which necessitated a post growth sulphurisation step. However, this resulted in the complete loss of oxygen and hydroxides and the formation of In_2S_3.[349, 393-395]

In contrast, controlled synthesis of $In_2O_{3-x}S_x$ films was achieved via alternating PVD of indium and sulphur layers and subsequent annealing under inert conditions. Oxysulphide formation was found to be the result of residual oxygen in the annealing atmosphere and was strongly dependent on temperature and duration of the annealing step. More importantly, the deposits showed phase purity and uniformity with an almost linear increase of the band gap with increasing oxygen content allowing fine tuning the electronic properties of the material.[386, 396-400] Efficient control over the band gap was also demonstrated by Bugot and co-workers, who applied *in situ* O_2 plasma pulses during ALD growth of In_2S_3 to yield $In_2O_{3-x}S_x$ films. Nevertheless, they failed to conclusively show oxysulphide formation as energy dispersive X-ray analysis (EDX) and XPS studies revealed non-stoichiometric composition suggesting sulphate formation and carbon contamination resulting from incomplete decomposition of the $In(acac)_3$ precursor (acac=acetylacetonate).[401, 402]

In conclusion, it seems obvious that gas phase processes are better suited for controlled formation of oxysulphide materials, although the required equipment is generally more complex. From

a chemical point of view, solution based processes lack control over composition and often result in the incorporation of other anions, such as sulphates or hydroxides. However, judging only device performance, also solution based materials show promising results.

1.4.7 Heterobimetallic oxides

Heterobimetallic oxides with the general formula $M^{II}M^{III}{}_2O_4$ belong to the group of ternary spinel oxides. As such they generally crystallise in the cubic space group $Fd\bar{3}m$ as depicted for the parent spinel system $MgAl_2O_4$ in figure 1-9.[403] The structure features octahedral and tetragonal coordinated cation sites in a ratio of 2:1. In classic spinel $MgAl_2O_4$, Mg^{2+} is occupying the tetrahedral sites, while Al^{3+} ions are located in the octahedral sites. Inverse spinels, e.g. magnetite Fe_3O_4, on the other hand feature M^{2+} on octahedral sites and M^{3+} ions distributed equally between tetrahedral and remaining octahedral positions.[404] Overall, cation sites remain only partly occupied allowing for random distribution of cations in many spinel and inverse spinel oxides.[405] As such, controlling the structure, degree of inversion and cation distribution has become an efficient way of controlling the macroscopic properties of the material.[406-409]

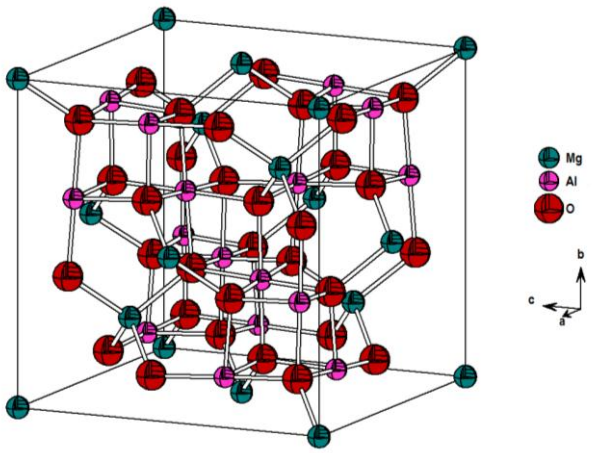

Figure 1-9: Crystal structure of spinel $MgAl_2O_4$. Data taken from reference [403].

Due to the easy possibility to incorporate transition metals in different oxidation states on either octahedral or tetrahedral sites, oxide spinels offer accessibility to a number of functional materials, with properties strongly dependent on the constituents and defect concentration, e.g. metal-on-metal anti-site substitution and cation distribution.[321, 410] Hence, oxide spinels have been exploited for ferroelectric and ferromagnetic[411-414] as well as catalytic properties,[415-419] just to name a few. For instance, mesoporous $ZnGa_2O_4$ was recently reported to be highly active in photocatalytic reduction of CO_2 to CH_4, while $NiGa_2O_4$ showed promising results in photocatalytic water splitting.[420-422]

Bulk samples of spinel oxides are readily accessible via solid state chemistry routes or co-precipitation reactions in solution.[423-425] Functional materials, such as thin films and various nanostructures, have been prepared via gas phase, hydrothermal or sol-gel routes.[108, 152, 426-429] Suitable molecular precursors include single-source precursors, such as (donor functionalised) alkoxides. For instance, Veith *et al.* showed the applicability of simple spiro-complexes in sol-gel processes to access phase pure MAl_2O_4 (M=Co, Ni, Cu, Zn) nanoparticles with controllable size as well as a size-dependent blue-shift of the band gap for M=Zn.[430, 431]

Similarly, Mathur *et al.* applied spirocyclic heterometallic gallium ^{t}butoxides in the synthesis of $NiGa_2O_4$ and $CoGa_2O_4$, respectively.[432, 433] They could demonstrate the applicability of the heterometallic alkoxides as single-source precursors in LPCVD and sol-gel experiments giving phase pure products in both cases. The applicability of multi-source approaches has been recently demonstrated by Knapp *et al.*, who used a mixture of gallium and copper ß-diketonates to produce $CuGa_2O_4$ thin films, although they also encountered phase separation and formation of CuO alongside the spinel.[429]

Ferrite spinels MFe_2O_4 are particularly interesting due to their magnetic behaviour.[434-436] For instance, Mathur *et al.* demonstrated temperature dependent deposition of iron oxides from the single-source precursor $[Fe(O^tBu)_3]_2$ in LPCVD experiments. They found that Fe_2O_3 (hematite) was deposited at 400 °C, while *in situ* reduction of the precursor at 450 °C and above formed Fe_3O_4 (magnetite) upon decomposition, which showed superparamagnetic behaviour because of the nanocrystallinity of the coating.[437] The compositional tunability of the magnetic properties of ferrites was highlighted by Li *et al.*, who applied pyrolysis of acac precursor-mixtures in high-boiling solvents in the presence of surfactants to obtain $M_xFe_{3-x}O_4$ (M=Co, Mn, x=0.06-0.55) nanocrystals with very sharp size distribution.[438]

1.5 MOTIVATION AND RESEARCH GOALS

Based on successful development of a synthesis protocol for thioether functionalised metal alkoxide derivatives, investigations of the coordination behaviour and also the thermal decomposition characteristics of these alkoxide derivatives have been targeted.[439] Comparison of the coordination tendencies in absence and presence of well-known donor moieties, such as amines and ethers, were envisioned. Furthermore, a comparison to homoleptic aminoalcoholates of group 13 metals with alcohol ligands of similar structural design was targeted.

The thermal decomposition of metal alkoxides is a popular choice for the formation of oxide coatings or nanoparticles in material synthesis. However, no reports on the influence of a thermally labile group, such as a thioether, in the organic backbone of the alcoholate ligand on the decomposition characteristics existed. In consequence, the application of the novel alkoxide species as

single-source precursors for *in situ* sulphide incorporation into oxide based materials with specific focus on thin layer formation via CVD techniques was targeted. Special attention was payed to the role of the thioether functionality on the composition of the resulting materials upon thermolysis as thioether adducts have been previously reported to allow formation of sulphide materials.[440-443] The chemical and physical properties of the obtained materials should be thoroughly analysed via EDX, electron microscopy techniques, X-ray diffraction (XRD) and XPS.

In addition, synthesis of a series of transition metal gallates MGa_2O_4 was targeted, because of their applicability in catalysis. In consequence, heterobimetallic gallium ^{t}butoxides should be synthesised, characterised and investigated for their applicability as single-source precursors in LPCVD and sol-gel processes.

CHAPTER 2

RESULTS AND DISCUSSION

"These go to eleven."

- From "This is Spinal Tap" (1984) -

2.1 AMINOALCOHOLATES OF AL(III), GA(III), IN(III)

A series of aminoalcoholates of aluminium, gallium and indium has been synthesised in high yield via alcohol exchange reactions (Al, Ga) or alcoholysis (In), respectively. For detailed synthesis procedures, refer to the experimental section. All room temperature ^{1}H and ^{13}C nuclear magnetic resonance (NMR) spectra clearly show the formation of the alkoxide species indicated by the pronounced low-field shift of the $C_{\alpha}H$ group (0.31 ppm on average for ^{1}H, 1.0-2.8 ppm for ^{13}C), as depicted in figure 2-1. Furthermore, NMR measurements hint towards monomeric species in solution as there are no observable signals for bridging and terminal alkoxo groups which would be observed in dimeric or oligomeric species as they differ significantly in chemical shift especially for $C_{\alpha}H$ protons.

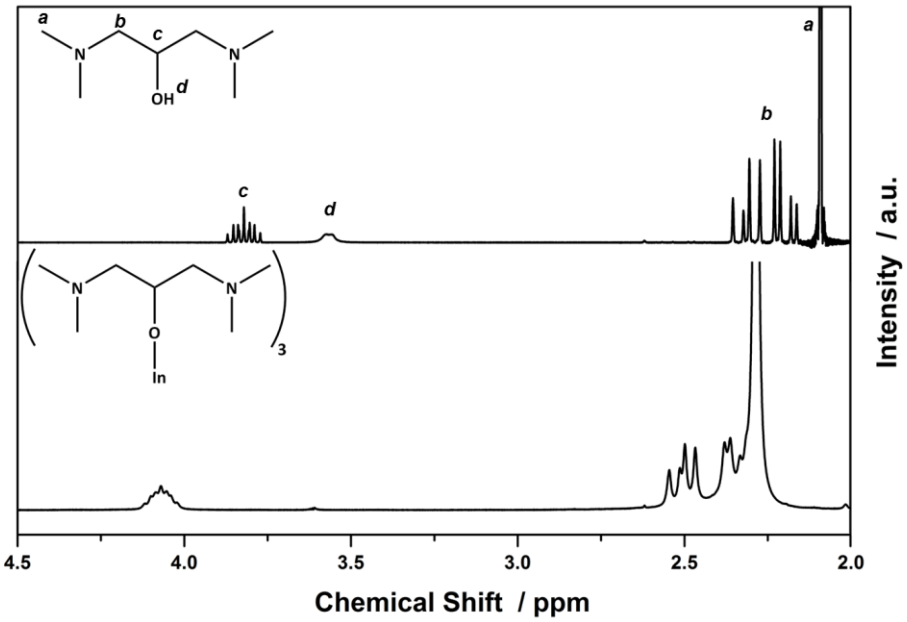

Figure 2-1: ^{1}H NMR of 1,3-bis(diethyamino)propan-2-ol and *In1* in C_6D_6.

In addition, there is also an unexpectedly large shift for signals of groups in vicinity of the nitrogen donor. For instance, the methyl group in 1,3-bis(dimethyamino)propan-2-olates (marked *a* in figure 2-1) is already five atoms apart from the metal centre. Thus, a low-field shift is only expected if there is a coordination of the corresponding nitrogen atom. Yet there are more donor atoms than available coordination sites at the central atom, which should lead to at least two sets of signals originating from coordinating and dangling donor moieties for protons in vicinity of the donor sites (protons *a* and *b* in figure 2-1). The absence of the second set is an indication for a fast exchange of coordinating and uncoordinating configuration in the aminoalcoholates in solution. Nevertheless, room temperature NMR data alone cannot provide sufficient prove for monomeric or dimeric nuclearity in solution, although different chemical shifts are frequently observed in stable dimers for bridging and

terminal alkoxo ligands.[444, 445] Although only one set of signals is observed for the presented aminoalcoholates, the quick exchange of coordination modes makes it difficult to determine the nuclearity with certainty. Thus, formation of dimers in solution cannot be completely ruled out.

More distinct prove of the alkoxides' nuclearity in the solid state could be provided by single-crystal XRD analysis. Crystals suitable for X-ray studies were obtained either from the pure, viscous alkoxides (*Al1*, *Ga1* and *Ga2*) or from saturated ^{n}hexane solutions at -9 °C (*Al2* and *In1*) with all compounds showing pronounced sensitivity towards atmospheric moisture. Twinning was observed for *In1* consistent with a (001) mirror plane as twin operation. Reflexes were manually analysed using the *RLATT* tool (Bruker, 2014) and refinement was conducted using the *HKLF 5* map. Detailed crystallographic and refinement data is listed in table 2-1.

All reported aminoalcoholates exhibit monomeric molecular structures in the solid state, which is in good agreement with NMR results discussed above. All aluminium and gallium alkoxides (*Al1*, *Al2*, *Ga1*, *Ga2*) show very similar structures featuring a distorted trigonal bipyramid, as shown in figure 2-2 and 2-3. The bipyramid consists of three alkoxo oxygen atoms in the equatorial positions and two amino donors occupying the apical positions. The coordinating nitrogen donors are from two different ligands leaving each with one dangling donor site, while the third alkoxo ligand does not exhibit any further chelating coordination to the central atom.

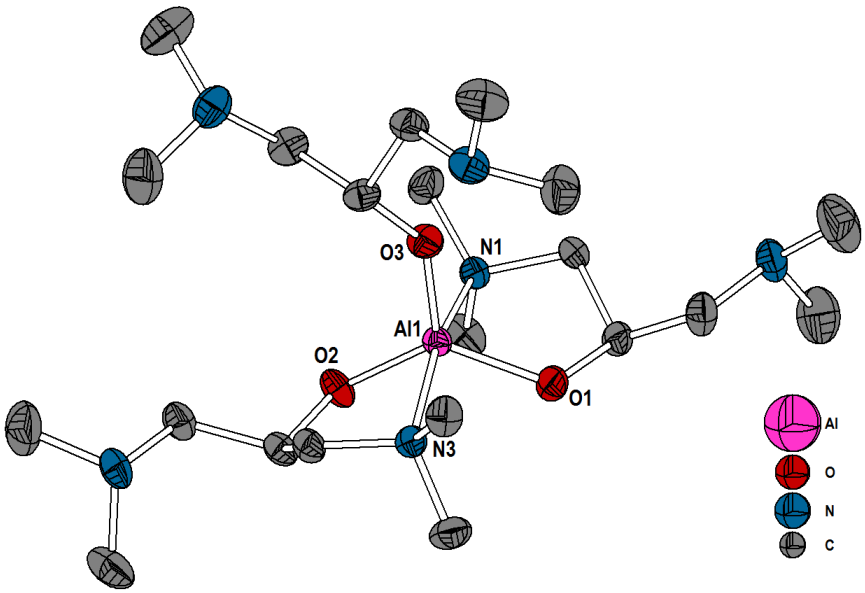

Figure 2-2: Molecular structure of *Al1* with 75 % probability ellipsoids. Hydrogen atoms have been omitted for clarity.

Table 2-1: Crystal and structure refinement details of *Al1*, *Ga1*, *In1*, *Al2* and *Ga2*.

Compound	*Al1*	*Ga1*	*In1*	*Al2*	*Ga2*
Emp. Formula	$C_{21}H_{51}AlN_6O_3$	$C_{21}H_{51}GaN_6O_3$	$C_{21}H_{51}InN_6O_3$	$C_{33}H_{75}AlN_6O_3$	$C_{33}H_{75}GaN_6O_3$
M_r / g mol^{-1}	462.66	505.39	550.49	630.97	673.71
Crystal system	Triclinic	Triclinic	Monoclinic	Triclinic	Triclinic
Space group	$P\bar{1}$	$P\bar{1}$	$P2_1/n$	$P\bar{1}$	$P\bar{1}$
a / Å	8.7143(5)	8.8072(1)	11.748(2)	9.1809(6)	9.0300(2)
b / Å	10.2591(6)	1.01961(1)	8.7847(18)	12.6626(8)	12.8097(3)
c / Å	16.0034(8)	16.0770(2)	27.908(6)	17.1388(11)	17.5425(4)
α / °	76.570(2)	75.8008(6)	90.00	97.919(2)	98.5460(10)
β / °	81.588(2)	82.0703(6)	99.14(3)	92.143(2)	93.6160(10)
γ / °	84.368(2)	84.4410(6)	90.00	96.908(2)	96.7740(10)
V / Å^3	1373.56(13)	1383.22(3)	2843.7(10)	1956.2(2)	1985.91(8)
Z	2	2	4	2	2
D_x / g cm^{-3}	1.119	1.213	1.286	1.071	1.127
μ / mm^{-1}	0.10	1.03	0.86	0.09	0.73
Crystal size / mm	0.6 x 0.6 x 0.6	0.4 x 0.4 x 0.2	0.4 x 0.36 x 0.2	0.6 x 0.4 x 0.3	0.7 x 0.5 x 0.4
No. measured refl.	79178	14117	64160	83378	32246
Obs. Refl. [I>2σ(I)]	7436	6229	9397	9413	11274
Θ_{max} / °	32.6	28.3	33.4	30.8	31.1
R [F^2>2σ(F)], wR (F^2), S	0.042, 0.111, 1.02	0.029, 0.076, 1.06	0.076, 0.212, 1.28	0.076, 0.232, 1.05	0.035, 0.098, 1.07
Refl./param.	10024/280	6836/292	10300/293	12165/557	12569/491
Weighting scheme*	a = 0.0516 b = 0.3731	a = 0.0436, b = 0.3702	a = 0.037, b = 41.8488	a = 0.1211, b = 1.3942	a = 0.0583, b= 0.3702

* $w = 1/[\sigma^2(F_o^2) + (aP)^2 + bP]$, where $P = (F_o^2 + 2F_c^2)/3$

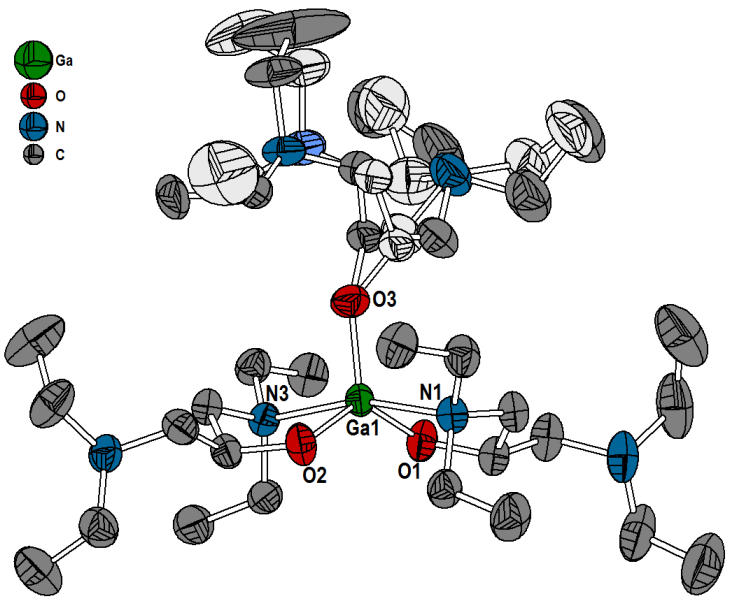

Figure 2–3: Molecular structure of *Ga2* with 75 % probability ellipsoids. Disordered parts are depicted in pale colours; hydrogen atoms were omitted for clarity.

These coordination arrangements are rather surprising as literature reports typically described group 13 alkoxides and aminoalcoholates being oxygen bridged dimers or higher oligomers.[8, 9, 30, 162] In addition, previous studies employing the same ligand system in the synthesis of heteroleptic alkoxides did not result in monomeric structures, but reported dimeric, trimeric and even higher oligomeric molecular structures for all alkoxides $R_2M(OR')$ with M=Ga, In, Zn, Cd and R=Cl, Me or Et (Et=ethyl, C_2H_5-).[50, 54, 69, 71, 446, 447] Monomeric motives of homoleptic group 13 alkoxides have only been observed in salts containing anionic alcoholate moieties formed by Lewis acid-base reactions in combination with sterically demanding cations[448, 449] or in structurally related aryloxides with a secondary donor functionality, such as hydroxyquinoline derivatives.[450, 451] Monomeric species of group 13 alkoxides can also be achieved by addition of other donor molecules, such as amines, ethers or other Lewis bases, yielding heteroleptic alkoxides of the general formula $[M(OR)_3D_x]$ with x = 1 for M = Al, x = 1, 2 for M = Ga and x = 1, 2, 3 for M = In.[27, 255, 452, 453] The only reported homoleptic gallium alkoxide featuring a similar trigonal bipyramidal coordination sphere was observed for $[Ga(OC_2H_4NMe_2)_3{\cdot}LiCl]_2$.[80] The compound shows chelating coordination of a pendant amino donor and a μ_2-alkoxo bridge to LiCl bridging two $[Ga(OR)_3]$ subunits. Efforts to synthesise the compound without LiCl contaminations produced low-quality crystals, yet the monomeric nature of the compound was confirmed.

M-O bond distances, where M = Al, Ga, are in good agreement with bond lengths reported for terminal alkoxo ligands, which are shorter than those of bridging alkoxo species.[8, 67] M-O bond distances for chelating ligands are almost identical, while the M-O bond distance for the ligand without further chelating coordination is significantly shorter, i.e. 1.765(1)/1.768(7) Å versus 1.737(9) Å for *Al1*. Shorter bond lengths for this kind of non-chelating, terminal aminoalcoholate ligand have been reported before.[454] Chelating nitrogen atoms N1 and N3 in apical positions are tilted away from the

non-chelating ligand leading to N1-M-N2 bond angles of 163.42(4)°-165.82(6)°, which is far from the expected 180° for an ideal trigonal bipyramid. This distortion is most likely caused by restrictions within the five-membered metallacycles for chelating ligands. It further leads to highly anisotropic O-M-O bond angles in the equatorial plane featuring O1-M-O2 angles ranging from 126.62(6)° to 130.04(4)°. O1-M-O3 and O2-M-O3 angles on the other hand exhibit compressed angles between 110.39(4)° and 119.59(7)°. A detailed list of bond distances and angles is given in table 2-2.

Table 2-2: Selected bond lengths and angles for *Al1*, *Al2*, *Ga1*, *Ga2* and *In1*.

Al1		*Ga1*		*In1*	
Bond	**Distance / Å**	**Bond**	**Distance / Å**	**Bond**	**Distance / Å**
Al1-O1	1.765(1)	Ga1-O1	1.849(1)	In1-O1	2.055(6)
Al1-O2	1.768(7)	Ga1-O2	1.849(1)	In1-O2	2.097(6)
Al1-O3	1.737(9)	Ga1-O3	1.834(1)	In1-O3	2.070(5)
Al1-N1	2.099(8)	Ga1-N1	2.152(1)	In1-N1	2.567(7)
Al1-N3	2.119(8)	Ga1-N3	2.180(1)	In1-N3	2.344(6)
				In1-N5	2.432(6)
Angle	**/ °**	**Angle**	**/ °**	**Angle**	**/ °**
O1-Al1-O2	128.55(4)	O1-Ga1-O2	128.78(5)	O1-In1-O2	95.7(2)
O1-Al1-O3	113.62(4)	O1-Ga1-O3	111.74(5)	O1-In1-O3	153.9(2)
O2-Al1-O3	117.83(4)	O2-Ga1-O3	119.47(5)	O2-In1-O3	105.2(2)
O1-Al1-N1	83.87(4)	O1-Ga1-N1	83.22(5)	O1-In1-N1	74.7(2)
O1-Al1-N3	87.59(4)	O1-Ga1-N3	87.65(5)	O2-In1-N3	77.6(2)
O2-Al1-N3	84.11(4)	O2-Ga1-N3	83.67(4)	O3-In1-N5	76.6(2)
N1-Al1-N3	165.26(4)	N1-Ga1-N3	164.26(4)	O1-In1-N3	111.8(2)
				O1-In1-N5	90.5(2)
Al2		*Ga2*			
Bond	**Distance / Å**	**Bond**	**Distance / Å**		
Al1-O1	1.762(2)	Ga1-O1	1.844(1)		
Al1-O2	1.763(1)	Ga1-O2	1.847(1)		
Al1-O3	1.723(1)	Ga1-O3	1.821(1)		
Al1-N1	2.161(2)	Ga1-N1	2.217(1)		
Al1-N3	2.157(2)	Ga1-N3	2.215(1)		
Angle	**/ °**	**Angle**	**/ °**		
O1-Al1-O2	126.62(6)	O1-Ga1-O2	130.04(4)		
O1-Al1-O3	119.59(7)	O1-Ga1-O3	119.57(4)		
O2-Al1-O3	113.79(6)	O2-Ga1-O3	110.39(4)		
O1-Al1-N1	84.15(6)	O1-Ga1-N1	83.85(4)		
O1-Al1-N3	90.61(6)	O1-Ga1-N3	97.97(4)		
O2-Al1-N3	83.52(6)	O2-Ga1-N3	82.42(4)		
N1-Al1-N3	165.82(6)	N1-Ga1-N3	163.42(4)		

Dimethylamino derivatives *Al1* and *Ga1* did not exhibit any disorder in the crystal structure. Diethylamino derivatives *Al2* and *Ga2* on the other hand featured almost the same disorder on the organic backbone of the ligand without further chelating coordination, as depicted in figure 2-3. Disorder is most likely the result of increased degrees of freedom for the non-chelating diethylamino moiety leading to different possible arrangements within the respective unit cells. The disorder has been accounted for by applying the split-atom model leading to occupational densities of approx. 50:50 and 60:40 % for *Al2* and *Ga2*, respectively.

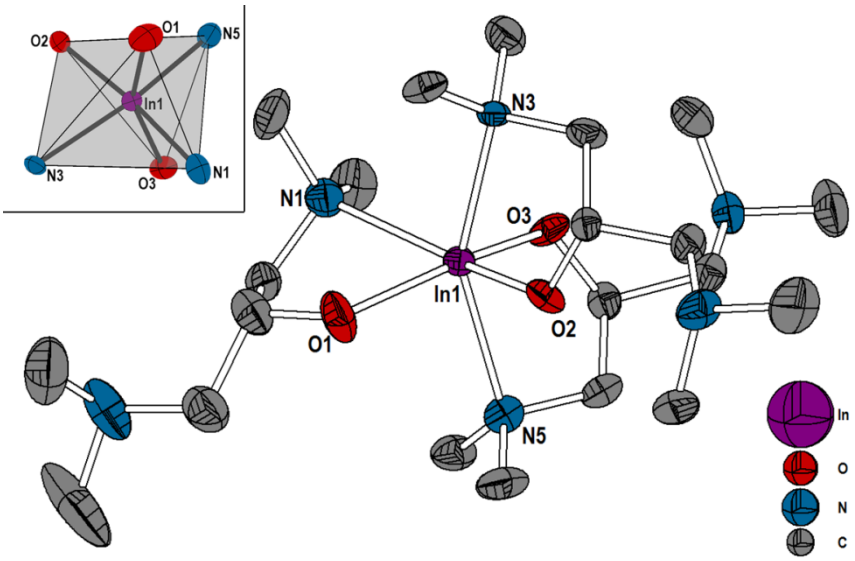

Figure 2–4: Molecular structure of *In1* shown with 75 % probability ellipsoids. Inset shows the coordination polyhedron. Hydrogen atoms omitted for clarity.

In contrast to the fivefold coordination of the aluminium and gallium aminoalcoholates discussed above, indium alkoxide *In1* exhibits a sixfold coordination featuring a distorted trigonal antiprismatic arrangement of the coordinating alcoholate oxygen atoms and amine donors, as shown in figure 2-4. The extension of the coordination number is most likely the result of the increased ion radius of the indium central atom compared to aluminium and gallium (0.8 versus 0.48 and 0.55 Å for In, Al and Ga, respectively).[455] The coordination sphere of *In1* constitutes of three sets of coordinating oxygen and nitrogen donors from the same ligands, leaving each ligand with one additional dangling donor site. The trigonal planes of the antiprisma consist of O1-O2-N5 and O3-N1-N3, which are slightly tilted by 3.65° with respect to each other, as can be seen in the inset of figure 2-4. Furthermore, these trigonal planes are distorted featuring edge lengths of 3.030(8) to 3.197(8) Å and 3.084(8) to 3.595(9) Å and angles ranging from 57.7(2) to 63.1(2)° and 57.4(2) to 69.3(2)° for triangles O1-O2-N5 and O3-N1-N3, respectively.

The observed In-O bond distances (2.055(6)-2.087(6) Å) are within the ranges reported for terminal alkoxo ligands and In-N bond lengths (2.343(6)-2.567(7) Å) are consistent with values reported for coordinating amino moieties in aminoalcoholates.[50, 454] In-O and In-N bond lengths correlate inversely with each other, showing constricting effects within the respective ligands. For instance, the shortest In-O bond (In1-O1, 2.055(6) Å) and the longest In-N bond (In1-N1, 2.567(7) Å) belong to the same ligand, while the reverse order is found for the longest In-O bond (In1-O2, 2.097(6) Å) and shortest In-N bond (In1-N3, 2.344(6) Å). The same effect can be seen from O-In1-N bond angles for atoms forming five-membered InOCCN metallacycles, i.e. belonging to the same ligands (O1-In1-N1, O2-In1-N3 and O3-In1-N5), exhibit values from 74.7(2) to 77.6(2)°, which are in agreement with other reports of terminal five-membered indium metallacycles.[182, 454] In contrast, O-In1-N bond angles between different ligands assume larger values between 83.6(2) and 111.8(2)°.

2.2 Coordination behaviour of thioether functionalised gallium and indium alkoxides

As mentioned in the chapter 1.1.1, literature studies so far have almost exclusively dealt with amines and ethers for donor functionalisation of alkoxide derivatives. Therefore, it was only logical to investigate the donating capabilities of other functionalities. We chose to focus on thioether functionalisation as this group of donors was of interest not only for the sake of coordination chemistry, but also for molecule-to-material type conversions due to possible sulphur incorporation into the oxide materials.

Two different molecular approaches were chosen for investigation of the thioether functionalised alkoxides. On the one hand, a ligand system was designed featuring two equal thioether moieties (called symmetrical ligands), which enabled examination of the coordination behaviour of this new type of donor functionality. On the other hand, a series of unsymmetrically functionalised alcohols combining thioether and amine or ether functionalities was synthesised. This approach allowed studying the coordination behaviour of the novel thioether moiety in direct comparison to those well-known donor systems. General molecular structures are depicted in figure 2-5. In addition, secondary and tertiary derivatives were synthesised to compare steric influences. Synthesis of the ligand species has been reported before for symmetrically functionalised alcohols as well as thioether functionalised aminoalcohols and is based on epoxides as educts.[439]

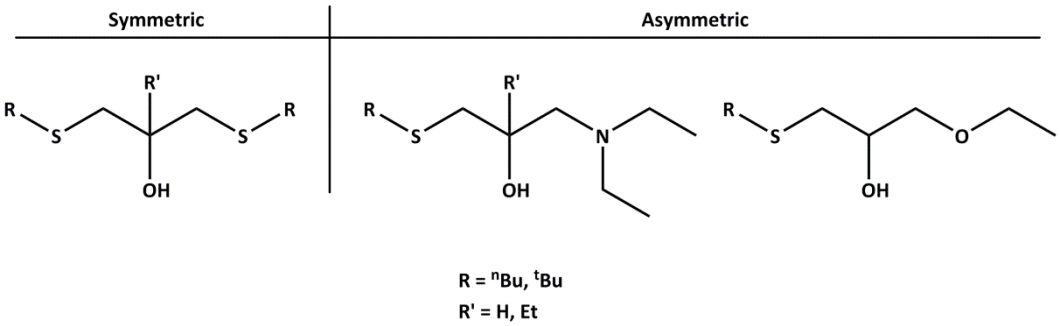

Figure 2-5: Molecular formulas of employed ligand systems.

The thioether functionalised alkoxides were synthesised in similar procedure as described for aminoalcoholates in section 2-1. Gallium alkoxides were prepared via alcohol exchange reactions and indium derivatives were synthesised by alcoholysis of amides. The desired alcoholates were obtained in high yields (>95 %) as highly viscous oils. All compounds were thoroughly characterised using ^{1}H and ^{13}C NMR spectroscopy. Similar to the aminoalcohols described above, alkoxide formation is clearly indicated by a pronounced low-field shift of the $C_{\alpha}H$ signal. Furthermore, for symmetrically functionalised alcoholates, a pronounced low-field shift of groups in vicinity to the sulphur donor is observed, as shown for *In3* in figure 2-6. Especially the shift for the first methylene group of the ^{n}butyl chain (marked in green in figure 2-6) is a strong indication for a dative interaction of the thioether moiety to the metal centre due to its large distance from coordinating alkoxo oxygen. The absence of multiple sets of signals for these groups is again an indication for a fast exchange in coordination modes in solution at room temperature as there are twice as many donor atoms as coordination sites available. It should also be noted that only one signal for the $C_{\alpha}H$ group is detected, which points towards a monomeric state in solution at room temperature.

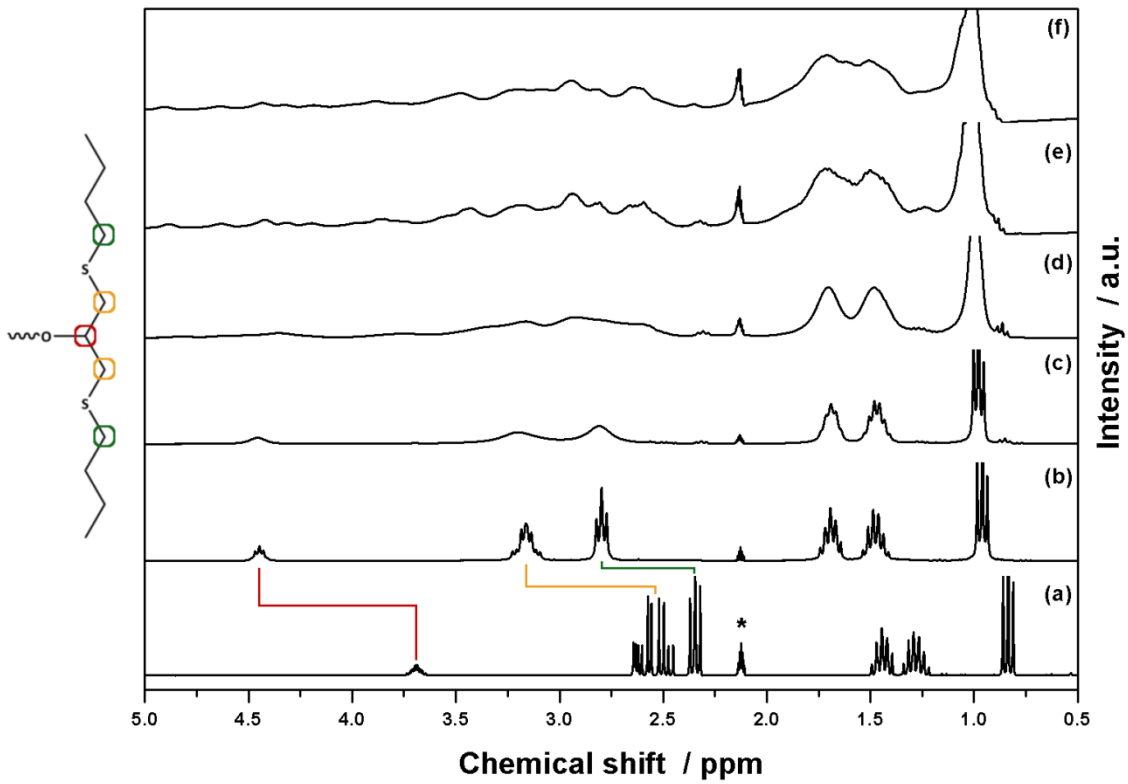

Figure 2-6: ^{1}H NMR spectra of (a) the free alcohol ligand and *In3* at (b) +25 °C, (c) -20 °C, (d) -40 °C, (e) -60 °C and (f) -70 °C in d8-toluene. Asterisk denotes solvent signals.

Low temperature NMR (LTNMR) spectroscopy was employed to gain further insight into the coordination behaviour by slowing down fluctuations in solution. Unfortunately, as can be seen in figure 2-6, there are several regimes of coalescence up to temperatures as low as -70 °C, which did not allow the identification of specific coordination modes due to broad overlapping signals. Yet, it is evident that the system is more complex than anticipated from room temperature NMR experiments. For instance, several signals for the $C_{\alpha}H$ group with chemical shifts reaching form approx. 4.4-4.9 ppm could indicate that there are various ligand systems with different connectivity at lowered temperature, i.e. chelating and pending in terminal or bridging positions. At this point, dimer formation at lower temperatures cannot be excluded from the obtained data. However, there are also several possible coordination isomers, e.g. *fac* and *mer* conformation in an octahedral arrangement, which have to be considered as the origin of multiple signals.

In contrast, the strong shift of the thioether bound side chain is not observed for asymmetrically functionalised aminoalcohols and signals of the thioether side chain stay virtually unaffected. Yet, a pronounced shift is found for groups attached to the amine donor as opposed to a minimal shift of sulphur bound groups, as depicted exemplary for *In5* in figure 2-7. For *In5*, the observed shifts at room temperature are 0.5 versus 0.08 ppm for the methylene groups of the diethylamino and ^{n}butylthioether functionalities, respectively. The nitrogen moiety obviously is a much more potent donor site and

suppresses dative coordination of the thioether to the metal centre. As with the symmetric counterparts, only one set of signals for the $C_{\alpha}H$ group is detected indicative of a monomeric state in solution. Although amine species are well-known to strongly coordinate to Lewis-acidic metals, only one set of signals is observed for the diethylamino functionality. This indicates dynamic coordination behaviour in solution at room temperature.

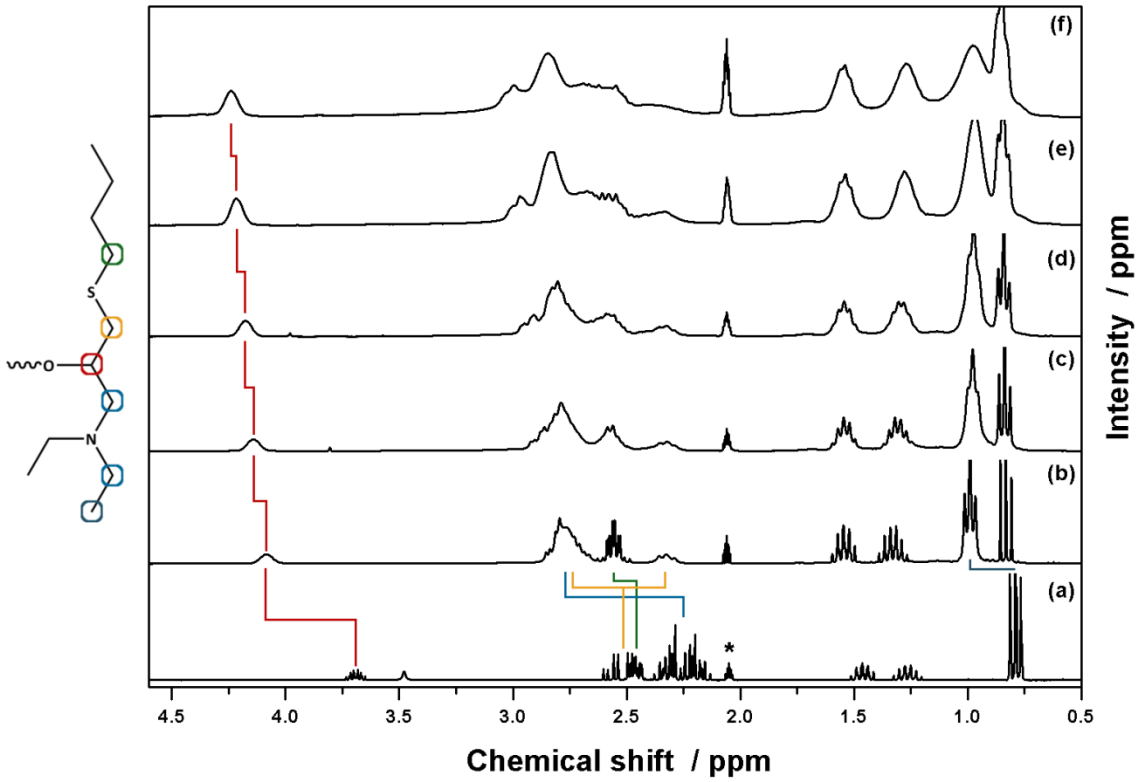

Figure 2-7: ^{1}H NMR spectra of (a) the free aminoalcohol ligand and *In5* at (b) +25 °C, (c) -20 °C, (d) -40 °C, (e) -60 °C and (f) -75 °C in d8-toluene. Asterisk denotes solvent signals.

As depicted in figure 2-7, employing LTNMR spectroscopy shows that there are several regimes of coalescence in the temperature window between room temperature and -75 °C and therefore no distinct species could be attributed with certainty. Nevertheless, the spectra are not as complex as for the symmetric counterparts (see figure 2-6). It is reasonable to assume that fluctuations in nitrogen donation are slowed down with decreasing temperature, which would lead to more distinct features for a coordinating and pendant donor species. This could explain broadening of overlapping signals at 2.5-3.0 ppm in figure 2-7. In addition it would be in agreement with the observed low-field shift of $C_{\alpha}H$ with decreasing temperature due to more permanently bound nitrogen donors as opposed to the average signal obtained at room temperature. 2D HSQC-TOCSY (heteronuclear single quantum correlation – total correlation spectroscopy) experiments show three sets of signals, which are shown colour-coded in figure 2-8. This further allowed the identification of the C_{β}-bound diastereomeric

protons located at 2.32 ppm as well as in the overlapping multiplet at 2.78-2.95 ppm, which is confirmed in 2D COSY (correlation spectroscopy) NMR experiments shown in figure 2-9.

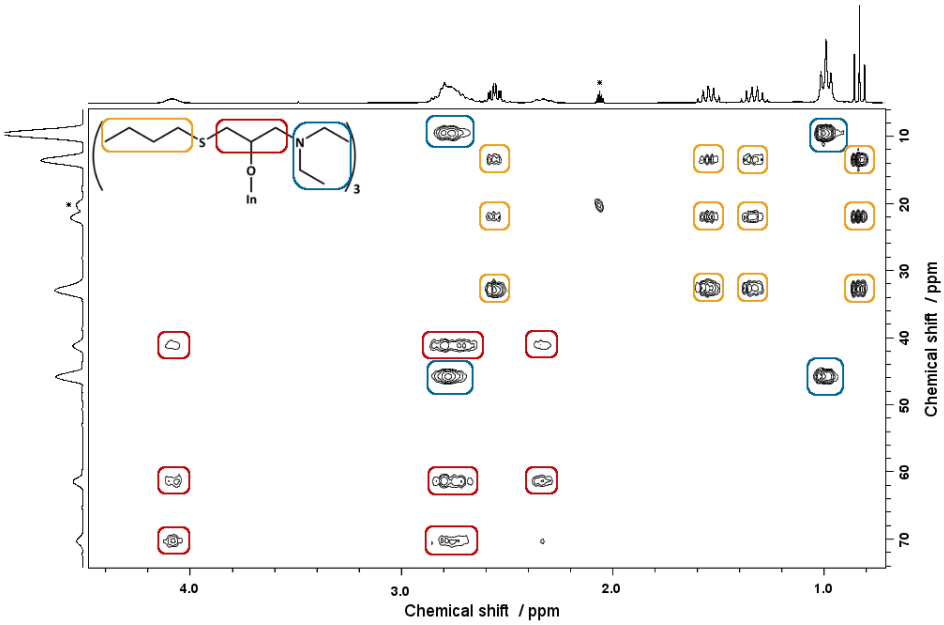

Figure 2-8: Colour coded 2D HSQC-TOCSY NMR of *In5* in d8-toluene at room temperature. Asterisk denotes solvent signals.

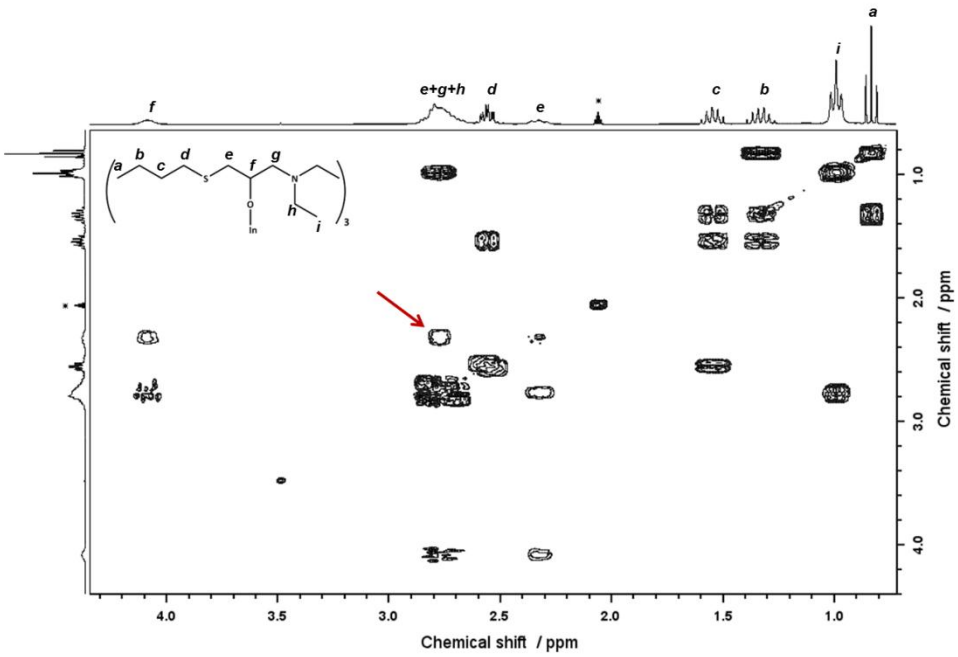

Figure 2-9: 2D COSY NMR of *In5* in d8-toluene showing the diastereomeric protons *e*. Asterisk indicates solvent signals.

All gallium alkoxides with symmetric alcohols and asymmetric aminoalcohols *Ga3-Ga10* showed very similar coordination behaviour compared to indium based species *In3-In10*. Indium alkoxides were chosen for the discussion due to less overlapping signals. According to the hard-soft acid-base (HSAB) principles one could argue that indium based alkoxides could tend towards the softer thioether donor, while the harder gallium central atoms would prefer the hard amine bases.[61, 62] Yet, literature reports still tabulate In^{3+} ions as hard Lewis acids and as such should also favour hard Lewis bases, i.e. the amine functionality. Furthermore, metal centres in homoleptic metal alkoxides can be considered borderline hard acids (also dependent on the alkyl substituent) and tertiary amines are rather borderline hard bases and as such complement each other well.[456, 457] These propositions are in good agreement with our experimental findings.

In contrast to the symmetrically functionalised alkoxides and asymmetric aminoalcoholates discussed so far, mixed ether/thioether functionalised alkoxides showed unexpected differences between gallium and indium based materials. As depicted in figure 2-10 for *Ga12* and *In12*, ^{1}H NMR spectra of gallium alkoxides clearly indicate the formation of a dimer in solution at room temperature, while they point towards a monomeric state for indium alcoholates as with other indium species discussed before. This is best noticeable for $C_{\alpha}H$ protons (marked in red in figure 2-10), which show one signal for indium species, while gallium alkoxides exhibit two signals with an integral ratio of 2:1 corresponding to terminal and bridging alkoxo species, respectively. Furthermore, this is also observable in ^{13}C NMR spectra, which exhibit multiple signals for gallium species, while only one set of signals is observed for indium alkoxides, as shown in figure 2-11.

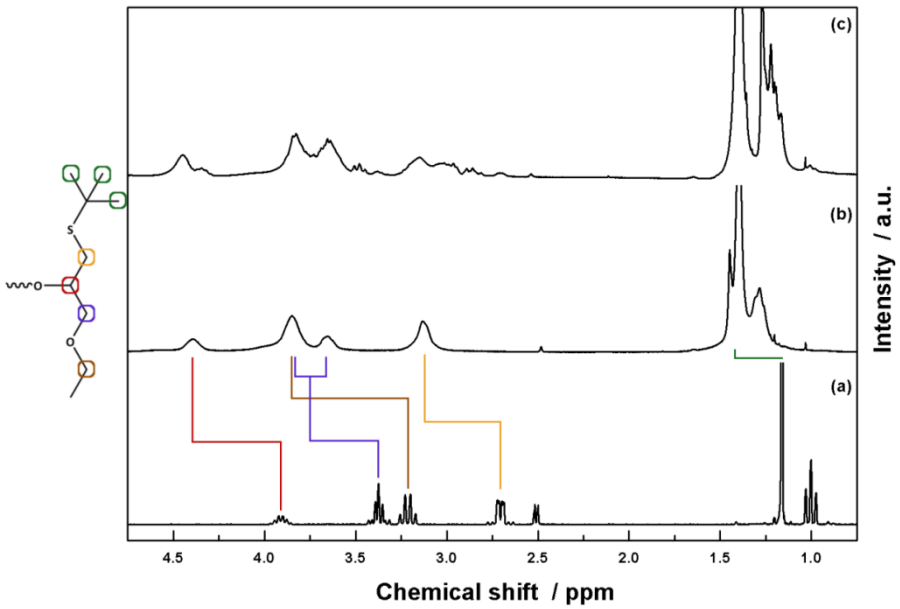

Figure 2-10: ^{1}H NMR spectra of (a) the free ligand, (b) *In12* and (c) *Ga12* at room temperature in C_6D_6.

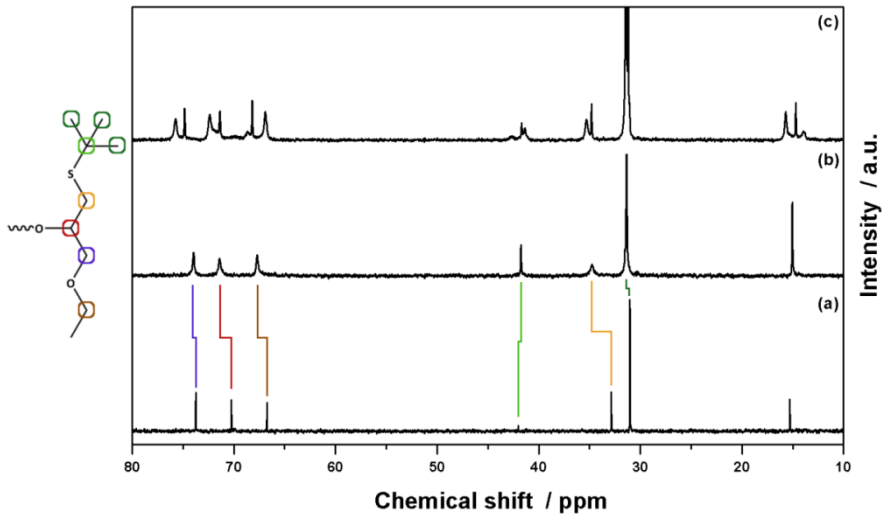

Figure 2-11: ^{13}C NMR spectra of (a) the free ligand, (b) *In12* and (c) *Ga12* at room temperature in C_6D_6.

The low-field shift of the methylene group attached to the oxygen donor upon coordination (0.64 ppm for *In12* in respect to the free ligand, marked in brown in figure 2-10) is much more pronounced than the shift observed for the ^{t}butyl group attached to the sulphur donor (0.26 ppm for *In12*, marked in green in figure 2-10). This indicates a similar scenario to asymmetric aminoalcoholates, with the ether functionality suppressing thioether coordination. This would be in agreement with HSAB principles as ethers are the harder Lewis-bases and is supported by ^{13}C NMR spectroscopy, where there is hardly any shift for signals related to the thioether sidechain.[458] Unfortunately, the most interesting region in ^1H NMR spectra shows strongly overlapping broad signals for gallium species, making it impossible to determine any specific molecular arrangements with certainty. Yet, ^{13}C NMR spectra show three sets of signals for the CH_2 group of the ethoxy side chain. This could indicate a coordinating and a dangling oxygen donor in addition to the bridging and terminal species. It is, however, not possible to assign the chelating ligand to either the bridging or terminal species, although both arrangements have been reported in literature.[272, 454] In addition, potential overlapping because of broadened signals should be taken into account so both arrangements could co-exist. The splitting could also be caused by differing coordination symmetries. Nevertheless, in comparison with other alkoxide derivatives discussed above, where potential symmetry caused splitting was only observed at very low temperatures, this is rather unlikely.

The formation of a dimeric compound for gallium alkoxides *Ga11* and *Ga12* as opposed to the monomeric indium species *In11* and *In12* is rather surprising as the tendency to form oligomeric species typically increases with the radius of the central atom. However, it is possible that the increased Lewis acidity of the smaller gallium metal centre plays a more important role in this specific case. Additionally, steric reasons should be considered as a co-factor. Indium complexes often exhibit octahedral coordination spheres allowing for coordination of all three ether moieties and thus sufficient coordinative saturation and shielding of the metal centre. The smaller ionic radius of gallium

generally leads to tetrahedral or trigonal bipyramidal configurations, which apparently does not provide sufficient shielding with the relatively small ethylether functionality. In contrast, secondary aminoalcoholates *Ga5* and *Ga6* formed monomeric compounds, which is most likely due to the increased steric demand of the diethylamino moiety in comparison to the ethylether group. In addition, ethers show a slightly weaker interaction with the metal centre as compared to amines.[63]

We were able to crystallise two of the presented alkoxides, *In8* and *Ga6*, from concentrated ^{n}pentane solutions at -28 °C. Detailed crystallographic and refinement data as well as selected bond lengths and angles are compiled in tables 2-3 and 2-4. CIF files were deposited at the CCDC with numbers 1004496 and 1004497. The molecular structure of *In8* is depicted in figure 2-12 and shows a monomeric nuclearity in the solid state. The central indium atom exhibits an octahedral coordination sphere with three alkoxo oxygen atoms and three thioether sulphur atoms in a *mer*-geometry. Each of the chelating sulphur donors is attached to a different ligand, leaving each alcohol with another dangling donor site.

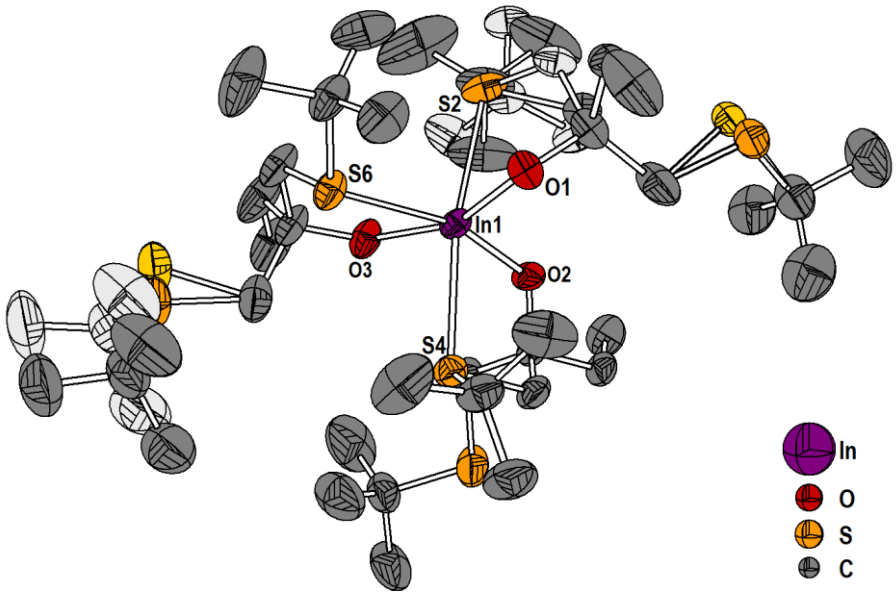

Figure 2-12: Molecular structure of *In8* drawn with 50 % probability ellipsoids. Disordered parts are represented in pale colours; hydrogen atoms and a ^{n}pentane solvent molecule have been omitted for clarity.

In-O bond distances range from 2.0467(15) to 2.0599(13) Å and fit reported values for terminal alkoxo ligands in homoleptic trisalkoxides and are expectedly shorter than those of bridging alkoxo species.[453, 459] In-S bond lengths are between 2.7210(6) and 2.8123(5) Å, which is much longer than In-S bond lengths found in thiolates (2.44 - 2.47 Å)[460], xanthates (2.55-2.63 Å)[302], thiocarboxylates (2.45-2.49 Å)[382] or dithiocarboxylates (2.56-2.62 Å).[303] Elongated In-S bond distances have been previously reported for coordinative interactions of thioethers.[461, 462] Internal angles within the chelate rings are compressed to 73.30(4) to 78.29(4)°, while angles along the meridian assume angles

of 156.61(3)° for O1-In1-O3 to 170.79(2)° for S2-In1-S4 leading to a distortion of the octahedral coordination sphere. O1-In1-O2 (103.26(6)°) and O2-In1-O3 (97.81(6)°) bond angles are far from the expected 90° for an ideal octahedron pushing O1 and O3 towards S6.

The crystal structure of *In8* featured some disorder, which was accounted for using the split-atom model for separate parts of the molecule. As depicted in figure 2-12 in pale colours, pendant donor sites (S1 and S5) were more commonly affected due to an increased degree of vibrational freedom compared to the chelating donor sites. For the same reasons disorder was only detected on the ^{t}butyl group (C10-C13) and the methylene bridge C9 bound to the chelating sulphur atom S2, but not on the donor atom itself.

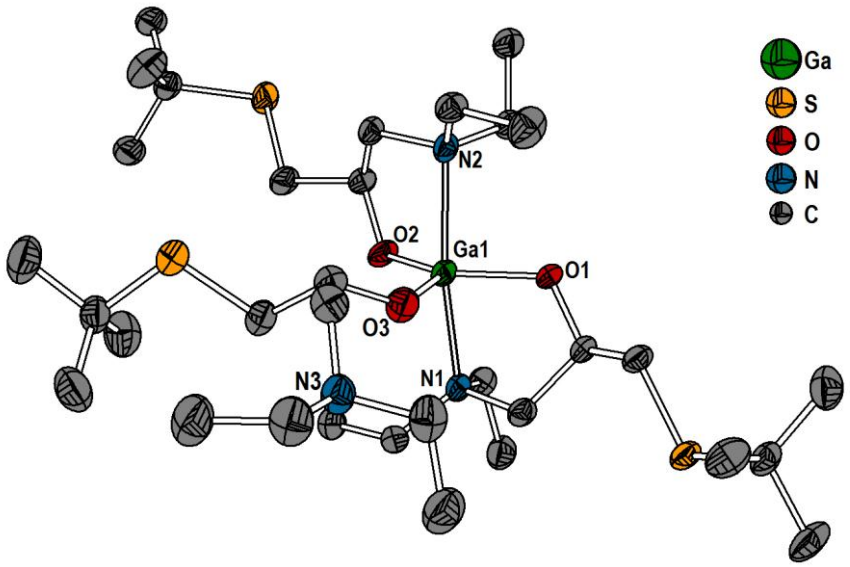

Figure 2–13: Molecular structure of *Ga6* shown with 50 % probability ellipsoids. Hydrogen atoms have been omitted for clarity.

The molecular structure of *Ga6*, as shown in figure 2-13, features a distorted trigonal bipyramidal coordination sphere with a monomeric nuclearity. Similar to the molecular structures described for *Ga1* and *Ga2*, the coordination sphere consists of three alkoxo oxygen atoms in the equatorial positions and two nitrogen donors in the apical positions. This leaves all thioether donors and one additional nitrogen donor site uncoordinated, which is in good agreement with NMR experiments discussed above.

Ga-O bond lengths are in good agreement with bond distances found in terminal gallium alkoxides and are shorter than those reported for bridging alkoxides.[27, 67, 463] Ga1-O3 distance is slightly shorter (1.842(2) Å) than Ga1-O1 and Ga1-O2 (1.866(2) and 1.863(2) Å, respectively), which is in agreement with experimental data found in *Ga1* and *Ga2* for non-chelating ligands. Ga-N distances

(1.234(2) and 2.219(3) Å) are also in a similar range. The N1-Ga1-N2 bond angle is 163.32(9)° with chelating ligands leaning away from the non-chelating one. Bond angles in the equatorial plane sum up to 360°, but are differing quite a lot showing a widened O1-Ga1-O2 angle of 131.75(10)° and a reduced O1-Ga1-O3 angle of 107.91(10)°, while O2-Ga1-O3 (120.09(10)°) is only minimally off the ideal 120°.

Table 2-3: Crystallographic and refinement data of *Ga6* and *In8*.

Compound	*Ga6*	*In8*+C_5H_{12}
Emp. Formula	$C_{33}H_{72}GaO_3N_3S_3$	$C_{44}H_{93}InO_3S_6$
M_r /g mol^{-1}	724.84	977.36
Crystal system	Triclinic	Triclinc
Space group	$P\bar{1}$	$P\bar{1}$
a / Å	10.9239(16)	10.5221(8)
b / Å	12.8002(12)	14.8955(11)
c / Å	17.470(4)	18.5318(13)
α / °	108.527(4)	84.795(2)
β / °	97.665(4)	83.722(2)
γ / °	108.690(2)	74.537(2)
V / Å^3	2117.5(6)	2776.94(4)
Z	2	2
D_x / g cm^{-3}	1.137	1.169
μ / mm^{-1}	0.83	0.683
Crystal size / mm	0.4 x 0.16 x 0.10	0.4 x 0.35 x 0.35
No. measured refl.	11387	144925
Obs. Refl. [I>2σ(I)]	5897	16308
Θ_{max} / °	25.0	32.2
R [F^2>2σ(F)], wR (F^2), S	0.048, 0.144, 1.05	0.040, 0.109, 1.13
Refl./param.	7385/403	20301/667
Weighting scheme*	a = 0.0954, b = 0	a = 0.0348, b = 2.3567

* $w = 1/[\sigma^2(F_o^2) + (aP)^2 + bP]$, where $P = (F_o^2 + 2F_c^2)/3$

Table 2-4: Selected bond lengths and angles for *In8* and *Ga6*.

In8		*Ga6*	
Bond	**Distance / Å**	**Bond**	**Distance / Å**
In1-O1	2.0504(14)	Ga1-O1	1.866(2)
In1-O2	2.0599(13)	Ga1-O2	1.863(2)
In1-O3	2.0467(15)	Ga1-O3	1.842(2)
In1-S2	2.7210(6)	Ga1-N1	2.234(2)
In1-S4	2.7821(6)	Ga1-N2	2.219(3)
In1-S6	2.8123(5)		
Angle	**/ °**	**Angle**	**/ °**
O1-In-O2	103.26(6)	O1-Ga-O2	131.75(10)
O1-In-O3	156.61(6)	O1-Ga-O3	107.91(10)
O2-In-O3	97.81(6)	O2-Ga-O3	120.09(10)
O1-In-S2	73.30(4)	O1-Ga-N1	82.99(9)
O1-In-S4	101.17(4)	O1-Ga-N2	90.67(9)
O1-In-S6	87.40(4)	O2-Ga-N1	89.19(9)
O2-In-S2	95.61(4)	O2-Ga-N2	83.56(9)
O2-In-S4	78.29(4)	O3-Ga-N1	93.58(10)
O2-In-S6	162.94(4)	O3-Ga-N2	103.06(10)
O3-In-S2	94.78(5)	N1-Ga-N2	163.32(9)
O3-In-S4	92.90(5)		
O3-In-S6	74.75(4)		
S2-In-S4	170.79(2)		
S2-In-S6	100.25(2)		
S4-In-S6	86.66(2)		

2.3 MOLECULE-TO-MATERIAL CONVERSION OF THIOETHER FUNCTIONALISED ALKOXIDES

2.3.1 Thin film deposition via LPCVD

After exploring the molecular properties of novel thioether functionalised alkoxides, their applicability in molecule-to-material conversion and thermal decomposition pathways were investigated. For that purpose, alkoxide precursors were employed in LPCVD experiments using a horizontal cold-wall reactor setup. The precursors showed good conversion of gallium alkoxides to $Ga_2O_{3-x}S_x$ oxysulphide thin films with varying sulphide concentrations. Film thickness was in the range of 0.2-0.5 µm with good adhesion to Si(100) and SiO_2 substrates.

Unfortunately, gallium alkoxides *Ga3*, *Ga4* and *Ga8* as well as all indium alkoxides did not provide reproducible and efficient decomposition or showed insufficient volatility leading to no or very slow thin film growth in LPCVD experiments. This is most likely caused by the weak interaction between thioether donor and metal centre in symmetrically substituted alkoxides, which could lead to the formation of oligomers at increased temperatures. In addition, molecular weights for the monomeric precursor species are already rather high, in particular for indium alkoxides. Further increase of the precursor temperature was not possible as the volatilisation temperature was already very close to the decomposition onset temperatures for many alkoxide precursors (*vide infra*) or the maximum operating temperature of the apparatus (190 °C).

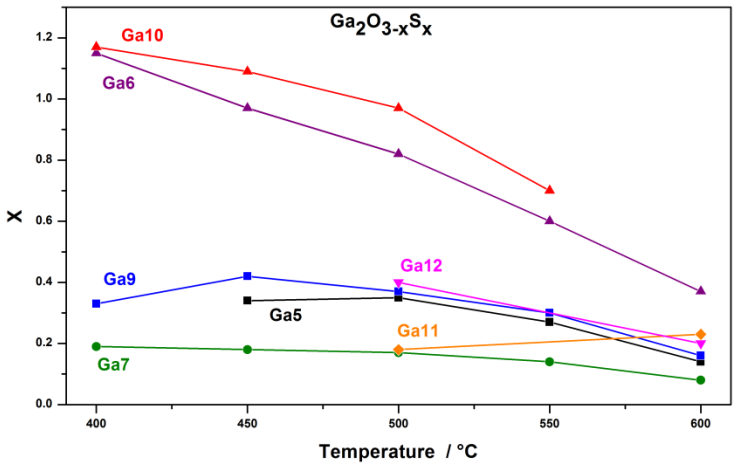

Figure 2-14: Sulphur content of $Ga_2O_{3-x}S_x$ thin films determined from EDX assuming all detected sulphur to be sulphidic.

The sulphur content of the deposited thin films was found to be strongly dependent on precursor species and decomposition/substrate temperature. Sulphur contents were determined via EDX analysis and are shown in figure 2-14 assuming that all measured sulphur content was sulphidic in nature. Asymmetric aminoalcoholate *Ga5* shows a rather constant sulphur content around x = 0.3 (6 at%) at temperatures below 500 °C, but drops to x = 0.14 (2.8 at%) at 600 °C. ^{t}Butyl-derivative *Ga6* on the other hand shows significantly higher sulphur contents up to x = 1.17 (23.4 at%) at 400 °C, but a more pronounced decrease with increasing temperature is found, giving x = 0.37 (7.4 at%) at 600 °C. The most likely reason for the decrease in sulphur content at higher temperature is the formation of the thermodynamically more stable oxide in combination with more effective decomposition of the organic backbone.[464]

Ga7 was the only alkoxide derivative with symmetrically functionalised alcoholate ligands that provided reproducible thin film growth. Although there is theoretically twice as much sulphur available in the precursor molecule compared to asymmetric aminoalcoholates, the observed sulphur content was the lowest of all precursors (x = 0.19 (3.8 at%) at 400 °C to x = 0.08 (1.6 at%) at 600 °C), pointing towards a less favourable decomposition pathway for sulphidisation compared to asymmetrically functionalised aminoalcoholates. *Ga9* and *Ga10* are almost the same as their secondary counterparts *Ga5* and *Ga6* showing only slightly higher sulphur contents and a similar trend with increasing temperature. Nevertheless, it should be noted that films deposited from tertiary alcoholates suffered from increased amounts of carbon contamination especially at low decomposition temperatures. This indicates incomplete decomposition of the organic backbone and subsequent incorporation of residual fragments of the ligand into the growing film. For precursors *Ga5* and *Ga6* featuring secondary alcohols, carbon contamination was generally under 3 w%, but decreased with increasing temperature to concentrations under 1 w% at 600 °C. Precursors with tertiary alcohols on the other hand yielded thin films with carbon contents ranging from 16 w% at 400 °C to 2 w% at 600 °C. It is well known that CVD derived coatings usually suffer from increased superficial carbon contaminations.[465] However, because of the high information depth of EDX analysis, this can be safely neglected.

Ga11 features sulphur contents in the same region as other asymmetric ^{n}butyl derivatives, but shows a minimal increase from x = 0.18 (3.6 at%) at 500 °C to x = 0.23 (4.6 at%) at 600 °C. *Ga12* on the other hand exhibits x = 0.4-0.2 at 500 and 600 °C, respectively, which is far below other asymmetric ^{t}butyl derivatives. Although they are secondary alcoholates, deposits from *Ga11* and *Ga12* show surprisingly high amounts of carbon contaminations even at increased temperatures. ^{n}Butyl derivative *Ga11* exhibits particularly high carbon contents of 20-12 w%. This points towards an unfavourable decomposition for asymmetric ether/thioether functionalised species. It could also explain the increase in sulphur for *Ga11* because of incorporation of fragments of the organic backbone of the ligand in combination with limited accuracy of EDX analysis.[466, 467] It should be noted that ^{t}butyl derivatives exhibit higher sulphur contents in every case when directly compared to their ^{n}butyl counterparts. This fact strongly points towards a decomposition path favourable for the formation of reactive intermediate species leading to sulphur incorporation.

All deposits using gallium alkoxide precursors were amorphous, as would be expected in the examined temperature range.[27, 468] Scanning electron microscopy (SEM) images show uniform and smooth films for all alkoxides as depicted exemplary for *Ga5* and *Ga6* in figure 2-15. A more pronounced microstructuring is observable for *Ga5* (figure 2-15 (a-d)), which is most likely due to the lowered sulphur content and thus facilitated formation of nuclei. For *Ga6* (figure 2-15 (e-h)) hardly any features are observable independent of temperature in agreement with high sulphur contents. Cross section SEM (figure 2-15 (i)) proves the film thickness to be uniform over the entire substrate area.

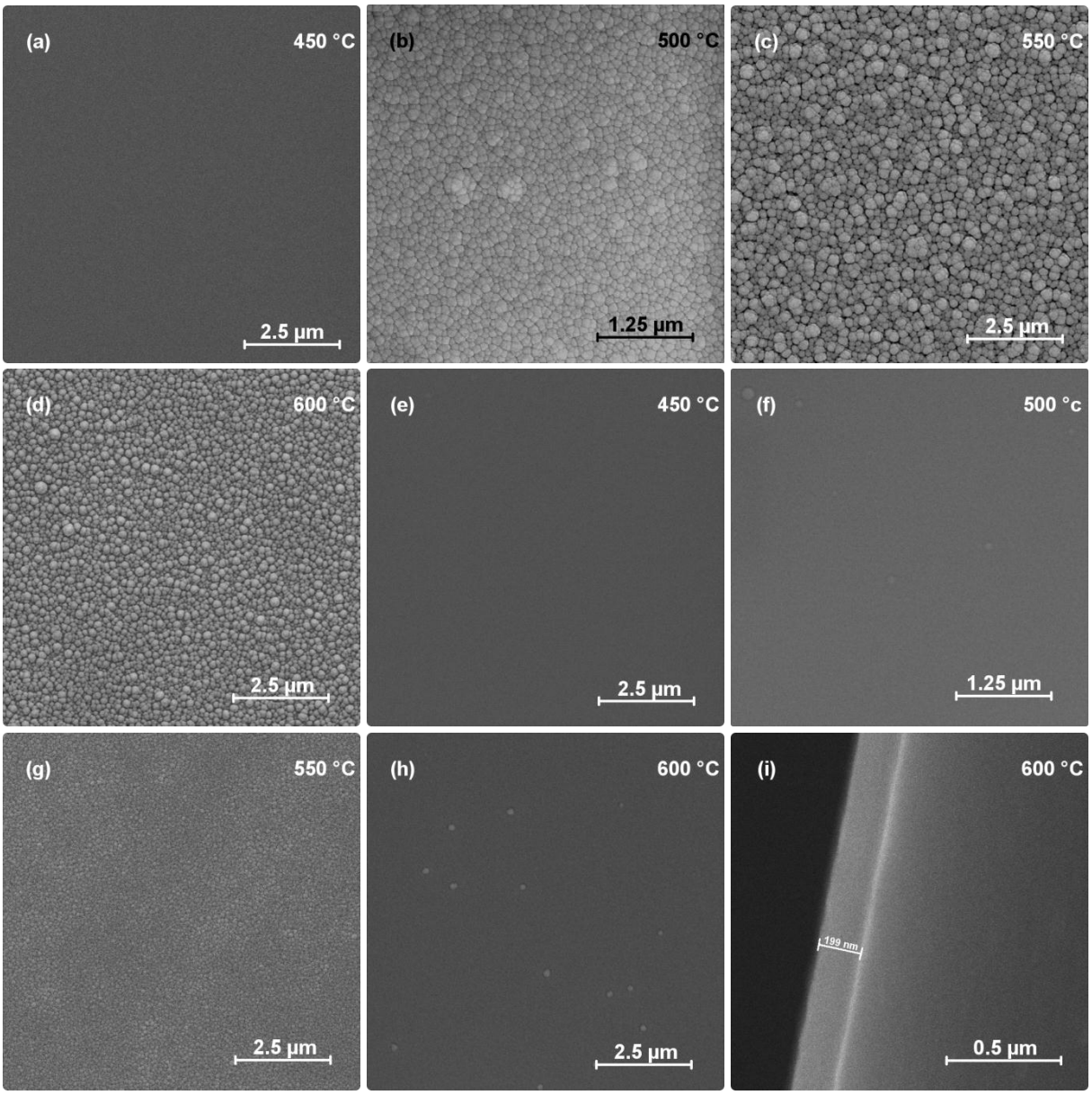

Figure 2–15: SEM micrographs of thin films deposited using *Ga5* (a-d) and *Ga6* (e-i) at various temperatures

Sulphide contents discussed so far were based on the assumption that all sulphur detected in EDX analysis was sulphidic. Yet, carbon contaminations indicated incomplete decomposition especially at lower decomposition temperatures and EDX does not give any information about the chemical nature or environment of the detected elements. Therefore, XPS was performed on selected deposits focussing on secondary systems with low carbon contamination and high sulphur content. All thin films were sputtered for 30 min with argon ions to eliminate any surface bound carbon contaminations. Exemplary spectral overviews of thin films produced from *Ga6* at 600 °C before and after sputtering are shown in figure 2-16. It is obvious that the carbon content is drastically reduced as seen by the decreased C1s signal at approx. 286 eV. Additionally, a small amount of argon is implanted into the thin film indicated by the Ar2p signal at 242.5 eV.

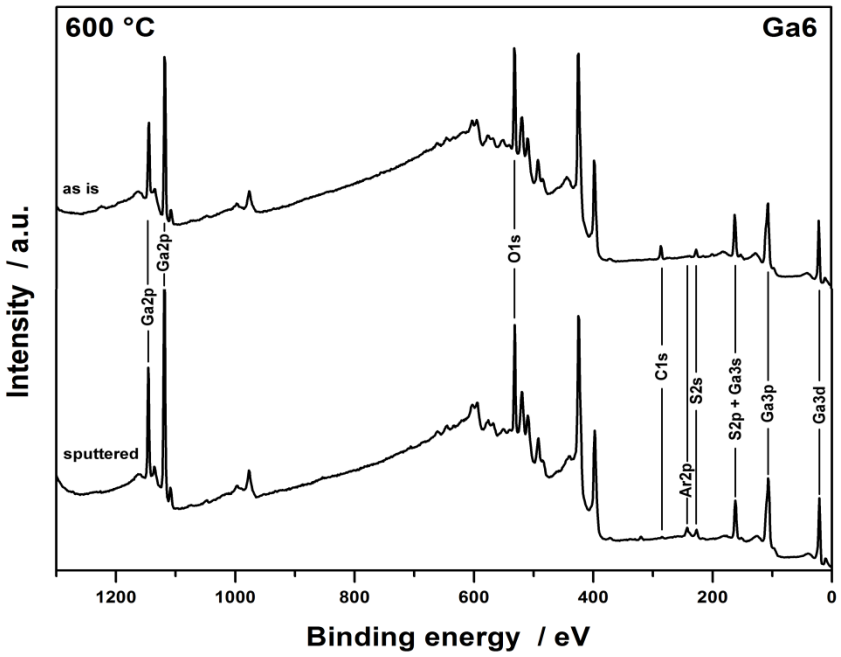

Figure 2-16: XPS spectra of thin films produced from *Ga6* at 600 °C before and after sputtering.

The S2s region was used for investigation of the chemical nature of the incorporated sulphur instead of the more commonly used S2p signals due to overlapping of S2p and Ga3s signals.[469] Detailed spectra of the S2s region of *Ga5* and *Ga6* derived deposits are depicted in figure 2-17. For ^{n}butyl derivative *Ga5* only a single signal centred around 225.5-226.0 eV could be detected at temperatures of 500 °C and above, which can be attributed to S^{2-} in gallium sulphides.[470] At 450 °C, however, a second signal with low intensity (4 % of the S2s peak area) was detected at higher binding energies of approx. 229 eV. It is difficult to assign this signal with absolute certainty as there is hardly any literature data available for the S2s region, especially for organic species. Sulphate species could be excluded as their signals usually exhibit binding energies of about 233 eV.[471-473] The only report on C-S-C bonds we were able to find was for sexithiophene, which exhibits a binding energy of 228.3 eV.[474] Therefore, it is

most likely that the signal originates from residual thioether fragments of the decomposing ligands, which were incorporated into the growing thin film. Taking this fraction into account the actual sulphide content for *Ga5* derived coatings at 450 °C is x = 0.17 (3.4 at%). Thin films deposited at higher temperatures gave sulphide contents of x = 0.15, 0.15 and 0.09 at 500, 550 and 600 °C, respectively.

Obviously, sulphur contents determined by XPS are continuously a few percent lower than found in EDX. Comparing XPS spectra for as prepared and sputtered samples show a rather strong decrease of sulphur signals upon sputtering. Since also as prepared samples showed pure sulphides without thioether contamination at higher temperatures, it can be assumed that this decrease is the result of preferential sputtering of sulphur (and oxygen) over gallium rather than removal of organic residues.[475, 476] Preferential sputtering of sulphur on the sample surface would lead to a significant underestimation of the overall sulphur content due to increased surface sensitivity of XPS. Therefore, EDX measurements should be considered as the more correct method for determination of the overall sulphur content of the coatings. Even though EDX analysis was conducted on unsputtered specimen, surface contaminations are only a very small contribution because of the high information depth of EDX analysis. For a detailed list of sulphide contents determined by EDX and XPS refer to table 2-5.

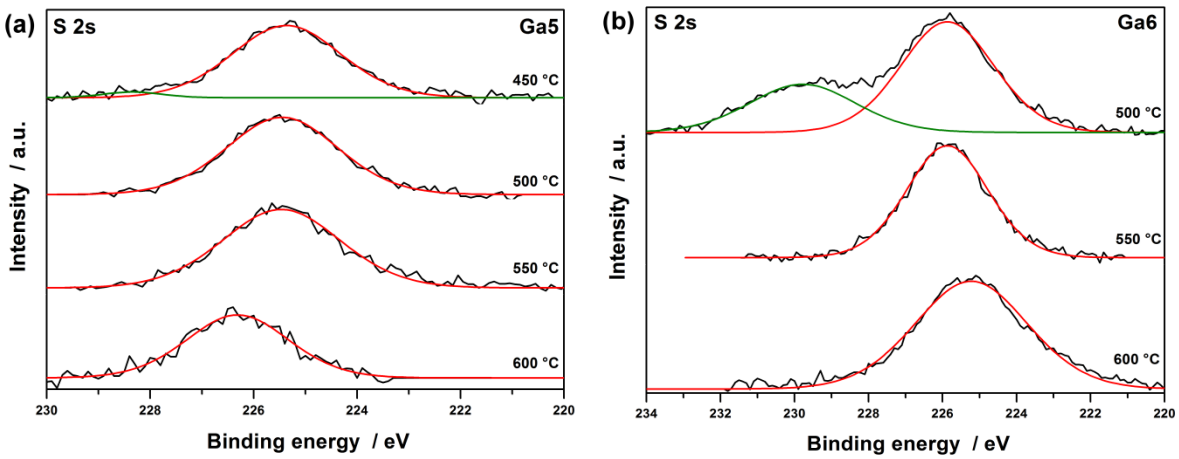

Figure 2-17: XPS spectra of the S2s region at various temperatures for thin films derived from (a) *Ga5* and (b) *Ga6*.

In contrast to the clean decomposition of *Ga5*, XPS spectra show a pronounced second signal in the S2s region for deposits derived from precursor *Ga6* at temperatures below 550 °C. At 500 °C, 1/3 of the total peak area of the S2s region could be attributed to undecomposed thioether species resulting in an actual sulphide content of the deposit of x = 0.49 (9.9 at%). However, no thioether impurities could be detected at 550 and 600 °C showing sulphide contents of x = 0.28 and 0.04, respectively. The fact that *Ga5* shows only minimal thioether contamination at 450 °C, while *Ga6* exhibits significant impurities at the increased temperature of 500 °C indicates a more efficient/clean decomposition pathway for ^{n}butyl derivatives. It should be noted, though, that despite their less efficient decomposition, ^{t}butyl derivatives show a more effective sulphidisation of the deposited materials resulting in higher overall sulphide contents. For *Ga11*, only the thin film deposited at 600 °C

was further analysed by XPS measurements. Despite the increased amount of carbon contamination even at 600 °C (>10 w%), only one species was found in the S2s region after sputtering (not shown graphically). The peak, centred at 226.5 eV, could be well attributed to gallium sulphide and translates to x = 0.08 (1.5 at%).

XPS spectra of the relevant S2s region for thin films deposited from *Ga7*, as a representative for symmetrically functionalised and tertiary alkoxides, also indicate a clean decomposition path. Spectra show no thioether impurities at the investigated deposition temperatures of 500 and 600 °C as shown in figure 2-18 (a). In fact, only a small amount of surface bound impurities were found at 500 °C, which was removed upon sputtering. As expected from EDX analysis, sulphide contents are far below those of *Ga5* and *Ga6*, but remain fairly stable with x = 0.15 and 0.05 (3.0 and 1.0 at%) at 500 and 600 °C, respectively. Even though sulphidisation is less effective, this clearly demonstrates that also symmetrically functionalised alkoxides have potential for oxysulphide formation.

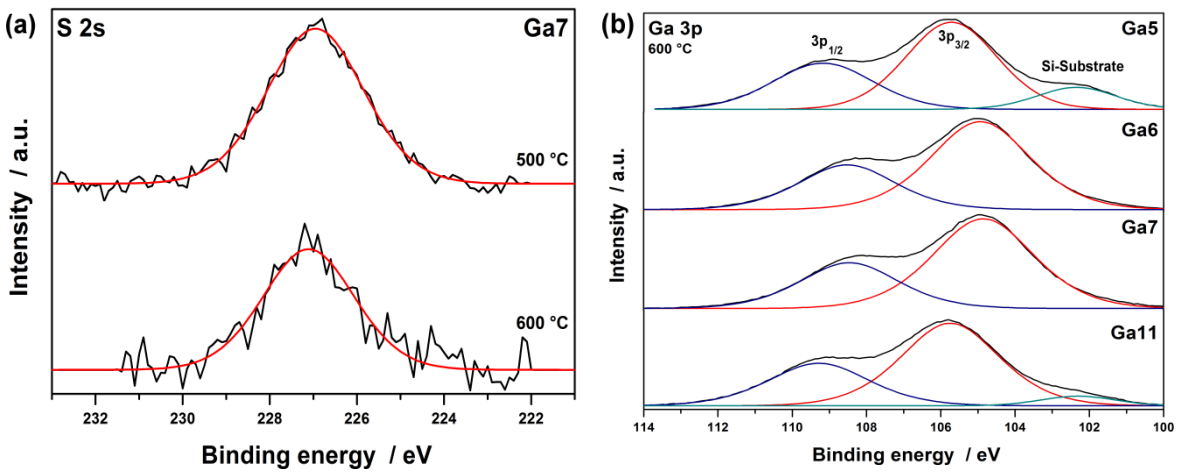

Figure 2–18: XPS spectra of (a) the S2s region for deposits produced from *Ga7* and (b) Ga3p region for deposits using various precursors at 600 °C.

In addition to the relevant S2s region, Ga3p peaks were also investigated. As depicted in figure 2-18, thin films derived from *Ga5*, *Ga6*, *Ga7* and *Ga11* showed only one set of signals with the well-documented spin orbit splitting. More importantly, all peaks are symmetrical in shape and show no secondary peaks or shoulders indicating a uniform chemical surrounding for Ga atoms in the deposits, i.e. there is no phase separation of oxide and sulphide material even at high sulphide contents for *Ga6*. As such, the results demonstrate that the developed molecular precursor species allow a uniform conversion to oxysulphide materials even for oxophilic metals such as gallium. This is especially important for potential applications to assure consistent and uniform material properties, i.e. band gap or electrical conductance. Similar findings were obtained independent of temperature, even as low as 450 °C.

Table 2-5: Sulphide contents (in at%) for LPCVD thin films at different substrate temperatures as found in EDX and XPS (in brackets) where applicable.

	400 °C	450 °C	500 °C	550 °C	600 °C
Ga5		6.8 (3.4)	7.0 (3.0)	5.4 (3.0)	2.8 (1.9)
Ga6	23.4	19.4	16.4 (9.9)	12.0 (5.8)	7.4 (0.89)
Ga7	3.8	3.6	3.4 (3.0)	2.8	1.6 (1.0)
Ga9	6.6	8.4	7.4	6.0	3.2
Ga10	23.4	21.8	19.4	14.0	
Ga11			3.6		4.6 (1.5)
Ga12			8.0		4.0

2.3.2 Electrical properties of $Ga_2O_{3-x}S_x$ thin films

To investigate the influence of oxysulphide formation on macroscopic properties of the thin film materials, electrical conductance was determined by means of impedance spectroscopy. For that purpose, thin films were deposited onto interdigitated platinum electrodes on quartz glass, which are depicted in figure 2-19. We used pure Ga_2O_3 films produced from $[Ga(O^tBu)_3]_2$ as a reference and $Ga_2O_{3-x}S_x$ films with x = 0.37 deposited from *Ga6* at 600 °C for testing electrical conductance because of the high sulphide content in combination with minimal carbon contaminations to assure representative results.

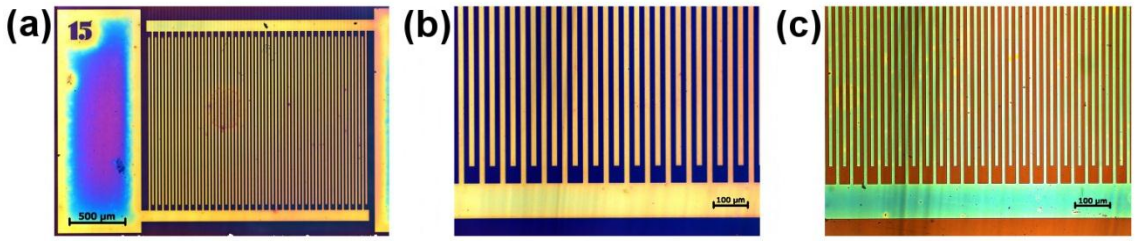

Figure 2-19: Optical micrographs of interdigitated platinum electrodes covered with a Ga_2O_3 thin film with (a+b) 15 µm and (c) 10 µm spacing.

Impedance spectroscopy measurements were performed at temperatures ranging from 200-500 °C in a reducing atmosphere of 2.5 % H_2 in argon to prevent sulphide oxidation in oxysulphide materials during the measurements. Although Ga_2O_3 can be used as H_2 gas sensor at elevated temperatures, the higher conductance values are steady state and therefore should not affect overall tendencies described in the section below. Impedance spectra, shown in figure 2-20, suggest an electronic charge transport as the origin of conductance (n-type conductivity) and clearly demonstrate that there is a significant difference between pure oxide and oxysulphide materials. Pure Ga_2O_3 thin film samples show almost ideal semicircles at 200-300 °C, while only a smaller part of the semicircle or

a real axis intercept could be observed in measurements at higher temperatures. Since no indication for additional electrode features was observed for frequencies as low as 10 mHz, it is assumed that the resistive contribution originates from an electronic conductivity in the thin film samples. The capacitance leading to the observed semi-circular patterns is usually caused by the substrates.[477] In contrast, much smaller resistances were measured on sulphide doped samples deposited from *Ga6* at 600 °C (x = 0.37) and no semicircles could be resolved even at low temperatures.

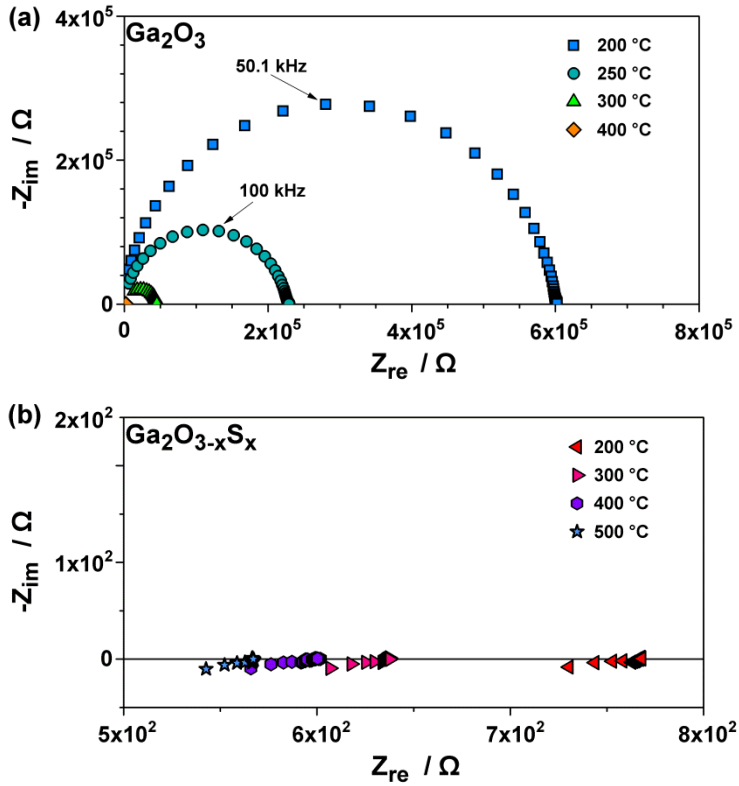

Figure 2-20: Impedance spectra (Nyquist plots) of (a) Ga_2O_3 and (b) $Ga_2O_{3-x}S_x$ thin films on interdigitated Pt electrodes with 15 µm electrode width and spacing.

$$\sigma = \frac{b}{l \cdot d \cdot N \cdot R} \qquad (1)$$

From impedance spectra we were able to calculate the thin film conductance σ employing equation (1), where b is the spacing between to current collecting electrodes, l the length of an electrode, d the thickness of the thin film layer (as determined by cross-section SEM), N the number of thin film areas between the interdigitate electrodes and R the DC resistance. DC resistance R was obtained by evaluating the low frequency intercept of the impedance spectra. Resistance of platinum electrodes usually contributed only 1 % of the total resistance and therefore can be safely neglected. The obtained results for electrical conductance are compiled in figure 2-21.

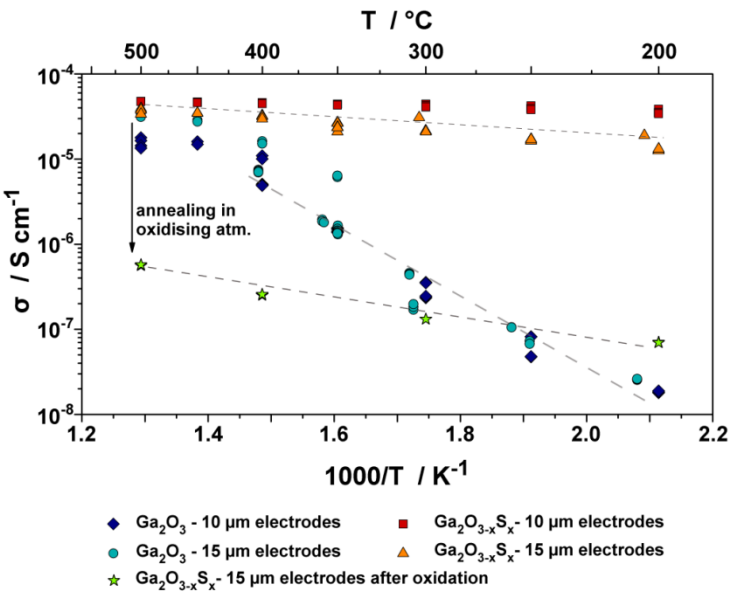

Figure 2–21: Arrhenius diagram of conductivities of Ga_2O_3 and $Ga_2O_{3-x}S_x$ (x = 0.37) thin films.

From the Arrhenius diagram in figure 2-21 it is clear that sulphide doping has a huge impact on the conductivity of the thin films. Especially in the low temperature range from 200-350 °C the sulphide containing $Ga_2O_{3-x}S_x$ thin films show an increased conductivity, which is up to three orders of magnitude higher than those of pure Ga_2O_3 thin films. At temperatures of 400 °C and above the conductance of Ga_2O_3 and $Ga_2O_{3-x}S_x$ thin films become more similar. It should also be noted that conductivity values do not depend on the size of the Pt interdigitates and only differ slightly. Thus, it is safe to assume that artefacts originating from the current collectors can be excluded.

In addition, the activation energy of the conductivity, represented by the slope of the curves in figure 2-21, is drastically reduced for the oxysulphide films in the low temperature range (0.12 ± 0.04 vs. 0.9 ± 0.08 eV for $Ga_2O_{3-x}S_x$ and Ga_2O_3, respectively), while it also gets more similar to those of pure Ga_2O_3 films at higher temperatures. Electrical conductivity is directly proportional to the number of charge carriers and their mobility in a material.[478] Due to the high sulphide content in the oxysulphide thin film sample, it can be assumed that the number of charge carriers is independent of temperature.[479] The increase in conductivity is hence a result of temperature dependence of the mobility and thus also the activation energy is governed by effects of the charge carrier mobility. For pure Ga_2O_3, charge carrier concentration is not independent of temperature and thus a stronger temperature-dependence of the conductivity is observed at lower temperatures.

After treating the oxysulphide thin film samples in oxidising atmosphere (50 mbar O_2) for 1 h at 500 °C, the conductance is drastically reduced in the whole temperature range as shown in green stars in figure 2-21. The activation energy, however, stays largely unaffected by the oxidising treatment. This indicates that the underlying conduction mechanism is not altered by the oxidative treatment, whereas a decrease in the number of charge carriers is the most likely explanation for the decreased

conductivity. It is thus assumed that the oxidative treatment led to a partial removal of the sulphide from the thin films with the remaining sulphide content enabling the same conduction mechanism as in the initial oxysulphide thin film. Nevertheless, it is clear that sulphide incorporation in amorphous Ga_2O_3 thin films is a highly complex matter and hence an unambiguous explanation for the conduction mechanism and influence of sulphide incorporation cannot be given without further extensive investigation of these properties.

2.3.3 Synthesis of powders via hot-injection pyrolysis

As mentioned before, especially indium alkoxide species proved insufficiently volatile for LPCVD processing. Yet, as thioether functionalised gallium alkoxides showed promising conversion to oxysulphide materials, also indium species should show sulphidisation upon thermolysis. For that purpose we used hot-injection methods to convert all alkoxide precursors to sub-micron chalcogenide particles. For experimental process details refer to section 3.3.2.

As expected, the obtained sub-micron particles showed significant amounts of sulphur, which was determined by EDX analysis, as shown in figure 2-22. We did not account for organic species adsorbed on the particle's surface, which could possibly lead to overestimation of the sulphur content of the material. Obviously, the sulphur content for indium based materials exceeded the content found in their gallium counterparts by far, even reaching sulphur contents of x = 3 (60 at%) for *In3*, which represents full conversion to the sulphide. The sulphide rich nature of all indium based oxysulphides was already indicated by the orange-beige colour of the materials as opposed to the colourless nature of In_2O_3.

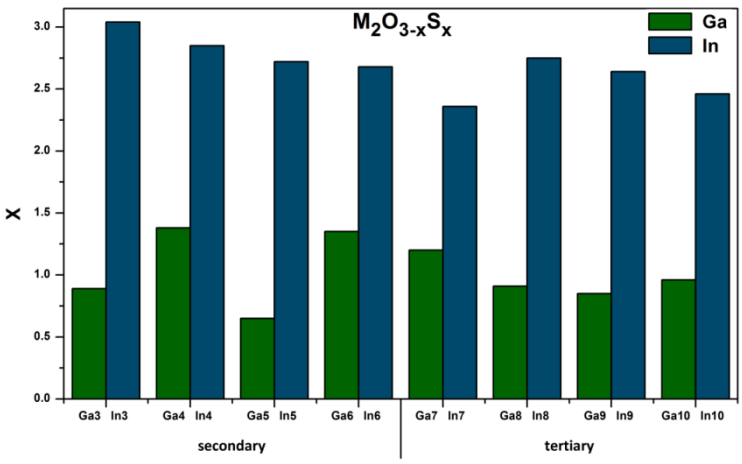

Figure 2-22: Sulphide content of $M_2O_{3-x}S_x$ particles as determined via EDX assuming all measured sulphur to be sulphidic.

For gallium species all found sulphur contents matched or exceeded those found in LPCVD experiments. This is most likely caused by the different mechanisms of the processes. In LPCVD experiments, the (reactive) by-products are removed via desorption, while they stay in solution and thus in close vicinity to the growing particles in hot-injection pyrolysis. This could lead to prolonged period of potential sulphidisation resulting in increased sulphur contents. *Ga4* and *Ga6* showed the highest conversion rates with sulphide contents of x = 1.38 and 1.35 (27.6 and 27.0 at%), respectively. These results are in agreement with LPCVD experiments, where ^{t}Bu derivatives also showed increased sulphide contents. *Ga10*, which showed the highest sulphide contents in LPCVD experiments (x = 1.09 at 450 °C), exhibits similar results in hot-injection experiments with x = 0.98.

Increased conversion for indium based materials is not entirely surprising considering that In_2O_3 is easily converted to In_2S_3 by H_2S.[228, 273] In fact, a stream of diluted H_2S even at temperatures as low as 500 °C for 1 h is sufficient for a > 90 % conversion for micron sized In_2O_3. Ga_2O_3 on the other hand shows only very little sulphidisation under the same conditions, because of higher Ga-O bond strength.[464, 480] Powder XRD analysis of H_2S treated In_2O_3 and Ga_2O_3 are shown in figure 2-23 (a-b). Different amounts of conversion are also easily followed visually as seen in pictures in figure 2-23 (c). Colourless In_2O_3 is transferred to orange In_2S_3 while no change in colour is observable for Ga_2O_3, which would turn to a yellowish colour upon conversion to Ga_2S_3.[273]

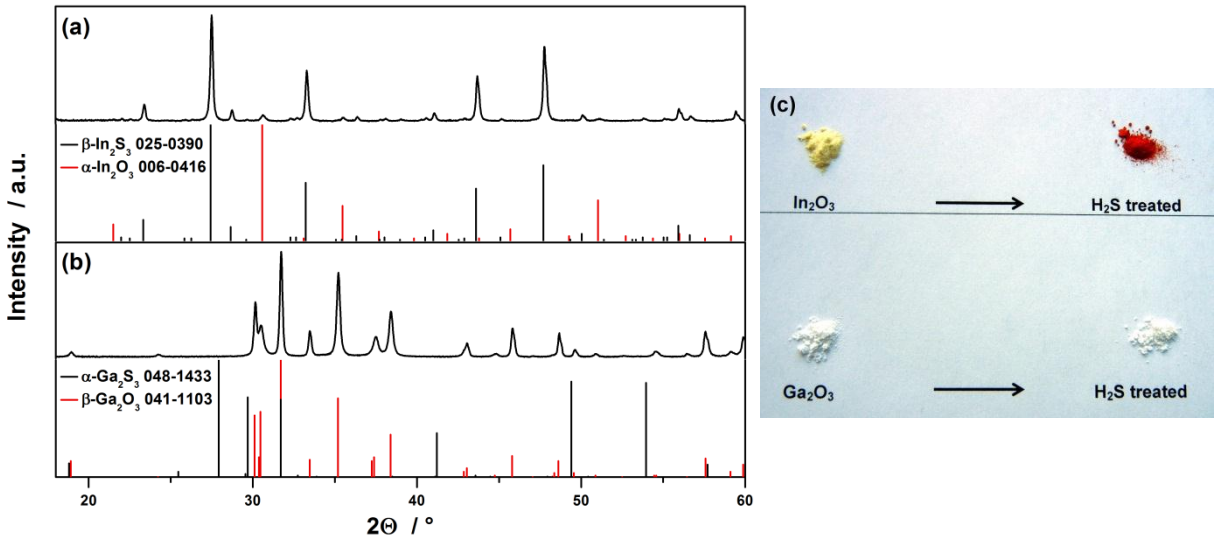

Figure 2-23: Powder XRD of (a) In_2O_3 and (b) Ga_2O_3 treated with H_2S for 1 h at 500 °C and the respective references. (c) Photograph of In_2O_3 and Ga_2O_3 powders before and after H_2S treatment.

XRD analysis showed that gallium based materials were amorphous similar to LPCVD deposits. In contrast, phase pure ß-In_2S_3 was obtained for all indium based materials as opposed to In_2O_3, which is usually obtained via thermolysis of indium alkoxides. Figure 2-24 shows XRD patterns of the obtained In_2S_3 powders and an In_2O_3 reference sample produced via similar hot-injection pyrolysis of $In(O^{t}Bu)_3$, which is known to form pure In_2O_3 upon thermolysis.[138]

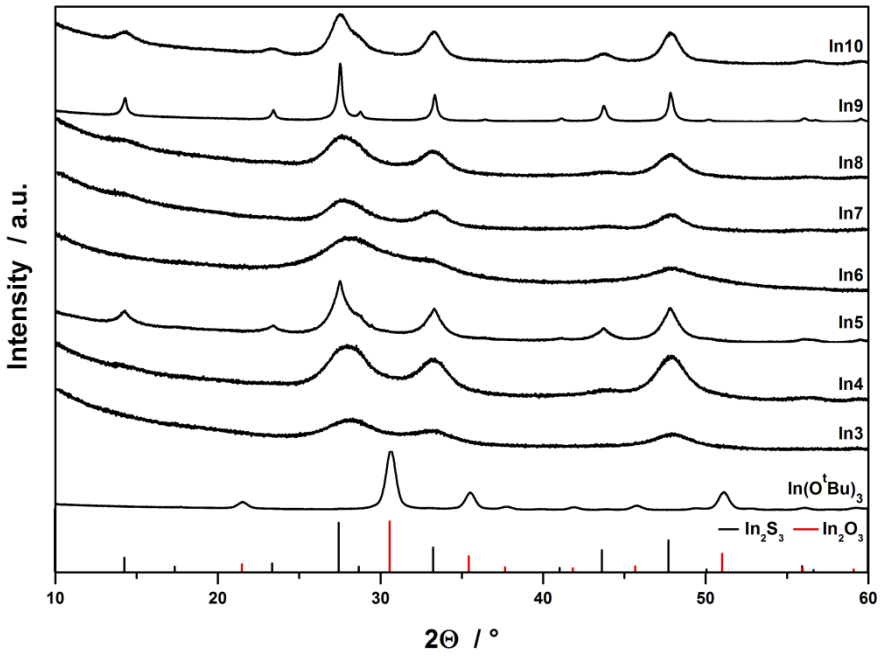

Figure 2–24: XRD patterns of powders obtained via hot-injection thermolysis of various indium based precursors and β-In_2S_3 (ICDD 06-0416) and α-In_2O_3 (ICDD 084-1385) references.

XRD patterns of powder samples derived from hot-injection pyrolysis of *In3-In10* also suggest varying crystallite size for the powder samples as indicated from the reflex widths. As such, particles derived from asymmetric aminoalcoholates and in particular ^{n}butylthioether functionalised species *In5* and *In9* show increased crystal size and a higher degree of crystallinity indicated by sharper reflexes, which points towards a cleaner decomposition pathway of these aminoalcoholates. This is in agreement LPCVD derived $Ga_2O_{3-x}S_x$ thin films, which also indicated clean decomposition of aminoalcoholate precursors. However, it is surprising that *In9* derived particles showed a higher degree of crystallinity than *In5* since tertiary alkoxide precursors led to increased amounts of carbon contamination in LPCVD experiments, which in turn should hinder the crystallisation process. Nevertheless, the XRD data clearly points towards high purity of the material obtained via hot-injection processing of *In5* and *In9*.

XPS on selected samples was performed to confirm the sulphidic nature of the precipitates. Due to the uneven surface of particle samples, these specimens have not been sputtered prior to analysis, which could potentially lead to measurement of surface contaminations. Nevertheless, XPS spectra of all analysed deposits from indium based precursors show only one set of signals, which can be perfectly referenced to In_2S_3.[481, 482] Except for the expected spin orbit splitting, neither In3d peaks nor peaks in the S2p regions show any second peaks or shoulders, which indicates a pure, single phase for the particles. S2p region was chosen for indium based particles since no peak overlapping is observed and the S2p region is more commonly used because of its higher sensitivity. In addition, the In:S ratio was determined to be 0.67 and 0.68 for *In3* and *In5*, respectively, which is in perfect agreement with the theoretical value of 0.67 for In_2S_3.

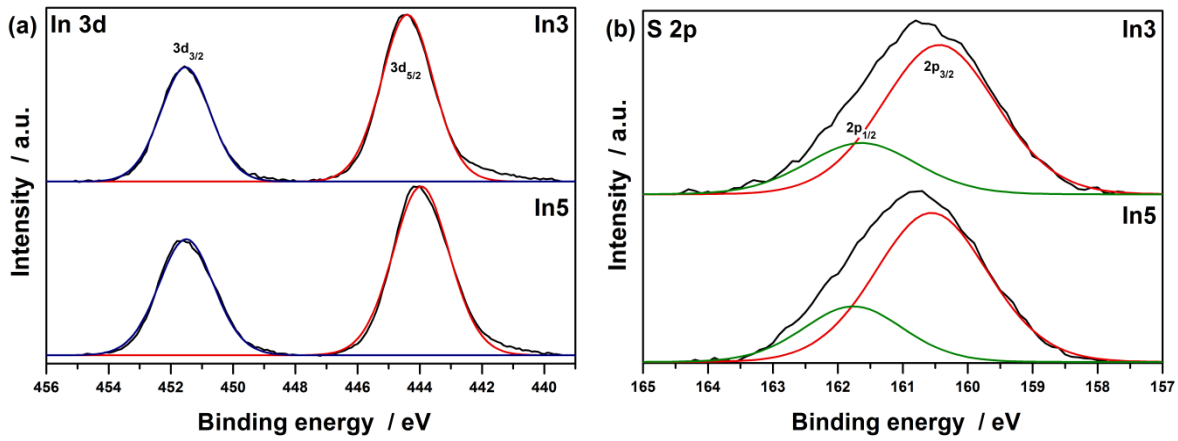

Figure 2-25: XPS spectra of (a) In3d and (b) S2p region of particles derived from *In3* and *In5*.

2.3.4 Investigation of the decomposition mechanism

It has been previously reported that thioether adducts of metal halides showed conversion to sulphide materials upon thermolysis. The decomposition and sulphidisation mechanism, however, is still largely unknown.[440-443] Literature reports generally refer to a kinetically favoured decomposition pathway due to the coordination of sulphur to the metal centre in thioether complexes.[483] However, it is unlikely that the thioether functionalised species reported here, exhibit thioether coordination at elevated temperatures necessary for volatilisation and decomposition due to the weak bonding observed at room temperature. In addition asymmetric alcoholates did not show thioether coordination at room temperature and in the solid state, which makes coordination in the gas phase even more unlikely. Therefore, also effects of secondary decomposition have to be taken into account. Thioethers have been reported to thermally decompose via a radical mechanism, often in connection with ß-hydride elimination, potentially forming highly reactive intermediate species, which in turn can lead to sulphidisation of the growing materials.[484-486]

Thermogravimetric analysis (TGA) and differential scanning calorimetry (DSC) coupled with mass spectrometry (MS) on selected precursors were employed to gain further insight into the decomposition behaviour and mechanism of the sulphide incorporation. As shown exemplary in figure 2-26, gallium based precursors *Ga3-Ga6* featuring secondary alcoholate ligands showed a two-step weight loss, which is more pronounced for the asymmetric aminoalcoholates. In contrast, *Ga7* with a tertiary alcoholate ligand as well as all secondary indium based precursors *In3-In6* showed single-step decomposition. Single-step decomposition would be preferred for material synthesis applications to give clean and stoichiometrically uniform deposits. DSC curves, depicted in red in figure 2-26, are in good agreement with TGA signals showing exothermic transitions for precursor decomposition and formation of the thermodynamically favoured solid concomitant with mass loss detected in TGA. The small endothermic signals at higher temperatures are likely the result of solid-solid rearrangements as no concomitant

mass loss was detected and the transitions are far below the expected melting temperatures of the oxide and sulphide materials.

More importantly, decomposition onset temperatures are comparably low, in particular for *Ga4*-*Ga6* and *In5* with 160-170 °C. Precursors featuring symmetric ^{n}butylthioether functionalisation *Ga3*, *Ga7* and *In3* showed higher onset temperatures of 200-210 °C indicating increased thermal stability of these precursor species. Additionally, residual masses of the decomposition products for symmetrically substituted species were found to exceed the theoretically calculated value for pure Ga_2O_3 by 1.2-2 % on average indicative of ineffective decomposition leading to high amounts of carbon contamination. For asymmetric aminoalcoholates on the other hand, residual masses are very close to the theoretical value for gallium species, i.e. 13.11 vs. 12.90 % for *Ga6*. Small differences could be accounted for by sulphur incorporation into the material as evidenced for LPCVD films as well as small amounts of carbon residues. Pyrolysis of *In5* led to a residual mass 0.55 % above the theoretical value for In_2O_3. This could either point towards ineffective decomposition and carbon contamination or towards large amounts of sulphur incorporation. The orange-brown colour of the residue, however, points towards formation of a sulphide rather than an oxide, which would be in agreement with high sulphide contents found in hot-injection pyrolysis experiments for indium based materials as discussed in chapter 2.3.3. Moreover, asymmetric gallium aminoalcoholates gave only minimal amounts of carbon contamination in LPCVD experiments indicating clean and efficient decomposition of these species. Hence, it is reasonable to assume that indium aminoalcoholates show similar decomposition behaviour and that the increased residual weight is thus caused by sulphide incorporation rather than carbon contaminations.

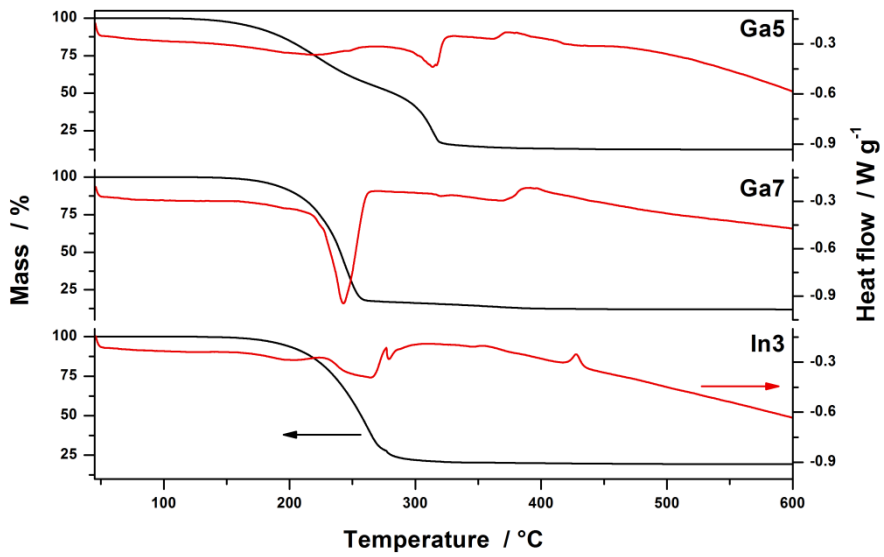

Figure 2-26: TGA (black) and DSC curves (red) of *Ga5*, *Ga7* and *In3*.

On-line MS data, shown in figure 2-27, can give further insight into the decomposition and sulphidisation mechanism. For symmetric thioether functionalised alkoxides most intense fragments were found with m/z = 29, 41, 44 and 56, which can be assigned to $C_4H_9^+$, $C_3H_5^+$, $C_4H_9S^{2+}$ and $C_4H_8^+$,

respectively, which can be attributed to the thioether side chain and the isopropyl backbone of the ligand. Fragmentation patterns of asymmetric aminoalcoholates are far more complex due to additional fragments of the amino side chain, which is best identifiable by fragments with m/z = 30 ($C_2H_6^+$), 72 (NEt_2^+) and 86 ($CH_2NEt_2^+$). More interesting though, aminoalcoholate species exhibit a significant amount of H_2S (m/z = 34), as well as its oxidation products SO and SO_2 (m/z = 48, 64). It should be noted that no H_2S was found for *Ga3* and *Ga4* and only small amounts were detected for *Ga7* and *In3*. H_2S is a potent sulphidisation agent known to convert oxides to their respective sulphides at elevated temperatures as discussed in chapter 2.3.3. It can be assumed that the *in situ* production of H_2S during the thermolysis of the precursor is essential for obtaining an effective, homogenous sulphidisation of the growing thin films. In contrast, post-growth sulphidisation with H_2S is limited by surface reactions and diffusion, in particular for oxophilic metals such as gallium.[197, 273, 464] While the presented data does not allow us to formulate a distinct decomposition mechanism, it clearly shows the supporting role of the amino side chain in the effective formation of reactive sulphidisation reagents. In addition, the formation of radical species as described in literature has to be considered for the actual sulphidisation reaction.[484-486]

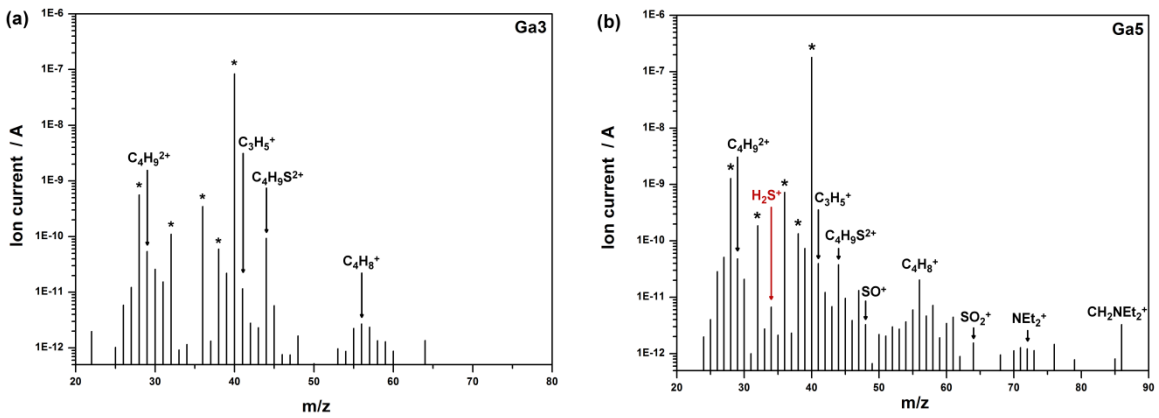

Figure 2–27: MS patterns during thermolysis of (a) *Ga3* and (b) *Ga5* showing the formation of H_2S in case of aminoalcoholate precursors. Asterisks denote signals of the carrier gas.

2.3.5 Synthesis of thin films and 1D structures via AACVD

As mentioned before, indium based precursors did not show sufficient volatility for LPCVD processing, but showed good applicability for molecule-to-material conversion in hot-injection pyrolysis providing high sulphide contents in the resulting materials. To study the applicability and behaviour of indium based derivatives in CVD processes, we developed an AACVD setup to circumvent volatility issues encountered for these precursors. The setup and experimental procedure are described in detail in the experimental section. Initial tests showed most consistent depositions using ^{n}hexane as the solvent, rather than the more commonly used toluene or mixtures with THF. ^{n}Hexane showed good

solubility of the precursors, efficient aerosol generation as well as fast vaporisation due to its low boiling point of 66 °C.

While asymmetric aminoalcohols showed reproducible thin film growth, asymmetric ether-thioether functionalised as well as symmetric alkoxides did not provide satisfactory deposition. The reason is most likely the very moderate temperatures (<440 °C) applied in the borosilicate setup. 400 °C was also found to provide only slow film growth in LPCVD and resulted in very thin coatings. Furthermore, symmetrically functionalised alkoxides also showed higher onset temperatures for decomposition in TGA/DSC experiments discussed in chapter 2.3.4. However, we were able to convert asymmetric aminoalcoholates to indium oxysulphide coatings with considerable sulphur contents, which was determined by EDX analysis as shown in figure 2-28. In agreement with results obtained in hot-injection pyrolysis, indium based thin films exhibited much higher sulphur contents than their gallium counterparts in LPCVD. AACVD using *Ga6* resulted in $Ga_2O_{3-x}S_x$ thin films with sulphur contents in a similar range as in LPCVD processes, namely 18 vs. 23 at% for AACVD and LPCVD, respectively. The differences might be the result of increased carbon contaminations at low temperatures, as well as thioether residues in the thin films as shown in XPS studies discussed for LPCVD derived coatings.

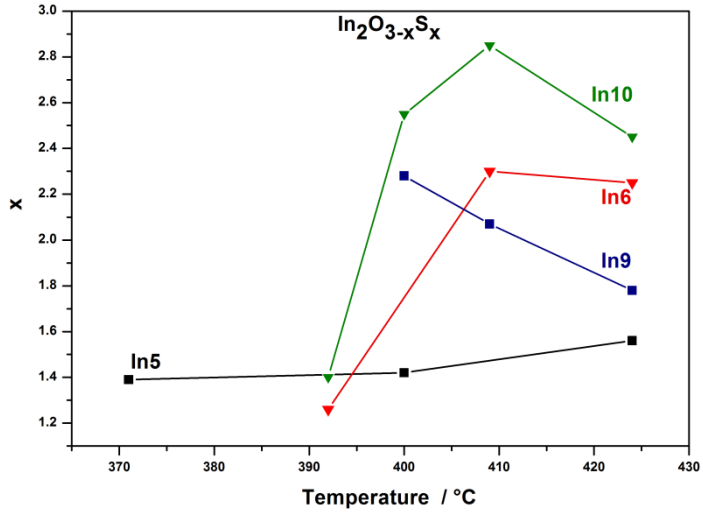

Figure 2-28: Sulphur contents of thin films deposited via AACVD of various asymmetric indium aminoalcoholates determined via EDX analysis assuming all sulphur to be sulphidic.

As evident from figure 2-28, ^{t}butylthioether derivatives *In6* and *In10* show a significantly higher sulphur content than ^{n}butyl species *In5* and *In9* in agreement with results obtained for their gallium counterparts in LPCVD experiments. The investigated temperature range was rather limited; however, *In6* and *In10* exhibit strong temperature dependence in the examined interval. They follow a similar trend, showing a strong increase in sulphur content around 400 °C and remaining more or less stable up to 430 °C. *In5* and *In9* on the other hand do not exhibit a comparable trend in the investigated temperature range, with *In5* staying rather constant around x = 1.5, while *In9* shows a decrease from x = 2.28 at 400 °C to x = 1.78 at 425 °C. Compared to LPCVD films, all AACVD layers display increased

amounts of carbon contamination usually in the range of 10-20 %, even for secondary aminoalcoholates, which showed very clean decomposition in LPCVD. The most likely reasons are the low temperature employed in the AACVD setup in combination with increased precursor delivery rates, because of the kinetical limitations of the heterogeneous surface reaction in this temperature regime. In addition, the solvent should also be considered as a possible source of carbon contamination.

In agreement with results obtained for particles derived from hot-injection pyrolysis of indium based precursors, XRD of thin films deposited from AACVD showed the formation of ß-In_2S_3 phases for all precursors. Because of the smaller size of the oxide ion compared to sulphide, substitution of sulphide with oxide does not lead to major physical distortion of the unit cell of the parent In_2S_3 lattice.[206] Hence, differences cannot be detected in XRD analysis, especially for the small crystallites sizes and subsequently broadened reflexes of the prepared samples. Exemplary XRD patterns for coatings deposited from *In6* are depicted in figure 2-29, showing temperature independence of In_2S_3 formation in the investigated temperature window. SEM micrographs show uniform coatings with microstructuring, as depicted in figure 2-30. While no microstructuring was observed for $Ga_2O_{3-x}S_x$ thin films from LPCVD experiments at temperatures below 500 °C, microstructuring in AACVD derived $In_2O_{3-x}S_x$ coatings is most likely the result of lowered crystallisation temperature for In_2S_3 combined with high sulphide contents found for *In6* and *In9*.[375]

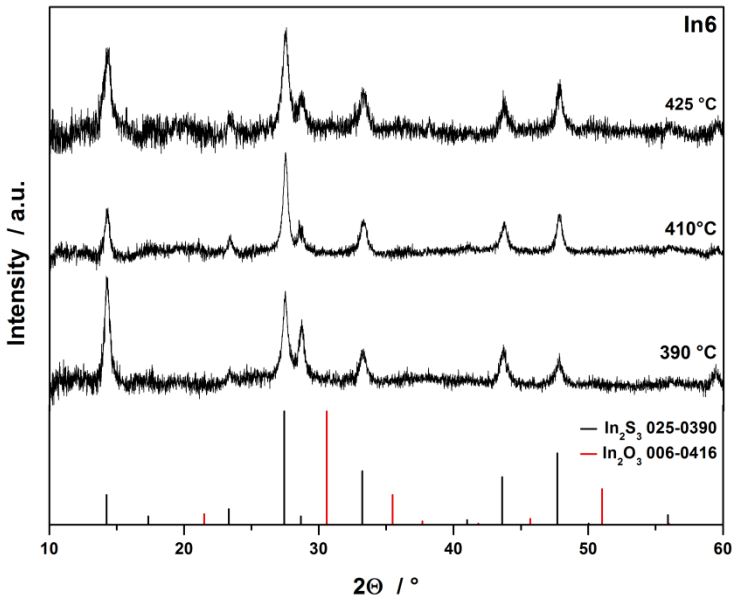

Figure 2-29: XRD patterns of thin film deposits derived from *In6* at various temperatures.

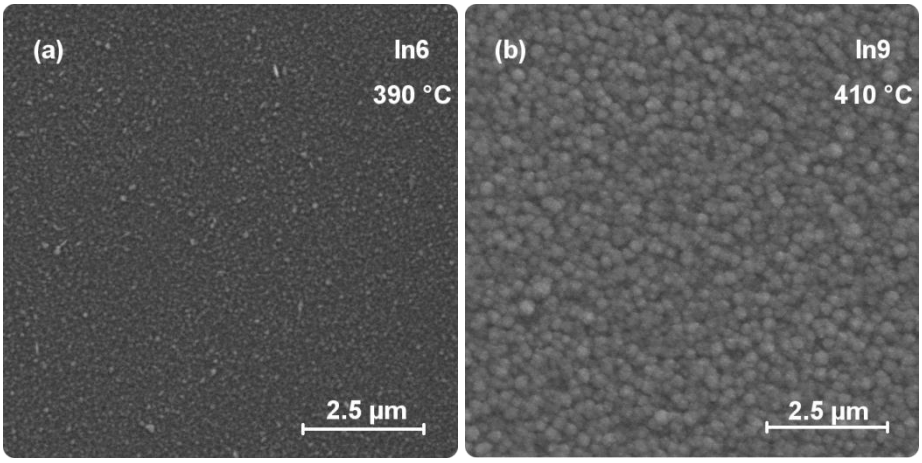

Figure 2-30: SEM micrographs of AACVD thin films employing (a) *In6* and (b) *In9* at various temperatures.

XPS was once more employed to investigate the chemical nature of the incorporated sulphur as well as the purity of the coatings. Spectra of In3d and S2p regions of sputtered thin films are displayed in figure 2-31. Both samples show symmetric signals without shoulders in the In3d region according to a uniform chemical environment without phase separation. In addition, only one set of S2p signals was observed, which indicates that no residual thioether moieties are present in the samples. Especially considering the low growth temperature of approx. 400 °C, this indicates a clean and effective decomposition of thioether functionalised indium aminoalcoholates. In comparison, gallium oxysulphide thin films derived from *Ga5* and *Ga6* via LPCVD showed thioether fragments in coatings below 450 and 500 °C, respectively. The differences could be caused by the variation of the reactor type since a cold-wall reactor was used in LPCVD experiments, while AACVD employed a hot-wall reactor. The latter would allow formation of a reactive intermediate species by homogenous gas phase reactions, which could potentially alter the decomposition path in subsequent heterogeneous reactions on the substrate.[169, 171]

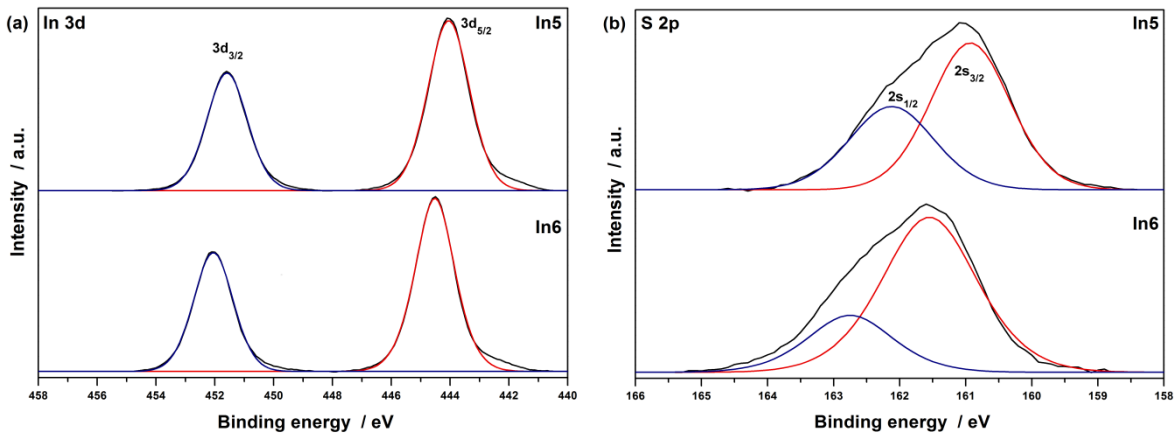

Figure 2-31: XPS spectra of (a) In3d and (b) S2p region of AACVD coatings using *In5* (390 °C) and *In6* (410 °C).

Sulphide contents after sputtering were found at x = 1.1 and 2.0 (22.1 and 40.4 at%) for *In5* and *In6*, respectively. These sulphide contents are again a little lower than found in EDX analysis, but are in good agreement if preferential sputtering is considered, which was already observed for $Ga_2O_{3-x}S_x$ thin films. Furthermore, peak positions for *In6* fit those of In_2S_3 references, while *In5* shows a deviation of about 0.4-0.6 eV.[481, 482] The shift towards lower binding energies can be most likely attributed to the higher oxide concentration in the thin film as In_2O_3 was reported to give signals in the same region, but are also within the range of error introduced by the laboratory X-ray source.[487] Nevertheless, no phase-separation and only ß-In_2S_3 phases were found.

At the highest applicable deposition temperature of 425 °C in combination with slightly increased carrier gas flow rates of 70 sccm, nanowire growth and formation of rod-type structures was observed for *In5*, *In9* and *In10*, rather than thin film growth found at lower temperatures. XRD analysis of 1D structures grown from *In5* and *In9* gave signals originating from ß-In_2S_3 and α-In_2O_3, as shown in figure 2-32. This indicates phase separation in these samples as opposed to formation of the pure ß-In_2S_3 phase observed for AACVD-derived thin films and particles from hot-injection pyrolysis. Rietveld analysis of the XRD pattern obtained for *In5* calculated a ß-In_2S_3 content of 44 %, which is in rough agreement with sulphide contents of 52 at% obtained from EDX analysis of thin films at similar temperatures. Differences are most likely the result of different morphologies of the products with and without phase separation. Furthermore, Rietveld analysis of nanocrystalline samples will not result in exact values due to broad reflexes with low signal/noise ratio, which also the reason why Rietveld analysis of samples derived from *In9* was not possible. In contrast, XRD of 1D structures obtained from *In10* show phase pure sulphide material similar to thin film samples indicating formation of oxysulphide material without phase separation. Phase separation for *In5* and *In9* is very likely the result of the approx. 50 at% sulphide content, which would lead to strong distortion of the crystal lattice, if anion replacement in this amount took place. For *In10*, which showed much higher sulphide contents of about 83 at%, these distortions are less pronounced and thus no phase separation is observed.

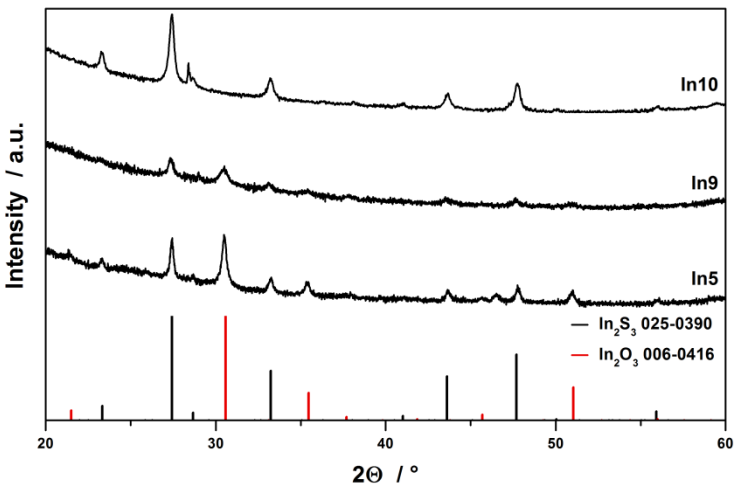

Figure 2-32: XRD patterns of 1D structures synthesised via AACVD of *In5*, *In9* and *In10*.

SEM studies, as shown in figure 2-33, revealed that morphology and length : diameter ratio of the 1D structures is strongly dependent on the precursor species. For ^{n}butyl derivatives *In5* and *In9*, tapered nanowires with smooth surfaces were observed, while ^{t}butyl derivative *In10* showed growth of rod-type structures with increased diameters and strong surface structuring. It has to be mentioned that 1D structures depicted in figures 2-33 (c) and (d) have grown on different positions on the same substrate. This indicates strong concentration dependence of the growth as varying position in respect to the inlet nozzle could lead to a variation of the incoming precursor concentration.

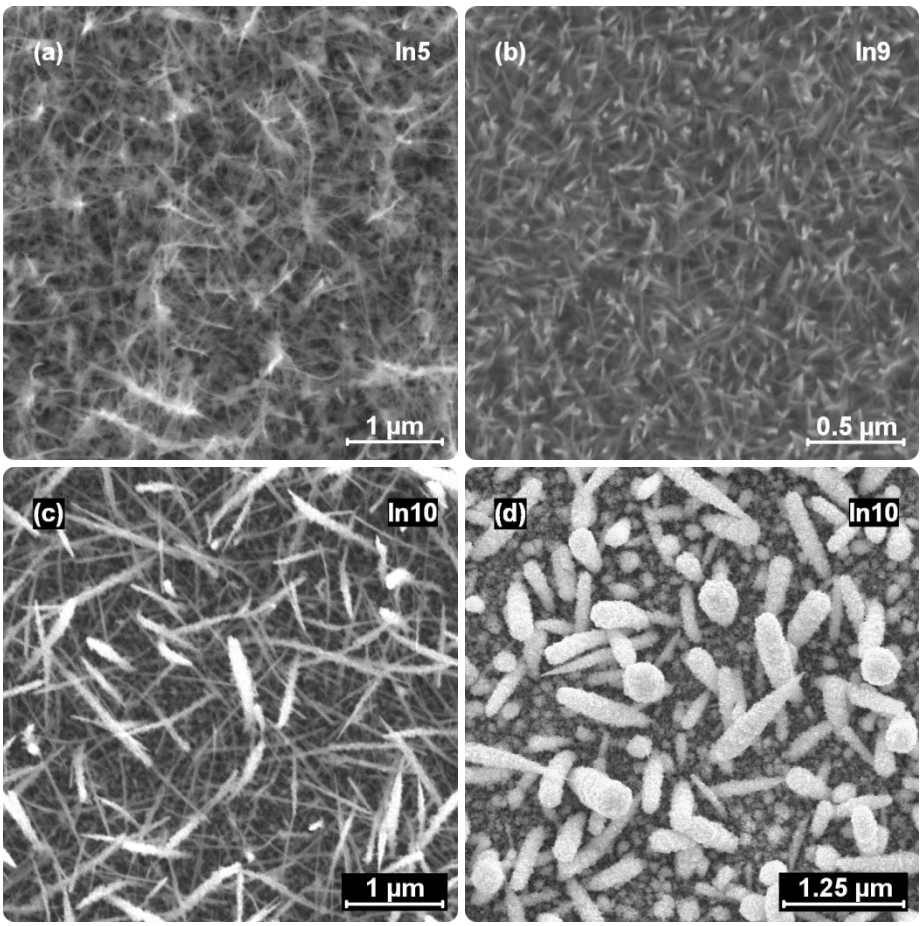

Figure 2–33: SEM micrographs of 1D nanostructures grown from (a) *In5,* (b) *In9* and (c,d) *In10*.

Synthesis of In_2S_3 1D nanostructures has been reported via various processes including hydro- and solvothermal routes,[488, 489] or thermolysis in high boiling point solvents.[490-492] Reports on gas phase processes on the other hand mainly deal with gold catalysed vapour-liquid-solid (VLS) growth or the use of hard templates.[362, 366, 381, 493] However, as neither growth seeds nor templates were used in this study, the obtained nanostructures are believed to have grown via a self-promoted 1D growth similar to reports by the group of P. O'Brien, who synthesised ß-In_2S_3 nanorods via AACVD of [$Et_2In(S_2CNMe^nBu)$] in toluene, but did not provide an explanation for the growth mechanism.[494] Similarly, a growth mechanism for the 1D structures presented here cannot be defined with certainty from the obtained data. However, SEM micrographs indicate that surface diffusion plays an important role in the growth process, because tapering of 1D structures as observed in the present study is typically observed for

small diffusion lengths.[495-497] As stated above, figures 2-33 (c, d) point towards strong concentration dependence and a competing 1D vs. film growth. It is possible that the concentration of the precursor solution increased with progressing deposition time because of the high volatility of the ^{n}hexane solvent. In combination with small diffusion lengths, this could lead to nucleation on the whole surface including substrate and preformed 1D structures, which would explain the strong surface textures observed in figure 2-33 (d). This would also be in agreement with smooth nanowires next to wires with textured surfaces as found in figure 2-33 (c), where secondary nucleation and growth on the nanowires has not progressed as much. It is possible that applying longer deposition times or increased precursor concentrations for specimen depicted in figure 2-33 (a-c) would lead to surface structures and increased diameter similar to 1D structures observed in figure 2-33 (d).

Transmission electron microscopy (TEM) was performed for further analysis of selected nanowires grown from *In5*. As depicted in figure 2-34 (a), nanowires show the expected polycrystalline nature as indicated by diffraction contrast of crystalline areas with different orientation. High resolution TEM micrographs depicted in figure 2-34 (b, c) indicate that the nanowires consist of single-crystalline twin domains. Twinning can be further seen from fast-Fourier transformation (FFT) of the single-crystalline domains in figure 2-34 (b), which exhibit the same orientation of the crystallites. As shown in figure 2-34 (c), the nanowires feature a high number of defects and twin domains with varying sequence and thus very small volumes of the phases can be accommodated. Figure 2-34 (d) further demonstrates the twinning in the FFT of the picture, where one can see spots very close together (marked in red) which indicate different crystal systems with a common interface of small lattice mismatch, i.e. indium oxide and sulphide. The oxide content of the sample was determined via EDX analysis within the TEM apparatus and was found to be within 25-40 %, varying between individual nanowires and the locations of the analysis. Nevertheless, no microphase separation was observed in these samples. Inhomogeneities could occur due to surface diffusion of the growing material and site-specific adsorption of decomposition products preferentially forming indium oxide or sulphide species. Diffusion induced tapering also leads to larger diameter at the bottom and small diameter at the tip of the nanostructures. The elucidation of the origin of this growth phenomenon, however, requires additional microscopic studies devoted to this specific topic. Nevertheless, specific alignment of crystals with different crystal structures but common interfaces and their interaction seem to favour the formation of the nanowire morphology.

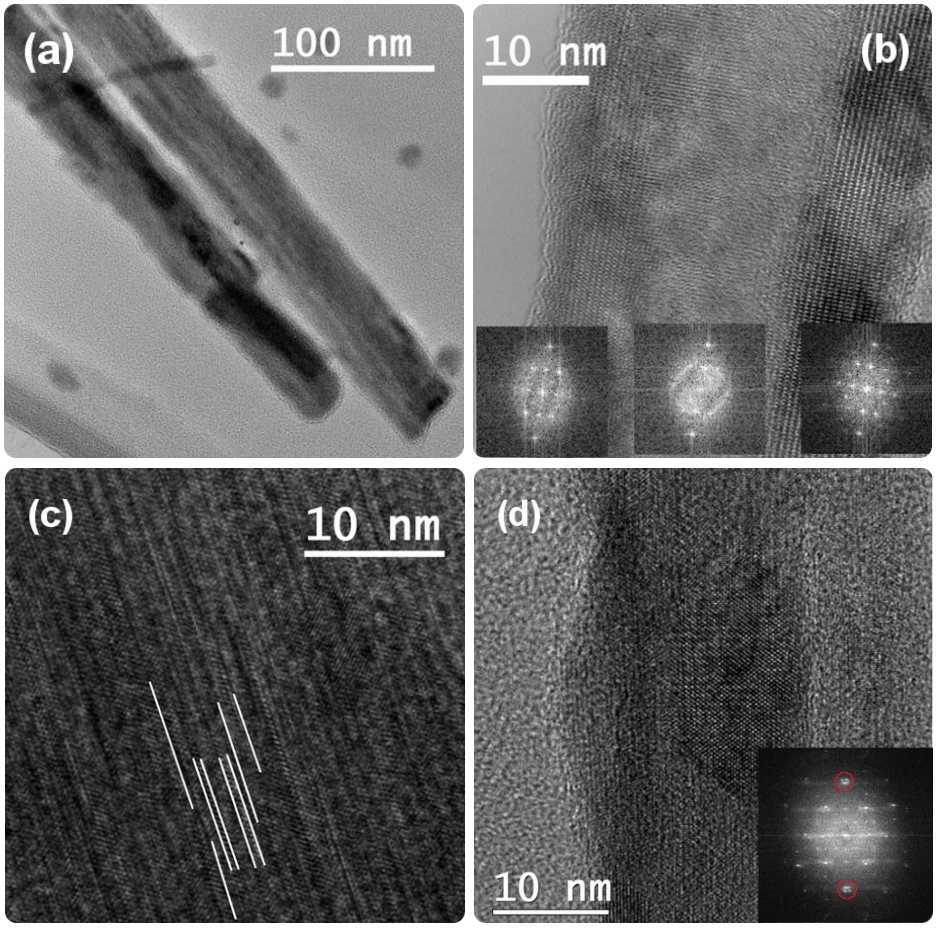

Figure 2–34: TEM micrographs of 1D nanostructures grown from *In5*.

XPS spectra of the In3d and S2p region of nanowires grown from *In5* are depicted in figure 2-35. The S2p region only shows one signal, which can be well referenced to In_2S_3.[482] Despite the phase separation observed in XRD and TEM studies, only one signal is observed in the In3d region, which is shown in figure 2-35 (b). This is due to the fact that In_2O_3 and In_2S_3 show very similar binding energies of 444.3-445.3 and 444.7-445.6 eV for oxide and sulphide, respectively, which cannot be resolved with a laboratory X-ray source.[487, 498, 499] In addition, as the oxide : sulphide ratio is close to 1:1, the signals should have about the same intensity, leading to a symmetric appearance of the peak. However, we were able to determine the sulphide content at 55 %, which is in good agreement with findings in EDX and Rietveld analysis.

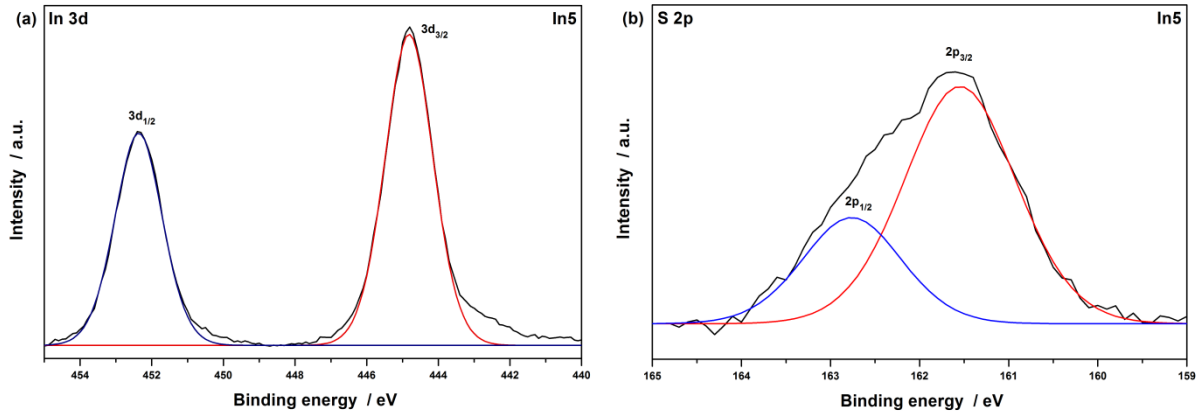

Figure 2-35: XPS spectra of (a) the In3d and (b) S2p region for nanowires deposited via AACVD from *In5*.

2.4 HETEROMETALLIC ALKOXIDES

2.4.1 Synthesis and characterisation

Heterometallic gallium ^{t}butoxides of Fe, Co, Ni and Cu were synthesised using a slightly modified version of reported synthesis for $[NiGa(O^{t}Bu)_8]$ by Mathur *et al.*.[432] Salt elimination reactions of transition metal halides with $[KGa(O^{t}Bu)_4]_n$, which was obtained by reacting $[KO^{t}Bu]_4$ and $[Ga(O^{t}Bu)_3]_2$, gave the desired products in moderate to good yields. Compared to *NiGa* and *CoGa*, *FeGa* and *CuGa* showed increased sensitivity towards oxygen and atmospheric moisture, respectively, as indicted by a fast colour change upon exposure to air. Sublimation of *FeGa*, *CoGa* and *NiGa* at 120-125 °C at 0.04 mbar gave pure alkoxides, but also resulted in substantial product loss due to formation of a residue, which we were unable to sublime. It is most likely that the heterobimetallic gallates form complexes of the general formula $[M^{II}Ga(O^{t}Bu)_5]_2$ under prolonged heating in analogy to reports of Veith and co-workers on aluminates.[113] In contrast, *CuGa* showed increased heat-sensitivity and decomposed leading to substantial loss of copper in the sublimate and large amounts of a non-volatile residue. Therefore, *CuGa* was used as synthesised without further purification.

The obtained products were paramagnetic, thus NMR spectroscopy was not possible via standard procedures and was therefore not used for analysis. However, we were able to grow crystals suitable for single-crystal XRD analysis for *FeGa* and *CuGa*. The molecular structure of *NiGa* has been published before.[432] Detailed crystallographic data is listed in table 2-6. Both substances showed strong twinning in the crystals. The measured *FeGa* crystal exhibited 8 % of a second domain with a twin law of a 179.456° rotation around (100) real space axis. The cells were separated with CELL_NOW and absorption correction was performed with TWINABS (Bruker) before structure refinement was performed with HKLF4 map, because HKLF5 proofed ineffective. *CuGa* showed a 180° rotation around the (100) real space axis as twin law. Twin domains were separated manually in APEX2 and structure refinement was conducted

with HKLF5 and BASF commands. Increased twinning is most likely the result of the zig-zag layer structure observed for both compounds, shown for *FeGa* in figure 2-36. Twinning would be consistent with an 'up-up' type layer instead of 'up-down' (zig-zag).

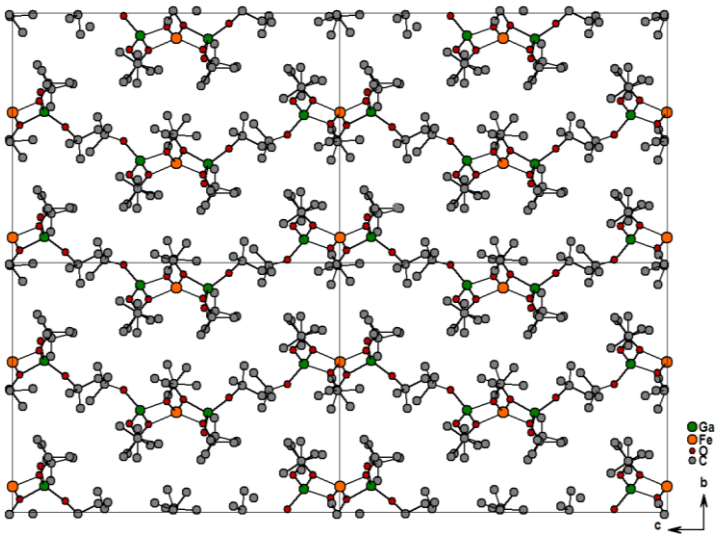

Figure 2-36: Crystal structure of *FeGa* viewed along the a-axis. Hydrogen atoms omitted for clarity.

FeGa crystallises in monoclinic space group *Cc*, while *CuGa* exhibits a triclinic crystal system in space group $P\bar{1}$. However, molecular structures for *FeGa* and *CuGa*, which are depicted in figure 2-37, exhibit similar features and are isostructural to previously reported *NiGa* (monoclinic space group $P2_1/n$) and related transition metal aluminates[113, 430, 432, 500] and ferrites.[501, 502] Both molecules feature a spirocyclic arrangement showing fourfold coordination for Ga in a distorted tetrahedral arrangement as well as elongated tetrahedral bisphenoids for Fe and Cu, respectively. The spirocyclic coordination is depicted in detail for *FeGa* in figure 2-38. Disorder was found for *FeGa* on C14, which was accounted for using the split-atom model. For C22 and C24, which show elongated displacement parameters, atom splitting did not result in stable solutions and where thus kept as is. No disorder was found for *CuGa*.

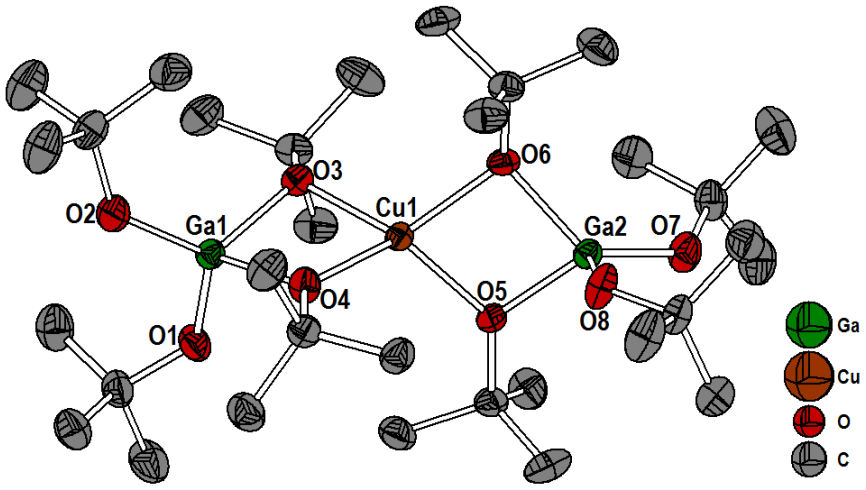

Figure 2–37: Molecular structure of *CuGa* displayed with 50 % probability ellipsoids. Hydrogen atoms have been omitted for clarity.

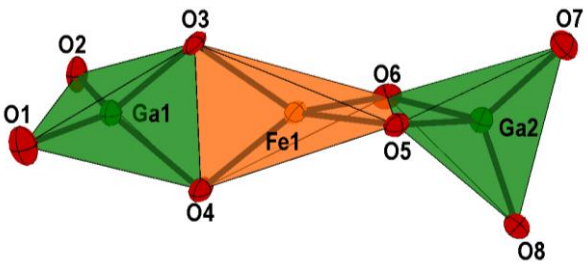

Figure 2–38: Spirocyclic coordination sphere of FeGa shown with 50 % probability ellipsoids.

Ga-O bonds for terminal ^{t}butoxides were found to be significantly shorter than bridging ones, namely 1.804 vs. 1.909 and 1.797 vs. 1.907 Å on average for *FeGa* and *CuGa*, respectively. Those values are well within the ranges previously reported for *NiGa* or homoleptic gallium alkoxides.[27, 432] Bridging Fe-O bond lengths (1.995(5)-2.018(5) Å) show only small deviations consistent with strong chelating effect of $[Ga(O^{t}Bu)_4]^-$ units. They also compare well to bridging Fe-O bond distances found in $[Fe(O^{t}Bu)_3]_2$ (1.959 Å) or $[ZnFe_2(O^{t}Bu)_8]$ (1.936(5)-1.963(5) Å) and are only slightly longer than Ni-O bonds in *NiGa* (1.965(4)-1.975(4) Å).[432, 437, 501, 503] In comparison, Cu-O bond lengths (1.944(2)-1.983(1) Å) are a bit shorter, but also in agreement with strong chelation and compare well with Cu-O bonds in $[CuAl_2(O^{t}Bu)_8]$ (1.930(3)-1.943(3) Å).[113]

O-Ga-O bond angles between terminal alkoxo ligands, i.e. O1-Ga1-O2 and O7-Ga2-O8, are slightly wider than the ideal 109.5°, showing values of 111.3(3)-113.0(3) and 115.74(7)-116.06(7)° for *FeGa* and *CuGa*, respectively. In contrast, O-Ga-O angles within four-membered metallacycles (O3-Ga1-O4 and O5-Ga2-O6) are heavily compressed assuming values of 82.3(2)-83.6(2) and 81.84(5)-81.89(6)°.

Similarly, the coordination spheres of Fe1 or Cu1, respectively, are highly anisotropic. For *FeGa*, O-Fe1-O bond angles within the GaOFeO metallacycles show values from 77.8(2)-78.6(2)°, while O-Fe1-O angles for oxygen atoms bound to different gallium atoms are strongly differing, assuming values of 117.3(2)-133.9(2)°. For *CuGa*, stronger anisotropy with values of 78.93(5)-79.07(5) and 114.24(5)-140.35(5)° was found, most likely caused by the slightly smaller ionic radius of copper.[455]

Table 2–6: Crystallographic and refinement data of *FeGa* and *CuGa*.

Compound	*FeGa*	*CuGa*
Emp. Formula	$C_{32}H_{72}FeGa_2O_8$	$C_{32}H_{72}CuGa_2O_8$
M_r / g mol^{-1}	780.18	787.87
Crystal system	Monoclinic	Triclinic
Space group	Cc	$P\bar{1}$
a / Å	11.159(2)	9.067(2)
b / Å	16.813(3)	13.640(3)
c / Å	22.529(5)	18.114(4)
α / °	90.00	71.52(3)
β / °	101.32(3)	87.29(3)
γ / °	90.00	70.77(3)
V / Å^3	4144.6(15)	2002.2(8)
Z	4	2
D_x / g cm^{-3}	1.250	1.307
μ / mm^{-1}	1.676	1.90
Crystal size /mm	0.45 x 0.3 x 0.1	0.4 x 0.2 x 0.15
No. measured refl.	47535	111696
Obs. Refl. [I>2σ(I)]	3809	10335
Θ_{max} / °	28.7	30.6
R [F^2>2σ(F)], wR (F^2), S	0.055, 0.131, 1.08	0.029, 0.076, 1.09
Refl./param.	4512/423	12201/413
Weighting scheme*	a = 0.0641	a = 0.0397
	b = 16.9699	b = 0.2923

* $w = 1/[\sigma^2(F_o^2) + (aP)^2 + bP]$, where $P = (F_o^2 + 2F_c^2)/3$

Table 2–7: Selected bond lengths and angles for *FeGa* and *CuGa*.

FeGa		*CuGa*	
Bond	**Distance / Å**	**Bond**	**Distance / Å**
Ga1-O1	1.797(6)	Ga1-O1	1.801(2)
Ga1-O2	1.821(5)	Ga1-O2	1.794(2)
Ga1-O3	1.886(5)	Ga1-O3	1.918(1)
Ga1-O4	1.906(5)	Ga1-O4	1.894(1)
Fe1-O3	2.006(4)	Cu1-O3	1.978(1)
Fe1-O4	2.018(5)	Cu1-O4	1.953(1)
Fe1-O5	1.998(5)	Cu1-O5	1.944(2)
Fe1-O6	1.995(5)	Cu1-O6	1.983(1)
Ga2-O5	1.911(5)	Ga2-O5	1.900(1)
Ga2-O6	1.933(5)	Ga2-O6	1.916(2)
Ga2-O7	1.784(6)	Ga2-O7	1.792(2)
Ga2-O8	1.812(5)	Ga2-O8	1.799(1)
Angle	**/ °**	**Angle**	**/ °**
O1-Ga1-O2	111.3(3)	O1-Ga1-O2	115.74(7)
O1-Ga1-O3	121.1(3)	O1-Ga1-O3	106.57(6)
O1-Ga1-O4	118.3(3)	O1-Ga1-O4	106.75(6)
O3-Ga1-O4	83.6(2)	O3-Ga1-O4	81.89(6)
Ga1-O3-Fe1	99.4(2)	Ga1-O3-Cu1	96.97(6)
Ga1-O4-Fe1	98.3(2)	Ga1-O4-Cu1	98.61(6)
O3-Fe1-O4	77.8(2)	O3-Cu1-O4	78.93(5)
O3-Fe1-O5	125.3(2)	O3-Cu1-O5	140.35(5)
O5-Fe1-O6	78.6(2)	O5-Cu1-O6	79.07(5)
Fe1-O5-Ga2	99.6(2)	Cu1-O5-Ga2	98.80(6)
Fe1-O6-Ga2	99.0(2)	Cu1-O6-Ga2	96.91(6)
O5-Ga2-O6	82.3(2)	O5-Ga2-O6	81.84(5)
O5-Ga2-O7	124.0(3)	O5-Ga2-O7	116.72(6)
O7-Ga2-O8	113.0(3)	O7-Ga2-O8	116.06(7)

2.4.2 Molecule-to-material conversion of heterometallic alkoxides

We were able to use the presented heterometallic ^{t}butoxides as single-source precursors to synthesise the respective mixed metal oxide spinel phases $M^{II}Ga_2O_4$ (M=Fe, Co, Ni, Cu). We employed LPCVD for the production of spinel thin films and sol-gel processing to gain access to spinel powder samples. For *CoGa* and *NiGa*, we were able to reproduce previously reported findings.[432, 433] Both precursors showed good coverage of Si(911) substrates at 500-600 °C in LPCVD experiments and XRD proved phase purity of the deposits. Similarly, XRD of particles obtained from sol-gel processing

showed the formation of phase pure $M^{II}Ga_2O_4$ spinels (M=Ni, Co) after annealing in air at 400-1000 °C with increasing crystallite size.

Sol-gel processing of *FeGa* gave an oxygen-sensitive amorphous precipitate. Centrifugation of the precipitate in air resulted in a fast colour change of the particles from dark green to brown indicating oxidation of Fe^{II} to Fe^{III}. Indeed, annealing at 400-900 °C in dry nitrogen still yielded $FeGaO_3$ nanopowders due to oxidation of the amorphous sol-gel product. Therefore, particles were separated by filtration, dried under reduced pressure and annealed in vacuum to avoid oxidation of the product. Powder XRD, depicted in figure 2-39, indicated the formation of nanocrystalline $FeGa_2O_4$ at 600 °C; however, higher temperatures gave additional signals for crystalline Ga_2O_3 as first observable by the small reflex at $2\theta = 31.7°$ at 700 °C. One explanation would be partial oxidation during sol-gel processing despite taking careful precautions against atmospheric oxygen due to the extreme susceptibility of *FeGa* towards oxidation and hydrolysis. Oxidation could lead to the formation of magnetite Fe_3O_4 particles and Ga_2O_3. Unfortunately Fe_3O_4 and $FeGa_2O_4$ show indistinguishable XRD patterns due to very similar size of Fe^{3+} and Ga^{3+} ions in the same spinel unit cell. EDX analysis of powder samples, however, showed only small deviations from the ideal 33.3 at% Fe. Complete phase separation is therefore rather unlikely.

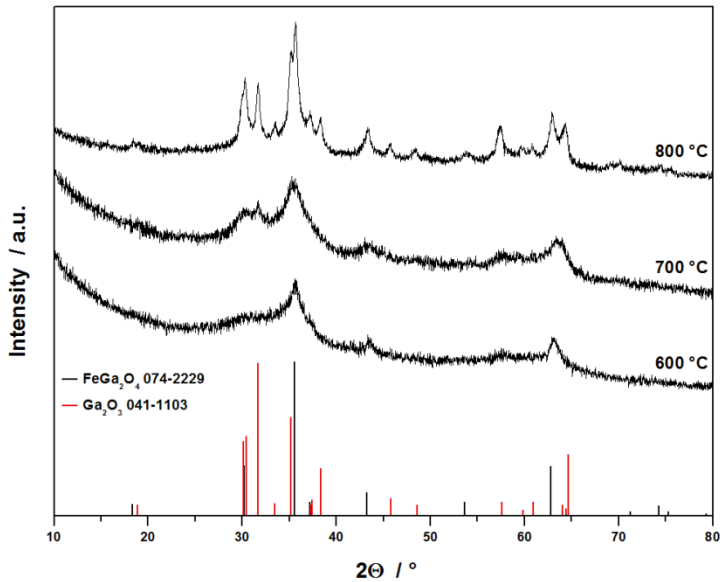

Figure 2-39: Powder XRD patterns of annealed particles derived from sol-gel processing of *FeGa*.

Employing *FeGa* in LPCVD experiments led to reproducible thin film growth with suitable growth rates and XRD showed phase purity for deposits synthesised at 500-700 °C as depicted in figure 2-40 (a). SEM micrographs of thin films deposited at 500 and 600 °C depicted in figure 2-40 (b-c) showed very similar and uniform film morphologies comparable to those obtained for $NiGa_2O_4$ coatings. However, EDX analysis showed that the coatings were iron deficient exhibiting approx. 30 at% iron. In addition, films grown at 700 °C exhibited inhomogeneous morphologies (figure 2-40 (d)) and EDX

revealed varying composition of the film ranging from 30.5-35.8 at% Fe. This could indicate partial decomposition prior to volatilisation or homogeneous gas phase thermolysis leading to iron and gallium rich intermediates that subsequently undergo heterogeneous decomposition reactions on the surface. This could lead to phase separation of gallium rich (Ga_2O_3) and iron rich ($FeGa_2O_4$, Fe_3O_4) phases as found in sol-gel processing. However, the complete absence of signals for Ga_2O_3 in XRD analysis of films deposited at 700 °C indicates that only small amounts are formed in LPCVD processes.

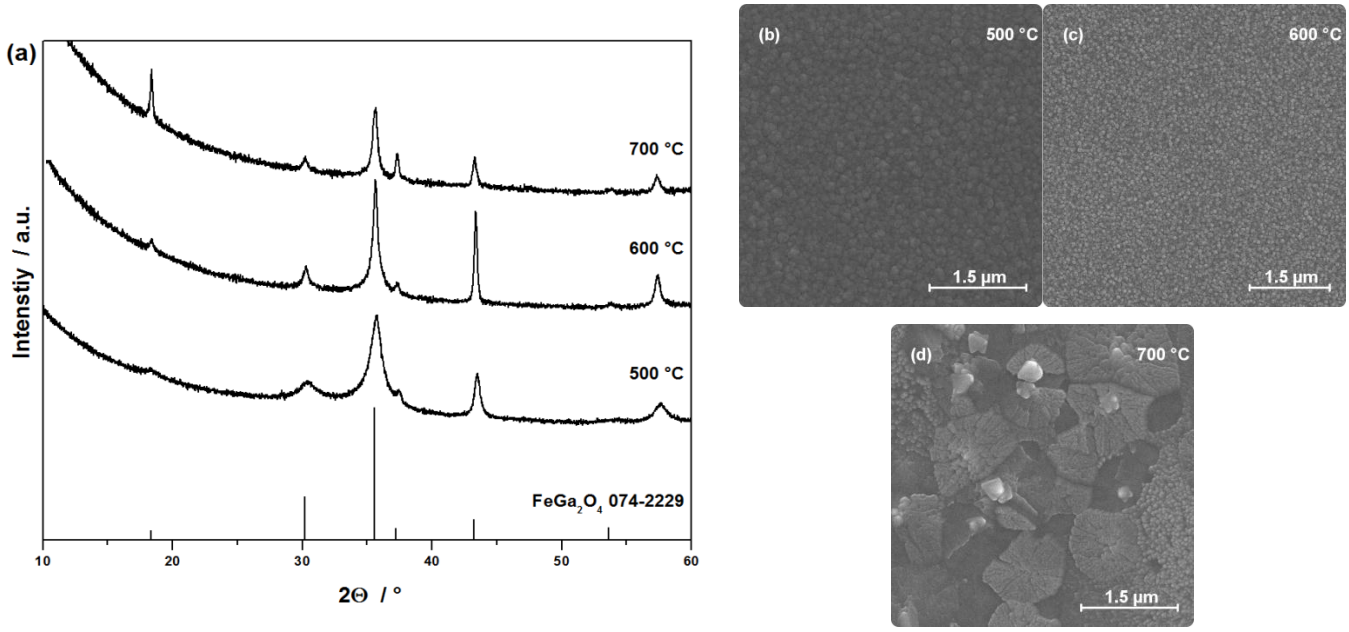

Figure 2–40: (a) XRD patterns and (b-d) SEM micrographs of $FeGa_2O_4$ thin films deposited via LPCVD of *FeGa* on Si(911) at 500-700 °C.

XPS measurements were performed on a selected thin film grown from *FeGa* at 500 °C. As shown in figure 2-41, both regions of interest, Fe2p and Ga2p, show two signals each. The $Ga2p_{3/2}$ peaks are centred at 1118.0 and 1119.0 eV, respectively, and the high energy peak could be well attributed to Ga_2O_3 representing 12 % of the total gallium content in the sample.[504] The more intense peak at 1118.0 eV correlates well with the intense peak in the Fe2p region centred at 710.8 eV giving a Fe:Ga ratio of 1.1:2, which is close to the expected value for $FeGa_2O_4$. Differences to EDX analysis might be the result of different information depths of the techniques and the possibility for differentiating components in XPS, which is not given in EDX. Moreover, reports of XPS on Fe^{II}-depleted $FeGa_2O_4$ single crystals show similar binding energies.[505] It is thus concluded that the intense signals originate from $FeGa_2O_4$, which is also in agreement with XRD analysis, where it was found as the main phase. The secondary iron containing phase could not be attributed with certainty as Fe^{2+} and Fe^{3+} are difficult to differentiate in XPS and iron oxides have been reported over a wide range of binding energies. In addition, the use of a laboratory X-ray source without monochromatisation leads to increased signal widths making assignment even more difficult. However, the small peak corresponds to 22 % of the total iron content, which is in good agreement with 12 % secondary gallium species found as there is

twice as much gallium in the precursor species. This indicates the formation of a simple homometallic iron oxide, most likely Fe_2O_3, alongside Ga_2O_3 as secondary phases.

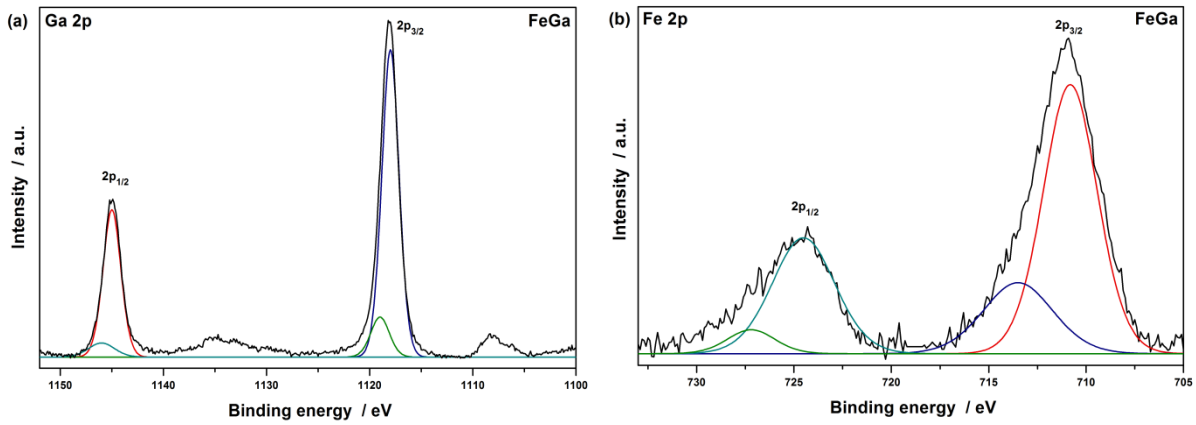

Figure 2-41: XPS spectra of the (a) Ga2p and (b) Fe2p region from LPCVD deposits using *FeGa*.

As mentioned before, *CuGa* showed increased thermal sensitivity as indicated by decomposition upon sublimation of the crude product. Similarly, LPCVD experiments, even at pressures $<10^{-5}$ mbar, only gave Ga_2O_3 coatings with negligible amounts of copper detected by EDX analysis. This indicates precursor decomposition and formation of a non-volatile copper species prior to volatilisation even at moderate precursor temperatures of 90 °C. In contrast, all other bimetallic ^{t}butoxides described here were readily sublimed at higher temperatures (120-125 °C) without loss of the bivalent transition metal.

Sol-Gel processing of *CuGa* in 1,4-dioxane or THF yielded green precipitates, which gave brown solids upon annealing in air. However, XRD analysis indicated phase separation and formation of CuO alongside $CuGa_2O_4$ upon annealing even at low temperatures of 400 °C, as can be seen in figure 2-42. Rietveld analysis of powder samples annealed at 800 °C showed a CuO content of 10.7 %. Phase separation and formation of CuO could be the result of preferential nucleophilic attack at the Cu centre due to its bigger size (ion radius 0.57 vs. 0.47 Å for Cu^{2+} and Ga^{3+} in tetrahedral environment, respectively) and thus less effective shielding of the ^{t}butoxide groups.[455, 506] This clearly demonstrates the extreme sensitivity of CuGa even under mild reaction conditions applied in sol-gel processing.

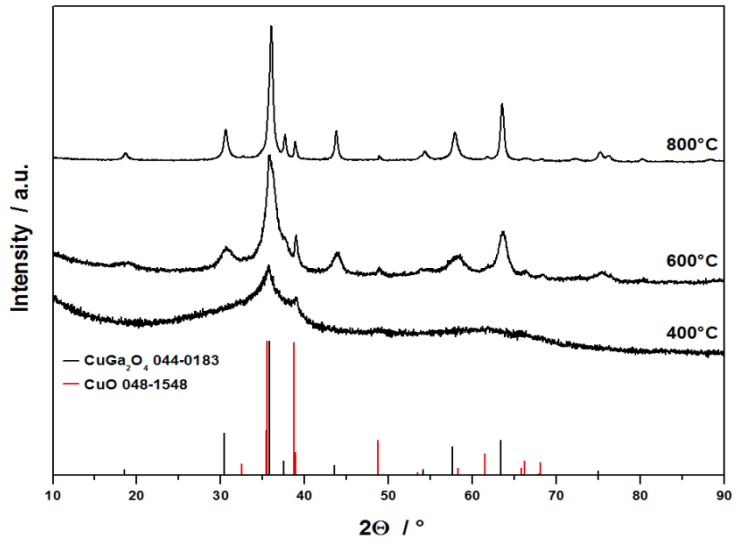

Figure 2-42: Powder XRD patterns of annealed particles derived from sol-gel processing using *CuGa*.

2.5 Summary and Conclusion

The first examples of monomeric, homoleptic aminoalcoholates of group 13 metals have been synthesised and characterised. The monomeric nuclearity of the alkoxides was demonstrated via single-crystal XRD as well as NMR spectroscopy, which is in contrast with generally found dimeric or oligomeric structures for this kind of compounds. Indium species featured a trigonal antiprismatic coordination sphere, while aluminium and gallium alkoxides showed a trigonal bipyramidal configuration. The latter has not been reported before for monomeric gallium species. The formation and stabilisation of monomeric compounds was realised by effective combination of steric shielding and coordinative saturation of the metal centres. As such, these species could be well-suited as molecular precursors in material synthesis, for example if incorporation of small concentrations of oxides into another matrix material is targeted.

In addition, a series of homoleptic thioether functionalised gallium and indium alkoxides were synthesised and characterised. Thioethers have not been used in donor functionalisation of alkoxides before. According to NMR spectroscopy and single-crystal XRD, this new functionality shows weak coordination to the metal centre in solution as well as the solid state for symmetric alcoholates without any other functionality, leading to monomeric species. However, the coordination of the thioether is effectively suppressed when stronger donor functionalities, namely ethers and amines, are incorporated as a secondary potential coordinating functionality in alcoholate ligands.

More importantly, the applicability of these precursors in molecule-to-material processes was demonstrated, where we were able to achieve conversion to oxysulphide materials with the thioether moiety being applied as the sulphur source in these single-source precursors. LPCVD experiments

showed that most gallium alkoxides are applicable in gas phase processes for the formation of thin film coatings. The sulphide content of the $Ga_2O_{3-x}S_x$ thin films was found to be strongly dependent on the type of precursor as well as the deposition temperature and could be effectively controlled in a range of 1.6-23.4 at% with good reproducibility of the results.

XPS analysis indicated homogenous sulphidisation of the thin films obtained by LPCVD without phase separation. However, XPS further showed the incomplete decomposition of precursor species at lower temperatures leading to incorporation of residual thioether fragments into the growing thin film in agreement with carbon contaminations found in EDX analysis. ^{t}Butyl derivative *Ga6* showed less effective decomposition as indicated by increased amounts of undecomposed thioether fragments in the coatings at 500 °C and below, while ^{n}butyl derivatives only showed very small amounts at 450 °C with pure coatings at temperatures >500 °C. Nevertheless, ^{t}butyl species showed higher sulphide contents despite the less effective decomposition and pure oxysulphide films with minimal carbon contamination could be produced at higher temperatures.

First investigations of the macroscopic properties of $Ga_2O_{3-x}S_x$ materials were performed by means of impedance spectroscopy of thin films on interdigitated electrodes, which allowed the calculation of the electrical conductance of the thin films. Gallium oxysulphide films showed significantly improved conductivity compared to pure amorphous Ga_2O_3 coatings, in particular at temperatures of 200-400 °C. Furthermore, the activation energy was lowered upon sulphide incorporation indicating a change in conduction mechanism.

Since indium alkoxides showed insufficient volatility for reproducible thin film growth in LPCVD experiments, all precursors were additionally used in hot-injection pyrolysis to access oxysulphide nanoparticles. Compared to LPCVD experiments, increased sulphide contents of up to 27.6 at% (x = 1.38) for gallium based particles were found. Indium based particles exhibited even higher sulphide contents even reaching full conversion for *In3*, which can be attributed to lower In-O bond strength and thus facilitated conversion compared to gallium based materials. This was emphasised by the formation of phase pure ß-In_2S_3 from all precursors as determined by powder XRD, which is in contrast to generally obtained oxide materials accessed from alkoxide precursors demonstrating the potency of the thioether functionality to act as a sulphidisation agent.

Coupled TG/DSC-MS experiments were conducted to investigate the decomposition and sulphidisation mechanism upon thermolysis of the molecular precursors. It could be demonstrated that symmetrically functionalised alkoxides showed higher onset temperatures indicating higher thermal stability, but also resulted in increased amounts of carbon contamination. Thioether functionalised aminoalcoholates on the other hand showed efficient decomposition with low onsets of 165-180 °C. More importantly, asymmetric aminoalcoholates showed the formation of significant amounts of H_2S upon thermolysis, while symmetric species showed no or only small amounts of H_2S indicating a supportive role of the amine functionality in the production of the active sulphidisation agent. The *in situ* generation of H_2S during growth of the material is assumed to play a key role for the higher efficiency of these precursor derivatives in the *in situ* sulphidisation of the material.

AACVD enabled the deposition of indium oxysulphide thin films from thioether functionalised aminoalcoholates in hexane at moderate temperatures. In agreement with findings for nanoparticles from hot-injection pyrolysis, indium based thin films showed high sulphide contents in the coatings, in particular for ^{t}butyl derivatives *In6* and *In10* and all deposits showed signals for phase pure ß-In_2S_3 in XRD investigations. At 425 °C, formation of nanowires and rod-like structures was observed for *In5*, *In9* and *In10*, which is most probably supported by defect-induced growth and preferential twinning. In contrast to phase pure ß-In_2S_3 found for coatings and particles, the polycrystalline nanowires showed nano-phase separation and multiple twinning of In_2O_3 and In_2S_3 segments in TEM and XRD investigations.

In conclusion, we were able to demonstrate the applicability of the thioether functionality for stabilisation of low nuclearity in alkoxide chemistry as well as its potency for effective *in situ* formation of oxysulphide materials by the use as molecular single-source precursors.

Finally, a series of transition metal heterobimetallic gallates $[M^{II}Ga_2(O^{t}Bu)_8]$ with M=Fe, Co, Ni and Cu was synthesised as single-source precursors to catalytically active oxide spinels MGa_2O_4. Characterisation via single-crystal XRD showed the expected spirocyclic configuration for M=Fe, Cu in good agreement with previous reports of aluminates and gallates. LPCVD and sol-gel processing of *CoGa* and *NiGa* lead to formation of the phase pure MGa_2O_4 deposits. In contrast, applying *FeGa* in this processes resulted in the formation of $FeGa_2O_4$ as the main phase, but with contaminations of Ga_2O_3 and a secondary iron oxide. This is most likely due to the increased susceptibility towards oxidation of the precursor and amorphous product in case of sol-gel derived particles. *CuGa* on the other hand showed thermal instability leading to Ga_2O_3 films with negligible amounts of copper in LPCVD, while sol-gel processing led to phase separation giving mixtures of $CuGa_2O_4$ and CuO.

CHAPTER 3

EXPERIMENTAL

"Everything is theoretically impossible,

Until it's done."

- Robert A. Heinlein (1907-1988) –

3.1 General methods and materials

Chemicals were purchased from Sigma Aldrich, abcr and TCI Europe and used as received, with exception of $GaCl_3$, which was sublimated before use. Manipulations of metal chlorides and metal alkoxides were performed taking stringent precautions against atmospheric moisture and oxygen using dry nitrogen or argon in combination with standard Schlenk-techniques, a modified Stock apparatus or glove-box techniques. Glassware was desiccated by heating under dynamic vacuum prior to use. Solvents were dried using standard methods and stored over sodium wire if applicable. Solvents for heterometallic alkoxides were further degassed by freeze-pump-thaw cycles.

Alcohol ligands used in this study have not been assigned an abbreviation and are not listed in the list of compounds. Nevertheless, their synthesis is described in the following sections unless reported before.

3.2 Instrumentation

3.2.1 Nuclear magnetic resonance

Room temperature ^{1}H and ^{13}C solution NMR spectra were recorded on a Bruker AVANCE 250 spectrometer (250.13 MHz {^{1}H}, 62.86 MHz {^{13}C}) equipped with a 5 mm BBO probe head and a z-gradient unit. Low temperature measurements and 2D experiments have been performed on a Bruker AVANCE 300 spectrometer (300.13 MHz {^{1}H}, 75.51 MHz {^{13}C}) equipped with a 5 mm BBI probe head and a z-gradient unit. Deuterated solvents were purchased from Euriso-top and stored over sodium wire.

3.2.2 X-Ray diffraction

Powder and thin film diffraction patterns were recorded on a PANanalytical XPERT Pro PW 3050/60 diffractometer with Cu Kα radiation (λ = 1.540598 Å) and an X'Celerator detector. Measurements were recorded in Bragg-Brentano geometry or grazing incidence in a 2θ range of 10-90 or 10-60°, respectively, with a step size of 0.1° using a 0.04 rad soller slit, 10 mm fixed mask and 0.5° divergence slit in the incident beam path as well as a 5.5 mm anti-scatter slit, 0.04 rad soller slit and a nickel filter in the diffracted beam path. Data analysis was performed using HighScore Plus software.

3.2.3 Single-crystal X-Ray diffraction

Single crystal XRD experiments were performed between 100-170 K on a Bruker-AXS SMART APEX II diffractometer with a CCD area detector and a crystal-to-detector distance of 45-50 mm using graphite-monochromated Mo-K_α radiation (λ = 7.1073 Å). Data were collected with φ and ω-scans and 0.5° frame width. The data were corrected for polarisation and Lorentz effects, and an empirical absorption correction (SADABS) was applied. The cell dimensions were refined using all unique reflections. The structures were solved with direct methods (SHELXS97)[507] or dual-space algorithms (SHELXT)[508] and refinement to convergence was carried out with the full-matrix least squares method based on F^2 (SHELXL97/SHELXL14)[509] with anisotropic structure parameters for all non-hydrogen atoms. Hydrogen atoms were placed on calculated positions and refined riding on their parent atoms.

3.2.4 Scanning electron microscopy and energy dispersive X-ray spectroscopy

Thin films and particles were analysed using a FEI Quanta 200 FEG scanning electron microscope equipped with an EDX detector for elemental analysis.

3.2.5 Transmission electron microscopy

1D structures were imaged using a FEI TECNAI F20 transmission electron microscope operated at 200 kV, which is equipped with high angle annular dark field (HAADF) STEM and EDX detector.

3.2.6 Thermogravimetric analysis/differential scanning calorimetry - mass spectrometry

Thermogravimetric analysis (TGA) and differential scanning calorimetry (DSC) were performed with a Mettler Toledo TGA/DSC1 1100 system equipped with a UMX1 balance. Thermogravimetric coupled mass spectrometry (TG-MS) experiments were performed with a Mettler Toledo TGA/DSC1 1600 system with an MX1 balance coupled with a Pfeifer Vacuum MS Thermostar GSD 301T2 mass spectrometer. The heating rate was set to 10 K/min with an argon flow rate of 60 ml/min. The fragmentation of the ligand components were compared with literature data from the NIST chemistry webbook database.

3.2.7 X-Ray photoelectron spectroscopy

XPS measurements were performed on a commercially available SPECS STM/XPS UHV setup. The base pressure in the UHV system for XPS measurements was in the low 10^{-9} mbar regime. For XPS measurements, the system is equipped with a non-monochromatised dual anode X-ray tube with Al and Mg Kα anode (XRC 50, SPECS) and a hemispherical analyser PHOIBOS 100 (SPECS) with multi channeltron detector. The samples were introduced into the UHV system via a load lock after mounting them on a steel or molybdenum plate. Samples were measured at room temperature with Al Kα radiation in the as is state and after sputtering for 45 min at $5x10^{-6}$ mbar Ar and an acceleration voltage of 1 kV. The obtained data was analysed by using the commercial software CasaXPS. The peak positions were corrected via the signal for graphitic carbon and double checked by measuring the Fermi Edge. Peak positions were identified by using the NIST XPS database (http://srdata.nist.gov/xps/). Peaks were fitted after Shirley background subtraction using a Gaussian-Lorentian mixed peak shape (30% L) without further constraints. For comparing gallium, indium, carbon and sulphur signals the intensity was corrected by the cross-sections obtained from the Elletra Trieste database (https://vuo.elettra.eu/services/elements/WebElements.html). Due to the overlap of the S2p signal with the Ga3s signal, the calculations were performed via the S2s and Ga3p signal for gallium based materials.

3.2.8 Impedance spectroscopy

Impedance spectroscopy measurements were carried out on thin-film coated quartz glass substrates with buried interdigitating Pt electrodes with 10 or 15 µm electrode spacing and electrode width. Impedance was measured in-plane by means of an Alpha-A high Performance Frequency Analyser equipped with a POT/GAL 30 V 2A test interface (both Novocontrol, Germany). The common frequency range was 10 mHz – 1 MHz, but was adjusted if necessary; the AC voltage was 10 mV root mean square. The measurements were done in 800 mbar reducing atmosphere (2.5 % H_2/97.5 % Ar) at temperatures between 200 °C and 500 °C. This atmosphere was chosen to avoid irreversible changes of the samples during the measurements, which might originate from a changing sulphide content caused by oxidation at elevated temperatures.

3.3 General procedures

3.3.1 Low-pressure chemical vapour deposition

LPCVD was performed in a home-built horizontal cold-wall reactor shown schematically in figure 3-1.[432] Si(100) or SiO_2 substrates were mounted on a wedge-shaped graphite susceptor using silver conductive paste and heated inductively using a high frequency generator (Linn High Therm). The substrate temperature was monitored using a Ni/Co-Ni thermocouple attached to the graphite susceptor. The apparatus was desiccated at 120 °C under dynamic vacuum for 2 h prior to deposition. Thin film growth was performed using approx. 100 mg alkoxide precursor at substrate temperatures of 400-600 °C under reduced pressure using a turbomolecular pump ($<10^{-5}$ mbar) for thioether functionalised alkoxides and 500-700 °C for heterometallic precursors. Depositions employing *NiGa* were performed using only a rotary pump at $<10^{-3}$ mbar; thin films from *FeGa* were produced with and without use of a turbomolecular pump. Precursor temperature was controlled via the oven temperature and was increased in 5 °C increments until thin film growth was observable. A summary of precursor temperatures is listed in table 3-1.

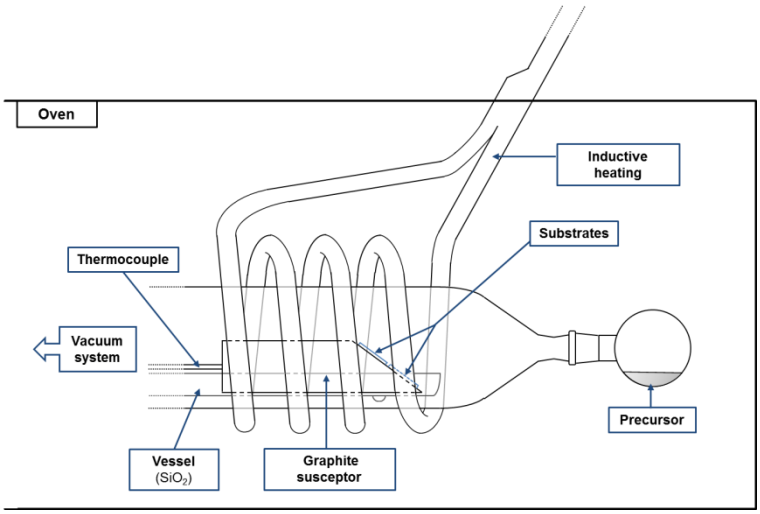

Figure 3-1: Schematic representation of the deposition chamber of the LPCVD apparatus.

Table 3-1: Precursor temperatures used in LPCVD experiments.

Precursor	Temperature / °C	Precursor	Temperature / °C
Ga5	155	*Ga11*	160
Ga6	142.5	*Ga12*	147.5
Ga7	165	*FeGa*	97.5
Ga9	150	*CoGa*	90
Ga10	130	*NiGa*	115

3.3.2 Hot-injection pyrolysis

10 ml dried squalane were placed in a three-necked flask equipped with air cooler, gas inlet and septum and heated to reflux temperature (approx. 415 °C) with a sand-bath under inert atmosphere. Subsequently, 75±5 mg of the alkoxide precursor dissolved in 1 ml squalane was injected under rigorous stirring and refluxed for 30 min. After cooling, particles were separated via centrifugation and washed four times with toluene to remove any residues.

3.3.3 Aerosol-assisted chemical vapour deposition

AACVD was conducted in a home-built hot-wall reactor consisting of a laboratory grade NS 29 glass tube in a tube furnace (Carbolite CF 12/65/550) equipped with a gas inlet nozzle attached to a 50 ml flask, as schematically shown in figure 3-2. For a deposition, 50-75 mg of precursor were dissolved in 10 ml dry ^{n}hexane and placed in the aerosol generator until no solution was left. The aerosol was generated ultrasonically and transported into the reactor by a stream of dry, deoxygenised nitrogen, which was controlled with a mass flow controller (MKS PR4000B) and set to 50-70 sccm. The apparatus was desiccated by heating to >400 °C for 1 h in a carrier gas stream prior to use. To counteract thermophoretic effects, substrates were fixed on a wedge-shaped piece of graphite. Due to the small size of the glass tube compared to the tube furnace opening, the substrate temperature was initially monitored *ex situ* via a thermocouple under reaction conditions and found to be approx. 100 °C lower than the oven temperature. In addition to thin film growth, gas phase nucleation was generally observed forming a particulate deposit at the end of the heated zone.

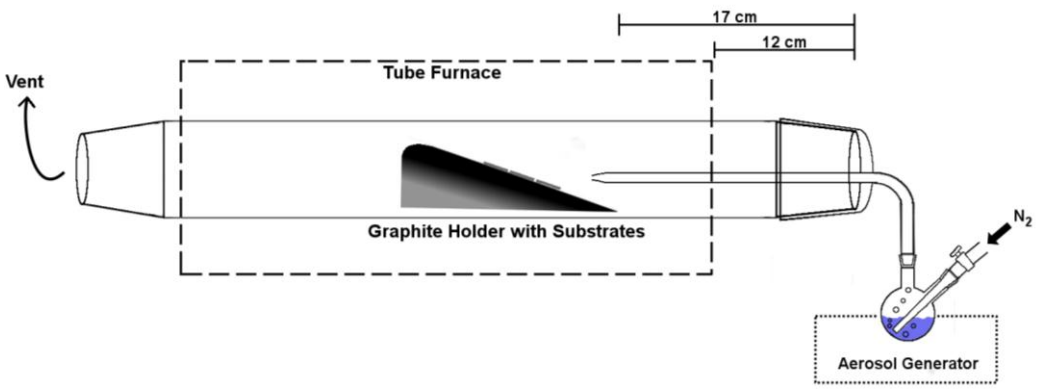

Figure 3-2: Schematic representation of the AACVD apparatus. Not drawn to scale.

3.3.4 Sol-Gel processing of heterometallic tert.-butanolates

500 mg of the heterometallic precursor was dissolved in 50 ml dry, degassed 1,4-dioxane and 10 ml toluene. Subsequently, 0.25 ml degassed water in 20 ml 1,4-dioxane were slowly added under vigorous stirring at 50 °C using a syringe pump. Injection rate was set to 2.5 ml/h. The solution was stirred for 18 h in total. The resulting solid was collected by centrifugation and washed three times with 1,4-dioxane before drying overnight at 70 °C. In case of *FeGa*, which showed increased sensitivity towards atmospheric oxygen, the solid was filtrated under inert atmosphere and dried under reduced pressure.

3.4 SYNTHESES

3.4.1 Synthesis of potassium tert.-butanolate, $[KO^tC_4H_9]_4$

$$\underset{39.10\ g/mol}{K} + \underset{47.12\ g/mol}{HO^tBu} \longrightarrow \underset{448.84\ g/mol}{1/4\ [KO^tBu]_4} + \underset{2.02\ g/mol}{1/2\ H_2}$$

Potassium metal was slowly added to a mixture of 500 ml toluene and 200 ml tert.-butanol. Once the gas evolution slowed down the mixture was heated and portions of tert.-butanol were added until all potassium dissolved. After distillation of toluene and residual alcohol, the crude product was purified by sublimation at 125 °C at 0.04 mbar.

3.4.2 Synthesis of gallium tris(tert.-butanolate), $[Ga(O^tC_4H_9)_3]_2$

$$\underset{176.08\ g/mol}{GaCl_3} + \underset{448.84\ g/mol}{3/4\ [KO^tBu]_4} \longrightarrow \underset{587.12\ g/mol}{1/2\ [Ga(O^tBu)_3]_2} + \underset{74.55\ g/mol}{3\ KCl}$$

$[Ga(O^tBu)_3]_2$ was synthesised following a modified procedure initially described by Mehrotra *et al.*.[13] 3.5 g $GaCl_3$ (19.9 mmol, 1 equiv.) were cooled with liquid nitrogen before adding 10 ml of dry THF and warming up. Subsequently 150 ml of toluene were added and the solution was cooled again. 6.8 g KO^tBu (6.06 mmol, 3.05 equiv.) were dissolved in 100 ml boiling toluene and slowly added to the cooled $GaCl_3$ solution. After refluxing for 60 h, the suspension was filtrated and the solvent was removed to give a light yellow powder, which was purified by sublimation at 120 °C at 0.04 mbar to give 4.38 g (7.45 mmol, 75 %) pure $[Ga(O^tBu)_3]_2$ as a colourless solid.

3.4.3 Synthesis of lithium bis(trimethylsilyl)amide, $[LiN(Si(CH_3)_3)_2]_3$

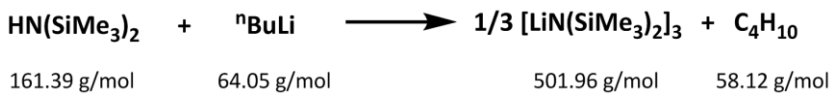

$[LiN(SiMe_3)_2]_3$ was synthesised according to a modified procedure published by Popowski *et al.*.[510] After freezing 30 g HMDS (185.9 mmol, excess) in liquid nitrogen, 45 ml 2.5 M ^{n}BuLi solution in ^{n}hexane (112.5 mmol, 1 equiv.) were slowly added and the mixture was allowed to warm up to room temperature. After stirring for 2 h, all volatiles were removed under reduced pressure and the crude product purified by sublimation at 110 °C at 0.03 mbar to yield 16.9 g (33.7 mmol, 90 %) of $[LiN(SiMe_3)_2]_3$ as a colourless solid.

3.4.4 Synthesis of indium tris(bis(trimethylsilyl)amide), $In(N(Si(CH_3)_3)_2)_3$

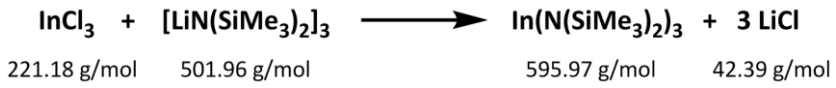

$In(N(SiMe_3)_2)_3$ has been synthesised following a modified procedure published by Bürger *et al.*.[511] 2.5 g of $InCl_3$ (11.3 mmol, 1 equiv.) was cooled to 77 K and 10 ml of THF were added. After warming up, 100 ml toluene were added and the solution cooled once more. 5.68 g (11.3 mmol, 1 equiv.) of $[LiHMDS]_3$ were dissolved in 100 ml toluene and subsequently added to the cooled $InCl_3$ solution. The solution was refluxed for 48 h, filtered and the solvent was removed at reduced pressure. The crude product was sublimated at 120 °C at 0.04 mbar to give 5.7 g (9.6 mmol, 85 %) of $In(N(SiMe_3)_2)_3$ as a colourless solid.

3.4.5 Synthesis of 1,3-bis(dimethyl)propanol, $HOCH(CH_2N(CH_3)_2)_3$

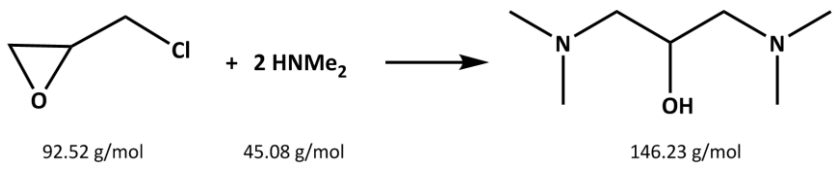

The aminoalcohol was synthesised following a known procedure by Campbell *et al.*.[512] 19 g (205 mmol, 1 equiv.) epichlorohydrin were slowly added to 324 g of dimethylamine (2.87 mmol, 40 % aqueous solution, excess) and subsequently refluxed for 18 h. Next, the reaction was cooled with an ice bath and 68 g of sodium hydroxide were added. The organic phase was separated, dried over Na_2SO_4 and filtered. The solvent and residual dimethylamine were removed under reduced pressure.

The crude product was purified by means of vacuum distillation with a vigreux column yielding 14.05 g (96 mmol, 47 %) of the 1,3-bis(dimethyl)propanol with a boiling point of 90 °C at 40 mbar.

^{1}H NMR (C_6D_6, 250.13 MHz, δ /ppm): 2.09 (s, 12H, N(C<u>H</u>$_3$)$_2$), 2.19 (dd, J=4.35/12.36 Hz, 2H, C<u>H</u>$_2$), 2.31 (dd, J=7.89/12.39 Hz, 2H, C<u>H</u>$_2$), 3.56 (s, 1H, O<u>H</u>), 3.82 (tt, J=3.34/7.91 Hz, 1H, C<u>H</u>)

^{13}C {1H} NMR (C_6D_6, 62.86 MHz, δ /ppm): 46.0 (s, <u>C</u>H$_3$), 64.4 (s, <u>C</u>H$_2$), 66.2 (s, <u>C</u>H)

3.4.6 Synthesis of 1,3-bis(diethyl)propanol, $HOCH(CH_2N(CH_2CH_3)_2)_3$

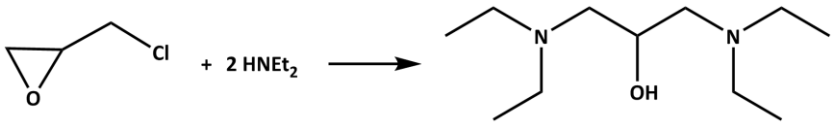

92.52 g/mol 73.14 g/mol 202.34 g/mol

15.9 g epichlorohydrin (172 mmol, 1 equiv.) were added dropwise to 56.8 g diethylamine (777 mmol, excess) in 50 ml of petrol ether. After refluxing for 7 h, the cooled reaction mixture is extracted with 1 M NaOH solution, organic phases dried over Na_2SO_4, filtered and solvent removed. Distillation of the crude product yielded 31.1 g (154 mmol, 89 %) of the 1,3-bis(diethyl)propanol with a boiling point of 104 °C at 12 mbar.

^{1}H NMR (C_6D_6, 250.13 MHz, δ /ppm): 0.92 (t, J=7.12 Hz, 12H, C<u>H</u>$_3$), 2.34-2.57 (m, 12H, C<u>H</u>$_2$CH$_3$, CHC<u>H</u>$_2$), 3.70 (s, 1H, O<u>H</u>), 3.82 (tt, J=5.24/6.87 Hz, 1H, C<u>H</u>)

^{13}C {^{1}H} NMR (C_6D_6, 62.86 MHz, δ /ppm): 12.43 (s, <u>C</u>H$_3$), 47.9 (s, <u>C</u>H$_2$CH$_3$), 58.6 (s, CH<u>C</u>H$_2$), 66.5 (s, <u>C</u>H)

3.4.7 Synthesis of aluminium tris(1,3-bis(dimethylamino)propan-2-olate), *Al1*

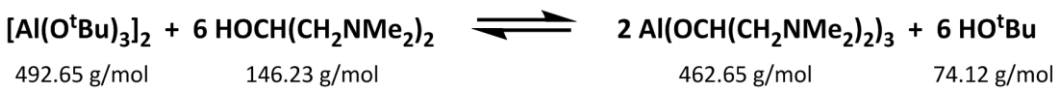

345 mg (0.7 mmol, 1 equiv.) of $[Al(OtBu)_3]_2$ in 5 ml toluene were reacted with 618 mg (4.22 mmol, 6.03 equiv.) 1,3-bis(dimethylamino)propan-2-ol at room temperature. After stirring overnight, removal of volatile residues yielded 622 mg (1.3 mmol, 96 %) of *Al1* as clear, colourless oil. Suitable crystals for single-crystal XRD analysis formed in the pure compound overnight at room temperature. Crystallographic information files (CIF) can be obtained from CCDC 1430667.

^{1}H NMR (C_6D_6, 250.13 MHz, δ /ppm): 2.32 (s, 30H, C$\underline{H}_3$), 2.35-2.60 (m, 18H, C$\underline{H}_3$, C$\underline{H}_2$), 4.12 (quint., J=6.15 Hz, C$\underline{H}$)

^{13}C {^{1}H} NMR (C_6D_6, 62.86 MHz, δ /ppm): 46.8 (s, $\underline{C}H_3$), 66.4 (s, $\underline{C}H_2$), 67.2 (s, $\underline{C}H$)

3.4.8 Synthesis of gallium tris(1,3-bis(dimethylamino)propan—2-olate), *Ga1*

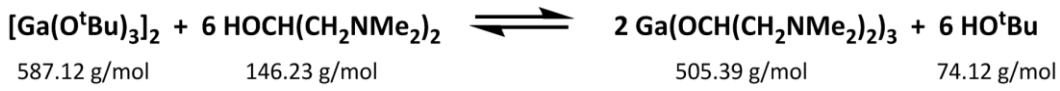

213 mg (0.36 mmol, 1 equiv.) [Ga(O^{t}Bu)$_3$]$_2$ and 334 mg (2.28 mmol, 6.3 equiv.) 1,3-bis(dimethylamino)propan-2-ol were stirred in 5 ml toluene overnight. After removing all volatile substances, 374 mg (7.4 mmol, 96 %) of *Ga1* were obtained as colourless oil. Crystals suitable for single-crystal XRD studies were grown from the pure compound at room temperature. CIF files can be obtained from CCDC 1430668.

^{1}H NMR (C_6D_6, 250.13 MHz, δ /ppm): 2.35 (s, 33H, C$\underline{H}_3$), 2.39 (s, 3H, C$\underline{H}_3$), 2.42 (dd, J=5.27/11.78 Hz, 6H, C$\underline{H}_2$), 2.51 (dd, J=7.18/11.78 Hz, 6H, C$\underline{H}_2$), 4.12 (tt, J=5.30/7.13 Hz, 3H, C$\underline{H}$)

^{13}C {^{1}H} NMR (C_6D_6, 62.86 MHz, δ /ppm): 46.8 (s, $\underline{C}H_3$), 67.1 (s, $\underline{C}H_2$), 68.3 (s, $\underline{C}H$)

3.4.9 Synthesis of indium tris(1,3-bis(dimethylamino)propan-2-olate), *In1*

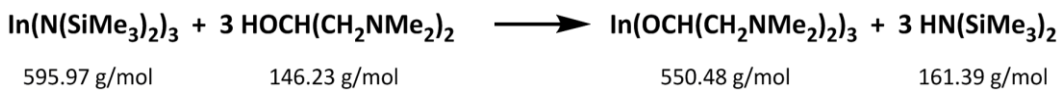

456 mg (0.77 mmol, 1 equiv.) of In(HMDS)$_3$ were mixed with 350 mg (2.39 mmol, 3.1 equiv.) of 1,3-bis(dimethylamino)propan-2-ol in 7 ml toluene. After stirring for 3 h at room temperature, volatiles were removed under reduced pressure to yield 415 mg (0.75 mmol, 98 %) of *In1* as colourless oil. Specimen suitable for single-crystal XRD analysis were grown in a concentrated ^{n}hexane solution at -9 °C. CIF files can be obtained from CCDC 1430669.

^{1}H NMR (C_6D_6, 250.13 MHz, δ /ppm): 2.30 (s, 36H, C$\underline{H}_3$), 2.35 (dd, J=4.23/11.61 Hz, 6H, C$\underline{H}_2$), 2.51 (dd, J=7.9/11.61 Hz, 6H, C$\underline{H}_2$), 4.07 (m, 3H, C$\underline{H}$)

^{13}C {^{1}H} NMR (C_6D_6, 62.86 MHz, δ /ppm): 47.1 (s, $\underline{C}H_3$), 67.3 (s, $\underline{C}H_2$), 68.6 (s, $\underline{C}H$)

3.4.10 Synthesis of aluminium tris(1,3-bis(diethylamino)propan-2-olate), *Al2*

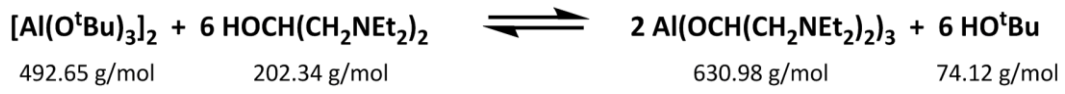

328 mg (0.67mmol, 1 equiv.) $[Al(OtBu)_3]_2$ and 821 mg (4.06 mmol, 6.05 equiv.) 1,3-bis(diethylamino)propan-2-ol were stirred in 5 ml toluene overnight. Removal of the solvent by-products under reduced pressure yielded 797 mg (1.26 mmol, 95 %) of *Al2* as colourless oil. Crystals suitable for single-crystal XRD measurements were grown in a concentrated ^{n}hexane solution at -9 °C. CIF files can be obtained from CCDC 1430670.

^{1}H NMR (C_6D_6, 250.13 MHz, +25 °C, δ /ppm): 1.07 (t, J=6.99 Hz, 36H, C$\underline{H}_3$), 2.53-2.99 (m, 36H, C$\underline{H}_2$CH$_3$, CHC$\underline{H}_2$), 4.14 (quint., J=6.26 Hz, 3H, C$\underline{H}$)

^{13}C {^{1}H} NMR (C_6D_6, 62.86 MHz, +25 °C, δ /ppm): 11.2 (s, $\underline{C}$H$_3$), 46.9 (s, $\underline{C}$H$_2$CH$_3$), 61.2 (s, CH$\underline{C}$H$_2$), 67.9 (s, $\underline{C}$H)

3.4.11 Synthesis of gallium tris(1,3-bis(diethylamino)propan—2-olate), *Ga2*

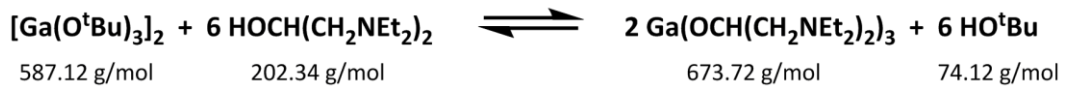

233 mg (0.40 mmol, 1 equiv.) $[Ga(OtBu)_3]_2$ were mixed with 500 mg (2.47 mmol, 6.1 quiv.) 1,3-bis(diethylamino)propan-2-ol in 6 ml toluene. After stirring overnight, all volatile substances were removed to obtain 526 mg (781 mmol. 97 %) of *Ga2* as colourless oil. Crystals formed in the pure substance over a few days and were separated before the whole substance solidified. CIF files can be obtained from CCDC 1430671.

^{1}H NMR (C_6D_6, 250.13 MHz, +25 °C, δ /ppm): 1.07 (t, J=7.10 Hz, 36H, C$\underline{H}_3$), 2.56-2.95 (m, 36H, C$\underline{H}_2$CH$_3$, CHC$\underline{H}_2$), 4.13 (quint., J=6.26 Hz, 3H, C$\underline{H}$)

^{13}C {^{1}H} NMR (C_6D_6, 62.86 MHz, +25 °C, δ /ppm): 11.3 (s, $\underline{C}$H$_3$), 47.0 (s, $\underline{C}$H$_2$CH$_3$), 61.0 (s, CH$\underline{C}$H$_2$), 68.9 (s, $\underline{C}$H)

3.4.12 Synthesis of indium tris(1,3-bis(diethylamino)propan-2-olate), *In2*

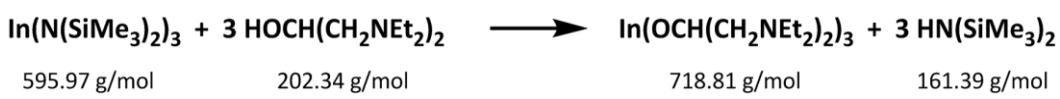

306 mg (0.51 mmol, 1 equiv.) $In(HMDS)_3$ and 308 mg (1.55 mmol, 3.04 equiv.) 1,3-bis(diethylamino)propan-2-ol were stirred in 8 ml toluene overnight. Removal of solvent and by-products yielded 355 mg (0.49 mmol, 97 %) of *In2* as colourless oil.

^{1}H NMR (C_6D_6, 250.13 MHz, +25 °C, δ /ppm): 1.07 (t, J=7.06 Hz, 36H, C$\underline{H}_3$), 2.58 (dd, J=7.04/12.36 Hz, 6H, CHC$\underline{H}_2$), 2.64-2.95 (m, 30H, C$\underline{H}_2$CH$_3$, CHC$\underline{H}_2$), 4.18 (quint., J=6,48 Hz, 3H, C$\underline{H}$)

^{13}C {^{1}H} NMR (C_6D_6, 62.86 MHz, +25 °C, δ /ppm): 11.3 (s, $\underline{C}$H$_3$), 47.3 (s, $\underline{C}$H$_2$CH$_3$), 62.3 (s, CH$\underline{C}$H$_2$), 69.3 (s, $\underline{C}$H)

3.4.13 General synthesis procedure for thioether functionalised gallium alkoxides

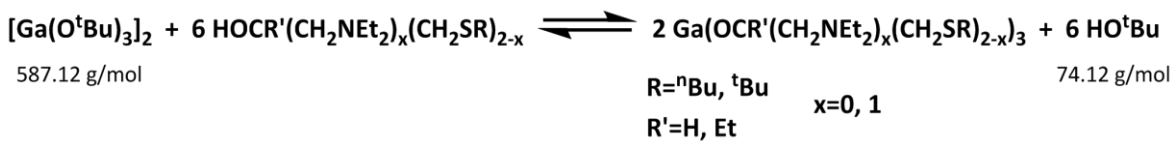

Approx. 300 mg of $[Ga(O^tBu)_3]_2$ were dissolved in 5 ml of dry toluene before adding 6.1 equiv. of the respective alcohol. After stirring overnight all volatile compounds were removed under reduced pressure. The reaction process was monitored via ^{1}H NMR spectroscopy. If applicable, a few drops of the alcohol were added to a concentrated toluene solution of the intermediate product to complete the reaction. After repeated removal of solvent and excess alcohol, all products were obtained as colourless, viscous oils. Alcohol ligands were synthesised as described in earlier studies.[439]

3.4.14 General synthesis procedure for thioether functionalised indium alkoxides

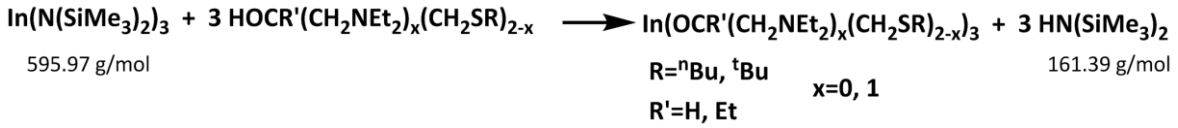

Approx. 500 mg of $In(N(SiMe_3)_2)_3$ were dissolved in 5 ml of dry toluene and 3.02 equiv. of the dry alcohol ligand were added. Alcoholysis usually occurred within a few hours at room temperature, after which all volatiles were removed under reduced pressure to yield the thioether functionalised alkoxides as colourless, viscous liquids.

3.4.15 Synthesis of 1-^{n}butylthio-3-ethoxy-2-propanol, $HOCH(CH_2S^nC_4H_9)(CH_2OC_2H_5)$

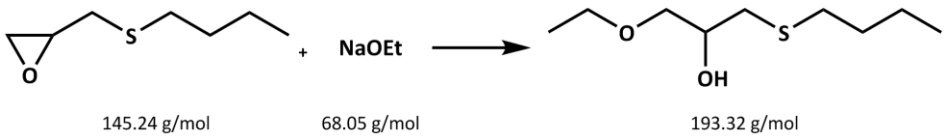

0.48 g (20.09 mmol, 1 equiv.) sodium metal was dissolved in 25 ml dry ethanol. After stirring for 10 min, 3.04 g (20.9 mmol, 1 equiv) 1,2-epoxy-3-^{n}butylthio-propan was added and the solution was refluxed for 2 h. After cooling, saturated brine was added and phases separated with CH_2Cl_2. Organic phases were dried over Na_2SO_4, filtrated and the solvent removed. Fractionated distillation yielded 3.60 g (18.63 mmol, 89 %) of 1-^{n}butylthio-3-ethoxy-2-propanol as a clear liquid with a boiling point of 110 °C at 5 mbar.

^{1}H NMR (C_6D_6, 250.13 MHz, +25 °C, δ /ppm): 0.76 (t, J=7.23 Hz, 3H $CH_2CH_2C\underline{H}_3$), 1.00 (t, J=6.99 Hz, 3H, $OCH_2C\underline{H}_3$), 1.22 (m, J=7.28 Hz, 2H, $CH_2C\underline{H}_2CH_3$), 1.40 (m, J=7.38 Hz, 2H, $SCH_2C\underline{H}_2$), 2.32 (t, J=7.32 Hz, 2H, $SC\underline{H}_2CH_2$), 2.38 (s, 1H, O$\underline{H}$), 2.57 (dd, J=5.87/21.68 Hz, 1H, $CHC\underline{H}_2S$), 2.62 (dd, J=6.74/21.68 Hz, 1H, $SC\underline{H}_2CH$), 3.21 (q, J=6.98 Hz, 2H, $OC\underline{H}_2CH_3$), 3.34 (d, J=5.33 Hz, $OC\underline{H}_2O$), 3.86 (quint., J=5.76 Hz, 1H, C$\underline{H}$)

^{13}C {^{1}H} NMR (C_6D_6, 62.86 MHz, +25 °C, δ /ppm): 13.8 (s, $CH_2CH_2\underline{C}H_3$), 15.3 (s, $OCH_2\underline{C}H_3$), 22.16 (s, $CH_2\underline{C}H_2CH_3$), 23.1 (s, $SCH_2\underline{C}H_2$), 32.5 (s, $S\underline{C}H_2CH_2$), 36.3 (s, $CH\underline{C}H_2S$), 66.7 (s, $O\underline{C}H_2CH_3$), 69.8 (s, $\underline{C}H$), 73.6 (s, $O\underline{C}H_2O$)

3.4.16 Synthesis of 1-^{t}butylthio-3-ethoxy-2-propanol, $HOCH(CH_2S^tC_4H_9)(CH_2OC_2H_5)$

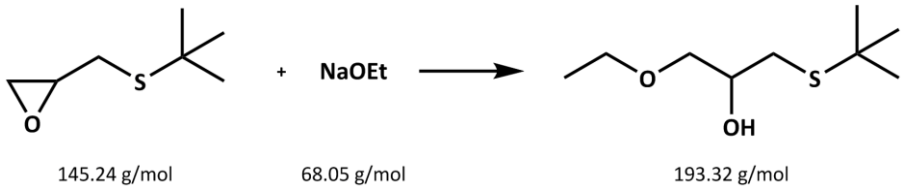

The synthesis was conducted similar to the ^{n}butyl analogue using and 1.8 g (12.4 mmol, 1 equiv.) 1,2-epoxy-3-^{t}butylthio-propan and 0.30 g (13.0 mmol, 1.05 equiv.) sodium yielding 2.18 g (11.27 mmol, 91 %) of 1-^{t}butylthio-3-ethoxy-2-propanol with a boiling point of 98 °C at 5 mbar.

^{1}H NMR (C_6D_6, 250.13 MHz, +25 °C, δ /ppm): 1.00 (t, J=7.10 Hz, 3H, $CH_2C\underline{H}_3$), 1.14 (s, 9H, $C(C\underline{H}_3)_3$), 2.50 (d, J=4.43 Hz, 1H, O$\underline{H}$), 2.67 (dd, J=6.55 / 14.98 Hz, 1H, $C\underline{H}_2S$), 2.72 (dd, J=6.10 / 15.23 Hz, 1H, $C\underline{H}_2S$), 3.21 (q, J=7.00 Hz, 2H, $C\underline{H}_2CH_3$), 3.33 (dd, J=5.59/9.29 Hz, 1H, $C\underline{H}_2O$), 3.39 (dd, J=4.69/9.42 Hz, 1H, $C\underline{H}_2O$), 3.90 (m, J=5.53 Hz, 1H, C$\underline{H}$)

^{13}C {^{1}H} NMR (C_6D_6, 62.86 MHz, +25 °C, δ /ppm): 15.3 (s, $CH_2\underline{C}H_3$), 31.0 (s, $C(CH_3)_3$), 32.8 (s, CH_2S), 42.0 (s, $\underline{C}(CH_3)_3$), 66.7 (s, $\underline{C}H_2CH_3$), 70.2 (s, $\underline{C}H$), 73.7 (s, $CH\underline{C}H_2O$)

3.4.17 Synthesis of gallium tris(1-^{n}butylthio-3-ethyloxy-2-propanolate), *Ga11*

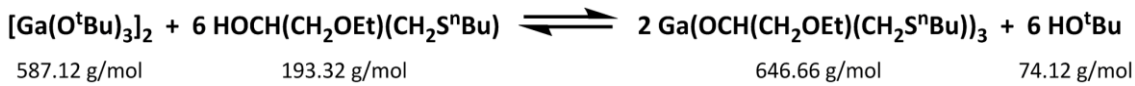

0.260 g (0.45 mmol, 1 equiv.) of $[GaO^tBu)_3]_2$ was dissolved in approx. 5 ml toluene and 0.536 g (2.79 mmol, 6.2 equiv.) 1-^{n}butylthio-3-ethoxy-2-propanol was added. After stirring at room temperature overnight, solvent and residual alcohol was removed under reduced pressure. Pure *Ga11* was obtained as a colourless, highly viscous oil.

^{1}H NMR (C_6D_6, 250.13 MHz, +25 °C, δ /ppm): 0.81 (t, J=7.40 Hz, 3H, μ_2-$CH_2CH_2C\underline{H}_3$), 0.88 (t, J=7.28 Hz, 6H, $CH_2CH_2C\underline{H}_3$), 1.21 (t, J=6.79 Hz, 9H, $OCH_2C\underline{H}_3$), 1.30 (m, J=7.47 Hz, 2H, μ_2-$CH_2C\underline{H}_2CH_3$), 1.41 (m, J= 7.40 Hz, 4H, $CH_2C\underline{H}_2CH_3$), 1.53 (m, J=7.48 Hz, 2H, μ_2-$SCH_2C\underline{H}_2$), 1.65 (quint., J=7.29 Hz, 4H, $SCH_2C\underline{H}_2$), 2.52 (t, J=6.55, 2H, $SCH_2C\underline{H}_2$), 2.66 (m, 4H, $SCH_2C\underline{H}_2$), 2.77-3.28 (m, 6H, μ_2-$CHC\underline{H}_2S$, $CHC\underline{H}_2S$), 3.41-3.99 (m, 12H, μ_2-$OC\underline{H}_2CH_3$, $OC\underline{H}_2CH_3$, μ_2-$OC\underline{H}_2O$, $OC\underline{H}_2O$), 4.31 (m, J= 5.34 Hz, 1H, μ_2-C$\underline{H}$), 4.43 (br, 2H, C$\underline{H}$)

^{13}C {^{1}H} NMR (C_6D_6, 62.86 MHz, +25 °C, δ /ppm): 14.0 (s, $CH_2CH_2\underline{C}H_3$), 14.7 (s, $OCH_2\underline{C}H_3$), 15.6 (br. s, μ_2-$OCH_2\underline{C}H_3$), 22.3 (s, $CH_2\underline{C}H_2CH_3$), 22.4 (s, μ_2-$CH_2\underline{C}H_2CH_3$), 32.3 (s, $SCH_2\underline{C}H_2$), 32.6 (s, μ_2-$SCH_2\underline{C}H_2$), 33.0 (s, $S\underline{C}H_2CH_2$), 33.4 (s, μ_2-$S\underline{C}H_2CH_2$), 38.4 (s, $S\underline{C}H_2CH$), 39.3 (br. s, μ_2-$S\underline{C}H_2CH$), 66.9 (br. s, μ_2-$O\underline{C}H_2CH_3$), 68.1 (s, $O\underline{C}H_2CH_3$), 71.3 (s, $\underline{C}H$), 72.6 (s, μ_2-$\underline{C}H$), 74.8 (s, $O\underline{C}H_2O$), 75.6 (s, μ_2-$O\underline{C}H_2O$)

3.4.18 Synthesis of gallium tris(1-^{t}butylthio-3-ethyloxy-2-propanolate), *Ga12*

0.298 g (0.52 mmol, 1 equiv.) $[Ga(O^tBu)_3]_2$ was reacted with 0.617 g (3.2 mmol, 6.17 equiv.) 1-^{t}butylthio-3-ethyloxy-2-propanol in 6 ml toluene. After stirring overnight, solvents and by-products were removed at reduced pressure yielding *Ga12* as clear, viscous oil.

^{1}H NMR (C_6D_6, 250.13 MHz, +25 °C, δ /ppm): 1.12-1.30 (m, 15H, $OCH_2C\underline{H}_3$, μ_2-$C(C\underline{H}_3)_3$), 1.40 (s, 21H, μ_2-$OCH_2C\underline{H}_3$, $C(C\underline{H}_3)_3$), 2.64-3.27 (m, 6H, μ_2-$C\underline{H}_2S$, $C\underline{H}_2S$), 3.27-3.94 (m, 12H, μ_2-$OC\underline{H}_2CH_3$, $OC\underline{H}_2CH_3$, μ_2-$OC\underline{H}_2O$, $OC\underline{H}_2O$), 4.34 (m, 1H, μ_2-$C\underline{H}$), 4.45 (m, 2H, $C\underline{H}$)

^{13}C {^{1}H} NMR (C_6D_6, 62.86 MHz, +25 °C, δ /ppm): 13.9 (s, $OCH_2\underline{C}H_3$), 14.7 (s, $OCH_2\underline{C}H_3$), 15.7 (s, μ_2-$OCH_2\underline{C}H_3$), 31.2 (s, μ_2-$C(\underline{C}H_3)_3$), 31.4 (s, $C(\underline{C}H_3)_3$), 34.8 (s, $\underline{C}H_2S$), 35.3 (s, μ_2-$\underline{C}H_2S$), 41.4 (s, $\underline{C}(CH_3)_3$), 41.7 (s, μ_2-$\underline{C}(CH_3)_3$)), 66.9 (br. s, μ_2-$O\underline{C}H_2CH_3$), 68.2 (s, $O\underline{C}H_2CH_3$), 68.6 (s, $O\underline{C}H_2CH_3$), 71.4 (s, $\underline{C}H$), 72.3 (br. s, μ_2-$\underline{C}H$), 74.8 (s, $O\underline{C}H_2O$), 75.7 (br. s, μ_2-$O\underline{C}H_2O$)

3.4.19 Synthesis of indium tris(1-^{n}butylthio-3-ethyloxy-2-propanolate), *In11*

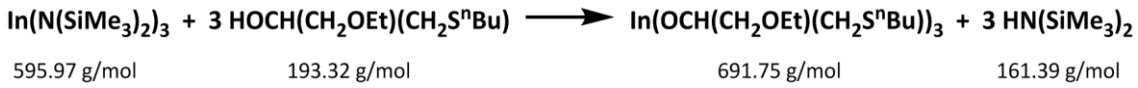

0.304 g (0.51 mmol, 1 equiv.) $In(N(SiMe_3)_2)_3$ was dissolved in 7 ml toluene before adding 0.301 g (1.57 g, 3.05 equiv.) 1-^{n}butylthio-3-ethyloxy-2-propanol. After stirring for three hours, solvent and by-products were removed under reduced pressure to yield *In11* as a colourless, viscous liquid.

^{1}H NMR (C_6D_6, 250.13 MHz, +25 °C, δ /ppm): 0.87 (t, J=6.85 Hz, 9H, $CH_2CH_2C\underline{H}_3$), 1.24 (br, 9H, $OCH_2C\underline{H}_3$), 1.41 (m, 6H, $CH_2C\underline{H}_2CH_3$), 1.65 (br, 6H, $SCH_2C\underline{H}_2$), 2.71 (br, 6H, $SC\underline{H}_2CH_2$), 3.09 (br, 6H, $CHC\underline{H}_2S$), 3.59-3.98 (m, 12H, $OC\underline{H}_2CH_3$, $CHC\underline{H}_2O$), 4.41 (br, 3H, $C\underline{H}$)

^{13}C {^{1}H} NMR (C_6D_6, 62.86 MHz, +25 °C, δ /ppm): 13.9 (s, $CH_2CH_2\underline{C}H_3$), 15.1 (s, $OCH_2\underline{C}H_3$), 22.3 (s, $CH_2\underline{C}H_2CH_3$), 32.4 (s, $SCH_2\underline{C}H_2$), 33.0 (s, $S\underline{C}H_2CH_2$), 39.0 (s, $CH\underline{C}H_2S$), 67.3 (s, $O\underline{C}H_2CH_3$), 70.8 (s, $\underline{C}H$), 74.6 (s, $CH\underline{C}H_2O$)

3.4.20 Synthesis of indium tris(1-^{t}butylthio-3-ethyloxy-2-propanolate), *In12*

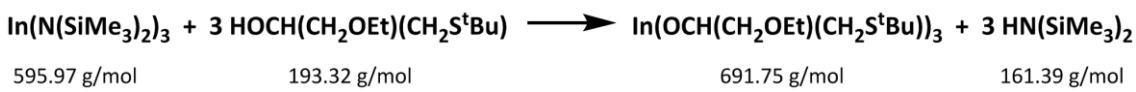

0.304 g (0.51 mmol, 1 equiv.) $In(N(SiMe_3)_2)_3$ was mixed with 0.298 g (1.55 mmol, 3.05 equiv.) 1-^{n}butylthio-3-ethyloxy-2-propanol in 8 ml toluene at room temperature. After removing all volatile compounds, *In12* was obtained as colourless, viscous liquid.

^{1}H NMR (C_6D_6, 250.13 MHz, +25 °C, δ /ppm): 1.28 (t, J=6.03 Hz, 9H, $CH_2C\underline{H}_3$), 1.40 (s, 21H, $C(C\underline{H}_3)_3$), 1.45 (s, 6H, $C(C\underline{H}_3)_3$), 3.13 (br, 6H, $SC\underline{H}_2$), 3.66 (br, 3H, $OC\underline{H}_2O$), 3.85 (br, 9H, $OC\underline{H}_2O$, $OC\underline{H}_2CH_3$), 4.39 (br, 3H, $C\underline{H}$)

^{13}C {^{1}H} NMR (C_6D_6, 62.86 MHz, +25 °C, δ /ppm): 15.0 (s, $CH_2\underline{C}H_3$), 31.6 (s, $C(\underline{C}H_3)_3$), 34.7 (s, $S\underline{C}H_2$), 41.7 (s, $\underline{C}(CH_3)_3$), 67.7 (s, $O\underline{C}H_2CH_3$), 71.4 (s, $\underline{C}H$), 74.0 (s, $O\underline{C}H_2O$)

3.4.21 Synthesis of tetrakis(μ$_2$-^{t}butanolato)-tetrakis(^{t}butanolato)-digallium-iron(II), *FeGa*

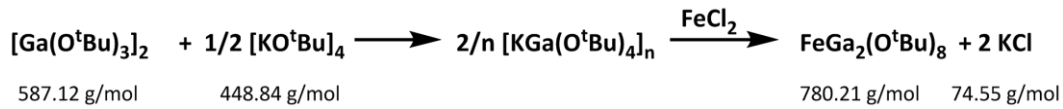

FeGa was synthesised following a modified procedure previously described by Barth and co-workers.[513] 1.508 g (3.36 mmol, 0.5 equiv.) $[KO^{t}Bu]_4$ in 50 ml toluene was added to 3.855 g (6.57 mmol, 1 equiv.) $[Ga(O^{t}Bu)_3]_2$ in 100 ml toluene and stirred at 100 °C for 48 h. Subsequently, 0.860 g (6.79 mmol, 1 equiv.) dry $FeCl_2$ was suspended in 10 ml THF and 40 ml toluene and added to the gel-like $[KGa(O^{t}Bu)_4]_n$ suspension. After heating to 100 °C for 48 h, the reaction mixture was filtrated and the solvent removed to yield a light brown solid. Sublimation at 125 °C at 0.04 mbar gave *FeGa* as a beige solid. Crystals suitable for single-crystal XRD analysis were grown from a concentrated toluene solution at -9 °C.

3.4.22 Synthesis of tetrakis(μ_2-^{t}butanolato)-tetrakis(^{t}butanolato)-digallium-cobalt(II), *CoGa*

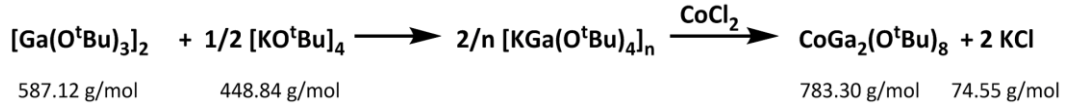

CoGa was synthesised following a modified procedure by Cavelius *et al.*.[433] 1.214 g (2.07 mmol, 1 equiv.) $[Ga(O^tBu)_3]_2$ was dissolved in 100 ml toluene and added to a solution of 0.473 g (1.05 mmol, 0.5 equiv.) $[KO^tBu]_4$ in 50 ml toluene. After heating to 100 °C for 48 h, a suspension of 0.261 g (2.01 mmol, 0.96 equiv.) dry $CoCl_2$ in 40 ml toluene and 10 ml THF was added and the mixture heated to 100 °C for another 96 h. Filtration and subsequent removal of the solvent resulted in 1.34 g (1.71 mmol, 83 %) of *CoGa* as a pink solid.

3.4.23 Synthesis of tetrakis(μ_2-^{t}butanolato)-tetrakis(^{t}butanolato)-digallium-nickel(II), *NiGa*

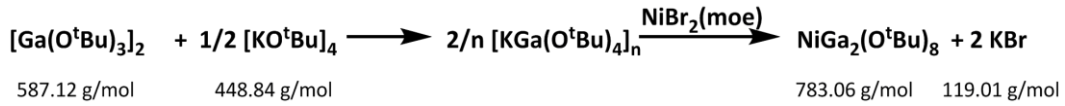

NiGa was synthesised following a modified procedure by Barth *et al.*.[432] A mixture of 1.420 g (2.42 mmol, 1 equiv.) $[GaO^tBu)_3]_2$ and 0.551 g (1.23 mmol, 0.5 equiv.) $[KO^tBu]_4$ in 150 ml toluene was heated to 100 °C for 48 h before adding a suspension of 0.862 g (2.44 mmol, 1 equiv.) dry $NiBr_2(O(C_2H_4OCH_3)_2)$ in 40 ml toluene and 10 ml THF. After stirring at 100 °C for approx. 48 h, the mixture was filtrated and the solvent removed, giving a purple powder. Sublimation at 125 °C at 0.04 mbar yielded *NiGa* as a dark purple solid.

3.4.24 Synthesis of tetrakis(μ_2-^{t}butanolato)-tetrakis(^{t}butanolato)-digallium-copper(II), *CuGa*

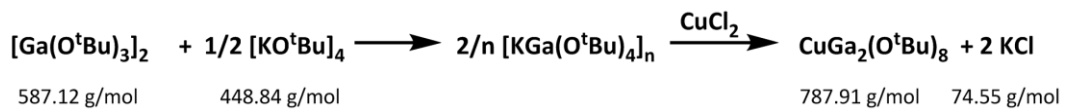

CuGa was synthesised following a modified procedure previously described by Barth and co-workers.[514] 2.047 g (3.49 mmol, 1 equiv.) $[Ga(O^tBu)_3]_2$ dissolved in 100 ml toluene was mixed with a solution of 0.802 g (0.18 mmol, 0.5 equiv.) $[KO^tBu]_4$ in 50 ml toluene. After stirring for 48 h at 100 °C,

a suspension of 0.445 g (3.31 mmol, 0.95 equiv.) in 10 ml THF and 40 ml toluene was added and allowed to stir for additional 96 h at 100 °C. The dark yellow dispersion was filtrated and the solvent removed thereafter to obtain 2.46 g (3.1 mmol, 68 %) of *CuGa* as a yellow solid. The product decomposes upon sublimation and gives a copper deficient gallium alkoxide. Thus, the product was used as received without further purification. Crystals suitable for single-crystal XRD analysis have been grown from a saturated toluene solution at -9 °C.

CHAPTER 4

APPENDIX

"Heute hab' ich selbstständig gedacht.

Das war ein Fehler."

- Rupert K.-

4.1 GLOSSARY

AACVD	aerosol-assisted chemical vapour deposition
acac	acetylacetone, $C_5H_8O_2$
ALD	atomic layer deposition
^{n}Bu	*normal*-butyl ($CH_3CH_2CH_2CH_2$-)
^{t}Bu	t*ertiary*-butyl ($(CH_3)_3C$-)
CVD	chemical vapour deposition
DSC	differential scanning calorimetry
EDX	energy dispersive X-Ray spectroscopy
equiv.	equivalent
Et	ethyl (CH_3CH_2-)
FFT	fast-Fourrier transformation
HMDS	hexamethyldisilazane ($((CH_3)_3Si)_2N$-)
HSAB	hard and soft acids and bases
LPCVD	low-pressure chemical vapour deposition
Me	methyl (CH_3-)
MOCVD	metal-organic chemical vapour deposition
MS	mass spectrometry
PLD	pulsed laser deposition
^{i}Pr	isopropyl ($(CH_3)_2CH$-)
PVD	physical vapour deposition
SEM	scanning electron microscopy
TEM	transmission electron microscopy
TGA	thermogravimetric analysis

THF	tetrahydrofuran, C_4H_8O
XPS	X-Ray photoelectron spectroscopy
XRD	X-Ray diffraction
2θ	diffraction angle

NMR abbreviations

NMR	nuclear magnetic resonance
LTNMR	low temperature nuclear magnetic resonance
COSY	correlation spectroscopy
HSQC	heteronuclear single quantum correlation
TOCSY	total correlation spectroscopy
δ	chemical shift
s	singlet
d	doublet
t	triplet
q	quartet
quint.	quintet
m	multiplet
br	broad

4.2 LIST OF FIGURES, SCHEMES AND TABLES

Figure 1-1: Schematic illustration of (a) σ- and (b,c) π-bonding and (d) μ_2-alkoxo bridges in metal alkoxides. Redrawn from reference [9]. 3

Figure 1-2: Possible coordination modes for a bidentate donor functionalised alkoxo ligand. Redrawn from reference [46]. 6

Figure 1-3: Schematic representation of key steps in CVD processes. Redrawn in style of reference [146]. 12

Figure 1-4: Temperature dependence of deposition rate and growth regimes. Redrawn in style of reference [127]. 13

Figure 1-5: Crystal structure of ß-Ga_2O_3. Tetrahedral sites are depicted in pale green. Data taken from reference [236]. 18

Figure 1-6: Crystal structure of α-Ga_2S_3. Data taken from reference [284]. 19

Figure 1-7: Unit cell of cubic In_2O_3. Data taken from reference [312]. 21

Figure 1-8: Crystal structure of tetragonal ß-In_2S_3. Data taken from reference [350]. 22

Figure 1-9: Crystal structure of spinel $MgAl_2O_4$. Data taken from reference [403]. 24

Figure 2-1: ^{1}H NMR of 1,3-bis(diethyamino)propan-2-ol and *In1* in C_6D_6. 28

Figure 2-2: Molecular structure of *Al1* with 75 % probability ellipsoids. Hydrogen atoms have been omitted for clarity. 29

Figure 2-3: Molecular structure of *Ga2* with 75 % probability ellipsoids. Disordered parts are depicted in pale colours; hydrogen atoms were omitted for clarity. 31

Figure 2-4: Molecular structure of *In1* shown with 75 % probability ellipsoids. Inset shows the coordination polyhedron. Hydrogen atoms omitted for clarity. 33

Figure 2-5: Molecular formulas of employed ligand systems. 35

Figure 2-6: ^{1}H NMR spectra of (a) the free alcohol ligand and *In3* at (b) +25 °C, (c) -20 °C, (d) -40 °C, (e) -60 °C and (f) -70 °C in d8-toluene. Asterisk denotes solvent signals. 36

Figure 2-7: ^{1}H NMR spectra of (a) the free aminoalcohol ligand and *In5* at (b) +25 °C, (c) -20 °C, (d) -40 °C, (e) -60 °C and (f) -75 °C in d8-toluene. Asterisk denotes solvent signals. 37

Figure 2-8: Colour coded 2D HSQC-TOCSY NMR of *In5* in d8-toluene at room temperature. Asterisk denotes solvent signals. 38

Figure 2-9: 2D COSY NMR of *In5* in d8-toluene showing the diastereomeric protons *e*. Asterisk indicates solvent signals. 38

Figure 2-10: ^{1}H NMR spectra of (a) the free ligand, (b) *In12* and (c) *Ga12* at room temperature in C_6D_6. 39

Figure 2-11: ^{13}C NMR spectra of (a) the free ligand, (b) *In12* and (c) *Ga12* at room temperature in C_6D_6. 40

Figure 2-12: Molecular structure of *In8* drawn with 50 % probability ellipsoids. Disordered parts are represented in pale colours; hydrogen atoms and a ^{n}pentane solvent molecule have been omitted for clarity. 41

Figure 2–13: Molecular structure of *Ga6* shown with 50 % probability ellipsoids. Hydrogen atoms have been omitted for clarity. 42
Figure 2–14: Sulphur content of $Ga_2O_{3-x}S_x$ thin films determined from EDX assuming all detected sulphur to be sulphidic. 45
Figure 2–15: SEM micrographs of thin films deposited using *Ga5* (a-d) and *Ga6* (e-i) at various temperatures 47
Figure 2–16: XPS spectra of thin films produced from *Ga6* at 600 °C before and after sputtering. 48
Figure 2–17: XPS spectra of the S2s region at various temperatures for thin films derived from (a) *Ga5* and (b) *Ga6*. 49
Figure 2–18: XPS spectra of (a) the S2s region for deposits produced from *Ga7* and (b) Ga3p region for deposits using various precursors at 600 °C. 50
Figure 2–19: Optical micrographs of interdigitated platinum electrodes covered with a Ga_2O_3 thin film with (a+b) 15 µm and (c) 10 µm spacing. 51
Figure 2–20: Impedance spectra (Nyquist plots) of (a) Ga_2O_3 and (b) $Ga_2O_{3-x}S_x$ thin films on interdigitated Pt electrodes with 15 µm electrode width and spacing. 52
Figure 2–21: Arrhenius diagram of conductivities of Ga_2O_3 and $Ga_2O_{3-x}S_x$ (x = 0.37) thin films. 53
Figure 2–22: Sulphide content of $M_2O_{3-x}S_x$ particles as determined via EDX assuming all measured sulphur to be sulphidic. 54
Figure 2–23: Powder XRD of (a) In_2O_3 and (b) Ga_2O_3 treated with H_2S for 1 h at 500 °C and the respective references. (c) Photograph of In_2O_3 and Ga_2O_3 powders before and after H_2S treatment. 55
Figure 2–24: XRD patterns of powders obtained via hot-injection thermolysis of various indium based precursors and ß-In_2S_3 (ICDD 06-0416) and α-In_2O_3 (ICDD 084-1385) references. 56
Figure 2–25: XPS spectra of (a) In3d and (b) S2p region of particles derived from *In3* and *In5*. 57
Figure 2–26: TGA (black) and DSC curves (red) of *Ga5*, *Ga7* and *In3*. 58
Figure 2–27: MS patterns during thermolysis of (a) *Ga3* and (b) *Ga5* showing the formation of H_2S in case of aminoalcoholate precursors. Asterisks denote signals of the carrier gas. 59
Figure 2–28: Sulphur contents of thin films deposited via AACVD of various asymmetric indium aminoalcoholates determined via EDX analysis assuming all sulphur to be sulphidic. 60
Figure 2–29: XRD patterns of thin film deposits derived from In6 at various temperatures. 61
Figure 2–30: SEM micrographs of AACVD thin films employing (a) *In6* and (b) *In9* at various temperatures. 62
Figure 2–31: XPS spectra of (a) In3d and (b) S2p region of AACVD coatings using *In5* (390 °C) and *In6* (410 °C). 62
Figure 2–32: XRD patterns of 1D structures synthesised via AACVD of *In5*, *In9* and *In10*. 63
Figure 2–33: SEM micrographs of 1D nanostructures grown from (a) *In5*, (b) *In9* and (c,d) *In10*. 64
Figure 2–34: TEM micrographs of 1D nanostructures grown from *In5*. 66
Figure 2–35: XPS spectra of (a) the In3d and (b) S2p region for nanowires deposited via AACVD from *In5*. 67

Figure 2–36: Crystal structure of *FeGa* viewed along the a-axis. Hydrogen atoms omitted for clarity. 68
Figure 2–37: Molecular structure of *CuGa* displayed with 50 % probability ellipsoids. Hydrogen atoms have been omitted for clarity. 69
Figure 2–38: Spirocyclic coordination sphere of *FeGa* shown with 50 % probability ellipsoids. 69
Figure 2–39: Powder XRD patterns of annealed particles derived from sol-gel processing of *FeGa*. 72
Figure 2–40: (a) XRD patterns and (b-d) SEM micrographs of $FeGa_2O_4$ thin films deposited via LPCVD of *FeGa* on Si(911) at 500-700 °C. 73
Figure 2–41: XPS spectra of the (a) Ga2p and (b) Fe2p region from LPCVD deposits using *FeGa*. 74
Figure 2–42: Powder XRD patterns of annealed particles derived from sol-gel processing using *CuGa*. 75
Figure 3–1: Schematic representation of the deposition chamber of the LPCVD apparatus. 83
Figure 3–2: Schematic representation of the AACVD apparatus. Not drawn to scale. 84

Scheme 1–1: Transmetallation reaction. 7
Scheme 1–2: Alcohol exchange reactions. 7
Scheme 1–3: Alcoholysis of metal amides. 8
Scheme 1–4: Lewis acid-base adduct formation for the synthesis of heterometallic alkoxides. 9
Scheme 1–5: Transmetallation reaction for the synthesis of heterometallic alkoxides. 9

Table 2–1: Crystal and structure refinement details of *Al1*, *Ga1*, *In1*, *Al2* and *Ga2*. 30
Table 2–2: Selected bond lengths and angles for *Al1*, *Al2*, *Ga1*, *Ga2* and *In1*. 32
Table 2–3: Crystallographic and refinement data of *Ga6* and *In8*. 43
Table 2–4: Selected bond lengths and angles for *In8* and *Ga6*. 44
Table 2–5: Sulphide contents (in at%) for LPCVD thin films at different substrate temperatures as found in EDX and XPS (in brackets) where applicable. 51
Table 2–6: Crystallographic and refinement data of *FeGa* and *CuGa*. 70
Table 2–7: Selected bond lengths and angles for *FeGa* and *CuGa*. 71
Table 3–1: Precursor temperatures used in LPCVD experiments. 83

4.3 LIST OF REFERENCES

[1] J. Narayan *Ceram. Eng. Sci. Proc.* **2013**, 33, 159-181.

[2] S. Barth, F. Hernandez-Ramirez, J. D. Holmes, A. Romano-Rodriguez *Prog. Mater. Sci.* **2010**, 55, 563-627.

[3] K. E. Ziemelis *Nature*. **2000**, 406, 1021-1021.

[4] R. D. Kamien *Science*. **2003**, 299, 1671, 1673.

[5] U. Schubert, N. Husing, G. Kickelbick *Berg- Huettenmaenn. Monatsh.* **2002**, 147, 268-272.

[6] J. B. Cohen, W. H. Archdeacon *J. Chem. Soc., Trans.* **1896**, 69, 91-96.

[7] G. P. Moss, P. A. S. Smith, D. Tavernier *Pure Appl. Chem.* **1995**, 67, 1307-1375.

[8] D. C. Bradley, R. C. Mehrotra, I. P. Rothwel, A. Singh, Alkoxo and Aryloxo Derivatives of Metals, Academic Press Inc, **2001**.

[9] C. J. Carmalt, S. J. King *Coord. Chem. Rev.* **2006**, 250, 682-709.

[10] P. T. Wolczanski *Polyhedron*. **1995**, 14, 3335-3362.

[11] N. C. Baird *Can. J. Chem.* **1969**, 47, 2306-2307.

[12] D. C. Bradley, R. C. Mehrotra, W. Wardlaw *J. Chem. Soc.* **1952**, 2027-2032.

[13] R. C. Mehrotra *Inorg. Chim. Acta, Rev.* **1967**, 1, 99-112.

[14] S. R. Bindal, V. K. Mathur, R. C. Mehrotra *J. Chem. Soc. A.* **1969**, 863-867.

[15] D. C. Bradley *Chem. Rev.* **1989**, 89, 1317-1322.

[16] A. F. Holleman, E. Wiberg, N. Wiberg, Lehrbuch der anorganischen Chemie, Walter de Gruyter & Co., Berlin, New York, **2007**.

[17] M. Czakler, C. Artner, U. Schubert *Monatsh. Chem.* **2015**, 146, 897-902.

[18] D. C. Bradley, R. C. Mehrotra, J. D. Swanwick, W. Wardaw *J. Chem. Soc.* **1953**, 2025-2030.

[19] D. C. Bradley, R. C. Mehrotra, W. Wardlaw *J. Chem. Soc.* **1952**, 4204-4209.

[20] D. C. Bradley, R. C. Mehrotra, W. Wardlaw *J. Chem. Soc.* **1952**, 5020-5023.

[21] S. Suh, D. M. Hoffman *J. Am. Chem. Soc.* **2000**, 122, 9396-9404.

[22] R. C. Mehrotra, A. Singh, S. Sogani *Chem. Rev.* **1994**, 94, 1643-1660.

[23] R. C. Mehrotra *J. Indian Chem. Soc.* **1953**, 30, 585-591.

[24] R. C. Mehrotra *J. Indian Chem. Soc.* **1954**, 31, 85-90.

[25] D. C. Bradley *Nature*. **1958**, 182, 1211-1214.

[26] R. C. Mehrotra, R. K. Mehrotra *Curr. Sci.* **1964**, 33, 241.

[27] M. Valet, D. M. Hoffman *Chem. Mater.* **2001**, 13, 2135-2143.

[28] R. C. Mehrotra, A. Singh *Prog. Inorg. Chem.* **1997**, 46, 239-454.

[29] M. Nabavi, S. Doeuff, C. Sanchez, J. Livage *J. Non-Cryst. Solids*. **1990**, 121, 31-34.

[30] R. Lichtenberger, U. Schubert *J. Mater. Chem.* **2010**, 20, 9287-9296.

[31] U. Schubert *J. Mater. Chem.* **2005**, 15, 3701-3715.

[32] W. G. Van der Sluys, A. P. Sattelberger *Chem. Rev.* **1990**, 90, 1027-1040.

[33] R. C. Mehrotra, A. Singh, S. Sogani *Chem. Soc. Rev.* **1994**, 23, 215-225.

[34] W. A. Herrmann, N. W. Huber, O. Runte *Angew. Chem., Int. Ed.* **1995**, 34, 2187-2206.

[35] B. A. Vaartstra, J. C. Huffman, P. S. Gradeff, L. G. Hubert-Pfalzgraf, J. C. Daran, S. Parraud, K. Yunlu, K. G. Caulton *Inorg. Chem.* **1990**, 29, 3126-3131.

[36] L. A. Miinea, D. M. Hoffman *J. Mater. Chem.* **2000**, 10, 2392-2395.

[37] L. G. Hubert-Pfalzgraf *Inorg. Chem. Commun.* **2003**, 6, 102-120.

[38] L. G. Hubert-Pfalzgraf *J. Mater. Chem.* **2004**, 14, 3113-3123.

[39] C. N. McMahon, S. J. Obrey, A. Keys, S. G. Bott, A. R. Barron *Dalton.* **2000**, 2151-2161.

[40] R. O. Bonsu, H. Kim, C. O'Donohue, R. Y. Korotkov, K. A. Abboud, T. J. Anderson, L. McElwee-White *Inorg. Chem.* **2015**, 54, 7536-7547.

[41] L. G. Hubert-Pfalzgraf *Coord. Chem. Rev.* **1998**, 178-180, 967-997.

[42] A. Devi *Coord. Chem. Rev.* **2013**, 257, 3332-3384.

[43] L. G. Hubert-Pfalzgraf, S. Daniele, J. M. Decams, J. Vaissermann *J. Sol-Gel Sci. Technol.* **1997**, 8, 49-53.

[44] M. Hellwig, K. Xu, D. Barreca, A. Gasparotto, M. Winter, E. Tondello, R. A. Fischer, A. Devi *Eur. J. Inorg. Chem.* **2009**, 2009, 1110-1117.

[45] S. J. Kim, V.-S. Dang, K. Xu, D. Barreca, C. Maccato, G. Carraro, R. K. Bhakta, M. Winter, H.-W. Becker, D. Rogalla, C. Sada, R. A. Fischer, A. Devi *Phys. Status Solidi A.* **2015**, 212, 1563-1570.

[46] L. G. Hubert-Pfalzgraf *Polyhedron.* **1994**, 13, 1181-1195.

[47] M. Bosund, K. Mizohata, T. Hakkarainen, M. Putkonen, M. Soederlund, S. Honkanen, H. Lipsanen *Appl. Surf. Sci.* **2009**, 256, 847-851.

[48] M. Coll, J. Gazquez, A. Palau, M. Varela, X. Obradors, T. Puig *Chem. Mater.* **2012**, 24, 3732-3737.

[49] A. C. Jones *J. Mater. Chem.* **2002**, 12, 2576-2590.

[50] S. Basharat, C. J. Carmalt, S. A. Barnett, D. A. Tocher, H. O. Davies *Inorg. Chem.* **2007**, 46, 9473-9480.

[51] S. Basharat, C. J. Carmalt, R. Binions, R. Palgrave, I. P. Parkin *Dalton Trans.* **2008**, 591-595.

[52] C. E. Knapp, G. Hyett, I. P. Parkin, C. J. Carmalt *Chem. Mater.* **2011**, 23, 1719-1726.

[53] A. L. Johnson, N. Hollingsworth, G. Kociok-Kohn, K. C. Molloy *Inorg. Chem.* **2008**, 47, 12040-12048.

[54] N. Hollingsworth, A. L. Johnson, A. Kingsley, G. Kociok-Kohn, K. C. Molloy *Organometallics.* **2010**, 29, 3318-3326.

[55] K. C. Molloy *J. Chem. Res.* **2008**, 549-554.

[56] H. S. Horowitz, S. J. McLain, A. W. Sleight, J. D. Druliner, P. L. Gai, M. J. VanKavelaar, J. L. Wagner, B. D. Biggs, S. J. Poon *Science.* **1989**, 243, 66-69.

[57] C. E. Knapp, D. Pugh, P. F. McMillan, I. P. Parkin, C. J. Carmalt *Inorg. Chem.* **2011**, 50, 9491-9498.

[58] A. A. Tahir, K. C. Molloy, M. Mazhar, G. Kociok-Koehn, M. Hamid, S. Dastgir *Inorg. Chem.* **2005**, 44, 9207-9212.

[59] G. A. Horley, G. Kociok-Koehn, K. C. Molloy, C. J. Rodriguez, S. Morreale *Z. Anorg. Allg. Chem.* **2012**, 638, 1699-1704.

[60] M. Shahid, A. A. Tahir, M. Hamid, M. Mazhar, M. Zeller, K. C. Molloy, A. D. Hunter *Eur. J. Inorg. Chem.* **2009**, 1043-1050.

[61] R. G. Pearson *J. Am. Chem. Soc.* **1963**, 85, 3533-3539.

[62] R. G. Pearson *Inorg. Chim. Acta.* **1995**, 240, 93-98.

[63] S. Woodward *Tetrahedron.* **2002**, 58, 1017-1050.

[64] P. B. Hitchcock, M. F. Lappert, I. A. MacKinnon *J. Chem. Soc., Chem. Commun.* **1988**, 1557-1558.

[65] A. W. G. Platt, P. G. Pringle *J. Chem. Soc., Dalton Trans.* **1989**, 1193-1196.

[66] P. Marchand, C. J. Carmalt *Coord. Chem. Rev.* **2013**, 257, 3202-3221.

[67] S. Basharat, C. E. Knapp, C. J. Carmalt, S. A. Barnett, D. A. Tocher *New J. Chem.* **2008**, 32, 1513-1518.

[68] C. E. Knapp, C. J. Carmalt, P. F. McMillan, D. A. Wann, H. E. Robertson, D. W. H. Rankin *Dalton Trans.* **2008**, 6880-6882.

[69] S. Basharat, C. J. Carmalt, R. Palgrave, S. A. Barnett, D. A. Tocher, H. O. Davies *J. Organomet. Chem.* **2008**, 693, 1787-1796.

[70] C. E. Knapp, D. A. Wann, A. Bil, J. T. Schirlin, H. E. Robertson, P. F. McMillan, D. W. H. Rankin, C. J. Carmalt *Inorg. Chem.* **2012**, 51, 3324-3331.

[71] A. L. Johnson, N. Hollingsworth, G. Kociok-Kohn, K. C. Molloy *Inorg. Chem.* **2008**, 47, 9706-9715.

[72] S. V. Pasko, L. G. Hubert-Pfalzgraf, A. Abrutis, P. Richard, A. Bartasyte, V. Kazlauskiene *J. Mater. Chem.* **2004**, 14, 1245-1251.

[73] W. A. Herrmann, N. W. Huber *Chemische Berichte.* **1994**, 127, 821-824.

[74] R. Anwander, F. C. Munck, T. Priermeier, W. Scherer, O. Runte, W. A. Herrmann *Inorg. Chem.* **1997**, 36, 3545-3552.

[75] R. C. Mehrotra *J. Non-Cryst. Solids.* **1988**, 100, 1-15.

[76] D. C. Bradley, Preperative Inorganic Reactions, Wiley, New York, **1965**.

[77] R. Reinmann, A. Tanner *Z. Naturforsch.* **1965**, 20b, 524-525.

[78] S. Chatterjee, S. R. Bindal, R. C. Mehrotra *J. Indian Chem. Soc.* **1976**, 53, 867-869.

[79] D. P. Gaur, G. Srivastava, R. C. Mehrotra *J. Organometal. Chem.* **1973**, 63, 221-231.

[80] D. Pugh, L. G. Bloor, I. P. Parkin, C. J. Carmalt *Chem. Eur. J.* **2012**, 18, 6079-6087.

[81] D. C. Bradley, E. V. Caldwell, W. Wardlaw *J. Chem. Soc.* **1957**, 4775-4776.

[82] D. C. Bradley, M. A. Saad, W. Wardlaw *J. Chem. Soc.* **1954**, 2002-2005.

[83] R. C. Mehrotra *J. Indian Chem. Soc.* **1955**, 32, 759-762.

[84] S. Halut-Desportes, M. Philoche-Levisalles *Acta Cryst. B.* **1978**, B34, 432-435.

[85] G. Jantsch, W. Urbach *Helv. Chim. Acta.* **1919**, 2, 490-500.

[86] U. D. Tripathi, J. M. Batwara, R. C. Mehrotra *J. Chem. Soc. A.* **1967**, 991-992.

[87] D. C. Bradley, R. K. Multani, W. Wardlaw *J. Chem. Soc.* **1958**, 4153-4155.

[88] I. Shiihara, W. T. Schwartz, Jr., H. W. Post *Chem. Rev.* **1961**, 61, 1-30.

[89] I. D. Varma, R. C. Mehrotra *J. Soc. Chem. (Resumed).* **1960**, 2966-2969.

[90] D. C. Bradley, M. J. Hillyer *Trans. Faraday Soc.* **1966**, 62, 2374-2381.

[91] D. C. Bradley, M. J. Hillyer *Trans. Faraday Soc.* **1966**, 62, 2367-2373.

[92] W. Wardlaw, D. C. Bradley *Nature*. **1950**, 165, 75-76.

[93] M. Lappert, P. Power, A. Protchenko, A. Seeber, Metal Amide Chemistry, John Wiley & Sons, Ltd, **2009**.

[94] M. Bochmann, G. Wilkinson, G. B. Young, M. B. Hursthouse, K. M. A. Malik *J. Chem. Soc., Dalton Trans.* **1980**, 901-910.

[95] I. M. Thomas *Can. J. Chem.* **1961**, 39, 1386-1389.

[96] M. H. Chisholm, V. F. DiStasi, W. E. Streib *Polyhedron*. **1990**, 9, 253-255.

[97] M. Veith *Adv. Organomet. Chem.* **1990**, 31, 269-300.

[98] D. C. Bradley, M. H. Chisholm *Acc. Chem. Res.* **1976**, 9, 273-280.

[99] M. Veith, S. Hill, V. Huch *Eur. J. Inorg. Chem.* **1999**, 1343-1350.

[100] K. G. Caulton, L. G. Hubert-Pfalzgraf *Chem. Rev.* **1990**, 90, 969-995.

[101] M. Veith, S. Mathur, C. Mathur *Polyhedron*. **1998**, 17, 1005-1034.

[102] L. G. Hubert-Pfalzgraf, V. G. Kessler, J. Vaissermann *Polyhedron*. **1997**, 16, 4197-4203.

[103] J. Hvoslef, H. Hope, B. D. Murray, P. P. Power *J. Chem. Soc., Chem. Commun.* **1983**, 1438-1439.

[104] M. F. Lappert, A. Singh, J. L. Atwood, W. E. Hunter *J. Chem. Soc., Chem. Commun.* **1981**, 1191-1193.

[105] M. Veith, M. Reimers *Chemische Berichte*. **1990**, 123, 1941-1944.

[106] D. J. Teff, J. C. Huffman, K. G. Caulton *Inorg. Chem.* **1995**, 34, 2491-2492.

[107] D. J. Teff, J. C. Huffman, K. G. Caulton *Inorg. Chem.* **1996**, 35, 2981-2987.

[108] S. Mathur, H. Shen, N. Lecerf, A. Kjekshus, H. Fjellvag, G. F. Goya *Adv. Mater.* **2002**, 14, 1405-1409.

[109] S. Mathur, M. Veith, H. Shen, S. Huefner, M. H. Jilavi *Chem. Mater.* **2002**, 14, 568-582.

[110] J. A. Meese-Marktscheffel, R. Weimann, H. Schumann, J. W. Gilje *Inorg. Chem.* **1993**, 32, 5894-5896.

[111] M. J. Hampden-Smith, D. S. Williams, A. L. Rheingold *Inorg. Chem.* **1990**, 29, 4076-4081.

[112] T. J. Boyle, D. C. Bradley, M. J. Hampden-Smith, A. Patel, J. W. Ziller *Inorg. Chem.* **1995**, 34, 5893-5899.

[113] M. Veith, K. Valtchev, V. Huch *Inorg. Chem.* **2008**, 47, 1204-1217.

[114] F. Labrize, L. G. Hubert-Pfalzgraf, J. Vaissermann, C. B. Knobler *Polyhedron*. **1996**, 15, 577-589.

[115] H. Guillon, L. G. Hubert-Pfalzgraf, J. Vaissermann *Eur. J. Inorg. Chem.* **2000**, 1243-1252.

[116] C. G. Screttas, B. R. Steele *Appl. Organomet. Chem.* **2000**, 14, 653-659.

[117] S. Yamasaki, M. Kanai, M. Shibasaki *Chem. - Eur. J.* **2001**, 7, 4066-4072.

[118] C. F. de Graauw, J. A. Peters, B. H. van, J. Huskens *Synthesis*. **1994**, 1007-1017.

[119] M. H. Chisholm, Z. Zhou *J. Mater. Chem.* **2004**, 14, 3081-3092.

[120] S. Dagorne, M. Normand, E. Kirillov, J.-F. Carpentier *Coord. Chem. Rev.* **2013**, 257, 1869-1886.

[121] S. M. Quan, P. L. Diaconescu *Chem. Commun.* **2015**.

[122] T. Tsukahara, D. C. Swenson, R. F. Jordan *Organometallics*. **1997**, 16, 3303-3313.

[123] J.-F. Carpentier *Dalton Trans.* **2010**, 39, 37-48.

[124] Y. Xu, X.-T. Yan, Chemical Vapour Deposition, Springer, London, **2010**.

[125] K. L. Choy, Handbook of Nanostructured Materials and Nanotechnology, Volume 1: Synthesis and Processing, Academic Press, San Diego (CA), **2000**.

[126] A. De Lodyguine Illuminant for incandescent lamps, Pat. No.: US 575002 A , **1897**.

[127] K. L. Choy *Prog. Mater. Sci.* **2003**, 48, 57-170.

[128] N. L. Jeon, W. Lin, M. K. Erhardt, G. S. Girolami, R. G. Nuzzo *Langmuir*. **1997**, 13, 3833-3838.

[129] C. Roger, T. S. Corbitt, M. J. Hampden-Smith, T. T. Kodas *Appl. Phys. Lett.* **1994**, 65, 1021-1023.

[130] S. Mathur, S. Barth *Small*. **2007**, 3, 2070-2075.

[131] S. Mathur, S. Barth, H. Shen, J.-C. Pyun, U. Werner *Small*. **2005**, 1, 713-717.

[132] N. D. Boscher, C. J. Carmalt, R. G. Palgrave, I. P. Parkin *Thin Solid Films*. **2008**, 516, 4750-4757.

[133] J. Cheon, J. E. Gozum, G. S. Girolami *Chem. Mater.* **1997**, 9, 1847-1853.

[134] R. Binions, C. J. Carmalt, I. P. Parkin, K. F. E. Pratt, G. A. Shaw *Chem. Mater.* **2004**, 16, 2489-2493.

[135] J. S. Wrench, K. Black, H. C. Aspinall, A. C. Jones, J. Bacsa, P. R. Chalker, P. J. King, M. Werner, H. O. Davies, P. N. Heys *Chem. Vap. Dep.* **2009**, 15, 259-261.

[136] D. A. Baxter, M. N. Chisolum, S. Doherty, N. E. Gruhn *Chem. Commun.* **1996**, 1129-1130.

[137] C. E. Knapp, P. Marchand, C. Dyer, I. P. Parkin, C. J. Carmalt *New J. Chem.* **2015**, 39, 6585-6592.

[138] S. Barth, M. S. Seifner, J. Bernardi *J. Mater. Chem. C.* **2014**, 2, 5747-5751.

[139] M. C. Johnson, S. Aloni, D. E. McCready, E. D. Bourret-Courchesne *Cryst. Growth Des.* **2006**, 6, 1936-1941.

[140] K. Van Nieuwenhuysen, F. Duerinckx, I. Kuzma, D. Van Gestel, G. Beaucarne, J. Poortmans *J. Cryst. Growth*. **2006**, 287, 438-441.

[141] T. Kuech, Handbook of Crystal Growth, Elsevier, **2014**.

[142] J. Zheng, R. Yang, L. Xie, J. Qu, Y. Liu, X. Li *Adv. Mater.* **2010**, 22, 1451-1473.

[143] M. J. Ludowise *J. Appl. Phys.* **1985**, 58, R31-R55.

[144] A. R. Barron *Adv. Mater. Opt. Electron.* **1995**, 5, 245-258.

[145] J. T. Zilko, Handbook of thin film deposition, Elsevier, **2012**.

[146] A. R. Barron, P.-T. Chiang, S. Gullapalli, C. E. Hamilton, J. Holden, C. Kelty, I. Kurganskaya, A. Luttge, A. Saha, C. Smith, R. Thaner, E. Whitsitt, B. Wilson, Chemistry of Electronic Materials, Rice University, Huston, Texas, **2011**.

[147] V. V. Srdic, M. Winterer *Chem. Mater.* **2003**, 15, 2668-2674.

[148] R. Djenadic, G. Akguel, K. Attenkofer, M. Winterer *J. Phys. Chem. C.* **2010**, 114, 9207-9215.

[149] H. O. Pierson, Handbook of Chemical Vapour Deposition, Elsevier, **1999**.

[150] N. O. Boadi, M. A. Malik, P. O'Brien, J. A. M. Awudza *Dalton Trans.* **2012**, 41, 10497-10506.

[151] D. Fan, M. Afzaal, M. A. Mallik, C. Q. Nguyen, P. O'Brien, P. J. Thomas *Coord. Chem. Rev.* **2007**, 251, 1878-1888.

[152] S. Mathur, M. Veith, T. Ruegamer, E. Hemmer, H. Shen *Chem. Mater.* **2004**, 16, 1304-1312.

[153] D. V. Shenai-Khatkhate, R. J. Goyette, R. L. DiCarlo Jr, G. Dripps *J. Cryst. Growth*. **2004**, 272, 816-821.

[154] C. Hahn, Z. Zhang, A. Fu, C. H. Wu, Y. J. Hwang, D. J. Gargas, P. Yang *ACS Nano*. **2011**, 5, 3970-3976.

[155] O. Danielsson, X. Li, L. Ojamae, E. Janzen, H. Pedersen, U. Forsberg *J. Mater. Chem. C*. **2016**, 4, 863-871.

[156] H. W. Kim, N. H. Kim *Appl. Phys. A: Mater. Sci. Process*. **2005**, 81, 763-765.

[157] S.-W. Chung, J.-Y. Yu, J. R. Heath *Appl. Phys. Lett*. **2000**, 76, 2068-2070.

[158] J. Wang, M. Pathak, X. Zhong, P. LeClair, T. M. Klein, A. Gupta *Thin Solid Films*. **2010**, 518, 6853-6857.

[159] F. Porrati, M. Pohlit, J. Müller, S. Barth, F. Biegger, C. Gspan, H. Plank, M. Huth *Nanotechnology*. **2015**, 26, 475701.

[160] L. McElwee-White *Dalton Trans*. **2006**, 5327-5333.

[161] A. Keys, S. G. Bott, A. R. Barron *Chem. Mater*. **1999**, 11, 3578-3587.

[162] S. Basharat, C. J. Carmalt, S. J. King, E. S. Peters, D. A. Tocher *Dalton Trans*. **2004**, 3475-3480.

[163] M. F. Mahon, K. C. Molloy, J. E. Stanley, D. W. H. Rankin, H. E. Robertson, B. F. Johnston *Appl. Organomet. Chem*. **2005**, 19, 658-671.

[164] G.-Y. Fang, L.-N. Xu, Y.-Q. Cao, L.-G. Wang, D. Wu, A.-D. Li *Chem. Commun*. **2015**, 51, 1341-1344.

[165] J. El Boucham, F. Maury, R. Morancho *J. Anal. Appl. Pyrolysis*. **1998**, 44, 153-165.

[166] Y. Suh, W. Chen, S. Maeng, S. Gu, R. A. Levy, H. Thridandam *Thin Solid Films*. **2010**, 518, 5452-5456.

[167] S. Shimada, Y. Takada, J. Tsujino *Surf. Coat. Technol*. **2005**, 199, 72-76.

[168] R. Gordon *J. Non-Cryst. Solids*. **1997**, 218, 81-91.

[169] C. E. Knapp, C. J. Carmalt *Chem. Soc. Rev*. **2016**, 45, 1036-1064.

[170] C. E. Knapp, A. Kafizas, I. P. Parkin, C. J. Carmalt *J. Mater. Chem*. **2011**, 21, 12644-12649.

[171] X. Hou, K.-L. Choy *Chem. Vap. Dep*. **2006**, 12, 583-596.

[172] P. O'Brien, N. L. Pickett, D. J. Otway *Chem. Vap. Dep*. **2002**, 8, 237-249.

[173] P. Marchand, I. A. Hassan, I. P. Parkin, C. J. Carmalt *Dalton Trans*. **2013**, 42, 9406-9422.

[174] F. E. Annanouch, S. Vallejos, T. Stoycheva, C. Blackman, E. Llobet *Thin Solid Films*. **2013**, 548, 703-709.

[175] C. Edusi, G. Sankar, I. P. Parkin *Chem. Vap. Dep*. **2012**, 18, 126-132.

[176] N. Hüsing, U. Schubert *Angew. Chem., Int. Ed*. **1998**, 37, 22-45.

[177] U. Schubert, N. Hüsing, Synthesis of Inorganic Materials, Wiley-VCH, Weinheim, **2012**.

[178] J. C. Brinker, G. W. Scherer, Sol-Gel Science The Physics and Chemistry of Sol-Gel Processing, Academic Press Inc. , Boston, **1990**.

[179] U. Schubert, N. Huesing, A. Lorenz *Chem. Mater*. **1995**, 7, 2010-2027.

[180] M. Lomoschitz, H. Peterlik, K. Zorn, S. O. Baumann, U. Schubert *J. Mater. Chem*. **2010**, 20, 5527-5532.

[181] C. Sanchez, J. Livage, M. Henry, F. Babonneau *J. Non-Cryst. Solids*. **1988**, 100, 65-76.

[182] S. Mishra, S. Daniele, S. Petit, E. Jeanneau, M. Rolland *Dalton Trans.* **2009**, 2569-2577.

[183] S. Abe, R. K. Capek, B. De Geyter, Z. Hens *ACS Nano*. **2013**, 7, 943-949.

[184] K. De Nolf, R. K. Capek, S. Abe, M. Sluydts, Y. Jang, J. C. Martins, S. Cottenier, E. Lifshitz, Z. Hens *J. Am. Chem. Soc.* **2015**, 137, 2495-2505.

[185] K. P. Acharya, E. Khon, T. O'Connor, I. Nemitz, A. Klinkova, R. S. Khnayzer, P. Anzenbacher, M. Zamkov *ACS Nano*. **2011**, 5, 4953-4964.

[186] B. H. Juarez, M. Meyns, A. Chanaewa, Y. Cai, C. Klinke, H. Weller *J. Am. Chem. Soc.* **2008**, 130, 15282-15284.

[187] E. T. Norton, Jr., C. Amato-Wierda *Chem. Mater.* **2001**, 13, 4655-4660.

[188] J. Lee, Y. S. Kim, T. Anderson *ECS Trans.* **2009**, 25, 41-49.

[189] Z. Mahmood, I. Hussain, R. E. Linney, D. K. Russell *J. Anal. Appl. Pyrolysis*. **1997**, 44, 29-48.

[190] W. Tumas, R. F. Foster, J. I. Brauman *J. Am. Chem. Soc.* **1988**, 110, 2714-2722.

[191] Y. K. Jung, J. I. Kim, J.-K. Lee *J. Am. Chem. Soc.* **2010**, 132, 178-184.

[192] M. Nandi, D. Rhubright, A. Sen *Inorg. Chem.* **1990**, 29, 3065-3066.

[193] E. F. Schubert, Doping in III-V Semiconductors, Cambridge University Press, **1993**.

[194] A. Chroneos, E. N. Sgourou, C. A. Londos, U. Schwingenschlogl *Appl. Phys. Rev.* **2015**, 2, 21306-21322.

[195] C. R. M. Grovenor, Microelectronic Materials, CRC Press, **1989**.

[196] S. Tiwari, S. L. Wright *Appl. Phys. Lett.* **1990**, 56, 563-565.

[197] R. Marschall, L. Wang *Catalysis Today*. **2014**, 225, 111-135.

[198] L. Mazeina, Y. N. Picard, S. I. Maximenko, F. K. Perkins, E. R. Glaser, M. E. Twigg, J. A. Freitas, Jr., S. M. Prokes *Cryst. Growth Des.* **2009**, 9, 4471-4479.

[199] I. Lopez, A. D. Utrilla, E. Nogales, B. Mendez, J. Piqueras, A. Peche, J. Ramirez-Castellanos, J. M. Gonzalez-Calbet *J. Phys. Chem. C.* **2012**, 116, 3935-3943.

[200] J. F. Shin, A. Orera, D. C. Apperley, P. R. Slater *J. Mater. Chem.* **2011**, 21, 874-879.

[201] T. W. Day, K. S. Weldert, W. G. Zeier, B.-R. Chen, S. L. Moffitt, U. Weis, K. P. Jochum, M. Panthöfer, M. J. Bedzyk, G. J. Snyder, W. Tremel *Chem. Mater.* **2015**, 27, 7018-7027.

[202] S. K. Pandey, S. Pandey, V. Parashar, R. S. Yadav, G. K. Mehrotra, A. C. Pandey *Nanoscale*. **2014**, 6, 1602-1606.

[203] E. M. Rockafellow, L. K. Stewart, W. S. Jenks *Appl. Catal., B.* **2009**, 91, 554-562.

[204] C. Persson, C. Platzer-Bjorkman, J. Malmstrom, T. Torndahl, M. Edoff *Phys. Rev. Lett.* **2006**, 97, 146403-146407.

[205] A. I. Kitaigorodsky, Mixed Crystals, Springer-Verlag Berlin Heidelberg, **1984**.

[206] E. Schur, E. Nauha, M. Lusi, J. Bernstein *Chem. - Eur. J.* **2015**, 21, 1735-1742.

[207] W. D. Callister Jr., Materials Science and Engineering: An Introduction John Wiley & Sons, **2006**.

[208] Z.-G. Lin, L.-C. Tang, C.-P. Chou *Inorg. Chem.* **2008**, 47, 2362-2367.

[209] S. Adachi, Properties of Aluminium Gallium Arsenide, IEE, INSPEC, **1993**.

[210] T. S. Kim, T. V. Cuong, C. S. Park, J. Y. Park, H. J. Lee, E. K. Suh, C. H. Hong *J. Korean Phys. Soc.* **2003**, 43, 758-761.

[211] T. S. Kim, T. V. Cuong, C. S. Park, J. Y. Park, H. J. Lee, E. K. Suh, C. H. Hong *J. Korean Phys. Soc.* **2003**, 43, 273-276.

[212] S. Barth, M. S. Seifner, J. Bernardi *Chem. Commun.* **2015**, 51, 12282-12285.

[213] M. S. Seifner, F. Biegger, A. Lugstein, J. Bernardi, S. Barth *Chem. Mater.* **2015**, 27, 6125-6130.

[214] H. Yamashita, M. Honda, M. Harada, Y. Ichihashi, M. Anpo, T. Hirao, N. Itoh, N. Iwamoto *J. Phys. Chem. B.* **1998**, 102, 10707-10711.

[215] B. Y. Geng, G. Z. Wang, Z. Jiang, T. Xie, S. H. Sun, G. W. Meng, L. D. Zhang *Appl. Phys. Lett.* **2003**, 82, 4791-4793.

[216] P. Qin, G. Fang, F. Cheng, W. Ke, H. Lei, H. Wang, X. Zhao *ACS Appl. Mater. Interfaces.* **2014**, 6, 2963-2973.

[217] H. Irie, Y. Watanabe, K. Hashimoto *J. Phys. Chem. B.* **2003**, 107, 5483-5486.

[218] G. Liu, L. Wang, C. Sun, X. Yan, X. Wang, Z. Chen, S. C. Smith, H.-M. Cheng, G. Q. Lu *Chem. Mater.* **2009**, 21, 1266-1274.

[219] C. Burda, Y. Lou, X. Chen, A. C. S. Samia, J. Stout, J. L. Gole *Nano Lett.* **2003**, 3, 1049-1051.

[220] C. Hebert, J. Perriere *Thin Solid Films.* **2014**, 553, 67-70.

[221] W. Tian, C. Zhi, T. Zhai, S. Chen, X. Wang, M. Liao, D. Golberg, Y. Bando *J. Mater. Chem.* **2012**, 22, 17984-17991.

[222] B. Opasanont, A. G. Kuba, E. G. Louderback, K. Roy Choudhury, J. B. Baxter *Chem. Mater.* **2014**, 26, 6674-6683.

[223] D. Lehr, M. Luka, M. R. Wagner, M. Bügler, A. Hoffmann, S. Polarz *Chem. Mater.* **2012**, 24, 1771-1778.

[224] A. V. G. Chizmeshya, C. Ritter, J. Tolle, C. Cook, J. Menendez, J. Kouvetakis *Chem. Mater.* **2006**, 18, 6266-6277.

[225] R. T. Beeler, G. J. Grzybowski, R. Roucka, L. Jiang, J. Mathews, D. J. Smith, J. Menéndez, A. V. G. Chizmeshya, J. Kouvetakis *Chem. Mater.* **2011**, 23, 4480-4486.

[226] H.-T. Chiu, C.-S. Shie, S.-H. Chuang *J. Mat. Res.* **1995**, 10, 2257-2259.

[227] K. C. Molloy, J. E. Stanley *Appl. Organomet. Chem.* **2009**, 23, 62-67.

[228] W. Klemm, H. U. v. Vogel *Z. Anorg. Allg. Chem.* **1934**, 219, 45-64.

[229] W. Klemm, I. Schnick *Z. Anorg. Allg. Chem.* **1936**, 226, 353-358.

[230] M. Zinkevich, F. Aldinger *J. Am. Ceram. Soc.* **2004**, 87, 683-691.

[231] H. Peelaers, C. G. Van de Walle *Phys. Status Solidi B.* **2015**, 252, 828-832.

[232] S. Yoshioka, H. Hayashi, A. Kuwabara, F. Oba, K. Matsunaga, I. Tanaka *J. Phys.: Condens. Matter.* **2007**, 19, 346211-346222.

[233] R. Roy, V. G. Hill, E. F. Osborn *J. Am. Chem. Soc.* **1952**, 74, 719-722.

[234] H. Y. Playford, A. C. Hannon, E. R. Barney, R. I. Walton *Chem. - Eur. J.* **2013**, 19, 2803-2813.

[235] F. Boschi, M. Bosi, T. Berzina, E. Buffagni, C. Ferrari, R. Fornari *J. Cryst. Growth.* **2016**, 443, 25-30.

[236] J. Ahman, G. Svensson, J. Albertsson *Acta Cryst. C.* **1996**, 52, 1336-1338.

[237] L. Binet, D. Gourier *J. Phys. Chem. Solids.* **1998**, 59, 1241-1249.

[238] G. Wang, J. Park, X. Kong, P. R. Wilson, Z. Chen, J.-h. Ahn *Cryst. Growth Des.* **2008**, 8, 1940-1944.

[239] M. Ogita, K. Higo, Y. Nakanishi, Y. Hatanaka *Appl. Surf. Sci.* **2001**, 175-176, 721-725.

[240] K. Matsuzaki, H. Hiramatsu, K. Nomura, H. Yanagi, T. Kamiya, M. Hirano, H. Hosono *Thin Solid Films.* **2005**, 496, 37-41.

[241] T. Miyata, T. Nakatani, T. Minami *Thin Solid Films.* **2000**, 373, 145-149.

[242] J. Hao, M. Cocivera *J. Phys. D: Appl. Phys.* **2002**, 35, 433-438.

[243] X. Chen, K. Liu, Z. Zhang, C. Wang, B. Li, H. Zhao, D. Zhao, D. Shen *ACS Appl. Mater. Interfaces.* **2016**, 8, 4185-4191.

[244] P. Ravadgar, R.-H. Horng, S.-D. Yao, H.-Y. Lee, B.-R. Wu, S.-L. Ou, L.-W. Tu *Opt. Express.* **2013**, 21, 24599-24611.

[245] M. Zhong, Z. Wei, X. Meng, F. Wu, J. Li *J. Alloys Compd.* **2015**, 619, 572-575.

[246] M. Bartic *Phys. Status Solidi A.* **2016**, 213, 457-462.

[247] M. Fleischer, H. Meixner *Sens. Actuators, B.* **1995**, B26, 81-84.

[248] T. Schwebel, M. Fleischer, H. Meixner, C. D. Kohl *Sens. Actuators, B.* **1998**, B49, 46-51.

[249] R. Binions, C. J. Carmalt, I. P. Parkin *Meas. Sci. Technol.* **2007**, 18, 190-200.

[250] A. L. Petre, A. Auroux, P. Gelin, M. Caldararu, N. I. Ionescu *Thermochim. Acta.* **2001**, 379, 177-185.

[251] S. Jin, X. Wang, X. Wang, M. Ju, S. Shen, W. Liang, Y. Zhao, Z. Feng, H. Y. Playford, R. I. Walton, C. Li *J. Phys. Chem. C.* **2015**, 119, 18221-18228.

[252] X. Wang, Q. Xu, M. Li, S. Shen, X. Wang, Y. Wang, Z. Feng, J. Shi, H. Han, C. Li *Angew. Chem., Int. Ed.* **2012**, 51, 13089-13092.

[253] P. O'Brien, R. Nomura *J. Mater. Chem.* **1995**, 5, 1761-1773.

[254] H. J. Queisser, E. E. Haller *Science.* **1998**, 281, 945-950.

[255] L. Miinea, S. Suh, S. G. Bott, J.-R. Liu, W.-K. Chu, D. M. Hoffman *J. Mater. Chem.* **1999**, 9, 929-935.

[256] Y. Chi, T.-Y. Chou, Y.-J. Wang, S.-F. Huang, A. J. Carty, L. Scoles, K. A. Udachin, S.-M. Peng, G.-H. Lee *Organometallics.* **2004**, 23, 95-103.

[257] F. Zhu, Z. Yang, W. Zhou, Y. Zhang *Appl. Surf. Sci.* **2006**, 252, 7930-7933.

[258] L. Cao, M. K. Li, Z. Yang, Q. Wei, W. Zhang *Appl. Phys. A: Mater. Sci. Process.* **2008**, 91, 415-419.

[259] N. C. Oldham, C. J. Hill, C. M. Garland, T. C. McGill *J. Vac. Sci. Technol., A.* **2002**, 20, 809-813.

[260] M. Orita, H. Hiramatsu, H. Ohta, M. Hirano, H. Hosono *Thin Solid Films.* **2002**, 411, 134-139.

[261] H. Lee, K. Kim, J.-J. Woo, D.-J. Jun, Y. Park, Y. Kim, H. W. Lee, Y. J. Cho, H. M. Cho *Chem. Vap. Dep.* **2011**, 17, 191-197.

[262] D. J. Comstock, J. W. Elam *Chem. Mater.* **2012**, 24, 4011-4018.

[263] D.-w. Choi, K.-B. Chung, J.-S. Park *Thin Solid Films.* **2013**, 546, 31-34.

[264] A. Ortiz, J. C. Alonso, E. Andrade, C. Urbiola *J. Electrochem. Soc.* **2001**, 148, F26-F29.

[265] R. Lorenzi, A. Paleari, N. V. Golubev, E. S. Ignat'eva, V. N. Sigaev, M. Niederberger, A. Lauria *J. Mater. Chem. C.* **2015**, 3, 41-45.

[266] B. Bonnetot, V. Rakic, T. Yuzhakova, C. Guimon, A. Auroux *Chem. Mater.* **2008**, 20, 1585-1596.

[267] S. Rafique, L. Han, C. A. Zorman, H. Zhao *Cryst. Growth Des.* **2016**, 16, 511-517.

[268] D. Pugh, P. Marchand, I. P. Parkin, C. J. Carmalt *Inorg. Chem.* **2012**, 51, 6385-6395.

[269] H. Schumann, S. Dechert, F. Girgsdies, B. Heymer, M. Hummert, J. Y. Hyeon, J. Kaufmann, S. Schutte, S. Wernik, B. C. Wassermann *Z. Anorg. Allg. Chem.* **2006**, 632, 251-263.

[270] S. Basharat, W. Betchley, C. J. Carmalt, S. Barnett, D. A. Tocher, H. O. Davies *Organometallics*. **2007**, 26, 403-407.

[271] C. E. Knapp, Ph.D. Dissertation, University College London, **2010**.

[272] L. G. Bloor, C. J. Carmalt, D. Pugh *Coord. Chem. Rev.* **2011**, 255, 1293-1318.

[273] A. Brukl, G. Ortner *Monatsh. Chem.* **1930**, 56, 358-364.

[274] W. Johnson, B. Warren *Naturwissenschaften*. **1930**, 18, 666-666.

[275] A. Kuhn, A. Chevy, R. Chevalier *Acta Cryst. B.* **1976**, B32, 983-984.

[276] A. Rizzo, C. De Blasi, S. Galassini, G. Micocci, L. Ruggiero, A. Tepore *Solid State Commun.* **1981**, 40, 641-644.

[277] T. Aono, K. Kase, A. Kinoshita *J. Appl. Phys.* **1993**, 74, 2818-2820.

[278] E. Aulich, J. L. Brebner, E. Mooser *Phys. Status Solidi*. **1969**, 31, 129-131.

[279] P. Hu, L. Wang, M. Yoon, J. Zhang, W. Feng, X. Wang, Z. Wen, J. C. Idrobo, Y. Miyamoto, D. B. Geohegan, K. Xiao *Nano Lett.* **2013**, 13, 1649-1654.

[280] D. J. Late, B. Liu, J. Luo, A. Yan, H. S. S. R. Matte, M. Grayson, C. N. R. Rao, V. P. Dravid *Adv. Mater.* **2012**, 24, 3549-3554.

[281] A. N. MacInnes, M. B. Power, A. R. Barron *Chem. Mater.* **1993**, 5, 1344-1351.

[282] A. N. MacInnes, M. B. Power, A. R. Barron *Chem. Mater.* **1992**, 4, 11-14.

[283] M. P. Pardo, A. Tomas, M. Guittard *Mater. Res. Bull.* **1987**, 22, 1677-1684.

[284] A. Tomas, M. P. Pardo, M. Guittard, M. Guymont, R. Famery *Mater. Res. Bull.* **1987**, 22, 1549-1554.

[285] T. C. Deivaraj, M. Lin, K. P. Loh, M. Yeadon, J. J. Vittal *J. Mater. Chem.* **2003**, 13, 1149-1155.

[286] H. F. Liu, K. K. A. Antwi, N. L. Yakovlev, H. R. Tan, L. T. Ong, S. J. Chua, D. Z. Chi *ACS Appl. Mater. Interfaces*. **2014**, 6, 3501-3507.

[287] C.-S. Yoon, F. D. Medina, L. Martinez, T.-Y. Park, M.-S. Jin, W.-T. Kim *Appl. Phys. Lett.* **2003**, 83, 1947-1949.

[288] T. Aono, K. Kase *Solid State Commun.* **1992**, 83, 749-752.

[289] T. Aono, K. Kase *Solid State Commun.* **1992**, 81, 303-305.

[290] A. Weber, I. Kötschau, H. W. Schock *Thin Solid Films*. **2007**, 515, 6252-6255.

[291] Y. Zhang, C. Chen, C. Y. Liang, Z. W. Liu, Y. S. Li, R. Che *Nanoscale*. **2015**, 7, 17381-17386.

[292] M. Zervos, A. Othonos, V. Gianneta, A. Travlos, A. G. Nassiopoulou *J. Appl. Phys.* **2015**, 118, 194302/194301-194302/194306.

[293] A. Brehault, L. Calvez, P. Adam, J. Rollin, M. Cathelinaud, B. Fan, O. Merdrignac-Conanec, T. Pain, X.-H. Zhang *J. Non-Cryst. Solids*. **2016**, 431, 25-30.

[294] A. Brehault, S. Cozic, R. Boidin, L. Calvez, E. Bychkov, P. Masselin, X. Zhang, D. Le Coq *J. Solid State Chem.* **2014**, 220, 238-244.

[295] C. Lu, H. Guo, Y. Xu, C. Hou, M. Lu, X. He, P. Wang, W. Li, B. Peng *Mater. Res. Bull.* **2014**, 60, 391-396.

[296] J. Ren, Q. Yan, T. Wagner, V. Zima, M. Frumar, B. Frumarova, G. Chen *J. Appl. Phys.* **2013**, 114, 023701.

[297] H.-C. Chiu, Y.-C. Huang, L.-B. Chang, F.-T. Chien *Semicond. Sci. Technol.* **2008**, 23, 35029-35034.

[298] G. Collin, J. Flahaut, M. Guittard, A. M. Loireau-Lozach *Mater. Res. Bull.* **1976**, 11, 285-292.

[299] X. Meng, J. A. Libera, T. T. Fister, H. Zhou, J. K. Hedlund, P. Fenter, J. W. Elam *Chem. Mater.* **2014**, 26, 1029-1039.

[300] M. Lazell, P. O'Brien, D. J. Otway, J.-H. Park *J. Chem. Soc., Dalton Trans.* **2000**, 4479-4486.

[301] M. R. Lazell, P. O'Brien, D. J. Otway, J.-H. Park *Chem. Mater.* **1999**, 11, 3430-3432.

[302] B. F. Hoskins, E. R. T. Tiekink, R. Vecchiet, G. Winter *Inorg. Chim. Acta.* **1984**, 90, 197-200.

[303] S. Ghoshal, V. K. Jain *J. Chem. Sci.* **2007**, 119, 583-591.

[304] P. Kostka, J. Zavadil, M. S. Iovu, Z. G. Ivanova, D. Furniss, A. B. Seddon *J. Alloys Compd.* **2015**, 648, 237-243.

[305] L. Petit, J. Abel, T. Anderson, J. Choi, V. Nazabal, V. Moizan, M. Couzi, M. Richardson, C. Maurel, T. Cardinal, K. Richardson *J. Solid State Chem.* **2009**, 182, 2646-2655.

[306] R. Zhang, Y. Liu, J. Ren, G. Chen *J. Non-Cryst. Solids.* **2013**, 362, 30-33.

[307] K. M. Othonos, M. Zervos, C. Christofides, A. Othonos *Nanoscale Res. Lett.* **2015**, 10, 1-7.

[308] J. S. Kim, S. B. Lee, J. H. Bahng, J. C. Choi, H. L. Park, S. I. Mho, T. W. Kim, Y. H. Whang, G. C. Kim *Phys. Status Solidi A.* **2001**, 187, 569-573.

[309] J. S. Kim, S. B. Lee, S. H. Sue, H. I. Kang, M. Lee, J. H. Bahng, J. C. Choi, H. I. Park, S. I. Mho, T. W. Kim, Y. H. Whang, J. H. Chang, B. K. Moon, G. C. Kim, J. W. Moon, H. S. Moon *J. Mater. Sci. Lett.* **2001**, 20, 2211-2212.

[310] A. Thiel, H. Luckmann *Z. Anorg. Allg. Chem.* **1928**, 172, 353-371.

[311] W. H. Zachariasen *Skrifter Norske Videnskaps Akad. Oslo. I, Matemat. Naturv. Klasse.* **1928**, 7-165.

[312] M. Marezio *Acta Crystallogr.* **1966**, 20, 723-728.

[313] C. T. Prewitt, R. D. Shannon, D. B. Rogers, A. W. Sleight *Inorg. Chem.* **1969**, 8, 1985-1993.

[314] A. N. Christensen, N. C. Boch, O. von Heidenstamm, A. Nilsson *Acta Chemica Scandinavica.* **1967**, 21, 1046-1056.

[315] D. Liu, W. Lei, S. Qin, L. Hou, Z. Liu, Q. Cui, Y. Chen *J. Mater. Chem. A.* **2013**, 1, 5274-5278.

[316] C. Y. Wang, V. Cimalla, H. Romanus, T. Kups, G. Ecke, T. Stauden, M. Ali, V. Lebedev, J. Pezoldt, O. Ambacher *Appl. Phys. Lett.* **2006**, 89, 11904-11907.

[317] C. A. Pan, T. P. Ma *Appl. Phys. Lett.* **1980**, 37, 163-165.

[318] P. D. C. King, T. D. Veal, F. Fuchs, C. Y. Wang, D. J. Payne, A. Bourlange, H. Zhang, G. R. Bell, V. Cimalla, O. Ambacher, R. G. Egdell, F. Bechstedt, C. F. McConville *Phys. Rev. B.* **2009**, 79, 205211.

[319] F. Fuchs, F. Bechstedt *Phys. Rev. B: Condens. Matter Mater. Phys.* **2008**, 77, 155107-155117.

[320] A. Walsh, J. L. F. Da Silva, S.-H. Wei, C. Körber, A. Klein, L. F. J. Piper, A. DeMasi, K. E. Smith, G. Panaccione, P. Torelli, D. J. Payne, A. Bourlange, R. G. Egdell *Phys. Rev. Lett.* **2008**, 100, 167402.

[321] S. Lany, A. Zunger *Phys. Rev. Lett.* **2007**, 98, 045501-045505.

[322] S. Lany, A. Zakutayev, T. O. Mason, J. F. Wager, K. R. Poeppelmeier, J. D. Perkins, J. J. Berry, D. S. Ginley, A. Zunger *Phys. Rev. Lett.* **2012**, 108, 16802-16807.

[323] P. D. C. King, T. D. Veal, D. J. Payne, A. Bourlange, R. G. Egdell, C. F. McConville *Phys Rev Lett.* **2008**, 101, 116808.

[324] H. Ohta, K. Nomura, H. Hiramatsu, K. Ueda, T. Kamiya, M. Hirano, H. Hosono *Solid-State Electronics.* **2003**, 47, 2261-2267.

[325] A. Cirpan, F. E. Karasz *J. Appl. Polym. Sci.* **2006**, 99, 3125-3129.

[326] K. Samedov, Y. Aksu, M. Driess *Chem. Mater.* **2012**, 24, 2078-2090.

[327] C. G. Granqvist *Appl. Phys. A.* **1993**, A57, 19-24.

[328] C. C. Wu, C. I. Wu, J. C. Sturm, A. Kahn *Appl. Phys. Lett.* **1997**, 70, 1348-1350.

[329] B. J. Luff, J. S. Wilkinson, G. Perrone *Appl. Opt.* **1997**, 36, 7066-7072.

[330] G. Domenech-Gil, J. Sama, P. Pellegrino, S. Barth, I. Gracia, C. Cane, A. Romano-Rodriguez *Procedia Eng.* **2015**, 120, 795-798.

[331] T.-Y. Chou, Y. Chi, S.-F. Huang, C.-S. Liu, A. J. Carty, L. Scoles, K. A. Udachin *Inorg. Chem.* **2003**, 42, 6041-6049.

[332] L.-J. Meng, M. P. dos Santos *Thin Solid Films.* **1998**, 322, 56-62.

[333] M. Nistor, W. Seiler, C. Hebert, E. Matei, J. Perriere *Appl. Surf. Sci.* **2014**, 307, 455-460.

[334] W. J. Maeng, D.-w. Choi, K.-B. Chung, W. Koh, G.-Y. Kim, S.-Y. Choi, J.-S. Park *ACS Appl. Mater. Interfaces.* **2014**, 6, 17481-17488.

[335] M. Gebhard, M. Hellwig, H. Parala, K. Xu, M. Winter, A. Devi *Dalton Trans.* **2014**, 43, 937-940.

[336] J. A. Libera, J. N. Hryn, J. W. Elam *Chem. Mater.* **2011**, 23, 2150-2158.

[337] V. Craciun, D. Craciun, X. Wang, T. J. Anderson, R. K. Singh *Thin Solid Films.* **2004**, 453-454, 256-261.

[338] R. Nomura, A. Moritake, K. Kanaya, H. Matsuda *Thin Solid Films.* **1988**, 167, L27-L29.

[339] M. Toki, M. Aizawa *J. Sol-Gel Sci. Technol.* **1997**, 8, 717-720.

[340] M. J. Alam, D. C. Cameron *Thin Solid Films.* **2002**, 420-421, 76-82.

[341] M. Veith, C. Bubel, M. Zimmer *Dalton Trans.* **2011**, 40, 6028-6032.

[342] S.-Y. Han, G. S. Herman, C.-h. Chang *J. Am. Chem. Soc.* **2011**, 133, 5166-5169.

[343] D. Pugh, L. G. Bloor, S. Sathasivam, I. P. Parkin, C. J. Carmalt *Eur. J. Inorg. Chem.* **2011**, 1953-1960.

[344] W. J. Duffin, J. H. C. Hogg *Acta Crystallogr.* **1966**, 20, 566-569.

[345] K. Schubert, E. Dörre, E. Günzel *Naturwissenschaften.* **1954**, 41, 448-448.

[346] R. Walther, H. J. Deiseroth *Z. Kristallogr.* **1995**, 210, 360.

[347] A. N. MacInnes, W. M. Cleaver, A. R. Barron, M. B. Power, A. F. Hepp *Adv. Mater. Opt. Electron.* **1992**, 1, 229-233.

[348] R. Iyer, R. R. Chang, D. L. Lile *Appl. Phys. Lett.* **1988**, 53, 134-136.

[349] A. M. A. Haleem, M. Ichimura *Jap. J. Appl. Phys.* **2009**, 48, 035506.

[350] G. A. Steigmann, H. H. Sutherland, J. Goodyear *Acta Crystallogr.* **1965**, 19, 967-971.

[351] H. Hahn, W. Klingler *Z. anorg. Chem.* **1949**, 260, 97-109.

[352] A. Likforman, M. Guittard, A. Tomas, J. Flahaut *J. Solid State Chem.* **1980**, 34, 353-359.

[353] K. J. Range, M. Zabel *Z. Naturforsch., B: Anorg. Chem., Org. Chem.* **1978**, 33B, 463-464.

[354] P. Buck *J. Appl.Cryst.* **1973**, 6, 1-8.

[355] X. Lai, F. Zhu, Y. Wu, R. Huang, X. Wu, Q. Zhang, K. Yang, S. Qin *J. Solid State Chem.* **2014**, 210, 155-159.

[356] W. Rehwald, G. Harbeke *J. Phys. Chem. Solids.* **1965**, 26, 1309-1324.

[357] R. S. Becker, T. Zheng, J. Elton, M. Saeki *Sol. Energy Mater.* **1986**, 13, 97-107.

[358] Y. Yasaki, N. Sonoyama, T. Sakata *J. Electroanal. Chem.* **1999**, 469, 116-122.

[359] N. Naghavi, S. Spiering, M. Powalla, B. Cavana, D. Lincot *Prog. Photovoltaics.* **2003**, 11, 437-443.

[360] T. T. John, M. Mathew, C. S. Kartha, K. P. Vijayakumar, T. Abe, Y. Kashiwaba *Sol. Energy Mater. Sol. Cells.* **2005**, 89, 27-36.

[361] S. Spiering, L. Bürkert, D. Hariskos, M. Powalla, B. Dimmler, C. Giesen, M. Heuken *Thin Solid Films.* **2009**, 517, 2328-2331.

[362] X. Xie, G. Shen *Nanoscale.* **2015**, 7, 5046-5052.

[363] R. Diehl, R. Nitsche *J. Cryst. Growth.* **1975**, 28, 306-310.

[364] P. N. Kumta, P. P. Phule, S. H. Risbud *Mater. Lett.* **1987**, 5, 401-404.

[365] A. Goswami, G. D. Talele, S. B. Badachhape *Indian J. Pure Appl. Phys.* **1976**, 14, 716-719.

[366] A. Datta, G. Sinha, S. K. Panda, A. Patra *Cryst. Growth Des.* **2009**, 9, 427-431.

[367] R. Nomura, S. Inazawa, K. Kanaya, H. Matsuda *Appl. Organomet. Chem.* **1989**, 3, 195-197.

[368] A. N. MacInnes, M. B. Power, A. F. Hepp, A. R. Barron *J. Organomet. Chem.* **1993**, 449, 95-104.

[369] M. A. M. Seyam *Vacuum.* **2001**, 63, 441-447.

[370] A. Timoumi, H. Bouzouita, M. Kanzari, B. Rezig *Thin Solid Films.* **2005**, 480-481, 124-128.

[371] J. George, K. S. Joseph, B. Pradeep, T. I. Palson *Phys. Status Solidi A.* **1988**, 106, 123-131.

[372] P. O'Brien, D. J. Otway, J. R. Walsh *Thin Solid Films.* **1998**, 315, 57-61.

[373] R. Nomura, K. Konishi, H. Matsuda *Thin Solid Films.* **1991**, 198, 339-345.

[374] R. Nomura, K. Konishi, S. Futenma, H. Matsuda *Appl. Organomet. Chem.* **1990**, 4, 607-610.

[375] W. T. Kim, C. D. Kim *J. Appl. Phys.* **1986**, 60, 2631-2633.

[376] M. Amlouk, M. A. B. Said, N. Kamoun, S. Belgacem, N. Brunet, D. Barjon *Jpn. J. Appl. Phys., Part 1.* **1999**, 38, 26-30.

[377] N. Naghavi, R. Henriquez, V. Laptev, D. Lincot *Appl. Surf. Sci.* **2004**, 222, 65-73.

[378] T. Asikainen, M. Ritala, M. Leskelae *Appl. Surf. Sci.* **1994**, 82/83, 122-125.

[379] C. D. Lokhande, A. Ennaoui, P. S. Patil, M. Giersig, K. Diesner, M. Muller, H. Tributsch *Thin Solid Films.* **1999**, 340, 18-23.

[380] T. Yoshida, K. Yamaguchi, H. Toyoda, K. Akao, T. Sugiura, H. Minoura, Y. Nosaka *Proc. - Electrochem. Soc.* **1997**, 97-20, 37-57.

[381] M. Zervos, P. Papageorgiou, A. Othonos *J. Cryst. Growth.* **2010**, 312, 656-661.

[382] G. Shang, K. Kunze, M. J. Hampden-Smith, E. N. Duesler *Chem. Vap. Dep.* **1996**, 2, 242-244.

[383] S. Ghoshal, N. P. Kushwah, M. K. Pal, V. K. Jain, M. Nethaji *J. Chem. Sci.* **2008**, 120, 305-308.

[384] V. G. Bessdergenev, E. N. Ivanova, Y. A. Kovalevskaya, S. A. Gromilov, V. N. Kirichenko, S. V. Larionov *Inorg. Mater.* **1996**, 32, 592-596.

[385] D. Hariskos, M. Ruckh, U. Ruehle, T. Walter, H. W. Schock, J. Hedstroem, L. Stolt *Sol. Energy Mater. Sol. Cells.* **1996**, 41/42, 345-353.

[386] N. Barreau, S. Marsillac, D. Albertini, J. C. Bernede *Thin Solid Films.* **2002**, 403–404, 331-334.

[387] A. Gantassi, H. Essaidi, K. Boubaker, J. C. Bernède, A. Colantoni, M. Amlouk, T. Manoubi *Mat. Sci. Sem. Proc.* **2014**, 24, 237-246.

[388] M. Zervos, A. Othonos, V. Gianetta, A. G. Nassiopoulou *Mater. Lett.* **2016**, 166, 129-132.

[389] R. Nomura, K. Konishi, H. Matsuda *J. Electrochem. Soc.* **1991**, 138, 631-632.

[390] R. Bayón, C. Maffiotte, J. Herrero *Thin Solid Films.* **1999**, 353, 100-107.

[391] R. Bayón, J. Herrero *Appl. Surf. Sci.* **2000**, 158, 49-57.

[392] R. Bayon, J. Herrero *Thin Solid Films.* **2001**, 387, 111-114.

[393] A. M. A. Haleem, M. Ichimura *Thin Solid Films.* **2008**, 516, 7783-7789.

[394] A. M. A. Haleem, M. Ichimura *J. Appl. Phys.* **2010**, 107, 034507-034513.

[395] A. M. A. Haleem, M. Sugiyama, M. Ichimura *Mater. Sci. Appl.* **2012**, 3, 802-806.

[396] N. Barreau, S. Marsillac, J. C. Bernede *Vacuum.* **2000**, 56, 101-106.

[397] N. Barreau, J. C. Bernède, H. El Maliki, S. Marsillac, X. Castel, J. Pinel *Solid State Comm.* **2002**, 122, 445-450.

[398] N. Barreau, J. C. Bernède, S. Marsillac, A. Mokrani *J. Crystal Growth.* **2002**, 235, 439-449.

[399] N. Barreau, S. Marsillac, J. C. Bernede, L. Assmann *J. Appl. Phys.* **2003**, 93, 5456-5459.

[400] R. Robles, N. Barreau, A. Vega, S. Marsillac, J. C. Bernède, A. Mokrani *Opt. Mater.* **2005**, 27, 647-653.

[401] C. Bugot, N. Schneider, D. Lincot, F. Donsanti *Beilstein J. Nanotechnol.* **2013**, 4, 750-757.

[402] C. Bugot, N. Schneider, M. Bouttemy, A. Etcheberry, D. Lincot, F. Donsanti *Thin Solid Films.* **2015**, 582, 340-344.

[403] F. Machatschki *Z. Kristallogr., Kristallgeom., Kristallphys., Kristallchem.* **1931**, 80, 416-427.

[404] E. Riedel, C. Janiak, Anorganische Chemie, de Gruyter, Berlin, Boston, **2011**.

[405] G. A. Petrakovskii, K. S. Aleksandrov, L. N. Bezmaternikh, S. S. Aplesnin, B. Roessli, F. Semadeni, A. Amato, C. Baines, J. Bartolome, M. Evangelisti *Phys. Rev. B: Condens. Matter Mater. Phys.* **2001**, 63, 184425-184433.

[406] P. F. Ndione, Y. Shi, V. Stevanovic, S. Lany, A. Zakutayev, P. A. Parilla, J. D. Perkins, J. J. Berry, D. S. Ginley, M. F. Toney *Adv. Funct. Mater.* **2014**, 24, 610-618.

[407] D. Ko, K. R. Poeppelmeier, D. R. Kammler, G. B. Gonzalez, T. O. Mason, D. L. Williamson, D. L. Young, T. J. Coutts *J. solid state chem.* **2002**, 163, 259-266.

[408] K. Petrov, L. Markov, R. Ioncheva, P. Rachev *J. Mat. Sci.* **1988**, 23, 181-184.

[409] C. Li, X. Han, F. Cheng, Y. Hu, C. Chen, J. Chen *Nat. Commun.* **2015**, 6, 7345.

[410] T. R. Paudel, A. Zakutayev, S. Lany, M. d'Avezac, A. Zunger *Adv. Funct. Mater.* **2011**, 21, 4493-4501.

[411] C.-C. Huang, C.-H. Su, M.-Y. Liao, C.-S. Yeh *Phys. Chem. Chem. Phys.* **2009**, 11, 6331-6334.

[412] Y. Yamasaki, S. Miyasaka, Y. Kaneko, J. P. He, T. Arima, Y. Tokura *Phys. Rev. Lett.* **2006**, 96, 207204-207208.

[413] S. Pongpadung, T. Kamwanna, V. Amornkitbamrung *J. Korean Phys. Soc.* **2016**, 68, 697-704.

[414] V. Zviagin, Y. Kumar, I. Lorite, P. Esquinazi, M. Grundmann, R. Schmidt-Grund *Appl. Phys. Lett.* **2016**, 108, 131901-131905.

[415] Y. Yuan, J. Huang, W. Tu, S. Huang *J. Alloys Compd.* **2014**, 616, 461-467.

[416] V. B. R. Boppana, R. F. Lobo *ACS Catal.* **2011**, 1, 923-928.

[417] K. Faungnawakij, N. Shimoda, T. Fukunaga, R. Kikuchi, K. Eguchi *Appl. Catal., A.* **2008**, 341, 139-145.

[418] J. R. Scheffe, J. Li, A. W. Weimer *Int. J. Hydrogen Energy.* **2010**, 35, 3333-3340.

[419] K. M. Yu, W. Tong, A. West, K. Cheung, T. Li, G. Smith, Y. Guo, S. C. Tsang *Nat Commun.* **2012**, 3, 1230.

[420] S. C. Yan, S. X. Ouyang, J. Gao, M. Yang, J. Y. Feng, X. X. Fan, L. J. Wan, Z. S. Li, J. H. Ye, Y. Zhou, Z. G. Zou *Angew. Chem., Int. Ed.* **2010**, 49, 6400-6404.

[421] S.-X. Zhou, X.-J. Lv, C. Zhang, X. Huang, L. Kang, Z.-s. Lin, Y. Chen, W.-F. Fu *ChemPlusChem.* **2015**, 80, 223-230.

[422] X.-J. Lv, S. Zhou, X. Huang, C. Wang, W.-F. Fu *Appl. Cat. B.* **2016**, 182, 220-228.

[423] W. Laqua *Z. Anorg. Allg. Chem.* **1976**, 426, 53-65.

[424] W. T. Jeong, J. H. Joo, K. S. Lee *J. Power Sources.* **2003**, 119-121, 690-694.

[425] J. E. Baker, R. Bruch, Y. Niu *Appl. Catal.* **1991**, 73, 135-152.

[426] M. Veith, S. Mathur, H. Shen, N. Lecerf, S. Huefner, M. H. Jilavi *Chem. Mater.* **2001**, 13, 4041-4052.

[427] S. Daniele, D. Tcheboukov, L. G. H. Pfalzgraf *J. Mater. Chem.* **2002**, 12, 2519-2524.

[428] H. Xue, Z. Li, Z. Ding, L. Wu, X. Wang, X. Fu *Cryst. Growth Des.* **2008**, 8, 4511-4516.

[429] C. E. Knapp, I. D. Prassides, S. Sathasivam, I. P. Parkin, C. J. Carmalt *ChemPlusChem.* **2014**, 79, 122-127.

[430] F. Meyer, R. Hempelmann, S. Mathur, M. Veith *J. Mater. Chem.* **1999**, 9, 1755-1763.

[431] S. Mathur, M. Veith, M. Haas, H. Shen, N. Lecerf, V. Huch, S. Hufner, R. Haberkorn, H. P. Beck, M. Jilavi *J. Am. Ceram. Soc.* **2001**, 84, 1921-1928.

[432] S. Mathur, S. Barth, H. Shen *Chem. Vap. Dep.* **2005**, 11, 11-16.

[433] S. Mathur, C. Cavelius, H. Shen *Z. Anorg. Allg. Chem.* **2009**, 635, 2106-2111.

[434] J. Mohapatra, S. Nigam, J. Gupta, A. Mitra, M. Aslam, D. Bahadur *RSC Adv.* **2015**, 5, 14311-14321.

[435] Y.-w. Jun, J.-w. Seo, J. Cheon *Acc. Chem. Res.* **2008**, 41, 179-189.

[436] F. Li, J. Liu, D. G. Evans, X. Duan *Chem. Mater.* **2004**, 16, 1597-1602.

[437] S. Mathur, M. Veith, V. Sivakov, H. Shen, V. Huch, U. Hartmann, H. B. Gao *Chem. Vap. Dep.* **2002**, 8, 277-283.

[438] D. Li, H. Yun, B. T. Diroll, V. V. T. Doan-Nguyen, J. M. Kikkawa, C. B. Murray *Chem. Mater.* **2016**, 28, 480-489.

[439] F. Biegger, MSc Thesis, Vienna University of Technology, **2013**.

[440] S. D. Reid, A. L. Hector, W. Levason, G. Reid, B. J. Waller, M. Webster *Dalton Trans.* **2007**, 4769-4777.

[441] C. H. Winter, T. S. Lewkebandara, J. W. Proscia *Chem. Mater.* **1992**, 4, 1144-1146.

[442] S. T. Lewkebandara, C. H. Winter *Adv. Mater.* **1994**, 6, 237-239.

[443] H. S. W. Chang, D. M. Schleich *J. Solid State Chem.* **1992**, 100, 62-70.

[444] R. Lichtenberger, M. Puchberger, S. O. Baumann, U. Schubert *J. Sol-Gel Sci. Technol.* **2009**, 50, 130-140.

[445] M. S. Bains *Can. J. Chem.* **1962**, 40, 381-383.

[446] H. Sun, Q. Zhao, Y. Liu, H. Hu, X. You, Z. Zhou *J. Coord. Chem.* **1999**, 47, 459-465.

[447] K. A. Fleeting, P. O'Brien, A. C. Jones, D. J. Otway, A. J. P. White, D. J. Williams *J. Chem. Soc., Dalton Trans.* **1999**, 2853-2859.

[448] I. Raabe, K. Wagner, K. Guttsche, M. Wang, M. Gratzel, G. Santiso-Quinones, I. Krossing *Chem. - Eur. J.* **2009**, 15, 1966-1976.

[449] A. Kraft, J. Beck, I. Krossing *Chem. - Eur. J.* **2011**, 17, 12975-12980.

[450] Y. Wang, W. Zhang, Y. Li, L. Ye, G. Yang *Chem. Mater.* **1999**, 11, 530-532.

[451] H. Li, F. Zhang, Y. Wang, D. Zheng *Mater. Sci. Eng., B.* **2003**, B100, 40-46.

[452] T. Saegusa, T. Ueshima *Inorg. Chem.* **1967**, 6, 1679-1681.

[453] L. A. Miinea, S. Suh, D. M. Hoffman *Inorg. Chem.* **1999**, 38, 4447-4454.

[454] S. Daniele, D. Tcheboukov, L. G. Hubert-Pfalzgraf, S. Lecocq *Inorg. Chem. Commun.* **2002**, 5, 347-350.

[455] R. D. Shannon *Acta Cryst. A.* **1976**, A32, 751-767.

[456] T. L. Ho *Tetrahedron.* **1985**, 41, 3-86.

[457] P. Pérez, Y. Simón-Manso, A. Aizman, P. Fuentealba, R. Contreras *J. Am. Chem. Soc.* **2000**, 122, 4756-4762.

[458] C. D. Beard, L. Carr, M. F. Davis, J. Evans, W. Levason, L. D. Norman, G. Reid, M. Webster *Eur. J. Inorg. Chem.* **2006**, 4399-4406.

[459] S. Chitsaz, E. Iravani, B. Neumüller *Z. Anorg. Allg. Chem.* **2002**, 628, 2279-2285.

[460] G. G. Briand, B. F. T. Cooper, D. B. S. MacDonald, C. D. Martin, G. Schatte *Inorg. Chem.* **2006**, 45, 8423-8429.

[461] I. Peckermann, A. Kapelski, T. P. Spaniol, J. Okuda *Inorg. Chem.* **2009**, 48, 5526-5534.

[462] K. George, M. Jura, W. Levason, M. E. Light, L. P. Ollivere, G. Reid *Inorg. Chem.* **2012**, 51, 2231-2240.

[463] K.-H. Thiele, E. Hecht, T. Gelbrich, U. Dümichen *J. Organomet. Chem.* **1997**, 540, 89-94.

[464] CRC handbook of chemistry and physics : a ready-reference book of chemical and physical data, CRC Press, **2013**.

[465] A. A. Amusan, B. Kalkofen, H. Gargouri, K. Wandel, C. Pinnow, M. Lisker, E. P. Burte *J. Vac. Sci. Techn. A.* **2016**, 34, 01A126.

[466] J. A. Belk, Electron Microscopy and Microanalyis of Crystalline Materials, Elsevier Science Ltd, London, **1979**.

[467] J. I. Goldstein, D. E. Newbury, P. Echlin, D. C. Joy, C. E. Lyman, E. Lifshin, L. Sawyer, J. R. Michael, Scanning Electron Microscopy and X-ray Microanalysis, Springer Science, **2003**.

[468] G. A. Battiston, R. Gerbasi, M. Porchia, R. Bertoncello, F. Caccavale *Thin Solid Films*. **1996**, 279, 115-118.

[469] A. V. Naumkin, A. Kraut-Vass, S. W. Gaarenstroom, C. J. Powell in NIST X-ray Photoelectron Spectroscopy Database, National Institute of Standards and Technology, **2012**.

[470] J. M. Thomas, I. Adams, R. H. Williams, M. Barber *J. Chem. Soc., Faraday Trans. 2*. **1972**, 68, 755-764.

[471] B. R. Strohmeier, D. M. Hercules *J. Phys. Chem.* **1984**, 88, 4922-4929.

[472] B. R. Strohmeier, D. M. Hercules *J. Catal.* **1984**, 86, 266-279.

[473] B. R. Strohmeier, D. E. Leyden, R. S. Field, D. M. Hercules *J. Catal.* **1985**, 94, 514-530.

[474] D. Oeter, C. Ziegler, W. Goepel *Synth. Met.* **1993**, 61, 147-150.

[475] R. Kelly *Nuc. Inst. Methods.* **1978**, 149, 553-558.

[476] G. Padeletti, G. M. Ingo *Surf. Interface Anal.* **2002**, 34, 266-270.

[477] M. Gerstl, E. Navickas, M. Leitgeb, G. Friedbacher, F. Kubel, J. Fleig *Solid State Ionics*. **2012**, 225, 732-736.

[478] M. N. Rudden, J. Wilson, A. Siemoneit, Elementare Festkörperphysik und Halbleiterelektronik, Spektrum Akademischer Verlag, **1995**.

[479] A. K. Sharma, Semiconductor Electronics, New Age International Publishers, **1996**.

[480] Y.-R. Luo, Comprehensive Handbook of Chemical Bond Energies, CRC Press, Boca Raton, FL, **2007**.

[481] G. E. McGuire, G. K. Schweitzer, T. A. Carlson *Inorg. Chem.* **1973**, 12, 2450-2453.

[482] Y. Tao, A. Yelon, E. Sacher, Z. H. Lu, M. J. Graham *Appl. Phys. Lett.* **1992**, 60, 2669-2671.

[483] S. T. Lewkebandara, P. J. McKarns, B. S. Haggerty, G. P. A. Yap, A. L. Rheingold, C. H. Winter *Polyhedron*. **1998**, 17, 1-9.

[484] G. Martin, J. Ascanio *React. Kinet. Catal. Lett.* **1989**, 38, 153-158.

[485] X. Zheng, E. M. Fisher, F. C. Gouldin, L. Zhu, J. W. Bozzelli *Proc. Comb. Inst.* **2009**, 32, 469-476.

[486] G. Martin, H. Martinez, J. Ascanio *Int. J. Chem. Kinet.* **1989**, 21, 193-206.

[487] C. D. Wagner, Handbook of X-Ray and Ultraviolet Photoelectron Spectroscopy, University of Michigan, **1977**.

[488] W. Du, J. Zhu, S. Li, X. Qian *Cryst. Growth Des.* **2008**, 8, 2130-2136.

[489] Y. Xing, H. Zhang, S. Song, J. Feng, Y. Lei, L. Zhao, M. Li *Chem. Commun.* **2008**, 1476-1478.

[490] M. A. Franzman, R. L. Brutchey *Chem. Mater.* **2009**, 21, 1790-1792.

[491] J. Tabernor, P. Christian, P. O'Brien *J. Mater. Chem.* **2006**, 16, 2082-2087.

[492] A. Lutfi Abdelhady, K. Ramasamy, M. A. Malik, P. O'Brien *Mater. Lett.* **2013**, 99, 138-141.

[493] J.-B. Shi, C.-J. Chen, Y.-T. Lin, W.-C. Hsu, Y.-C. Chen, P.-F. Wu *Nanoscale Res. Lett.* **2009**, 4, 1059-1063.

[494] M. Afzaal, M. A. Malik, P. O'Brien *Chem. Commun.* **2004**, 334-335.

[495] V. G. Dubrovskii, Nucleation Theory and Growth of Nanostructures, Springer Berlin Heidelberg, **2013**.

[496] M. Karakiz, B. Toydemir, B. Unal, L. Colakerol Arslan *Eur. Phys. J.: Appl. Phys.* **2014**, 65, 20403-20409.

[497] V. G. Dubrovskii, N. V. Sibirev, G. E. Cirlin, J. C. Harmand, V. M. Ustinov *Phys. Rev. E.* **2006**, 73, 021603-021613.

[498] W. K. Liu, W. T. Yuen, R. A. Stradling *J. Vac. Sci. Technol., B.* **1995**, 13, 1539-1545.

[499] C. Battistoni, L. Gastaldi, A. Lapiccirella, G. Mattogno, S. Viticoli *J. Phys. Chem. Solids.* **1986**, 47, 899-903.

[500] S. Mathur, M. Veith, M. Haas, H. Shen, N. Lecerf, V. Huch, S. Hufner, R. Haberkorn, H. P. Beck, M. Jilavi *J. Am. Ceram. Soc.* **2001**, 84, 1921-1928.

[501] M. Veith, M. Haas, V. Huch *Chem. Mater.* **2005**, 17, 95-101.

[502] S. Mathur, C. Cavelius, K. Moh, H. Shen, J. Bauer *Z. Anorg. Allg. Chem.* **2009**, 635, 898-902.

[503] J. Spandl, M. Kusserow, I. Bruedgam *Z. Anorg. Allg. Chem.* **2003**, 629, 968-974.

[504] G. Cossu, G. M. Ingo, G. Mattogno, G. Padeletti, G. M. Proietti *Appl. Surf. Sci.* **1992**, 56-58, 81-88.

[505] F. Leccabue, R. Panizzieri, B. E. Watts, D. Fiorani, E. Agostinelli, A. Testa, E. Paparazzo *J. Cryst. Growth.* **1991**, 112, 644-650.

[506] B. Lee, S. Komarneni, Chemical Processing of Ceramics, CRC Press, **2005**.

[507] G. M. Sheldrick *Acta Cryst. A.* **2008**, 64, 112-122.

[508] G. M. Sheldrick *Acta Cryst. A.* **2015**, 71, 3-8.

[509] G. Sheldrick *Acta Cryst. C.* **2015**, 71, 3-8.

[510] E. Popowski, P. Kosse, H. Kelling, H. Jancke *Z. Anorg. Allg. Chem.* **1991**, 594, 179-190.

[511] H. Bürger, W. Sawodny, U. Wannagat *J. Organomet. Chem.* **1965**, 3, 113-120.

[512] K. N. Campbell, R. A. LaForge, B. K. Campbell *J. Org. Chem.* **1949**, 14, 346-354.

[513] S. Barth, PhD, Saarland University, **2008**.

[514] S. Barth, Universität des Saarlandes, **2003**.

4.4 CRYSTALLOGRAPHIC DATA

4.4.1 Al11

Bond	Distance /Å	Bond	Distance /Å	Bond	Distance /Å	Bond	Distance /Å
Al1-O2	1.7680(8)	N1-C4	1.4782(13)	N3-C12	1.4833(13)	N6-C20	1.4615(16)
Al1-O3	1.7369(8)	N1-C5	1.4778(13)	N4-C10	1.4625(13)	N6-C21	1.4527(16)
Al1-N1	2.0991(9)	N2-C3	1.4615(13)	N4-C13	1.4567(15)	C1-C2	1.5273(14)
Al1-N3	2.1192(9)	N2-C6	1.4554(16)	N4-C14	1.4563(15)	C1-C3	1.5230(15)
O1-C1	1.4051(12)	N2-C7	1.4489(17)	N5-C16	1.4610(14)	C8-C9	1.5333(14)
O2-C8	1.4070(11)	N3-C9	1.4789(13)	N5-C18	1.4686(15)	C8-C10	1.5262(14)
O3-C15	1.3995(12)	N3-C11	1.4751(13)	N5-C19	1.4619(14)	C15-C16	1.5211(14)
N1-C2	1.4859(12)	Al1-O1	1.7648(8)	N6-C17	1.4648(14)	C15-C17	1.5339(15)

Angle	/°	Angle	/°	Angle	/°	Angle	/°
Al1-O1-C1	119.45(6)	O1-C1-C2	109.61(8)	N2-C3-C1	114.07(9)	C9-N3-C12	109.90(8)
Al1-O2-C8	119.39(6)	O1-C1-C3	108.63(8)	N3-C9-C8	107.54(8)	C10-N4-C13	111.88(9)
Al1-O3-C15	141.21(7)	O2-Al1-N1	91.84(3)	N4-C10-C8	113.67(8)	C10-N4-C14	109.75(9)
Al1-N1-C2	100.83(6)	O2-Al1-N3	84.11(3)	N5-C16-C15	114.84(9)	C11-N3-C12	108.26(8)
Al1-N1-C4	117.13(6)	O2-Al1-O3	117.83(4)	N6-C17-C15	113.39(9)	C13-N4-C14	109.23(9)
Al1-N1-C5	110.39(6)	O2-C8-C10	109.37(8)	C2-N1-C4	109.43(8)	C16-C15-C17	109.91(8)
Al1-N3-C11	115.00(6)	O2-C8-C9	109.16(8)	C2-N1-C5	110.47(8)	C16-N5-C18	111.80(9)
Al1-N3-C12	111.28(6)	O3-Al1-N1	94.77(4)	C3-N2-C6	109.79(10)	C16-N5-C19	110.76(9)
Al1-N3-C9	100.56(6)	O3-Al1-N3	99.66(4)	C3-N2-C7	111.47(10)	C17-N6-C20	110.86(9)

O1-Al1-N1	83.87(3)	O3-C15-C16	111.56(8)	C4-N1-C5	108.36(8)	C17-N6-C21	111.90(9)
O1-Al1-N3	87.59(3)	O3-C15-C17	110.08(8)	C6-N2-C7	110.06(11)	C18-N5-C19	108.57(9)
O1-Al1-O2	128.55(4)	N1-Al1-N3	165.26(4)	C9-C8-C10	111.17(8)	C20-C1-C3	110.87(8)
O1-Al1-O3	113.62(4)	N1-C2-C1	107.99(8)	C9-N3-C11	111.67(8)	C20-N6-C21	109.02(10)

4.4.2 Ga1

Bond	Distance /Å	Bond	Distance /Å	Bond	Distance /Å	Bond	Distance /Å
Ga1-O1	1.8485(10)	N1-C2	1.4822(17)	N3-C12	1.4768(18)	N6-C20	1.455(2)
Ga1-O2	1.8489(10)	N1-C4	1.4779(18)	N4-C10	1.4619(18)	N6-C21	1.459(2)
Ga1-O3	1.8339(10)	N1-C5	1.4767(18)	N4-C13	1.460(2)	C1-C2	1.5379(19)
Ga1-N1	2.1517(11)	N2-C3	1.443(2)	N4-C14	1.457(2)	C1-C3	1.541(2)
Ga1-N3	2.1803(12)	N2-C6	1.453(2)	N5-C17	1.4650(18)	C8-C9	1.5330(19)
O1-C1	1.3988(17)	N2-C7	1.459(3)	N5-C18	1.465(2)	C8-C10	1.5250(19)
O2-C8	1.4106(16)	N3-C9	1.4785(17)	N5-C19	1.4619(19)	C15-C16	1.5346(19)
O3-C15	1.4122(16)	N3-C11	1.4836(17)	N6-C16	1.4695(17)	C15-C17	1.5261(19)

Angle	/°	Angle	/°	Angle	/°	Angle	/°
Ga1-O1-C1	117.18(8)	O1-C1-C2	111.40(11)	N2-C3-C1	114.04(13)	C9-N3-C11	110.33(11)
Ga1-O2-C8	117.57(8)	O1-C1-C3	106.94(12)	N3-C9-C8	108.65(11)	C9-N3-C12	112.08(11)
Ga1-O3-C15	130.31(9)	O2-C8-C9	110.46(11)	N4-C10-C8	114.31(12)	C10-N4-C13	111.93(12)
Ga1-N1-C2	99.80(8)	O2-C8-C10	108.24(11)	N5-C17-C15	114.84(11)	C10-N4-C14	109.61(13)
Ga1-N1-C3	116.50(9)	O2-Ga1-O3	119.47(5)	N6-C16-C15	114.15(11)	C11-N3-C12	108.35(11)
Ga1-N1-C5	110.14(9)	O2-Ga1-N1	92.07(4)	C2-C1-C3	109.94(12)	C13-N4-C14	109.22(14)
Ga1-N3-C11	110.86(8)	O2-Ga1-N3	83.67(4)	C2-N1-C4	109.48(11)	C16-C15-C17	109.88(11)
Ga1-N3-C12	114.50(9)	O3-Ga1-N1	94.17(4)	C2-N1-C5	111.03(11)	C16-N6-C20	111.66(12)

Ga1-N3-C9	100.59(8)	O3-Ga1-N3	101.13(4)	C3-N2-C6	111.07(15)	C16-N6-C21	110.79(12)
O1-Ga1-O2	128.79(5)	O3-C15-C16	109.54(11)	C3-N2-C7	111.45(14)	C17-N5-C18	112.15(12)
O1-Ga1-O3	111.74(5)	O3-C15-C17	110.30(11)	C4-N1-C5	109.54(12)	C17-N5-C19	110.07(12)
O1-Ga1-N1	83.22(4)	N1-Ga1-N3	164.26(4)	C6-N2-C7	108.90(17)	C18-N5-C19	108.53(12)
O1-Ga1-N3	87.66(4)	N1-C2-C1	109.48(11)	C9-C8-C10	110.85(11)	C20-N6-C21	109.81(13)

4.4.3 In1

Bond	Distance /Å	Bond	Distance /Å	Bond	Distance /Å	Bond	Distance /Å
In1-O1	2.055(6)	N1-C2	1.486(11)	N4-C10	1.468(11)	C1-C2	1.529(13)
In1-O2	2.096(6)	N1-C4	1.462(11)	N4-C13	1.455(12)	C1-C3	1.532(13)
In1-O3	2.071(5)	N1-C5	1.474(11)	N4-C14	1.470(12)	C8-C9	1.528(10)
In1-N1	2.567(7)	N2-C3	1.464(13)	N5-C16	1.475(11)	C8-C10	1.535(10)
In1-N3	2.343(6)	N2-C6	1.453(15)	N5-C18	1.460(10)	C15-C17	1.535(11)
In1-N5	2.432(7)	N2-C7	1.459(17)	N5-C19	1.470(12)	C15-C16	1.554(11)
O1-C1	1.401(11)	N3-C11	1.491(10)	N6-C17	1.463(11)		
O2-C8	1.390(9)	N3-C12	1.484(10)	N6-C20	1.470(11)		
O3-C15	1.394(9)	N3-C9	1.477(10)	N6-C21	1.461(11)		

Angle	/°	Angle	/°	Angle	/°	Angle	/°
In1-O1-C1	121.7(5)	O1-In1-O2	95.7(2)	N1-In1-N3	94.0(2)	C6-N2-C7	108.3(10)
In1-O2-C8	118.1(4)	O1-In1-O3	153.8(2)	N1-In1-N5	108.7(2)	C9-C8-C10	107.0(6)
In1-O3-C15	118.7(4)	O1-C1-C2	112.3(7)	N1-C2-C1	112.0(7)	C9-N3-C11	107.7(6)
In1-N1-C2	95.9(5)	O1-C1-C3	108.1(8)	N2-C3-C1	113.5(9)	C9-N3-C12	111.1(6)
In1-N1-C4	112.1(5)	O2-In1-O3	105.2(2)	N3-In1-N5	152.0(2)	C10-N4-C11	110.1(8)

In1-N1-C5	119.4(5)	O2-In1-N1	164.1(2)	N3-C9-C8	111.9(6)	C10-N4-C14	113.2(7)
In1-N3-C11	115.3(5)	O2-In1-N3	77.6(2)	N4-C10-C8	114.4(7)	C11-N3-C12	110.5(6)
In1-N3-C12	111.4(5)	O2-In1-N5	83.6(2)	N5-C16-C15	110.5(6)	C13-N4-C14	109.6(8)
In1-N3-C9	100.4(4)	O2-C8-C9	110.2(6)	N6-C17-C15	114.4(6)	C16-C15-C17	106.7(6)
In1-N5-C16	97.6(5)	O2-C8-C10	113.6(6)	C2-C1-C3	110.6(7)	C16-N5-C18	111.1(6)
In1-N5-C18	118.2(5)	O3-In1-N1	87.9(2)	C2-N1-C4	110.0(7)	C16-N5-C19	110.8(6)
In1-N5-C19	109.7(5)	O3-In1-N3	88.4(2)	C2-N1-C5	109.0(6)	C17-N6-C20	110.0(7)
O1-In1-N1	74.7(2)	O3-In1-N5	76.6(2)	C3-N2-C6	111.0(8)	C17-N6-C21	113.1(6)
O1-In1-N3	111.8(2)	O3-C15-C16	111.9(6)	C3-N2-C7	110.6(11)	C18-N5-C19	108.9(7)
O1-In1-N5	90.5(3)	O3-C15-C17	113.2(6)	C4-N1-C5	109.4(8)	C20-N6-C21	108.9(7)

4.4.4 Al2

Bond	Distance /Å	Bond	Distance /Å	Bond	Distance /Å	Bond	Distance /Å
Al1-O1	1.7625(13)	N3-C15	1.498(2)	N6-C30A	1.485(6)	C21A-C22A	1.459(7)
Al1-O2	1.7632(12)	N3-C17	1.485(2)	N6-C30B	1.350(9)	C21B-C22B	1.457(8)
Al1-O3	1.7234(13)	N4-C14	1.463(2)	N6-C32A	1.397(8)	C23A-C24A	1.365(6)
Al1-N1	2.1614(15)	N4-C19A	1.421(5)	N6-C32B	1.565(9)	C23A-C24C	1.565(5)
Al1-N3	2.1573(15)	N4-C19B	1.460(6)	C1-C2	1.534(3)	C23A-C25A	1.460(9)
O1-C1	1.399(2)	N4-C21A	1.399(4)	C1-C3	1.518(3)	C23B-C24B	1.517(5)
O2-C12	1.4030(19)	N4-C21B	1.748(8)	C4-C5	1.524(3)	C23B-C25B	1.547(9)
O3-C23A	1.387(4)	N5A-C24A	1.502(7)	C6-C7	1.516(3)	C26A-C27A	1.445(14)
O3-C23B	1.419(4)	N5A-C24C	1.435(7)	C8-C9	1.478(7)	C26B-C27B	1.549(13)
N1-C2	1.482(2)	N5A-C26A	1.421(11)	C10-C11	1.524(4)	C28A-C29A	1.385(11)
N1-C4	1.494(2)	N5A-C28A	1.503(8)	C12-C13	1.527(2)	C28B-C29B	1.517(7)

N1-C6	1.487(2)	N5B-C24B	1.433(7)	C12-C14	1.523(2)	C30A-C31A	1.537(9)
N2-C3	1.471(3)	N5B-C26B	1.421(10)	C15-C16	1.526(3)	C30B-C31B	1.432(14)
N2-C8	1.437(4)	N5B-C28B	1.460(6)	C17-C18	1.521(2)	C32A-C33A	1.375(10)
N2-C10	1.459(4)	N6-C25A	1.497(6)	C19A-C20A	1.347(9)	C32B-C33B	1.073(12)
N3-C13	1.485(2)	N6-C25B	1.410(5)	C19B-C20B	1.495(10)		

Angle	/°	Angle	/°	Angle	/°	Angle	/°
Al1-O1-C1	120.25(11)	O3-C23A-C25A	111.9(4)	N6-C25A-C23A	113.6(6)	C19B-N4-C21B	104.7(3)
Al1-O2-C12	119.95(10)	O3-C23B-C24B	108.5(3)	N6-C25B-C23B	115.8(5)	C23B-C25B-C32B	162.3(6)
Al1-O3-C23A	150.7(2)	O3-C23B-C25B	109.0(4)	N6-C25B-C32B	52.7(4)	C24A-C23A-C25A	117.4(4)
Al1-O3-C23B	146.97(19)	N1-Al1-N3	165.82(6)	N6-C30A-C31A	112.2(5)	C24A-N5A-C26A	134.0(6)
Al1-N1-C2	99.42(10)	N1-C2-C1	108.46(14)	N6-C30B-C31B	109.9(8)	C24A-N5A-C28A	115.2(5)
Al1-N1-C4	109.28(10)	N1-C4-C5	116.17(16)	N6-C32A-C33A	136.4(9)	C24B-C23B-C25B	112.7(5)
Al1-N1-C6	115.54(11)	N1-C6-C7	114.20(14)	N6-C32B-C25B	45.8(3)	C24B-N5B-C26B	105.6(6)
Al1-N3-C13	98.29(9)	N2-C10-C11	111.9(3)	N6-C32B-C33B	117.8(11)	C24B-N5B-C28B	114.9(5)
Al1-N3-C15	109.09(10)	N2-C3-C1	112.36(17)	C2-N1-C4	111.15(14)	C24C-C23A-C25A	109.2(4)
Al1-N3-C17	117.05(11)	N2-C8-C9	112.0(3)	C2-N1-C6	109.39(13)	C24C-N5A-C26A	122.6(7)
O1-Al1-O2	126.62(7)	N3-C13-C12	107.64(13)	C2-C1-C3	110.91(18)	C24C-N5A-C28A	109.9(5)
O1-Al1-O3	119.58(7)	N3-C15-C16	116.01(15)	C3-N2-C8	112.0(2)	C25A-N6-C30A	86.6(5)
O1-Al1-N1	84.14(6)	N3-C17-C18	113.70(14)	C3-N2-C10	111.0(2)	C25A-N6-C30A	113.2(7)
O1-Al1-N3	90.62(6)	N4-C14-C12	111.99(14)	C4-N1-C6	111.48(14)	C25A-N6-C32A	143.5(7)
O1-C1-C2	108.94(14)	N4-C19A-C20A	114.3(5)	C8-N2-C10	110.0(3)	C25A-N6-C32B	105.9(5)
O1-C1-C3	109.75(15)	N4-C19B-C20B	114.2(6)	C13-C12-C14	111.34(14)	C25B-C32B-C33B	158.3(14)
O2-Al1-O3	113.80(6)	N4-C21A-C22A	116.6(4)	C13-N3-C15	111.09(13)	C25B-N6-C30A	114.2(4)
O2-Al1-N1	89.04(6)	N4-C21B-C22B	109.3(5)	C13-N3-C17	108.49(12)	C25B-N6-C30B	138.3(6)
O2-Al1-N3	83.52(6)	N5A-C24A-C23A	124.1(5)	C14-N4-C19A	114.6(2)	C25B-N6-C32B	81.5(5)

O2-C12-C13	108.53(12)	N5A-C24C-C23A	115.2(4)	C14-N4-C19B	121.8(3)	C26A-N5A-C28A	110.8(6)
O2-C12-C14	110.57(13)	N5A-C26A-C27A	123.6(10)	C14-N4-C21A	109.8(2)	C26B-N5B-C28B	114.8(6)
O3-Al1-N1	96.99(6)	N5A-C28A-C29A	113.5(6)	C14-N4-C21B	116.3(2)	C30A-N6-C32A	113.1(5)
O3-Al1-N3	97.05(6)	N5B-C24B-C23B	117.5(4)	C15-N3-C17	112.01(14)	C30B-N6-C32B	107.9(7)
O3-C23A-C24A	128.1(4)	N5B-C26B-C27B	111.5(6)	C19A-N4-C21A	116.3(3)		
O3-C23A-C24C	111.4(4)	N5B-C28B-C29B	118.2(4)	C19A-N4-C21B	129.1(3)		

4.4.5 Ga2

Bond	Distance /Å	Bond	Distance /Å	Bond	Distance /Å	Bond	Distance /Å
Ga1-O1	1.8440(9)	N3-C13	1.4860(14)	N6-C30B	1.479(3)	C23A-C24A	1.517(5)
Ga1-O2	1.8468(9)	N3-C15	1.4852(15)	N6-C32A	1.464(5)	C23A-C25A	1.518(4)
Ga1-O3	1.8210(9)	N3-C17	1.4933(15)	N6-C32B	1.5308(16)	C23B-C24B	1.540(3)
Ga1-N1	2.2170(10)	N4-C14	1.4614(15)	C1-C2	1.5286(17)	C23B-C25B	1.529(5)
Ga1-N3	2.2150(9)	N4-C19	1.4606(17)	C1-C3	1.5135(18)	C26A-C27A	1.463(6)
O1-C1	1.4083(13)	N4-C21	1.4733(17)	C4-C5	1.5269(18)	C26B-C27B	1.519(5)
O2-C12	1.4026(13)	N5A-C24A	1.453(4)	C6-C7	1.504(3)	C28A-C29A	1.476(4)
O3-C23A	1.438(3)	N5A-C26A	1.398(5)	C8-C9	1.526(2)	C28B-C29B	1.472(14)
O3-C23B	1.376(2)	N5A-C28A	1.470(4)	C10-C11	1.5282(16)	C30A-C31A	1.491(17)
N1-C2	1.4830(15)	N5B-C24B	1.489(3)	C12-C13	1.5294(16)	C30B-C31B	1.502(7)
N1-C4	1.4889(16)	N5B-C26B	1.414(4)	C12-C14	1.5199(17)	C32A-C33A	1.514(11)
N1-C6	1.4943(16)	N5B-C28B	1.474(4)	C15-C16	1.5230(17)	C32B-C33B	1.426(3)
N2-C3	1.4687(16)	N6-C25A	1.429(4)	C17-C18	1.516(2)		
N2-C8	1.475(2)	N6-C25B	1.473(2)	C19-C20	1.509(2)		
N2-C10	1.460(2)	N6-C30A	1.526(4)	C21-C22	1.518(6)		

Angle	/°	Angle	/°	Angle	/°	Angle	/°
Ga1-O1-C1	117.96(7)	O2-Ga1-N1	88.01(4)	N4-C19-C20	111.76(13)	C4-N1-C6	112.25(10)
Ga1-O2-C12	118.03(7)	O2-Ga1-N3	82.41(4)	N4-C21-C22	112.39(12)	C8-N2-C10	112.55(13)
Ga1-O3-C23A	132.74(11)	O3-Ga1-N1	99.53(4)	N5A-C24A-C23A	115.1(4)	C13-C12-C14	110.89(9)
Ga1-O3-C23B	141.57(15)	O3-Ga1-N3	96.49(4)	N5B-C24B-C23B	111.9(2)	C13-N3-C15	108.87(9)
Ga1-N1-C2	99.50(7)	O3-C23A-C24A	111.6(3)	N5A-C26A-C27A	113.2(4)	C13-N3-C17	111.88(9)
Ga1-N1-C4	115.69(8)	O3-C23B-C24B	109.8(2)	N5B-C26B-C27B	117.2(4)	C14-N4-C19	112.69(11)
Ga1-N1-C6	107.45(7)	O3-C23A-C25A	113.2(3)	N5A-C28A-C29A	112.6(4)	C14-N4-C21	110.69(10)
Ga1-N3-C13	97.05(6)	O3-C23B-C25B	111.14(16)	N5B-C28B-C29B	112.2(3)	C15-N3-C17	112.51(9)
Ga1-N3-C15	116.32(7)	N1-Ga1-N3	163.42(4)	N6-C25A-C23A	113.6(3)	C19-N4-C21	111.20(11)
Ga1-N3-C17	109.26(7)	N1-C2-C1	109.72(9)	N6-C25B-C23B	115.69(17)	C24A-C23A-C25A	110.5(3)
O1-Ga1-N1	83.85(4)	N1-C4-C5	114.70(11)	N6-C30A-C31A	120.9(14)	C24B-C23B-C25B	112.91(19)
O1-Ga1-N3	91.97(4)	N1-C6-C7	116.36(11)	N6-C30B-C31B	104.5(17)	C24A-N5A-C26A	116.6(3)
O1-Ga1-O2	130.04(4)	N2-C3-C1	112.24(10)	N6-C32A-C33A	112.7(4)	C24B-N5B-C26B	115.3(3)
O1-Ga1-O3	119.57(4)	N2-C8-C9	112.65(14)	N6-C32B-C33B	111.0(7)	C24A-N5A-C28A	111.6(4)
O1-C1-C2	110.48(9)	N2-C10-C11	112.45(14)	C2-C1-C3	109.63(10)	C24B-N5B-C28B	108.9(2)
O1-C1-C3	109.38(10)	N3-C13-C12	108.72(9)	C2-N1-C4	109.31(9)	C26A-N5A-C28A	113.7(3)
O2-Ga1-O3	110.38(4)	N3-C15-C16	113.64(10)	C2-N1-C6	112.02(10)	C26B-N5B-C28B	113.5(3)
O2-C12-C13	110.06(9)	N3-C17-C18	115.57(10)	C3-N2-C10	110.96(11)		
O2-C12-C14	110.36(9)	N4-C14-C12	110.70(9)	C3-N2-C8	111.22(12)		

4.4.6 Ga6

Bond	Distance /Å	Bond	Distance /Å	Bond	Distance /Å	Bond	Distance /Å
Ga1-O1	1.866(2)	N2-C13	1.509(4)	S3-C30	1.863(4)	C16-C17	1.541(4)
Ga1-O2	1.863(2)	N2-C14	1.512(4)	C1-C2	1.551(4)	C19-C20	1.536(5)
Ga1-O3	1.842(2)	N2-C16	1.506(4)	C1-C7	1.549(4)	C19-C21	1.532(5)
Ga1-N1	2.234(2)	N3-C24	1.483(4)	C3-C4	1.549(4)	C19-C22	1.547(4)
Ga1-N2	2.219(3)	N3-C25	1.498(4)	C5-C6	1.539(4)	C23-C24	1.537(5)
O1-C1	1.429(3)	N3-C27	1.482(4)	C8-C9	1.548(4)	C23-C29	1.552(5)
O2-C12	1.423(4)	S1-C7	1.836(3)	C8-C10	1.543(5)	C25-C26	1.537(6)
O3-C23	1.416(4)	S1-C8	1.850(3)	C8-C11	1.537(5)	C27-C28	1.541(6)
N1-C2	1.499(4)	S2-C18	1.833(3)	C12-C13	1.540(4)	C30-C31	1.532(5)
N1-C3	1.506(4)	S2-C19	1.862(3)	C12-C18	1.540(4)	C30-C32	1.542(5)
N1-C5	1.496(4)	S3-C29	1.836(3)	C14-C15	1.521(5)	C30-C33	1.531(5)

Angle	/°	Angle	/°	Angle	/°	Angle	/°
Ga1-O1-C1	116.75(17)	O2-C12-C13	110.2(2)	S1-C8-C11	110.7(2)	C13-N2-C14	109.3(2)
Ga1-O2-C12	118.28(18)	O2-C12-C18	109.1(2)	S1-C8-C9	102.8(2)	C13-N2-C16	111.4(2)
Ga1-O3-C23	129.4(2)	O3-Ga1-N1	93.58(10)	S2-C18-C12	110.8(2)	C13-C12-C18	111.2(3)
Ga1-N1-C2	97.00(17)	O3-Ga1-N2	103.06(10)	S2-C19-C20	110.1(2)	C14-N2-C16	111.7(2)
Ga1-N1-C3	109.79(18)	O3-C23-C24	110.0(3)	S2-C19-C21	110.5(2)	C18-S2-C19	103.43(15)
Ga1-N1-C5	115.61(18)	O3-C23-C29	110.6(3)	S2-C19-C22	104.3(2)	C20-C19-C21	111.7(3)
Ga1-N2-C13	99.92(17)	N1-Ga1-N2	163.32(9)	S3-C29-C23	108.3(2)	C20-C19-C22	109.4(3)
Ga1-N2-C14	118.56(19)	N1-C2-C1	110.1(2)	S3-C30-C31	110.5(2)	C21-C19-C22	110.5(3)
Ga1-N2-C16	105.38(17)	N1-C3-C4	115.7(3)	S3-C30-C32	104.3(3)	C24-N3-C25	110.8(3)
O1-Ga1-O2	131.75(10)	N1-C5-C6	114.2(3)	S3-C30-C33	110.2(3)	C24-N3-C27	110.5(3)

O1-Ga1-O3	107.91(10)	N2-C13-C12	109.1(2)	C2-N1-C3	111.3(2)	C24-C23-C29	112.5(3)
O1-Ga1-N1	82.97(9)	N2-C14-C15	114.2(3)	C2-N1-C5	108.8(2)	C25-N3-C27	109.7(3)
O1-Ga1-N2	90.67(9)	N2-C16-C17	116.6(2)	C2-C1-C27	109.8(2)	C29-S3-C30	103.92(16)
O1-C1-C2	111.2(2)	N3-C24-C23	114.6(3)	C3-N1-C5	113.3(2)	C31-C30-C32	110.4(3)
O1-C1-C7	109.1(2)	N3-C25-C26	113.4(3)	C7-S1-C8	104.71(14)	C32-C30-C33	110.5(3)
O2-Ga1-O3	120.09(10)	N3-C27-C28	112.6(3)	C9-C8-C10	110.2(3)	C33-C30-C31	110.8(3)
O2-Ga1-N1	89.19(9)	S1-C7-C1	108.7(2)	C9-C8-C11	110.7(3)		
O2-Ga1-N2	83.56(9)	S1-C8-C10	111.2(2)	C10-C8-C11	111.0(3)		

4.4.7 In8

Bond	Distance /Å	Bond	Distance /Å	Bond	Distance /Å	Bond	Distance /Å
In1-O1	2.0504(14)	S4-C22	1.820(2)	C10A-C13A	1.527(9)	C31A-C33A	1.526(7)
In1-O2	2.0599(13)	S4-C23	1.861(3)	C10B-C11B	1.541(11)	C31A-C34A	1.521(7)
In1-O3	2.0467(15)	S5A-C30	1.819(3)	C10B-C12B	1.488(13)	C31B-C32B	1.505(14)
In1-S2	2.7210(6)	S5A-C31A	1.813(7)	C10B-C13B	1.507(13)	C31B-C33B	1.524(14)
In1-S4	2.7821(6)	S5B-C30	1.923(7)	C14-C15	1.545(3)	C31B-C34B	1.521(14)
In1-S6	2.8123(5)	S5B-C31B	1.84(2)	C14-C17	1.542(3)	C36-C37	1.505(4)
O1-C1	1.415(3)	S6-C35	1.809(2)	C14-C22	1.538(3)	C36-C38	1.518(3)
O2-C14	1.395(2)	S6-C36	1.852(2)	C15-C16	1.513(4)	C36-C39	1.521(4)
O3-C27	1.398(3)	C1-C2	1.517(3)	C18-C19	1.507(5)	C40A-C41A	1.497(5)
S1A-C4A	1.837(3)	C1-C4A	1.539(4)	C18-C20	1.533(4)	C40B-C41B	1.497(5)
S1A-C4B	1.889(5)	C1-C4B	1.539(4)	C18-C21	1.508(5)	C41A-C42A	1.503(5)
S1A-C5	1.795(3)	C1-C9A	1.545(3)	C23-C24	1.519(4)	C41B-C42B	1.497(5)
S1B-C5	1.964(5)	C1-C9B	1.717(7)	C23-C25	1.517(4)	C42A-C43A	1.502(5)

S2-C10A	1.785(7)	C2-C3	1.484(4)	C23-C26	1.521(4)	C42B-C43B	1.498(5)
S2-C10B	1.976(15)	C5-C6	1.528(6)	C27-C28	1.541(3)	C43A-C44A	1.494(5)
S2-C9A	1.872(3)	C5-C7	1.525(4)	C27-C30	1.535(4)	C43B-C44B	1.495(5)
S2-C9B	1.595(7)	C5-C8	1.499(4)	C27-C35	1.541(3)		
S3-C17	1.818(2)	C10A-C11A	1.525(9)	C28-C29	1.527(4)		
S3-C18	1.819(3)	C10A-C12A	1.493(7)	C31A-C32A	1.525(8)		

Angle	/°	Angle	/°	Angle	/°	Angle	/°
In1-O1-C1	120.51(11)	O3-C27-C30	107.50(19)	S5A-C31A-C34A	111.7(4)	C19-C18-C21	109.7(4)
In1-O2-C14	122.79(12)	O3-C27-C35	112.21(19)	S5B-C31B-C32B	108.9(14)	C20-C18-C21	109.3(3)
In1-O3-C27	129.26(12)	S1A-C5-C6	105.5(3)	S5B-C31B-C33B	104.1(15)	C23-S4-C22	104.11(12)
In1-S2-C9A	83.57(10)	S1A-C5-C7	103.8(2)	S5B-C31B-C34B	112.5(14)	C24-C23-C25	110.3(3)
In1-S2-C9B	101.2(2)	S1A-C5-C8	117.6(3)	S6-C35-C27	109.29(15)	C24-C23-C26	111.1(3)
In1-S2-C10A	117.4(2)	S1B-C5-C6	123.3(3)	S6-C36-C38	103.73(18)	C25-C23-C26	111.0(3)
In1-S2-C10B	111.9(4)	S1B-C5-C7	104.9(2)	S6-C36-C39	107.9(2)	C27-C28-C29	113.8(2)
In1-S4-C22	90.39(7)	S1B-C5-C8	97.8(3)	C1-C2-C3	114.9(2)	C28-C27-C30	111.7(2)
In1-S4-C23	117.98(9)	S2-In1-S4	170.790(19)	C1-C4A-S1A	115.6(2)	C28-C27-C35	106.82(19)
In1-S6-C35	89.92(8)	S2-In1-S6	100.250(19)	C2-C1-C4A	110.7(2)	C30-S5A-C31A	106.2(2)
In1-S6-C36	119.43(9)	S2-C9A-C1	108.2(2)	C2-C1-C9A	117.5(2)	C30-S5B-C31B	95.3(6)
O1-In1-O2	103.25(6)	S2-C9B-C1	113.7(4)	C2-C1-C9B	85.6(3)	C30-C27-C35	110.6(2)
O1-In1-O3	156.61(6)	S2-C10A-C11A	112.9(5)	C4A-S1A-C5	105.80(13)	C32A-C31A-C33A	110.5(5)
O1-In1-S2	73.30(4)	S2-C10A-C12A	111.8(5)	C4A-C1-C9A	98.6(2)	C32A-C31A-C34A	109.8(6)
O1-In1-S4	101.17(4)	S2-C10A-C13A	101.1(5)	C6-C5-C7	111.3(3)	C32B-C31B-C33B	110.6(16)
O1-In1-S6	87.40(4)	S2-C10B-C11B	106.9(9)	C6-C5-C8	108.3(3)	C32B-C31B-C34B	110.5(17)
O1-C1-C2	108.08(18)	S2-C10B-C12B	111.0(10)	C7-C5-C8	110.2(3)	C33A-C31A-C34A	108.5(5)
O1-C1-C4A	108.09(19)	S2-C10B-C13B	104.1(8)	C9A-S2-C10A	103.7(3)	C33B-C31B-C34B	110.1(16)

O1-C1-C9A	113.17(19)	S3-C17-C14	112.21(14)	C9B-S2-C10B	112.2(5)	C35-S6-C36	104.85(11)
O1-C1-C9B	107.0(3)	S3-C18-C19	110.5(2)	C11A-C10A-C12A	111.2(7)	C37-C36-C38	110.6(3)
O2-In1-O3	97.80(6)	S3-C18-C20	104.4(2)	C11A-C10A-C13A	109.3(7)	C37-C36-C39	112.0(3)
O2-In1-S2	95.61(4)	S3-C18-C21	110.3(2)	C11B-C10B-C12B	110.2(11)	C38-C36-C39	110.2(2)
O2-In1-S4	78.29(4)	S4-In1-S6	86.662(17)	C12A-C10A-C13A	110.0(7)	C40A-C41A-C42A	110.6(8)
O2-In1-S6	162.94(4)	S4-C22-C14	111.67(13)	C12B-C10B-C13B	111.7(12)	C40B-C41B-C42B	123(2)
O2-C14-C15	107.59(16)	S4-C23-C24	103.9(2)	C11B-C10B-C13B	112.6(10)	C41B-C42B-C43B	136(3)
O2-C14-C17	109.01(16)	S4-C23-C25	108.9(2)	C14-C15-C16	114.30(19)	C41A-C42A-C43A	110.7(7)
O2-C14-C22	111.19(16)	S4-C23-C26	111.28(19)	C15-C14-C17	111.08(16)	C42A-C43A-C44A	107.3(7)
O3-In1-S2	94.78(5)	S5A-C30-C27	118.2(2)	C15-C14-C22	106.84(16)	C42B-C43B-C44B	116(3)
O3-In1-S4	92.90(5)	S5B-C30-C27	96.5(4)	C17-S3-C18	105.14(12)	S5A-C31A-C32A	111.2(4)
O3-In1-S6	74.75(4)	S5A-C31A-C32A	111.2(4)	C17-C14-C22	111.07(18)		
O3-C27-C28	108.0(2)	S5A-C31A-C33A	104.9(5)	C19-C18-C20	112.4(3)		

4.4.8 FeGa

Bond	Distance /Å	Bond	Distance /Å	Bond	Distance /Å	Bond	Distance /Å
Ga1-O1	1.797(6)	O1-C1	1.422(10)	C5-C7	1.527(12)	C21-C22	1.491(15)
Ga1-O2	1.820(5)	O2-C5	1.441(9)	C5-C8	1.527(12)	C21-C23	1.507(11)
Ga1-O3	1.886(5)	O3-C9	1.468(9)	C9-C10	1.528(11)	C21-C24	1.502(14)
Ga1-O4	1.906(5)	O4-C13	1.453(10)	C9-C11	1.499(11)	C25-C26	1.524(13)
Ga2-O5	1.911(5)	O5-C17	1.454(8)	C9-C12	1.518(12)	C25-C27	1.512(12)
Ga2-O6	1.934(5)	O6-C21	1.440(9)	C13-C14A	1.530(15)	C25-C28	1.538(12)
Ga2-O7	1.785(6)	O7-C25	1.428(10)	C13-C14B	1.50(2)	C29-C30	1.504(11)
Ga2-O8	1.812(5)	O8-C29	1.432(9)	C13-C15	1.532(13)	C29-C31	1.525(12)

Fe1-O3	2.005(5)	C1-C2	1.520(12)	C13-C16	1.485(14)	C29-C32	1.544(12)
Fe1-O4	2.017(6)	C1-C3	1.517(14)	C17-C18	1.515(11)		
Fe1-O5	1.999(5)	C1-C4	1.548(13)	C17-C19	1.511(10)		
Fe1-O6	1.995(5)	C5-C6	1.508(12)	C17-C20	1.519(11)		

Angle	/°	Angle	/°	Angle	/°	Angle	/°
Ga1-O1-C1	132.5(5)	O2-Ga1-O3	110.7(2)	O5-C17-C18	109.6(6)	C10-C9-C12	111.3(7)
Ga1-O2-C5	128.7(5)	O2-Ga1-O4	109.0(2)	O5-C17-C19	106.9(6)	C11-C9-C12	110.0(7)
Ga1-O3-Fe1	99.4(2)	O2-C5-C6	110.2(7)	O5-C17-C20	109.2(6)	C14A-C13-C15	103.4(14)
Ga1-O3-C9	125.9(4)	O2-C5-C7	110.4(7)	O6-Ga2-O7	116.7(2)	C14B-C13-C15	129(2)
Ga1-O4-Fe1	98.3(2)	O2-C5-C8	105.4(7)	O6-Ga2-O8	109.1(2)	C14A-C13-C16	117.1(16)
Ga1-O4-C13	128.4(5)	O3-Ga1-O4	83.5(2)	O6-C21-C22	108.4(9)	C14B-C13-C16	91(2)
Ga2-O5-Fe1	99.6(2)	O3-Fe1-O4	77.8(2)	O6-C21-C23	110.4(7)	C15-C13-C16	110.0(9)
Ga2-O5-C17	125.2(4)	O3-Fe1-O5	125.2(2)	O6-C21-C24	105.8(8)	C18-C17-C19	109.3(7)
Ga2-O6-Fe1	98.9(2)	O3-Fe1-O6	132.1(2)	O7-Ga2-O8	113.0(2)	C18-C17-C20	110.7(8)
Ga2-O6-C21	129.1(5)	O3-C9-C10	106.1(6)	O7-C25-C26	107.8(7)	C19-C17-C20	111.0(7)
Ga2-O7-C25	135.5(5)	O3-C9-C11	108.7(6)	O7-C25-C27	110.5(7)	C22-C21-C23	109.1(9)
Ga2-O8-C29	126.2(5)	O3-C9-C12	110.2(6)	O7-C25-C28	107.5(7)	C22-C21-C24	115.0(14)
Fe1-O3-C9	127.7(5)	O4-Fe1-O5	133.9(2)	O8-C29-C30	111.6(7)	C23-C21-C24	108.1(10)
Fe1-O4-C13	133.0(5)	O4-Fe1-O6	117.3(2)	O8-C29-C31	110.7(7)	C26-C25-C27	111.4(8)
Fe1-O5-C17	129.6(4)	O4-C13-C14A	109.3(9)	O8-C29-C32	104.8(6)	C26-C25-C28	109.6(8)
Fe1-O6-C21	131.9(5)	O4-C13-C14B	107.9(18)	C2-C1-C3	111.0(8)	C27-C25-C28	110.0(8)
O1-Ga1-O2	111.3(3)	O4-C13-C15	107.8(7)	C2-C1-C4	110.2(8)	C30-C29-C31	110.4(7)
O1-Ga1-O3	121.1(3)	O4-C13-C16	108.8(7)	C3-C1-C4	108.9(8)	C30-C29-C32	108.8(7)
O1-Ga1-O4	118.2(2)	O5-Ga2-O6	82.4(2)	C6-C5-C7	109.7(8)	C31-C29-C32	110.4(7)
O1-C1-C2	111.6(7)	O5-Ga2-O7	124.0(2)	C6-C5-C8	109.5(7)		

O1-C1-C3	108.0(8)	O5-Ga2-O8	107.8(2)	C7-C5-C8	111.5(8)
O1-C1-C4	107.1(7)	O5-Fe1-O6	78.7(2)	C10-C9-C11	110.4(7)

4.4.9 CuGa

Bond	Distance /Å	Bond	Distance /Å	Bond	Distance /Å	Bond	Distance /Å
Ga1-O1	1.8009(13)	Cu1-O6	1.9833(16)	C1-C4	1.534(3)	C17-C19	1.522(3)
Ga1-O2	1.7941(14)	O1-C1	1.429(2)	C5-C6	1.530(3)	C17-C20	1.522(3)
Ga1-O3	1.9179(15)	O2-C5	1.429(2)	C5-C7	1.534(3)	C21-C22	1.522(3)
Ga1-O4	1.8945(13)	O3-C9	1.465(2)	C5-C8	1.527(3)	C21-C23	1.522(3)
Ga2-O5	1.9004(15)	O4-C13	1.456(2)	C9-C10	1.523(3)	C21-C24	1.528(3)
Ga2-O6	1.9159(13)	O5-C17	1.458(2)	C9-C11	1.525(3)	C25-C26	1.533(3)
Ga2-O7	1.7923(14)	O6-C21	1.462(2)	C9-C12	1.528(2)	C25-C27	1.531(3)
Ga2-O8	1.7992(13)	O7-C25	1.437(2)	C13-C14	1.529(3)	C25-C28	1.530(3)
Cu1-O3	1.9780(14)	O8-C29	1.430(2)	C13-C15	1.529(3)	C29-C30	1.533(3)
Cu1-O4	1.9530(15)	C1-C2	1.527(3)	C13-C16	1.523(2)	C29-C31	1.528(3)
Cu1-O5	1.9437(13)	C1-C3	1.529(3)	C17-C18	1.523(3)	C29-C32	1.527(3)

Angle	/°	Angle	/°	Angle	/°	Angle	/°
Ga1-O1-C1	130.97(11)	O1-C1-C4	105.32(14)	O5-Ga2-O6	81.84(6)	C7-C5-C8	108.78(16)
Ga1-O2-C5	133.06(12)	O2-Ga1-O3	122.86(6)	O5-Ga2-O7	116.71(6)	C10-C9-C11	110.23(17)
Ga1-O3-Cu1	96.97(6)	O2-Ga1-O4	117.69(6)	O5-Ga2-O8	106.91(6)	C10-C9-C12	109.68(16)
Ga1-O3-C9	122.97(10)	O2-C5-C6	112.03(15)	O5-Cu1-O6	79.06(6)	C11-C9-C12	110.75(15)

Ga1-O4-Cu1	98.61(6)	O2-C5-C7	106.90(17)	O6-Ga2-O7	123.11(6)	C14-C13-C15	109.83(16)
Ga1-O4-C13	129.68(11)	O2-C5-C8	108.35(15)	O6-Ga2-O8	106.74(6)	C14-C13-C16	110.30(14)
Ga2-O5-Cu1	98.80(6)	O3-Ga1-O4	81.89(6)	O6-C21-C22	110.10(14)	C15-C13-C16	111.35(16)
Ga2-O5-C17	129.26(10)	O3-Cu1-O4	78.93(6)	O6-C21-C23	107.92(13)	C18-C17-C19	110.41(14)
Ga2-O6-Cu1	96.91(6)	O3-Cu1-O5	140.35(5)	O6-C21-C24	108.06(15)	C18-C17-C20	110.08(16)
Ga2-O6-C21	123.82(10)	O3-Cu1-O6	116.41(5)	O7-Ga2-O8	116.06(7)	C19-C17-C20	111.18(17)
Ga2-O7-C25	132.36(12)	O3-C9-C10	108.47(13)	O7-C25-C26	106.70(16)	C22-C21-C23	109.69(16)
Ga2-O8-C29	130.91(11)	O3-C9-C11	108.04(14)	O7-C25-C27	111.60(15)	C22-C21-C24	110.75(15)
Cu1-O3-C9	124.87(10)	O3-C9-C12	109.62(15)	O7-C25-C28	108.47(15)	C23-C21-C24	110.25(16)
Cu1-O4-C13	131.69(10)	O4-Cu1-O5	114.24(5)	O8-C29-C30	110.05(16)	C26-C25-C27	109.97(15)
Cu1-O5-C17	131.87(10)	O4-Cu1-O6	139.09(5)	O8-C29-C31	105.43(14)	C26-C25-C28	109.36(16)
Cu1-O6-C21	123.88(10)	O4-C13-C14	108.50(15)	O8-C29-C32	110.36(14)	C27-C25-C28	110.63(18)
O1-Ga1-O2	115.74(7)	O4-C13-C15	108.73(13)	C2-C1-C3	110.54(16)	C30-C29-C31	110.45(15)
O1-Ga1-O3	106.57(6)	O4-C13-C16	108.06(14)	C2-C1-C4	109.81(17)	C30-C29-C32	110.52(15)
O1-Ga1-O4	106.75(6)	O5-C17-C18	108.55(15)	C3-C1-C4	110.00(15)	C31-C29-C32	109.92(17)
O1-C1-C2	110.67(14)	O5-C17-C19	107.80(14)	C6-C5-C7	110.37(15)		
O1-C1-C3	110.38(16)	O5-C17-C20	108.74(13)	C6-C5-C8	110.29(18)		

4.5 Curriculum Vitae

Personal data

Name	Dipl.-Ing. Felix Biegger, BSc.
Address	Fröbelgasse 62/10, 1160 Wien
Date and Place of Birth	January, 8th 1988, Bregenz
Citizenship	Austrian
Email:	bieggerfelix@gmx.at

Education

Since 03/2013	PhD studies (supervised by Privdoz. Sven Barth) Institute of Materials Chemistry, Vienna University of Technology
11/2010 – 01/2013	Master studies Materials Chemistry, Vienna University of Technology Master thesis: "Synthesis and Characterisation of Novel Donor-functionalised Group 13 Alkoxides for CVD Applications" (supervised by Prof. Ulrich Schubert and Privdoz. Sven Barth)
09/2011 – 12/2012	Exchange semester (TASSEP), University of Calgary, Canada Research internship with Prof. Thomas Baumgartner on extended phospholes for optoelectronic applications
09/2007 – 11/2010	Bachelorstudies Technical Chemistry, Vienna University of Technology, Bachelor thesis: "Synthese und Charakterisierung von sauer/basisch modifizierten Silicafilmen mit hierarchisch aufgebautem Porennetzwerk" (supervised by Prof. Ulrich Schubert)
09/2006 – 03/2007	Compulsory military service, HsV MilKdo V, Bregenz
09/1998 - 07/2006	Secondary school, BG Blumenstraße, Bregenz

Work experience

Since 03/2013	University assistant, Institute of Materials Chemistry, Vienna University of Technology
05/2012-06/2012	Study assistant, Institute of Applied Synthetic Chemistry, Vienna University of Technology
07/2009-08/2009 07/2010-08/2010	Bezema AG Montlingen, Switzerland. Quality assurance division of textile dyes and additives.

Competences

Languages	German (mother tongue), English (fluent, spoken and written), French (advanced), Spanish (basics)
Technical competences	Handling of moisture and oxygen sensitive compounds, Schlenk techniques, CVD, powder XRD, single-crystal XRD, NMR, IR, Glovebox techniques, nitrogen sorption (BET)
IT competences	Windows and Mac OS, MS Office, chemistry related software (ChemDraw, X'Pert Highscore, SciFinder, etc.), image processing (GIMP)
Driving licenses	Class A and B
Further competences	Basic electronics, pcb design (Eagle CAD)

Awards

2010 & 2011	Merit scholarship, Vienna University of Technology

Further information

Hobbies	E-guitar, audio-related electronics, archery
Memberships	GÖCH (Gesellschaft österr. Chemiker)

Publications

- *"Molecular Engineering of the Physical Properties of Highly Luminescent π-Conjugated Phospholes"*
  Y. Ren, **F. Biegger**, T. Baumgartner, *J. Phys. Chem. C,* **2013**, 117, 4748-4758.

- *"Microwave-assisted $Ge_{1-x}Sn_x$ Nanowire Synthesis: Precursor Species and Growth Regimes"*
  M. S. Seifner, **F. Biegger**, A. Lugstein, J. Bernardi, S. Barth, *Chem. Mater.,* **2015**, 27, 6125-6130.

- *"Synthesis and Characterisation of Thioether functionalised Gallium and Indium Alkoxides"*
  S. Barth, **F. Biegger**, M. Puchberger, *Dalton Trans.,* **2015**, 44, 16439-16445.

- *"Direct Writing of CoFe Alloy Nanostructures by Focused Electron Beam Induced Deposition From a Heteronuclear Precursor"*
  F. Porrati, M. Pohlit, J. Müller, S. Barth, **F. Biegger**, C. Gspan, H. Plank, M. Huth, *Nanotechnology,* **2015**, 26, 475701.

- *"Monomeric aminoalcoholates of Aluminium(III), Gallium(III) and Indium(III)"*
  F. Biegger, S. Barth, *Monatsh. Chem.,* **2016**, 147, 341-348.

Posters and Talks

- F. Biegger*, S. Barth: "*Synthesis and Characterisation of Novel Donor-Functionalised Group 13 Alkoxides*"
  Poster: 15. Österreichische Chemietage 2013, TU Graz, Austria; 23.09.2013 - 26.09.2013

- F. Biegger*, S. Barth: "*Donorstabilisierte Gallium- und Indiumalkoxide als Precursoren in der Materialsynthese*"
  Oral Presentation: 8. Workshop Anorganische Chemie in Österreich(WACÖ), University Salzburg, Austria; 14.04.2014 - 15.04.2014

- S. Barth*, F. Biegger: "*Volatile Precursor Species for the Growth of Semiconductors*"
  Oral presentation: 5th Workshop on Focused Electron Beam Induced Processing, Frankfurt am Main, Germany; 21.07.2014 - 24.07.2014

- F. Biegger*, S. Barth: "*New Molecular Gallium And Indium Alkoxide Precursors For Material Synthesis*"
  Poster: 5th EuCheMS Chemistry Congress, Istanbul, Turkey; 31.08.2014 - 04.09.2014

- S. Barth*, F. Biegger: "*New Molecular Gallium and Indium Alkoxide Precursors for Material Synthesis*"
  Poster: 17. Vortragstagung für Anorganische Chemie der Wöhler-Vereinigung, Saarbrücken, Germany; 26.09.2014 - 29.09.2014

- S. Barth*, F. Biegger: "*Semiconductor Synthesis using Molecular Sources*"
  Oral presentation: Chemiedozententagung 2015, University Regensburg, Germany; 02.03.2015 - 04.03.2015

- S. Barth*, F. Biegger, F. Porrati, M. Huth: "*Synthesis and characterization of heterometallic carbonyls for focused electron beam induced deposition*"
  Poster: Annual Meeting of COST Action CM1301; Chemistry for Electron Induced Nanofabrication, Bratislava, Slovakia; 06.05.2015 - 09.05.2015

- F. Biegger*, S. Barth: "*Thioether-functionalized alkoxides: a novel precursor system for gallium and indium oxysulphides*"
  Oral Presentation: 16. Österreichische Chemietage, University Innsbruck, Austria; 21.09.2015 - 24.09.2015

- S. Barth*, F. Biegger: "*A new class of molecular alkoxide precursors and their behaviour in gas-phase processes*"
  Oral Presentation: EuroCVD 20, Sempach, Switzerland; 13.07.2015 - 17.07.2015